Sheffield Hallam University

A Sheffield Hallam University thesis

Development of Hybrid Sol-Gel Coatings on AA2024-T3 with Environmentally Benign Corrosion Inhibitors

Magdi Mussa

A thesis submitted in partial fulfilment of the requirements of

Sheffield Hallam University

for the degree of Doctor of Philosophy

June 2020

Declaration

I have not been enrolled for another award of the University, or other academic or professional organisation, whilst undertaking my research degree. None of the material contained in the thesis has been used in any other submission for an academic award. I am aware of and understand the University's policy on plagiarism and certify that this thesis is my own work. The use of all published or other sources of material consulted have been properly and fully acknowledged. The work undertaken towards the thesis has been conducted in accordance with the SHU Principles of Integrity in Research and the SHU Research Ethics Policy.

The word count of the thesis is 42508

Name	Magdi Hassn B. Mussa
Award	Degree of Doctor of Philosophy
Date of the Submission to the University	June 2020
Faculty	Industry and Innovation Research institute
Director(s) of Studies	Dr Oliver D Lewis & Dr Nicholas Farmilo

Abstract

Aluminium alloys are still considered as one of the primary light alloys with high strength that can be used in aerospace and marine structure with a moderate economic cost. However, aluminium alloys are affected by atmospheric and marine corrosion which reduces their overall reliability. The application of coatings is one of the strategies for mitigating the corrosion on aluminium alloys. Sol-gel technology is one of the coating strategies with potential for excellent chemical and environment stability, providing eco-friendly performance improvement. Sol-gel coatings can enhance corrosion resistance by adopting many corrosion inhibitors that can protect aluminium alloys substrates from corrosion.

In this project, three approaches are developed and studied to protect AA 2024 in high salinity of 3.5% NaCl environment. The first approach involved studying the direct application of film-forming environmentally benign corrosion inhibitors on the surface of the substrate without any involvement of the coating, these inhibitors are benzimidazole (BZI) and oleic acid (OA), and were studied alone and in combination. The second approach, investigated the corrosion protection of two sets of novel hybrid organic-inorganic sol-gel derived coatings using low-temperature cure processes at 80°C. The base sol-gel formula was made using alkoxide silane-based precursors including; tetraethylorthosilicate silane (TEOS) and trimethoxymethyl silane (MTMS) and this was labelled as (SBX- 80). The other enhanced formula was developed by adding the fluorinated precursor, 1H.1H.2H.2H-perfluorodecyltriethoxy silane (PFOTS), to the base SBX-80 formula to synthesis the fluorinated-sol-gel formula and this was labelled as (F-SBX-80). The third approach investigated the addition of corrosion inhibitors of benzimidazole (BZI) and oleic acid (OA) to the base SBX formula to increase the corrosion protection, either alone or in combination.

All sol-gel derived coating systems, including those modified with BZI or OA corrosion inhibitors exhibited excellent corrosion protection as evidenced visually, or by electrochemical methods with various levels of stability when immersed in saline solution. The coatings exhibited high capacitance and resistance that might provide active/barrier corrosion protection at small thicknesses less than 20 μm. Furthermore, there was an enhancement on mechanical properties of coating films with insignificant effect on the adhesion to the aluminium alloy substrate combined with excellent cracking-resistance. There was also a significant increase in surface water contact angle for these systems, which indicates the potential for enhanced easy-cleaning features.

Acknowledgement

I wish to express my sincere appreciation and deep gratitude to my directors of study (DOS) *Dr Oliver Lewis, Dr Nick Farmilo* and former-DOS *Dr Heming Wang*, for their invaluable help and skilful guidance, patience throughout this project. Their example is an inspiration for me about how scientific research should be conducted with enthusiasm, rigour and perseverance. Working with them was invaluable.

I owe my deepest gratitude to MERI laboratory Assist team and office mates for being with me from the first day to the final day of this work by all means. It would not have been possible to complete this thesis without their endless patience, support, encouragement, help and love. I also express my thanks to the FTIR team with particular *Miss Zahoor, Deeba* for their generous donations. Moreover, greater appreciations and thankful for all other MERI colleagues for their contribution, with particular *Kitchen, Matthew*, for his guidance and support.

Definitely, I would also like to thank my precious parents *Hassn & Salma,* my dear sisters and brother. They were always supporting me and encouraging me with their best wishes and endless love even with the far distance between us, and for believing in me and supporting me unconditionally at each turn of the studying road.

 I would also like to dedicate this thesis to my dear wife, *Sarra Takita*, whom I am indebted to for her patient, help, encouragement in this journey, and insightful comments to my thesis, alongside to my beloved kids, for their endless support, patience and understanding. Without them, I could not have made it here.

Finally, and by never means least in the name of *(Allah ﷲ),* the most gracious and the most merciful, all praise to Allah for all strength and blessing that he gave me for achieving and accomplish this project.

List of Contributions, Publications and Conferences

Papers:

1. M. H. Mussa, Y. Rahaq, F. D. Zahoor, N. Farmilo, H. Wang, and O. Lewis, "Enhancing the Sol-gel Coating Corrosion Protection by Increasing the Hydrophobicity on Aluminium alloy AA2024-T3," Prog. Org. Coatings, 2019 (submitted).

2. Y. Rahaq, M. Mussa, A. Mohammad, A. Hassan, and H. Wang, "Highly Reproducible Perovskite Solar Cells via Controlling the Morphologies of the Perovskite Thin Films by the Solution-processed Two-step Method," J. Mater. Sci. Mater. Electron., vol. 29, pp. 16426–16436, 2018.

Conferences:

1. The 19th International Sol-gel conference, "Liege Sol-gel 2017", Liege, Belgium Conference, Developing a Hybrid Sol-Gel Coating with Good Corrosion Protection for Maritime and Aerospace Applications, Id: SG2017-2232

2. MERI Annual Symposium 2017, Sheffield, Oral Presentation, topic: New hybrid Sol-gel coatings with excellent anti-corrosion properties for marine and aerospace applications.

3. BMRC/MERI Winter Posters Event 2017, Sheffield, Poster Presentation, topic: The Influence of AA2024-T3 Sample Preparation Techniques on Sol-Gel Coatings.

4. MERI Annual Symposium 2016, Sheffield, Poster Presentation, topic: The Effect of adding Fluoro-alkysilane (PFOTS) to Hybrid Sol-gel Coating on Anti-corrosion & Self-cleaning Properties for using on Aluminium Alloy AA2024 T3.

Consultancy Project

Investigating the Durability of Sol-Gel Coatings Corrosion Protection by Using the Cerium Nitrate Salt on AZ-31 Alloys for Aerospace Applications, The Project for Indestructible Paint Limited, MERI, Sheffield, 2018-19

Table of Contents

Table of Figures

List of Tables

List of Abbreviations

AA	Aluminum Alloy
IPM	Intermetallic particles
EIS	Electrochemical impedance spectroscopy
SEM	Scanning electron microscopy
FTIR	Fourier Transformation infrared spectroscopy
WCA	Water contact angle
AFM	Atomic force microscopy
EDX	Energy diffraction X-ray
PDPS	Potentiodynamic polarization scanning
OCP	Open-circuit potential
IFM	Infinite focus microscopy
I_{corr}	Corrosion current
E_{corr}	Corrosion potential
R	Resistance
C	Capacitance
Q	Time-constant
IZI	Impedance
Z_{img}	The imaginary part of the impedance
Z_{real}	The real part of the impedance
VCI	Volatile corrosion inhibitors
Sol-gel	A wet-chemical process that involves the formation of an inorganic colloidal suspension for metallic coating
BZI	Benzimidazole
OA	Oleic acid
SBX	Base sol-gel formula
F-SBX	Fluorinated-Sol-gel formula
BZI-SBX	Benzimidazole-Base sol-gel formula
OA-SBX	Oleic acid-Base sol-gel formula
BZI-OA-SBX	Benzimidazole-Oleic Acid-Base sol-gel formula

Chapter 1- Introduction

1.1 Background and Motivation

Marine and aviation environments are aggressive for engineering metals. Different issues arise when metal alloys are exposed to high salinity, microorganisms, algae, plants and nutrients, leading to the formation of corrosion. Corrosion has a significant impact on the loss of assets by degradation [1].

More recently, light alloys have been widely used in aircraft, offshore structures and facilities, engineering construction and many industrial applications. For example, aluminium, titanium and magnesium alloys as non-ferrous metals show excellent operational, ductility, and strength. However, the initial costs and operational life of aluminium alloys show their competency compared to other light metal alloys.

Pure aluminium is not suitable for structural applications due to its poor mechanical properties, which is why it is alloyed by the addition of elements such as magnesium, copper and silicon to improve the mechanical properties of the metal. For example, in 2000 series aluminium alloys, the primary alloying element is copper; these alloys types are essential in general construction and aerospace applications. Unfortunately, these alloys have a drawback which is that the corrosion resistance is not sufficient to use these alloys without protection against aggressive environments [2].

Surface protection is essential for preserving metal alloys from corrosion in corrosive environments [3]. Chromate-based conversion coatings have been widely used to protect aluminium alloys and these provide excellent corrosion protection. However, these contain chromium (VI) which banned in many industries due to their high toxicity and carcinogenicity. That is why legislation has imposed more significant limitations on the use of these techniques and demanded alternative coatings which are eco-friendlier and safer.

One of the potentially convenient and environmentally friendly alternative techniques is sol-gel coatings. For instance, a novel hybrid sol-gel coating with polyaniline has been developed for corrosion protection which showed excellent performance [4], [5]. Generally, sol-gel protective coatings have revealed excellent chemical stability, good oxidation control, and enhanced corrosion resistancefor metal substratesby encapsulating functionalized nanoparticles and/or inhibitors; sol-gel technology provides the potential protection for extreme applications [6], [7]. Current sol-gel coatings need to be cured at high temperature (usually above 100°C), while the low-temperature cure sol-gel coatings

which have been developed lack long-term stability after immersion in aqueous solutions. The requirement for a high-temperature cure is one of the factors which limit the application of sol-gels. Thus, it is crucial to develop low-temperature-cure and robust sol-gel coatings with superior anti-corrosion and/or antifouling properties.

Many techniques were advised to use for corrosion protection, basically, their theories based on reducing the direct contact with the aquatic media, which consider as an excellent achieving by creating new precursors capable of enhancing the sol-gel coating properties by increasing their` hydrophobicity. These coatings can be used as a top, or single -layer coating.

In addition, corrosion inhibitors such as organic volatile compounds which are commonly used to protect metal surfaces are another potential solution among the most efficient and commercially available means of corrosion protection on aluminium alloys. Usually, the organic corrosion inhibitor is a compound or mixture that is very active at service temperatures. The vaporised or liquid phase can inhibit the metal corrosion process, by interacting with a metallic surface chemically and/or physically to create an environment that inhibits metal corrosion[8]–[10].

Benzimidazole and oleic acid have both been used as corrosion inhibitors. These inhibitors have been used surrounded they may be encapsulated in a polymer coating such as acrylic or epoxy, both of which have shown excellent corrosion protection on both ferrous and nonferrous alloys[8], [9].

In this study, a novel hybrid organic-inorganic sol-gel with low-temperature cure will be developed from more than one precursor and optimised. The film-forming organic corrosion inhibitors of benzimidazole and oleic acid will then be combined with the organic-inorganic hybrid sol-gel formula to combine the corrosion properties of benzimidazole and/or oleic acid as corrosion inhibitors. It will be taking into consideration the benefits of using this new sol-gel coating to produce a thin film coating with excellent adhesion to suit applying top industrial coatings.

1.2 The research question

" Is it applicable to use film-forming corrosion inhibitors including benzimidazole and/or oleic acid encapsulated in sol-gel coating technology to protect light alloys for instance AA 2024-T3 from direct corrosion in 3.5% v/v NaCl?"

1.3 Aims and Objectives

This project aims and objectives will be structured as the following:

- Study the corrosion protection mechanism that is offered by direct applying of film-forming eco-corrosion inhibitors on aluminium alloy AA2024-T3 surface.

- Develop novel hybrid organic-inorganic sol-gel-derived low-temperature cure at 80°C which improve the anti-corrosion to AA2024-T3 aluminium alloy substrates. The modified hybrid sol-gel will be formed by using alkoxide silane-based precursors including a tetraethylorthosilicate silane (TEOS), trimethoxymethyl silane (MTES) and/or 1H.1H.2H.2H-perfluorodecyltriethoxy silane (PFOTS) in various combinations to obtain hybrid sol-gel coatings with good corrosion functionality for marine and/or aerospace applications.

- Promote hybrid organic-inorganic sol-gel coating by adding the eco-friendly film-forming corrosion inhibitors of benzimidazole (BZI) and oleic acid (OA), and check the enhancement on corrosion protection of the coating systems, and investigate the mechanism of corrosion protection. Then examine the mechanical performances of all sol-gel coating systems.

1.4 Thesis structure and organization

This thesis is organised into nine chapters, including the introduction, as follows:

Chapter 2 will present a literature review, expanding on various issues that will be discussed starting with concerning aluminium alloy corrosion mechanisms and their protection, before reviewing the use of organic inhibitors on aluminium alloys, such as benzimidazole and oleic acid that might be used in this work. Then it will discuss the use of sol-gels as an eco-friendly coating, explaining the sol-gel processes and synthesis and their use as corrosion protection coatings.

Chapter 3 will describe the characterisation and experimental procedures that have been conducted, such as the substrate material surface preparation, formulation of the hybrid organic-inorganic sol-gel formula and performances and investigating techniques against corrosion and other material analysis.

Chapter 4 will cover the bare and treated AA2024-T3 by direct exposure to benzimidazole and/or oleic acid and showing the performance of against corrosion;

Chapter 5 will talk about the performance of using two types of hybrid organic-inorganic sol-gel formula as a base and/or as a top-coat without the presence of any inhibitors;

Chapter 6 will present different results, discussing film-forming organic inhibitors of Benzimidazole and/or Oleic-oil, individually or in conjunction with one another, to the base organic-inorganic hybrid sol-gel formula to protect the AA2024-T3 from corrosion.

Chapter 7 will present the mechanical performances of Sol-gel coatings by examining the mechanical properties with including adhesion, film hardness and/or nano-indentation. All results and discussion chapters will be briefed with an individual summary of the findings, then

Chapter 8 will present the overall conclusions of the study.

Chapter 9 will suggest possible future work resulting from this study.

Chapter 2- Literature Review

2.1 Corrosion in Offshore and Aerospace Environment

The corrosion is an electrochemical reaction based on naturally irreversible oxidation on any metals to return existing standard form a transformation that involves charges transport at the interface from a metallic conductor to an ionic conductor in electrolyte surrounding. In offshore and aerospace industries, the development of the engineering materials for that are long-lasting or convenient is a challenge with significant impacts in different application, especially in high salinity areas. For instance, when dealing with materials in the design of various products, the designer should be aware of the effects that come from the surrounding environment. Therefore, the main concern for the selected material is to serve longer without an effective degradation and structural failure from direct or indirect corrosions in the services period, also the chosen materials must have properties that ensure the product can operate safely with minimum environmental impact [11]; Figure 2-1 shows the corrosion failures that could occur on the marine and offshore facilities.

Figure 2-1 Corrosion failures in marine and offshore environment[12]

2.2 Aspects of corrosion failure

The main points and characteristics can briefly be associated with the economic and operational consequences of corrosion in domestic and industrial assets including marine, and offshore facilities are as follows: [13]

- Loss of mechanical particulate properties including the strength of stressed parts due to the decreased cross-sectional area;

- Formation of rust leading to contamination for sensitive containers such as food and paint products;

- Leakage from pipelines and storage tanks caused by pitting corrosion and corrosion underneath insulation;

- Cracking and fracture;

- Effects on operational health and safety;

- Reduction in the lifetime of industrial and operational assets.

2.3 Common corrosion classifications

Corrosion is typically classified into various forms. These classifications are based on the appearance of the surface of the corroded material. As shown in Figure 2-2, the following classifications are commonly used: [14]–[16]

1. General or uniform corrosion

2. Pitting corrosion

3. Crevice corrosion

4. Intergranular corrosion

5. Galvanic corrosion

6. Cavitation erosion and impingement

7. Hydrogen penetration corrosion

8. Stress corrosion

9. Corrosion fatigue

Uniform

Intergranular

Galvanic

Crevice

Pitting

Hydrogen damage

Surface cracks   Internal voids

Stress corrosion

Corrosion fatigue

Hydrogen induced cracking

Fretting   Erosion   Cavitation

Cavitation, erosion and fretting
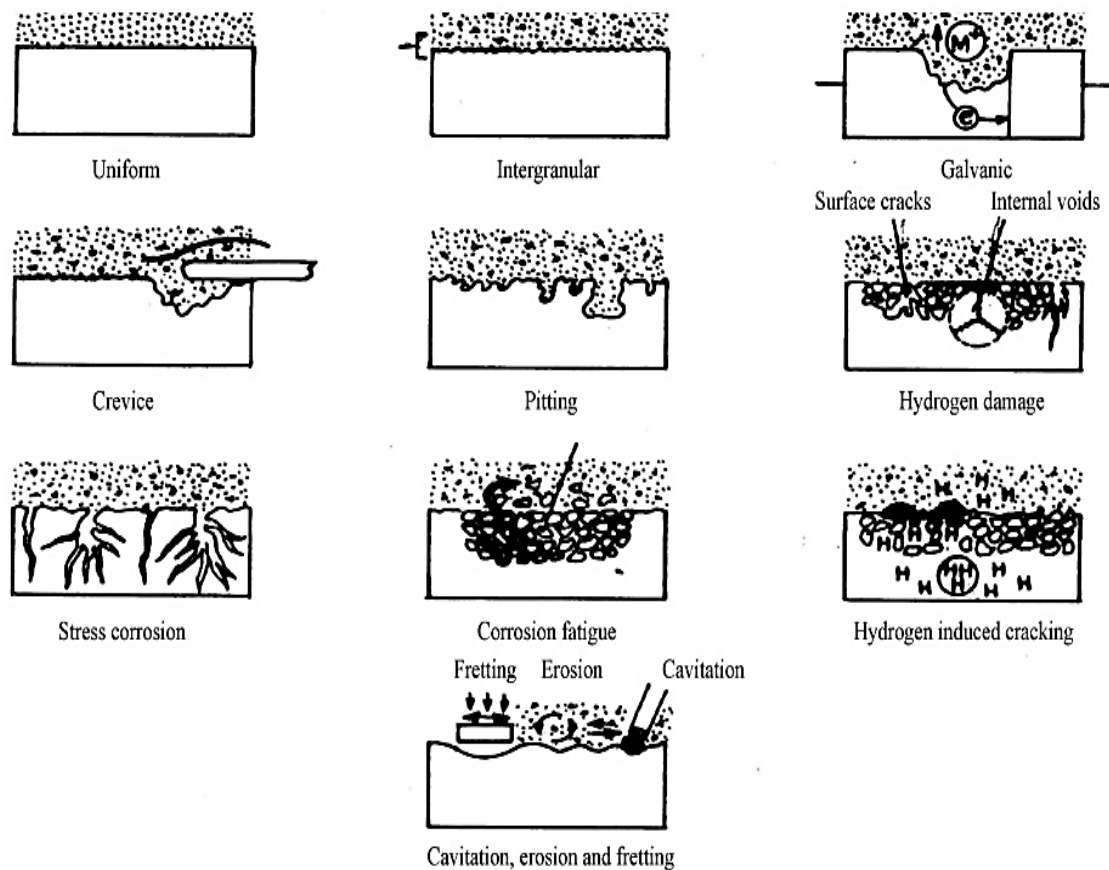
Figure 2-2 Corrosion types and forms classifications commonly used [17]

2.4 Corrosion cost

As mentioned in the National Association of Corrosion Engineers (NACE) IMPACT report 2016, the real cost of corrosion is about US$ 2.5 trillion. This corresponds to 3.4% of the global Gross Domestic Product GDP in 2013. The obtainable corrosion control management systems (CMS) that are available now could save between 15 to 35% of the total cost of corrosion, and as such could realize between $375 to 875 billion annually on a global basis and this number could increase of depreciation of the assists overall. Furthermore, these costs typically do not include any individual safety and environmental impacts. The fact that corrosion control delivers a cost-benefit is an accumulating lesson learned by industry, often too late and following disastrous occasions (e.g., accidents, failures, and external loss) [18].

2.5 Corrosion Control

The responsibility of corrosion engineering is to mitigate deterioration processes. Many measures can be applied to reduce the corrosion rate. Minimising corrosion mitigation

expenditures (both direct and indirect) requires more than one technology; it requires integrating corrosion decisions into an organisational management system. The elements that are considered as keys to corrosion protection are listed in the following sections.

2.5.1 Material design

The proper planning and execution of any project are based on good design. The appropriate strategy for corrosion protection is based on a design for corrosion control including all geometric design methods and functional mechanical and strength properties with acceptable corrosion resistance [15], [17] There are some points applicable during the design phase as follows:

- Use of welding instead of rivets;

- Avoiding direct contact between dissimilar metals;

- Designing systems with easy-fixing and replaced functional parts;

- Designing tanks to be easy to drain;

- Fewer sharp bends in pipeline systems;

- Implementing proper maintenance and inspection systems

2.5.2 Control of operational environment

The method of controlling the environment applies to enclosed atmospheric spaces or closed fluid systems using potent chemical inhibitors by injecting corrosion inhibitors directly to the medium in the system. Controlling pH value, solution concentration, velocity, and other factors are all effective ways to reduce corrosion [1], [15].

2.5.3 Cathodic protection & sacrificial anodes

Cathodic protection was applied for the first time for marine applications in the early 1820s by Sir Humphry Davy, in a scientific project for the British Navy [19], [20]. Cathodic protection is considered as one of the effective ways to control corrosion problems on active metals in continuous contact with electrolyte media such as seawater. Cathodic protection depends on reversing the metal-dissolution reactions, there are two main of protection which are impressed-current anodes and sacrificial anodes, these two techniques could be used together in the most cases   [17], [21] .

The concept of protection by sacrificial anodes is similar to the principle of impressed cathodic protection which passed on supply direct DC current to the anode to reverse and

stop the cathodic corrosion potential. However, it is using a sacrificial anode of Aluminium-Zinc alloys instead of the electrical DC supply. The sacrificial anode works by presenting another electronegative and more anodic metal surface alongside, the original structural metal being protected. The current will flow from the newly presented sacrificial metal as an anode, making the protected metal the cathode, creating a galvanic cell. Must reactions then will be transferred from the metal surface to the galvanic anode and are thus the anode is sacrificed in favour of the protected metals in the marine environment [22], [23].

2.5.4 Coatings

Use of coatings is one of the most common methods to preserve metals from corrosion. The basic principle of coatings is usually not to stop the electrochemical reaction with the environment but to isolate the metallic substrate from the corrosive environment. Corrosion protection coatings are designed to address various conditions of applications. Some of these coatings are single-layer films that are applied to the metal substrate, while multi-layered coatings can provide better protection in different service conditions [21], [24].

2.5.4.1 Types of Coating

The types of coating available for corrosion protection include:

- Metallic coatings, such galvanisation, electroplating and metal spray processes;

- Non-metallic inorganic coatings such as anodised conversion coatings

- Chemical vapour deposition (CVD) or physical vapour deposition (PVD) coatings;

- Organic coatings, such as paints, lacquers, and polymer sheets;

- Hybrid organic-inorganic coatings such as hybrid sol-gel coatings

2.5.5 Implementing an integrated corrosion management system

A corrosion management system (CMS) is a system based on the integration between corrosion mitigation and control alongside a management system which includes policies, procedures, planning, work instruction, top management reviews and a philosophy of continuous improvement to mitigate the threat of corrosion for existing and future assets. In most cases, this comes from optimising corrosion control activities, minimising life-cycle corrosion costs, and meeting safety and environmental restrictions. [18]

The implementation of a CMS includes inspection activities which can be divided into time-based inspection (TBI) or risk-based inspection (RBI).[25]

In any CMS to link between corrosion control and management systems it is important that the following two strategies should be employed:

- Extend the corrosion expert's competence to comprise financial optimisation of corrosion control investments; this includes the use of the risk assessment and other tools to the return on investment (ROI) of corrosion control activities.

- Extend the scope of recognised activities and other communications targeted at decision-making business leaders and representatives to ensure that recommended changes to management system elements are communicated in a language that facilitates business improvement [25], [26].

2.6 Material criteria selections

According to Ashby. M et al. [27], choosing a material with consideration for corrosion resistance is a sensible idea in the material selection phase of the design process. However, industrial processes are affected by many issues such as economic and design restrictions and where mechanical properties are prioritised. For instance, selecting high corrosion resistant alloys will be costly, while inexpensive materials may offer weak corrosion resistance in the operational environment. Therefore, a decision has to be made whether to control and actively manage the environment or to choose expensive alloys [9], [6], [10].

2.7 Light Metals alloys

The engineering design view where the property of lightness is associated with improvement of the material properties of many products where the maximum reduction in weight is achieved through a decrease in density [28].

This demonstrates why light metals are associated with the transportation sector, especially aerospace, which has provided a great incentive to develop light alloys over the past century. The strength: weight ratio is also a paramount consideration, and the central positions of aluminium, magnesium and titanium light alloys in relation to other engineering alloys and non-metallic materials in the Ashby scheme are shown in Figure 2-3.
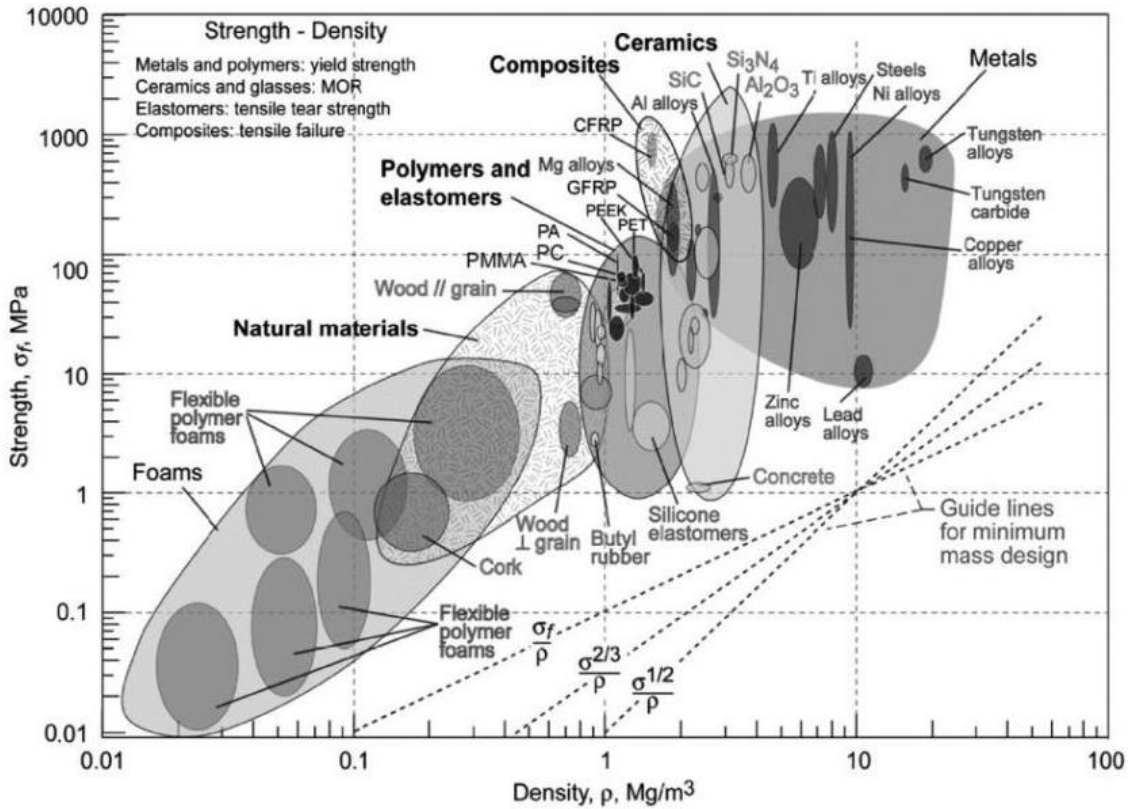
Figure 2-3 The Ashby chart for strength: density ratios for light alloys and other

engineering materials[29]

Therefore, the lower density starting point becomes even more critical in material selection when other parameters such as stiffness and buckling resistance are included. The significance of the relationship is demonstrated by this nomograph that is shown in Figure 2-4 which allows the weights of similar beams of different materials to be estimated for equal values of stiffness [29].
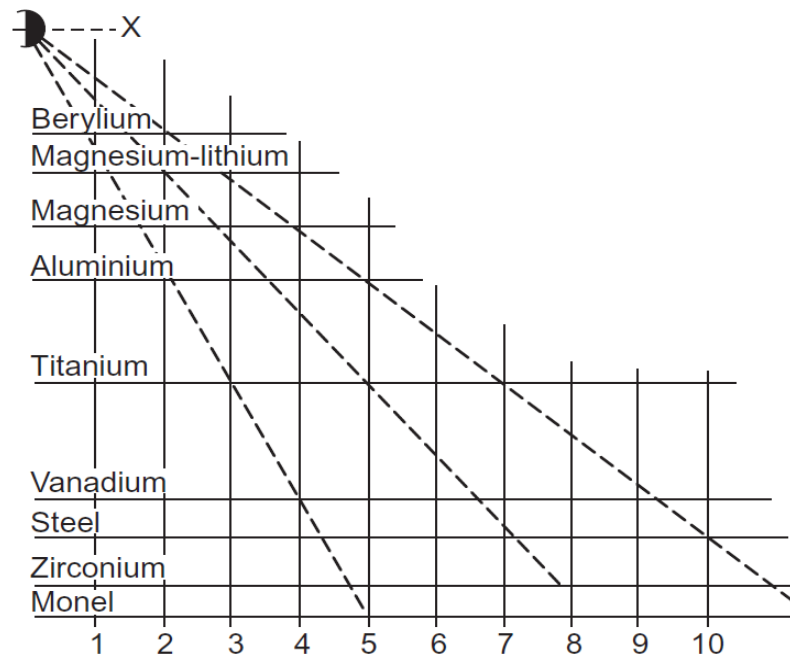
Figure 2-4 Nomograph, which allows weighting of different metals or alloys to equal levels

of stiffness[27]

As an explanation of this nomogragh, a steel beam weighing 10 kg will show the same stiffness as a beam of equal width and length of 7 kg in titanium, about 5 kg aluminium, 4 kg of magnesium, or about 2.2 kg of beryllium (note that the Mg-Li alloy was included for its lightness - relative density is about 1.35). Comparative stiffness of a similar structural increase in the ratios approximately 1:3:8:18 for steel, titanium, aluminium, and magnesium accordingly [28], [29]. While the focus on weight saving should be obvious; The fact is that light metals exhibit other properties of substantial technological importance, for instance, the generally high corrosion resistance and high electrical and thermal conductivities in metals such as aluminium, and the castability and machinability of magnesium, and the extreme corrosion resistance of titanium [29].

2.8 Aluminium

Aluminium is the most widely used non-ferrous metal in the aerospace and in industrial structures that need light components [30], and this can be attributed to its low density and its ability to resist corrosion through the phenomenon of surface passivation. Aluminium has many advantages such as light-weight, thermally and electrically conductivity, recyclability, and ability to endure the stresses induced by sudden changes in temperature due to its crystal structure which is face-centred cubic (FCC). Moreover, it is well-known

for its corrosion resistance properties. However, due to the poor mechanical properties of pure Aluminium such as a strength and ductility, means that it is not involved in industrial processes without alloying. The alloying elements used with aluminium usually do not account for more than 10% of the weight of overall the alloy but have a significant impact on the mechanical and operational properties [2].

2.9 Aluminium Alloys

The International designation systems for wrought alloys which are that world recognised and accepted scheme for wrought alloys. Each aluminium alloy is tagged with a four-digit number, where the first digit indicates the major alloying elements, the second - if different from zero - indicates a variation of the alloy, and the third and fourth numbers classify the specific alloy in the series. Furthermore, according to this system, there are nine major series of aluminium alloys.

2.9.1 Aluminium Alloy AA2024

AA2024 is one of the structural and aerospace aluminium alloys that is widely used, attributable to its high specific strength compared to the other metal alloys, along with its attractive cost. In the 2xxx wrought alloy series, the principal alloying element is copper, which is generally added at concentrations between 3.8 as 4.9 wt. % [2], [31]. The common chemical composition of AA2024 is shown in Table 2-1:

Table 2-1 Aluminium alloy AA2024 composition [32]

Element	Si	Fe	Cu	Mn	Mg	Cr	Zn	Ti	Other Elements
Wt. (%)	0.50	0.50	3.8–4.9	0.30–0.9	1.2–1.8	0.10	0.25	0.15	0.05-0.15

In addition to the alloy composition, the alloys may have a heat treatment temper designation code. In the case of AA2024, the alloy is often used in the 'T3' state. T3 refers to the processing of the alloy especially to improve strength after solution heat treatment at 495 C$^\circ$ for 48 hours and for that mechanical properties have been stabilised by the room temperature ageing [33].

The high strength of AA2024-T3 is coming from the reacting of supersaturated solid solution phase from the alloying elements such as Al_2CuMg about 2.69 %, Al_6(Cu, Fe, Mn) about 0.85 %, Al_7Cu_2Fe about 5.2%,(Al, Cu)$_6$Mn about 0.11% and another

indeterminate about 0.37% of area persent [34]. However, the creation of these phases and intermetallics has the effect of significantly decreasing the corrosion resistance compared to pure aluminium. Additionally to that the non-even distribution of Cu with these phases and intermetallic particles creates a source of internal galvanic corrosion cells [35]. For instance, when the Al_2CuMg phase interacts with copper in the presence of an electrolyte, a galvanic corrosion cell will be formed.

2.10 Corrosion on Pure Aluminium

Due to the thermodynamic behaviour of pure aluminium and its high electronegativity (approximately -1610 mV vs standard hydrogen electrode, SHE), means aluminium reacts readily with oxygen to create oxides in air and water, forming a stable passive thin film of aluminium oxide on the surface of pure aluminium metal [36].
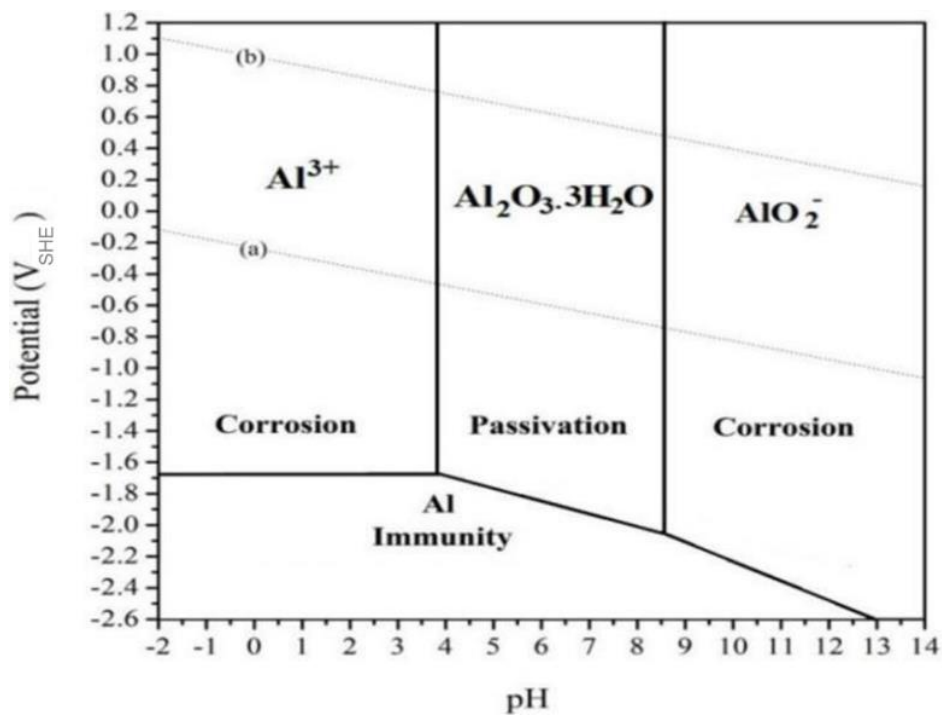
Figure 2-5 E-pH corrosion diagram of aluminium at 25ºC[37]

The aluminium E-pH (Pourbaix) diagram as shown in Figure 2-5 can graphically illustrate this behaviour. The diagram is derived by collating and examining pure aluminium metal/water equilibriums and the diagram is constructed based on utilising the Nernst equation with solubility data [38]. In this diagram four phases containing the aluminium element will be considered [39]:

Two solid phases (Al and $Al_2O_3.3H2O$)

Two ionic phases (Al^{3+} and AlO^{2-})

The next phase for creating the aluminium Pourbaix diagram is to consider all possible reactions between the four chemical phases containing aluminium, i.e. Al, $Al_2O_3.H_2O$, Al^{3+}, and AlO^{2-}. These reactions are summarised in the equilibrium Equations 2-1:

$$Al^{3+} + 2H_2O \leftrightarrow AlO_2^- + 4H^+$$

$$Al \leftrightarrow Al^{3+} + 3e$$

$$2Al + 6H_2O \leftrightarrow Al_2O_3.3H_2O + 6H^+ + 6e$$

$$2Al^{3+} + 6H_2O \leftrightarrow AlO_2^- + 4H^+$$

$$Al_2O_3.3H_2O \leftrightarrow AlO_2^- + 2H^+ + 2H_2O$$

$$Al + 3H_2O \leftrightarrow AlO_2^- + 4H^+ + 3e$$
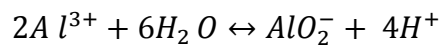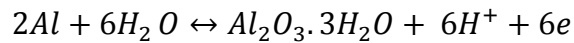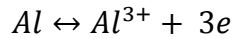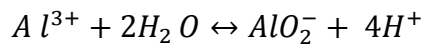
Equations 2-1

The three regions on the diagram designate:

- Immunity region, in which the metal can be considered to be safe from corrosion degradation.

- Corrosion regions, where the corrosion takes place, resulting in degradation of the metal

- The passive region, which indicates that the aluminium is covered with a stable metal oxide that protects it from corrosion

For instance, it is clear from this diagram that pure aluminium will be protected from corrosion in aqueous solutions with pH values between approximately 4 and 9 also the change in potential will affect these values accordingly. However, while the diagram provides information on whether or not metal will corrode, it does not provide information on the rate of corrosion [39].

2.10.1 General Corrosion on Aluminium alloy AA-2024

Aluminium alloy 2xxx series is usually susceptible to corrosion more than pure aluminium due to micro galvanic effects and pitting corrosion caused by the presence of copper-containing intermetallic particles (IMPs) which disrupt the passivating aluminium oxide film on the alloy surface [40].

The different types of IMPs have their specific behaviour and electrochemical nature. These ionised phases include iron, manganese and silicon, which are considered as

impurities, and it can create cathodic compound consistent with aluminium itself. In the case of AA2024, Al-Cu-Fe-Mn-(Si)-containing intermetallic particles are generally termed as α-phase particles. Table 2-2 can brief this nature of these second-phase intermetallic particles:

Table 2-2 Electrochemical behaviours of second-phase intermetallic particles in deionised water and NaCl solution [41]

	Cathodic	**Neutral**	**Anodic**
Deionized water	Al_3Fe, α-Al(Mn, Fe)Si	Al_6Fe, Al_6(MnFe), AlFeSi, Si, Al_2Cu	Mg_2Si
NaCl solution	Al_3Fe, α-Al(Mn, Fe)Si , AlFeSi, Si	Al_6Fe, Al_6(MnFe)	Mg_2Si

The pitting corrosion mechanism generally consists of two stages which are initiation and propagation.

In the presence of chloride ions on the oxide passive film on alloy, the weakest points on the passive oxide film will occur where some intermetallic particles (IMPs) are near the surface, pitting corrosion will initiate and possibly grow depending on the local conditions, the alloy and electrolyte. In many cases, if the pit remains active, it will involve an internal micro galvanic cell and will result in propagation-based upon physically separated aluminium oxidation and the oxygen or with hydrogen reduction depending upon the electrode potential of metal and the solution.

$$O_2 + 2H_2O + 4e^- \rightarrow 4OH^-$$ **Equation 2-2**

$$O_2 + 4H^+ + 4e^- \rightarrow 2H_2O$$ **Equation 2-3**

$$2H^+ + 2e^- \rightarrow H2$$ **Equation 2-4**
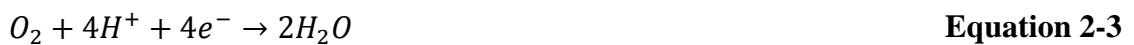
These equations [42] can briefly give a describing mechanism of pitting corrosion on AA2024 alloy, in aerated neutral and alkaline solution it is clear from Equation 2-2 that reduction of dissolved hydrogen and oxygen formation will be started. On the other hand, in the acidic solution from Equation 2-3 and Equation 2-4, the reduction reaction may also be represented by hydrogen ions reduction.

$$H_2O + 2e^- \rightarrow 2OH^- + H_2$$ **Equation 2-5**

2H$_2$O reduction will occur in the absence of oxygen and hydrogen ions, as can be seen from Equation 2-5. Meanwhile, at the anode, pitting will start creating positively charged ions of Al^{3+} via dissolution of Al, leading to migration of negatively charged Cl^- ions by attraction into the pit leading to the creation of complex hydro-chlorinated aluminium such as $AlCl^{4-}$.

$$Al^{3+} + 3H_2O \rightarrow Al(OH)_3 + 3H^+ \hspace{4cm} \textbf{Equation 2-6}$$

In Equation 2-6 the creation of H^+ will occur as results of re-hydrolysis of aluminium ions Al^{3+} and this will lead to acidify the media around the pit and lowering the pH lower than 3 pH.

$$2Al \rightarrow 2Al^{3+} + 6e^- \hspace{4cm} \textbf{Equation} \text{ 2-7}$$

Therefore, from Equation **2-7**, as a result of acidifying the solution inside the pit, the local environment will become more aggressive, causing Al dissolution. The process continues, hence causing the autocatalytic propagation of the pit. Figure 2-6 shows the schematic of the mechanism of pitting in the aluminium-copper based alloys.
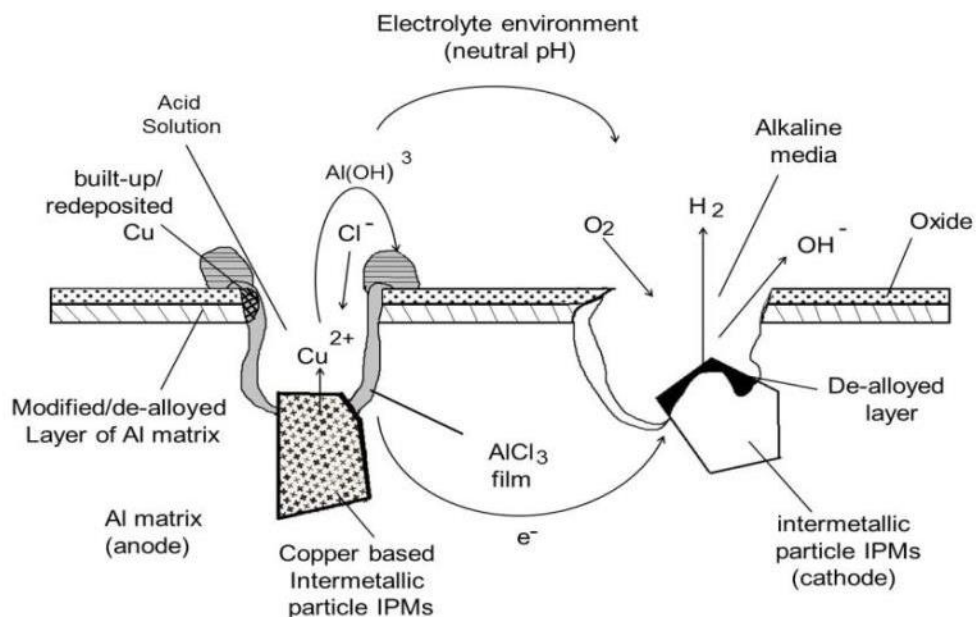
Figure 2-6 Mechanism of pitting corrosion on aluminium AA2024, modified from [34], [35]

Figure 2-6 shows the common mechanism of pitting in AA2024-T3 alloy resulting from the presence of intermetallic particles which cover about 3 to 4% of the overall surface area. A majority of these (approximately 60%) IPMs are (Al$_2$MgCu) S-phase- saturated

sold solution [43], [44]. This S-phase is the main responsible for activation of the corrosion on this alloy as it is more electrochemically active (anodic) compared to the alloy itself. The electrochemical dissolution of Al and Mg from the S-phase will start during the initial stages of the corrosion process leaving behind copper which accumulates on the side of pits as a thin film as a result of the continuous dissolution of remaining copper [34], [40], [42], [44]. This thin film of copper around the pits is the key factor in developing the localised and micro-galvanic corrosion causing a growth in the cathodic area and thereby increasing the anodic current density in the pit. Thus, the suppression of S-phase de-alloying and deposited copper on AA2024 alloys will positively affect any localised corrosion inhibition strategy.

To solve this issue on 2xxx series alloys there are many techniques such as cladding with a thin film of pure aluminium or copper to improve its surface corrosion protection. However, this thin film will be affected by the alloy's strength, and it can be easily damaged making it a source of micro-galvanic or localised corrosion especially under the effect of fatigue stress [45]. Alternatively, organic inhibitors that can either react with IPMs and S-phase will provide a robust inhibition process. Organic volatile corrosion inhibitors may also provide good protection on light alloys [46], [47].

2.11 Chromate conversion film

Chromate conversion coatings applied to clad AA2024-T3 were widely used in the aerospace industry; these coatings showed excellent corrosion protection. However, Some governments have banned their use or have pending legislation to ban its use. The effectiveness for corrosion protection due to the presence of Cr (VI), the personal exposure limit of hexavalent chromium has been reduced to a level of $1\eta g/m^3$ globally in 2006, according to OSHA. Furthermore, due to the highly toxic and carcinogenic effects of hexavalent chromium, there has been an effective ban of use chromate conversion coating beyond 2010 in the USA [48]–[50]. As a result, the trend in corrosion protection technology has been to replace chromate conversion coating technology with environmentally friendly coatings and inhibitors.

2.12 Corrosion inhibitors

The term 'corrosion inhibitor' covers chemical elements and compounds that reduce the rate of corrosion on the material [51]. Nowadays, corrosion inhibitors are commonly used,

especially in marine and oil and gas industries, and also could be ordered from over the counter products from prominent vendors [52].

Over the last years, extensive efforts have been made to find suitable corrosion inhibitors, the broader range being inorganic inhibitors such as those based on rare earth metals, for instance, cerium and samarium which are deployed on light alloys such as AA2024-T3 to reduce the pitting, and acting like a Passivation corrosion inhibitor replacing the loss of ionic charge by compensating the release of electrons that could increase the corrosion rates [52], [53].

The other form of inhibitor is the organic inhibitor, which can be used as a source in various corrosive environments. In acid media, nitrogen-based materials and their derivatives, sulphur-containing compounds, aldehydes, thioaldehydes, acetylenic compounds, and various alkaloids, for instance, papaverine, strychnine, quinine, and nicotine are used as inhibitors.

In the real environment, nitrite, phosphate, and chromate act as effective inhibitors. Inhibitors reduce or prevent the reaction of the metallic part with the media [54]. They could reduce the corrosion rate by:

- Adsorption of ions/molecules onto the metal surface

- Accelerate or de-accelerate the anodic and/or cathodic reaction.

- the diffusion rate will be reduced for reacted free ions to the surface of the metal

2.12.1 Volatile corrosion inhibitor

Volatile corrosion inhibitors are a branch of organic inhibitors which used to protect metal alloys in both ferrous and non-ferrous metals against oxidation, commonly with low pH as film-forming corrosion inhibitors. Where it is practical, an inhibitor can be applied to metal surfaces by evaporation or deposited in many ways including the use of films, papers, desiccant, coatings and evaporation chambers [47], [55]. Figure 2-7 shows the VCI vacuum chamber as one of an application technique on metal parts
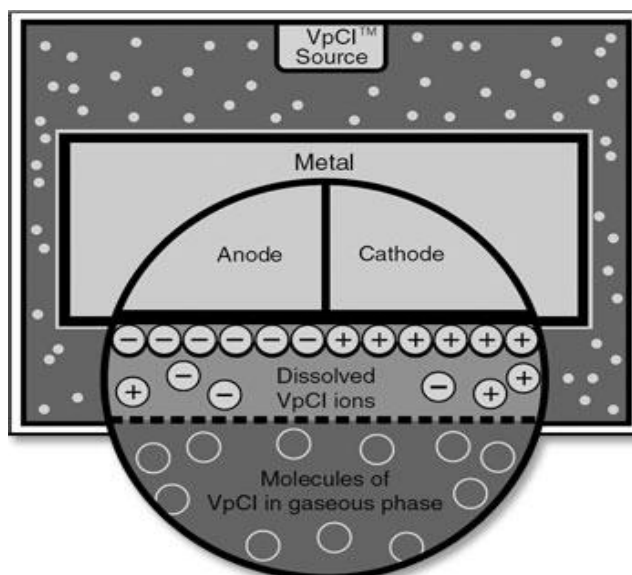
Figure 2-7 film-forming volatile corrosion inhibitor applied to metallic parts[56]

2.12.1.1 Historical background of volatile corrosion inhibitor

The adsorption ability of organics on metal surfaces gives an advantage of high efficiency compared to other inhibitors. Furthermore, the strength of this adsorption and the temperature are a factor to its evaporation pressure. In the 1920s and 1930s, lower amines and ammonia were used as protectors from corrosion by creating a film on the surface of metals [46]. Although, the considerable number of corrosion inhibitors that was with the US military, the new compound dicyclohexylammonium nitrite (DICHAN) which was developed in the 1940s is considered as being the first work on this type of inhibitor in film-forming inhibitors sector [10], [47]. The chemical structure of these inhibitors is based on active aliphatic and alicyclic base compounds, making them easy to transfer from the liquid to the vapour-phase more effectively than other organic inhibitors. By experiment and industrial trials, it was found that not all VCIs work on all metals, for instance, some of them were effective on ferrous metals, such as cyclohexylamine, hexamethyleneimine, piperidine, morpholirne, and benzylamine [47].

Today there is a wide range of volatile inhibitor formulations which may be used for corrosion protection of both ferrous or non-ferrous metals, for example, benzimidazole, 2-benzimidazolethiol, and 2-mercaptobenzothiazole, these having been reported as effective inhibitors on copper, aluminium, zinc and their alloys [47].

2.12.2 Benzimidazole

Corrosion inhibitors are compounds that protect the metal from deterioration by corrosion. The development of these compounds has created many effective inhibitors with heterocyclic organic functional groups consisting of oxygen, nitrogen, phosphorus and sulphur attached as heteroatoms [57], [58]. The common feature of these types was the azole functional group which has been effectively used to inhibit copper oxidisation and corrosion. Some azole groups such as pyrazole, triazole and imidazole and their derivatives which are considered non-toxic inhibitors can work with effectiveness in several environments such as acidic and alkaline media, and this is due to the high negative electrostatic potential of these groups [59]–[61]. Figure 2-8 shows the main Azoles groups.

(a) Imidazole   (b) 1,2,3-Triazole   (c) Pyrazole
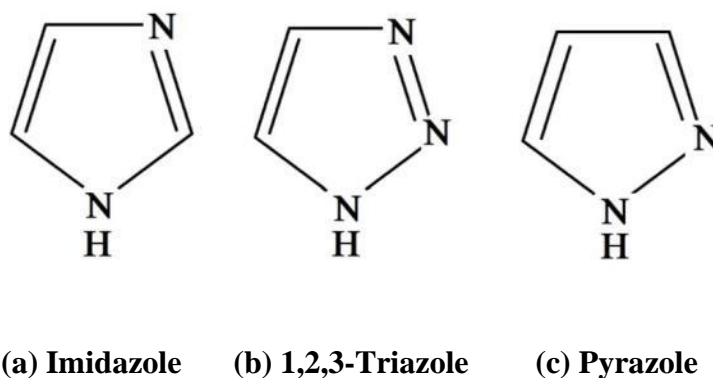
Figure 2-8 Chemical structure diagrams of some of the active azole groups, (a) Pyrazole, (b) Triazole and (c) Imidazole

Benzimidazole (BZI) is one of the imidazole derivatives that has been identified as low pH film-frorming corrosion inhibitors with the structure of a heterocyclic aromatic organic compound, which could be used as both effective VCI or injectable inhibitor with other soluble carriers due to the chemical structure that contains both a benzene group and also the active group imidazole which can be used in oil and gas industry by using inhibitors injection pumps [62], as shown in Figure 2-9.
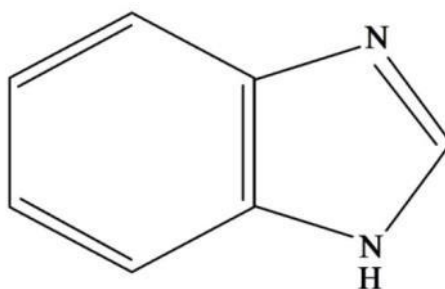
Figure 2-9 chemical structure of The Benzimidazole (BZI)

BZI is available commercially as a raw material for many applications, the primary use being in pharmaceutical applications to use as a fungicide [63].

However, applied engineering was involving this kind of materials and their derivatives in many applications. For instance, Antonijevic 2009 et al. [58] mentioned it as an inhibitor which demonstrated excellent inhibition of corrosion, for example as a directly injectable inhibitor to protect carbon steel in corrosive acidic media of hydrochloride solution in [58], [64].

Likewise, E.A. Frame [65] mentioned in the interim report of Belvoir Fuels and Lubricants- Research Facility (BFLRF) No 209 under U.S. Army Belvoir Research centre in 1990, that there were some applications being investigated under army research that use of BZI and its derivatives as volatile corrosion inhibitors on ferrous and nonferrous materials including copper, aluminium and silver. The study recommended using this inhibitor as one of the packages of inhibitors for various corrosion protection applications in the US Army equipment [65], [66].

2.12.2.1 The mechanism of inhibition of BZI on light alloys that copper one of alloying elements

The mechanism of inhibition by BZI and its derivatives on metal, especially on copper and steel, could be explained by using the results by utilising the quantum chemical calculation. E. Gutiérrez et al., I.B. Obot et al. and F Grillo et al. tried to demonstrate this corrosion inhabitation mechanism through the way that shows the distribution of the electrostatic charge of all compounds, but these data were not sufficient to predict the tendency of the inhibition performance although of the achievement in exploring the active sites and reactivity of the inhibitors [64], [67], [68].

Therefore, the argument still so far opened to explain this mechanism, some studies recommended using of the simulation system [56], and it was an easy way to bring the nearest explanation about how was this compound acting on the substrate surface. Figure 2-10 shows the simulated adsorption geometries of benzimidazole on the surface of the steel. There were initial studies about the adsorption of benzotriazole on copper and copper alloys by using Scanning tunnelling microscope find that the STM images illustrated that a regular unequal pseudo hexagonal pattern starts to form on the surface of copper. This structure results in the formation of a monolayer system, to which the passivation of surface character is associated[68].
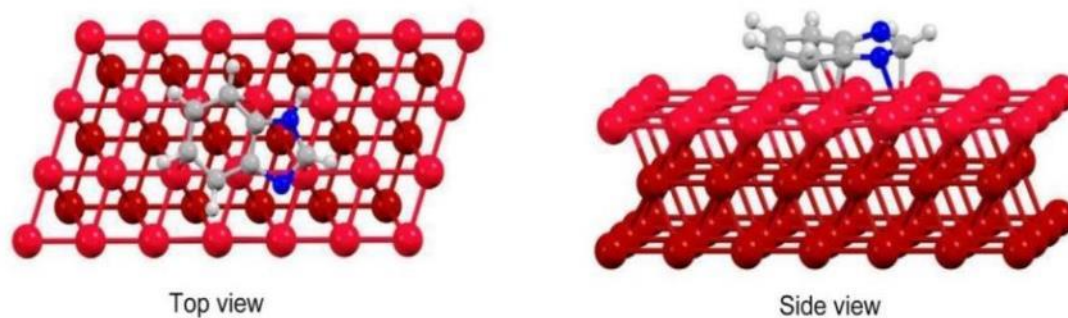
Figure 2-10 Adsorption geometries of Benzimidazole on the surface of the steel, adapted from [64]

Generally; it was found that the BZI and its derivatives may be seen in this inhibitor molecule positioned in a parallel adsorption arrangement and there was a close joining with the surface [64], [67]. The rearrangement and adsorption of BZI in this position are due to the donation of Pi electron (π electron), also to the one pair of electrons on the nitrogen atoms, compensating the benzimidazole molecules to the iron atoms or copper that unoccupied D-orbital. These interactions explain the strong adsorption connection to the surface, and as a result, it will protect the mild steel from direct corrosion [64], [67].

Despite there was some mentioned of using BZI and its derivatives in some studies and patents, J. Colreavy et al. and S. Vijaykumar et al. mentioned in their patents to use the same family of inhibitor with sol-gel technique on steel or other light metals as a limitation of the use only. The truth is there have been no real studies to combine BZI, or its derivatives, with the silicate sol-gel coating technique to use as a corrosion inhibitor on aluminium alloy AA2024-T3 [69], [70].

2.12.3 Fatty acids

Natural greasing oils have generally been used to cover metallic parts for a long time to prevent direct contact with the environment. There are many types of fatty acids; the general chemical structure amongst all of them can be described as a carboxylic acid with a long aliphatic chain, which can be present as saturated or unsaturated fatty acids. Fatty acids are naturally created in living organisms and usually have a non-branched chain of even number from 4 to 28 carbon atoms. Some of the saturated and unsaturated fatty acids are shown in Table **2-3** and Table **2-4** as follows:

Table 2-3 Examples of Saturated Fatty Acids

Common name	Chemical structure	C:D ratio
Lauric acid	$CH_3(CH_2)_{10}COOH$	12:0
Myristic acid	$CH_3(CH_2)_{12}COOH$	14:0
Palmitic acid	$CH_3(CH_2)_{14}COOH$	16:0
Stearic acid	$CH_3(CH_2)_{16}COOH$	18:0
Arachidic acid	$CH_3(CH_2)_{18}COOH$	20:0
Behenic acid	$CH_3(CH_2)_{20}COOH$	22:0

Table 2-4 Examples of Unsaturated Fatty Acids

Common name	Chemical structure	C:D ratio
Myristoleic acid	$CH_3(CH_2)_3CH=CH(CH_2)_7COOH$	14:1
Palmitoleic acid	$CH_3(CH_2)_5CH=CH(CH_2)_7COOH$	16:1
Oleic acid	$CH_3(CH_2)_7CH=CH(CH_2)_7COOH$	18:1
Elaidic acid	$CH_3(CH_2)_7CH=CH(CH_2)_7COOH$	18:1
Linoleic acid	$CH_3(CH_2)_4CH=CHCH_2CH=CH(CH_2)_7COOH$	18:2
Arachidonic acid	$CH_3(CH_2)_4CH=CHCH_2CH=CHCH_2CH=CHCH_2$ $CH=CH(CH_2)_3COOH$	20:4

2.12.4 Oleic acid

Oleic acid was one of the recommended fatty acids mentioned previously in a US Army report from 1991 for use as a corrosion inhibitor in engines [65]. Oleic acid is created in nature in various animal lards and vegetable fats and oils with the chemical structure of $C_8H_{17}CH=CH(CH_2)_7COOH$ [71]. It is pH neutral and colourless in its appearance, though commercially produced material may be yellowish in colour. It is an unsaturated fatty acid with non-polar properties. The chemical structure can be seen in Figure 2-11.
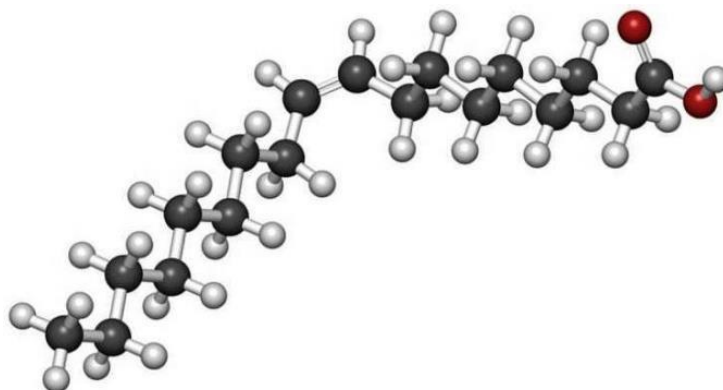
Figure 2-11 the chemical structure of Oleic acid [72]

E.A. Frame [65] in his studies including the US interim Report No 269 and Ben Hmamou D. et al. [73] recommended using oleic acid as the primary or corporate corrosion inhibitor in lubrication systems. Zhao J. et al. [74] mentioned in his experiment that the oleic acid-based imidazole with sodium benzoate showed an excellent corrosion inhibition for steel in carbon dioxide-brine solution. Also, in another technique by Zhang. W et al. [75] as mentioned, it can be made water-soluble by the synthesis in polyethene glycol and imidazole to use as an injectable inhibitor in aquatic media.

2.12.4.1 The mechanism of inhibition of oleic acid on steel and other light metals

Fatty acids (including oleic acid) have unique properties of a surface-active molecule as it shown in Figure 2-12 which can be working as a corrosion inhibitor to provide a barrier on the metal surface preventing the diffusion of charged ions [76], [77].
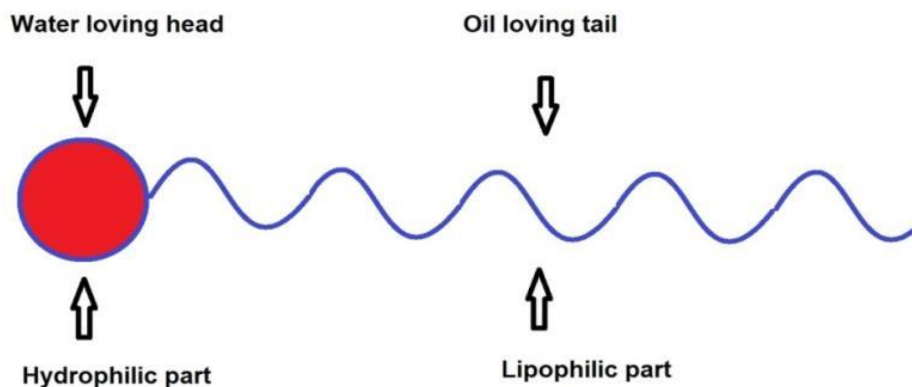
Figure 2-12 Surface-active fatty acid molecule

Malik M. A. et al. and Migahed A. et al. [76], [77], mentioned in their publications that the mechanism of inhibition is complicated and depends on many factors including the creation of mono/multidimensional protecting layers on the metal surface. As well as the other factors that work with the protective layers are the interactions between inhibitors and substrate, chemical reactions that could occur, electro-potentials effects, operational temperatures, the concentration of the inhibitor and finally the properties of the treated surface.

This mechanism could be summarized in the following sequence: firstly, the fatty acid acts as surfactant inhibitors in the surrounded aggressive environment and then is adsorption of surfactant molecules on top of the metallic surface by creating a metallic binding. This process is usually affected by surface charges, the chemical structure of the surfactant and the surrounding electrolyte. Consequently, the adsorption will occur due to the interaction potential between the surfactant and metal surface, and as a result, the inhibiting effect of the molecules is credited to its functional groups that attach to surfactants on the metallic surface. There are three individual types of adsorption coordination that the carboxylate group in fatty acid can adopt for bonding to the metallic surface. Which are proposed structures of the mono-dentate, bidentate and bridging coordination types as shown in Figure 2-13, In the bridge-bonded configuration, the oxygen atoms are identical but on different aluminium atoms while on the other bonding will be connected to one metallic atom [78]. Besides, the rate of adsorption is usually rapid, and henceforth the weak metallic alloy surface will be shielded well and protected from direct contact with the aggressive media. [76], [77]
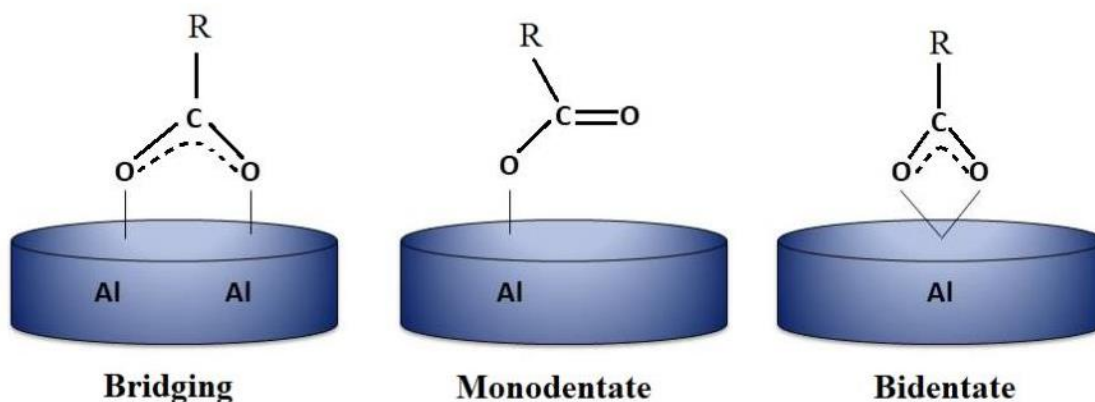
Figure 2-13 Schematic representations for three types binding adsorption process of carboxylate groups in fatty acid on steel aluminium surface [71]

There is some limitation of direct use the fatty acids with other coatings including Sol-gel, which is decreasing the cross-links in the coating matrix and will be preventing to create a coating with good adhesion on the substrates due to increasing the hydrophobicity on top of the metal surface. Hughes A. et al. [79] mentioned in his review the encapsulation of La(dibutyl phosphate)$_3$ with micelle oleic acid in epoxy coatings. There has been mention of the use of oleic acid in some patients to be used in conjunction with other inhibitors in sol-gels. Simendinger W. et al. [80] mentioned in his patent the use of oleic acid with other material in sol-gel as an antifouling release agent.

Although, the previous studies presented functional corrosion inhibition of oleic acid on steel and light alloys, the term of use oleic acid as corrosion inhibitor encapsulated in sol-gel was not mentioned so far on published work or patents. Therefore, as a research gap, this part will be investigated and try to be covered in this thesis.

2.13 Introduction of sol-gel technology

Sol-gel protective coatings have revealed excellent chemical stability, reasonable oxidation control, and enhanced corrosion resistance for metal substrates by encapsulating functionalized nanoparticles and inhibitors. The sol-gel process is an eco-friendly method of surface protection and provides the potential for the replacement of toxic chromate-based pre-treatment/primer coatings [81], [5].

2.13.1 Review of the historical development of sol-gel

A conventional sol-gel technology was first reported in the 1840s by Elbelem. The technology then stayed almost a century as an interest for chemists without any

applications. In the 1930s, Geffcken started to explore the possibility of using alkoxides to produce thin films of metal oxides. In the 1960s, the sol-gel method was developed mainly due to the need for new synthetic methods in the industrial revolution. This technology was developed and understood well by Schott Glass. In the early of the 1970s until the middle of the 1980s, the direct conversion of monolithic inorganic gels to glass at low temperature without melting at high temperature was the driving force behind the development [82]. In the 1990s, hybrid organic and inorganic sol-gel precursors were considered as a new approach to obtain homogeneous organic-inorganic materials. This approach gave enormous advantages and tremendous opportunities in the field of organic-inorganic hybrid materials [82].

2.14 Contemporary sol-gel technology

The sol-gel is an outcome of a process based on the colloidal suspension of molecular particles in a liquid called a "sol" and gelation of the sol in a multi-network continuity to form the "gel". By the condensation process in the sol-gel, the gel will grow consequently as a giant molecule. The intelligible stable 3D network inside the liquid stage is called a gel, and the range size of particles is from a few to hundred nanometres. Metal alkoxides are the most common precursors in the use of synthesising those colloids (sol-gel); e.g. tetraethyl orthosilicate (TEOS) Si $(OC_2H_5)_4$ and tetramethyl orthosilicate (TMOS) Si $(OCH_3)_4$. Furthermore, other common alkoxides contain metal elements in their molecular formulation such as aluminates, titanates and borates.[83]

The sol-gel reaction mechanism occurs, in general, in four stages as follows: (a) hydrolysis; (b) monomer condensation and polymerisation and forming particles and chains; (c) particle growth; (d) polymer structure accumulation leading to the formation of a gel coating. In fact, hydrolysis and condensation reactions follow instantaneously when the hydrolysis reaction starts. Figure 2-14 shows the primary hydrolysis and condensation reactions. Hydrolysis and condensation create the low-molecular-weight by-products, for instance, alcohol and water. Until thoroughly dry, these low-molecules are pushed away, leading to the network shrinkage when condensation occurs. Hydrolysis and condensation processes are affected by the initial reaction conditions; for instance, temperature, pH, contents, precursor molecular ratios and solvent properties. [84], [85].

HYDROLYSIS

CONDENSATION

$$\equiv Si-OH \ + \ RO-Si\equiv \ \rightleftharpoons \ \equiv Si-O-Si\equiv \ + \ ROH$$

$$\equiv Si-OH \ + \ HO-Si\equiv \ \rightleftharpoons \ \equiv Si-O-Si\equiv \ + \ HOH$$
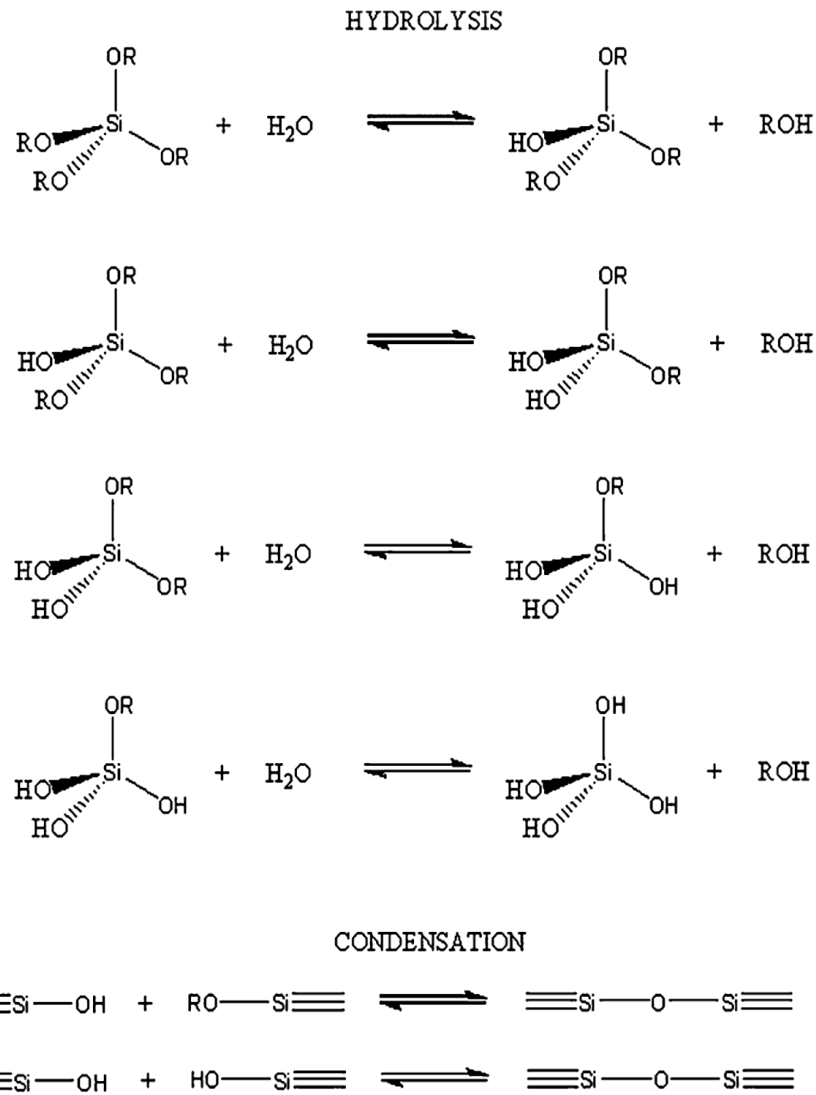
Figure 2-14 Hydrolysis and condensation involved in making sol-gel derived silica materials [86]

2.15 Sol-gel process steps

There are some steps involved in the sol-gel preparation process to achieve the final formula including mixing, gelation, ageing, drying, and sintering [82]. Variations of these processing steps can affect the sol-gel properties by physical and chemical routes. Figure 2-15 shows the synthesizing steps. A brief explanation is given in the following sections.
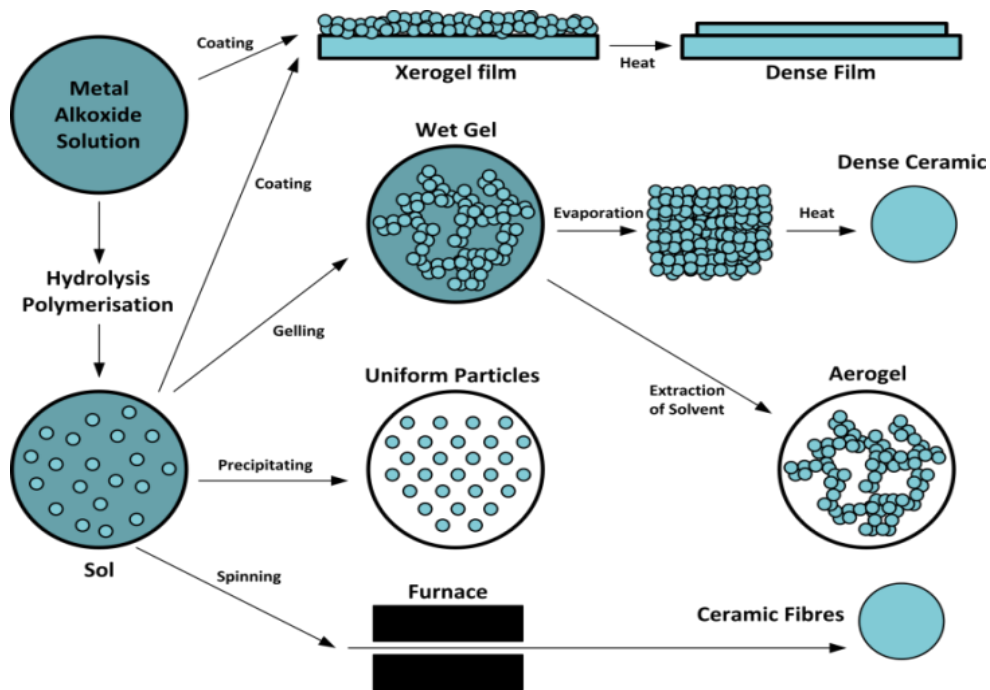
Figure 2-15 Steps of industrial sol-gel products [87]

2.15.1 Mixing

All alkoxide precursors having the general formula $M-(OR)_n$ (for example, $Si (OR)_4$) when mixed with water, undergo hydrolysis and condensation reactions[86]. Hydrocarbon-based solvents (such as alcohol) are often used to disperse the precursors. A colloidal dispersion in the liquid is finally obtained with nanoparticles [83], [82].

2.15.2 Gelation

The colloidal particles in the sol-gel link together via polycondensation to form a network-structured material. The catalyst plays a significant part in this process due to the ionic charge of nanoparticles with a direct effect on the polycondensation rate. For example, at low pH (~1.5), the silica nanoparticles tolerate minimum ionic charge around the silica isoelectric point wherein the silica surface electro-charge is zero and thus can collide and connect into chains networks, creating a polymeric gel [86]. On the other hand, at high pH, the dissolution rate is high, and the nanoparticles propagate into the regular size and a decrease in number as the smaller nanoparticles deposited around, the larger particles[83]. In this case, the reaction will start forming a colloidal gel. The colloidal gels with the high specific surface area and lower density will be obtained. Figure 2-16 shows the relationship between pH and the size of nanoparticles.[88],[82]
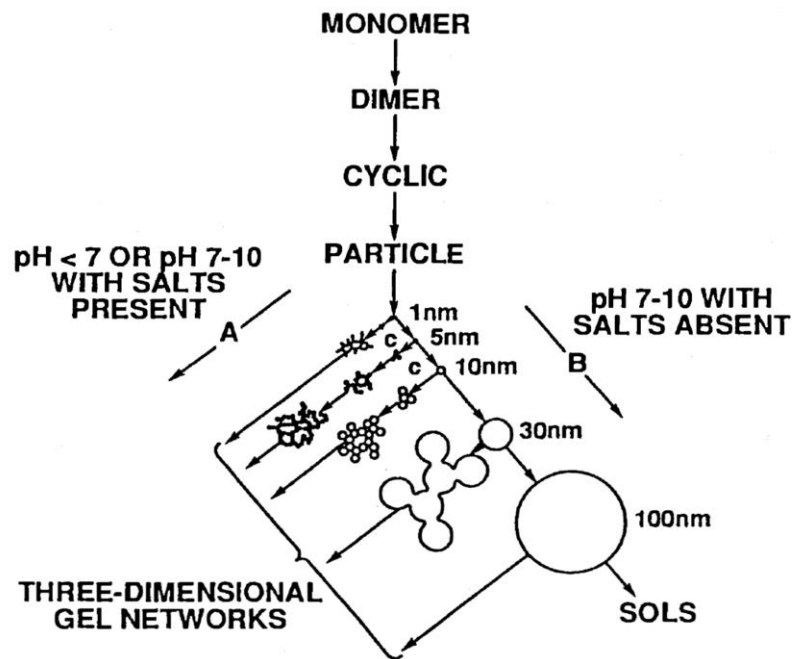
Figure 2-16 the relation between pH and the size of particles [16]

2.15.3 Ageing

The ageing process occurs via three steps, including polymerisation, syneresis, and coarsening. The connectivity and continuity of the gel network increase with polymerisation of unreacted hydroxyl groups. There is some shrinkage during the ageing process. Syneresis is irreversible shrinkage of the gel network caused by the expulsion of the relocating liquid, leading to compressive stresses that draw the solid network to the liquid state. Coarsening, also known as ripening, is considered as a process of re-precipitation and dissolution and is driven by solubility differences between surfaces and other radii of curvature. In the coarsening process, no shrinkage of the network will happen. [83]

2.15.4 Drying

This process starts with liquid removal from interconnected pores in networks of the gel. To avoiding cracking of the gel while drying is one of the main problems in bulk materials preparation. The capillary pressure associated with the gas-liquid interfaces causes stresses in the dried gel (xerogel). Cracks are then originated if those internal stresses exceed the tensile strength of the material. Flaws and capillary stresses grow during this process when pores are small, about 20 nm[86].

The sol-gel drying process may take a period from a few hours to weeks to enable drying to occur throughout the gel. The drying process may be accelerated by adding some

chemical additives such as oxalic acid or formamide, which will increase the surface tension of inner fluids. [83]

2.15.5 Densification

By sintering the dried gel at high temperature, densification of the gel will occur. The reduction in interfacial energy takes place on this process, leading to increased strength and consolidation of the xerogel, thus reducing internal porosity. It is evident that the densification kinetics in gels is considerably complicated as a result of the concurrent reactions of dihydroxylation and structural relaxation[83], [82].

2.16 Hybrid inorganic-organic sol-gel

Different materials typically have their particular properties, with advantages and disadvantages for each. Firstly, organic polymers are usually accessible to process, are lightweight, easy to form, and flexible. Yet, they sometimes have a weakness at high temperature. On the other hand, inorganic materials commonly have high mechanical and thermal properties, nevertheless sometimes with some drawback such as high brittleness and heavy density [89].

The modern industrial developments and the desire for innovative functions have generated a vast need for novel materials. One consequence of this has been the creation of so-called hybrid materials which have been used for many diverse systems covering a wide range of different constituent materials. They can be defined as materials that include two moieties blended on the molecular scale. Commonly one of these compounds is inorganic and the other one organic in nature [90].

Inorganic-organic hybrids can be applied in many branches of materials and chemical engineering because they are simple to process and are amenable to design on the molecular scale. At present, many of the colloidal systems already known are being re-inspected by modern analytical techniques to gain new insights into the origin of the specific chemistry and physics behind these materials. In particular, the silicon-based sol-gel process was one of the significant driving forces what has become the broad field of inorganic-organic hybrid materials[89], [90].

A hybrid organic-inorganic sol-gel employs both materials with a homogeneous and smart combination, gaining the advantages of both organic and inorganic components. By using hybrid sol-gel technology, it is possible to control the mechanism, the outcome and the mechanical properties for different applications. Also, the hybrid organic-inorganic

synthesis can present new physical, chemical and functional properties in low-temperature processing, which itself can be easily allowing for both organic and inorganic to be more homogenous without affecting the original properties of the organic part. Hybrid organic-inorganic sol-gels are usually produced by involving of the inorganic precursor such as tetraethyl orthosilicate (TEOS) with an organic precursor containing one or more desired organic group(s) to engender the desired properties, such as making the sol-gel hydrophobic, conductive, easy to dry or even to be very flexible or harder. Figure 2-18 shows many types of sol-gel precursor organic groups that are used in coating applications[91], [92].

VTMS
Vinyltrimethoxysilane

GPMTS
Diethoxy(3-glycidyloxypropyl)methyl silane

AEAES
3-(2-Aminoethylamino) propyldimethoxymethyl silane

MTES
Triethoxymethylsilane

MTMS
Trimethoxymethylsilane

FAS-17
1*H*,1*H*,2*H*,2*H*-Perfluorooctyltriethoxysilane
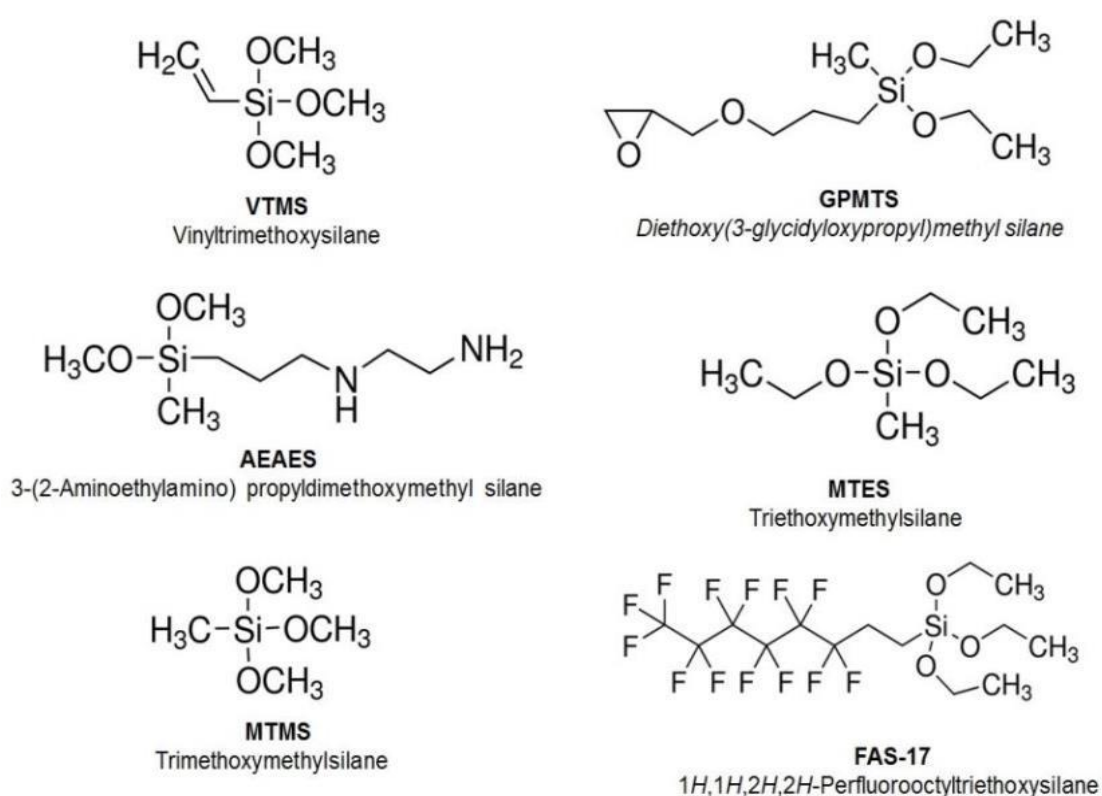
Figure 2-17 Different sol-gel precursors used in coating applications, adapted from [92]

2.17 Application of sol-gel technology

There are potentially numerous applications in industries involving sol-gel derived technologies. The sol-gel processes can produce a variety of different materials, including coatings, films, fibres, monoliths, and nanosized powders. Coatings or thin films produced by the sol-gel technology are the typical representatives in the early commercial involvement. Spinning, spraying, dipping and spreading methods can be used to create thin films without forming any cracks, for instance, the sol-gel optical coatings on

substrates enhance and improve optical properties such as reflection, transmission and/or absorbance. There are other examples of coating applications of the sol-gel films such as self-cleaning coatings, hydrophobic or hydrophilic coatings, and anti-corrosion and wear-resistance coatings[81], [82], [93].

Monoliths can be defined as a gel casting process to produce a particular shape with high purity. It can be done without cracking or shrinking, and with high or minimum density. Monoliths are used for many applications including fibre optics, lenses, transparent foams and classified reflective glasses.

Nano-sized powders produced by sol-gel technology are another typical example. Ultra-fine and uniform metal oxides can be produced. These powders are used in various applications, for example, dental and biomedical applications, and powder metallurgy (PM) industries. [82], [94]

The sol-gel technique can also produce ceramic membranes for applications such as filtration, reverse osmosis, chromatography, and catalysis.

2.18 Sol-gel corrosion protection applications

The conventional methods for corrosion protection using the Cr^{6+}-based corrosion inhibitors will be entirely banned in aerospace industries. Environmental protection organizations have put their efforts into removing toxic Cr^{6+}-contained substances from industries. Moreover, considerable efforts have been made to replace the conventional conversion coatings (i.e., phosphating and chromating) for corrosion protection on metallic surfaces. Electrochemical methods have also been devoted to producing new materials for corrosion protection such as polyaniline, polythiophene, and polypyrrole as corrosion inhibitors[95].

The sol-gel protecting coatings on metallic surfaces can improve their corrosion resistance in various corrosive media. The replacement of Cr^{6+}-based coatings and/or pre-treatments by environmentally friendly sol-gel coatings on metallic surfaces can be expected. Furthermore, the sol-gel coatings can also provide additional properties such as water resistance, oxidation resistance, abrasion resistance, and many other useful features [94], [5]. Conventionally, inorganic sol-gel coatings have been widely investigated, including SiO_2, Al_2O_3, TiO_2, ZrO_2, and CeO_2 or binary or mixed metallic oxides [84]. However, the limitations of inorganic sol-gel coatings can be stated as the following:

a)   Cracks often occur in inorganic sol-gel coatings during drying and densification processes, particularly with high-thickness coatings.

b)   The thermal expansion coefficient of metallic materials and inorganic coatings are incompatible, causing film peeling-off during temperature variation.

c)   The high porosity of the inorganic sol-gel coatings hinder their use in the barrier protection of metallic surfaces.

The development of a variety of organically-modified precursors to produce sol-gel coatings with desirable properties has created hybrid sol-gel systems, wherein various metal oxides and organic functional groups also can be combined to introduce various functionalities. The advantage of inorganic components provides properties of wear resistance, durability, and adhesion to metallic surfaces while organic groups increase density, flexibility, and functional compatibility with the inorganic systems. Other advantages of organic components for hybrid sol-gel systems are to produce crack-free, thick, hydrophobic, and low-temperature-cure coatings. [96], [5].

2.18.1 Sol-gel corrosion protection on aluminium alloys

 Sol-gels are considered to be one of the excellent alternative techniques to replace conventional treatments , many of which are almost banned, such as chromate conversion coatings. This comes via the low initial cost and effectiveness of this coating. Spatially it is considered as eco-friendly coating comparing to the other alternative surface treatments. Also, the advantages of sol-gel over the conventional coating methods is the ease of preparation, and controlled crack-free films also can ease deposit a wide range of inorganic oxide in the matrix at a lower temperature [97], [98].

Aluminium alloys and especially AA2024-T3 are widely used in the aerospace and structural industries because of high specific strength ratio. However, the element of copper in these alloys is used to improve its mechanical stiffness. However, this, in turn, can result in microscopic galvanic couples which increase the potential for corrosion on these alloys. For avoiding localised corrosion that could damage the mechanical properties of structures, the general practice is to prevent the direct interaction of the electrochemically active matrix with the environment by applying a protective coating system with the intention of prolonging the service life of parts, before applying a painting application, the alloy is frequently clad or anodised to provide good bonding between the paint and the substrate[43].

The advantage of using the sol-gel coating in this scenario is to directly form robust Van der Waals bonds between metallic surfaces and gels with alkoxides networks to provide a film barrier without using the pre-treatment processes of cladding or anodising. The bonds will then be transformed from Van der Waals to stable covalent Al-O-Si bonds in the transition period of drying and sintering. Additionally, polymers can be included in the hybrid sol-gel coatings in order to increase their resistance to corrosion. Figure 2-18 shows the alumina-silica backbone interfacial structures. As well as applying sol-gel on the metallic substrate can protect by itself as a barrier the coated metal from corrosion due to the formation of a backbone aluminium oxide film capable of blocking the pores in the original aluminium oxide film to create a highly corrosion-resistance layer. This layer is preventing the ionic and oxygen diffusion to the metal surface [97], [99].
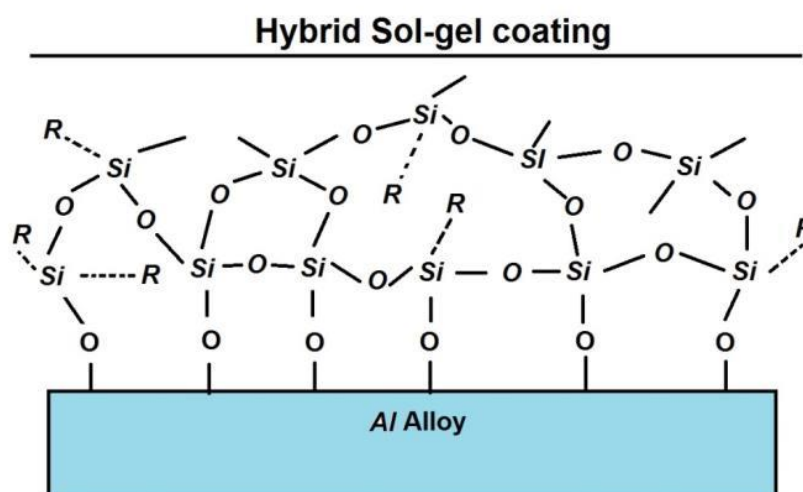
Figure 2-18 Schematic drawing of Al-O-Si- backbone interfacial structures in Hybrid Sol-gel coating, adapted from [99]

Since the coating contains micro-pores, micro or nano-cracks, and of low cross-links which provide a path for the diffusion of water, chloride ions and oxygen to the coating-metal interface [100], adding organic functional groups such as epoxy, vinyl and polytetrafluoroethylene, will increase the resistance of corrosion and improve the barrier function of the coating film[101][102]. However, there remains a general disadvantage compared to other coatings, and that is a lack of active corrosion protection, so industrial organisations and researchers have started to improve this ability by the incorporation of inorganic and/or organic inhibitors into the main matrix of the sol-gel formula[103].

For instance, adding cerium, vanadates and molybdenum were implemented in some sol-gel coatings. Wang H. et al. [103] investigated the effect of adding the cerium nitrate salt to a sol-gel coating, and it demonstrated excellent protection to the mild steel. The main issue regarding these inorganic materials which are known as rare earth metals was the initial cost, which could increase the cost of coating, even though the cerium salts have started to be encapsulated in sol-gels for aerospace use as an alternative for chromate conversion coatings [104][103].

On the other hand, enhancing the sol-gel matrix with organic components as inhibitors has proved attractive to researchers, and this came after the cost and compatible with hybrid sol-gel, for example, Akid R. et al. [105] mentioned that the use of polyaniline (PANI) with a hybrid titania-silicate containing sol-gel system with PVD improved the corrosion protection performance. Also, Sharifiyan M. et al. [106] investigated the effect of adding a high concentration of benzotriazole on the corrosion behaviour of a titania-alumina sol-gel to protect aluminium alloys. The results illustrate that the amount of benzotriazole plays an important role in the corrosion protection and self-healing behaviour of the coatings, while the gradual release of benzotriazole from the coatings during exposure to an aqueous solution produces the self-healing ability.

Therefore, it has been established that hybrid organic-inorganic sol-gel coatings can work both as barriers, and able to carry organic or inorganic inhibitors by direct mixing or encapsulation without affecting cross-linking, adhesion, flexibility, and provide active corrosion protection.

Chapter 3- Testing and Experimental Procedure

Overview

In this chapter; will firstly present a general explanation for different testing and evaluation methods that have been used in this project, including corrosion evaluation techniques such as electrochemical analysis methods, including electrochemical impedance spectroscopy (EIS) and potentiodynamic polarisations scanning (PDPS). Then surface and morphology evaluation including scanning electron microscopy (SEM), atomic force microscopy (AFM), Infinite Focus Microscope (IFM), and water contact angle measurement (WCA). For chemical composition analysis including Fourier-transform infrared spectroscopy FTIR, and Energy-dispersive X-ray spectroscopy (EDX). Finally, the mechanical properties assessment including pull-off adhesion, cross-hatch test, tackiness measurement and nanoindentation.

Secondly, the experimental work itself; this part will present how was the setting and preparation for all materials that have been used, including the substrates preparation, sol-gel preparation and inhibitors mixing and ratios for inhibitors with sol-gel, then coating deposition and coating characterisation parameters for all equipment that has been used in this study.

3.1 Testing Theories and Techniques

3.1.1 Corrosion electrochemical techniques

The precise and quick measurements of electrochemical cells are of considerable importance for a variety of studies, not only for scientific research in corrosion but also in practical engineering and industrial applications. Although, it is possible to measure the effects of corrosion by direct analytical techniques; for instance, the corrosion rate can be determined by weight loss or solution analysis by spectroscopy. However, these techniques are usually slow, and time is consumed and sometimes inefficient [107], [108].

The electrochemical methods evaluation of "the corrosion process and protection performance" was based on Faraday's law Equation **3-1**. That can be described by the relationship of the charge in the mass per unit area to the current flow.

$$m = \frac{QM}{nF} = \frac{ItM}{nF} \qquad\qquad \textbf{Equation 3-1}$$

Where: Q is the charge (coulomb, C), I = the current(amperes, A), F= Faraday's constant, n=number of equivalents (mols of electrons), m= mass of metal (g) and M= molecular (atomic) weight of metal (g/mols)

This approach has some advantages when compared with traditional methods, including short measuring time, reasonable accuracy with the possibility of continual monitoring and testing with other techniques at the same time. One of the disadvantages of using electrochemical techniques is that the tested system has to be disturbed from the real state by an external electrical signal, which inevitably changes some of the properties of the system [107]–[109].

Today, electrochemical testing by using direct current (DC) techniques are widely used for corrosion measurement, the issue with these methods is that they require a relatively large polarisation signal, and the drawback is a possibility of failure when corrosion measurements are made in low conductivity electrolytes. Also, high polarisations can easily destroy the tested sample. Therefore, looking for other electrochemical techniques with small polarisation also can be used in the low conductivity media, which can be achieved by alternating current (AC) methods [107], [108].

3.1.2 The Electrochemical Impedance Spectroscopy (EIS)

As one of the nondestructive electrochemical techniques based on the use of a range of low magnitude polarising potentials, EIS uses a spectrum of alternating current (AC) frequencies and works in potential cycles typically from anodic to cathodic [109].

The concept of electrical resistance is defined as the ability of an electrical circuit element to resist a flowing electrical current. As per Ohm's law in Equation 3-2Equation 3-2, it is defining the resistance regarding a ratio between voltage (E), and current (I).

$$R = \frac{E}{I} \qquad \textbf{Equation 3-2}$$

However, in the real world, the circuit elements have much more complex behaviour. These factors push to shed the simple concept of resistance, leading to replacing it with impedance. Similar to resistance, impedance is a measure of the ability of a circuit to resist the flow of an electrical current, except it is unlike resistance, and not limited by the simplifying properties mentioned above in Ohm's relation.

Electrochemical impedance is measured using an excitation signal. As a result, the cell's react is pseudo-linear. In a pseudo-linear (or linear) system, the current will response with sinusoidal potential as a sinusoid at the same frequency but with shifted in phase as shown in Figure **3-1** [110].
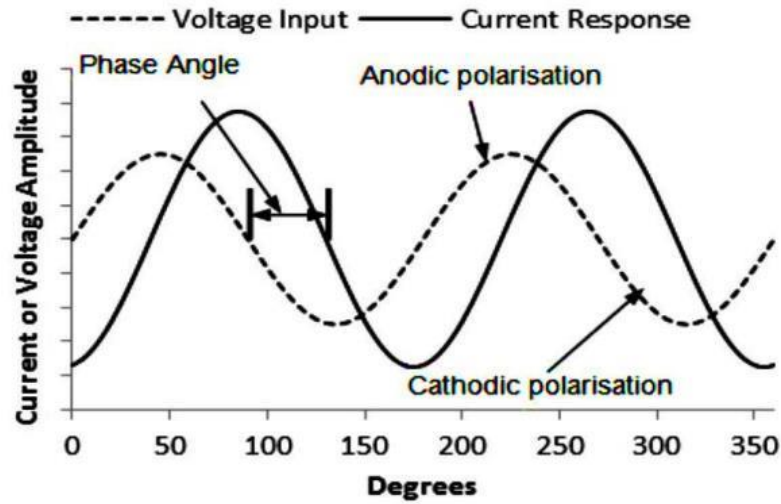
Figure 3-1 Sinusoidal curves of applied AC voltage and current response

The excitation signal has the form and stated as a function of time in Equation 3-2.

Equation 3-3

$$Et = E_\circ Sin(\omega t)$$

Since E_t is a potential at time t, and E_0 is an amplitude of the signal, and ω is the radial frequency. The relationship between radial frequency ω and frequency f is as in Equation 3-3:

Equation 3-4

$$\omega = 2\pi f$$

Moreover, in linear systems, the response signal, I_t, is shifted in phase (Φ) and has a different amplitude than I_0. As in Equation 3-4:

Equation 3-5

$$It = I_\circ Sin(\omega t + \phi)$$

The impedance of the system will be calculated by the expression analogous to Ohm's Law as in Equation 3-5:

$$Zt = \frac{E_oSin(\omega t)}{I_oSin(\omega t + \phi)} = Z_o\frac{Sin(\omega t)}{Sin(\omega t + \phi)} \qquad \textbf{Equation 3-6}$$

Therefore, the impedance is defined in terms of a magnitude $\pmb{Z_o}$ and a phase shift $\mathit{\Phi}$.

Moreover, using the relationship of Eulers,

$$\textbf{Equation 3-7}$$
$$\exp(j\emptyset) = \cos\emptyset + j\sin\emptyset$$

It is possible to show the impedance as a complex function, also described by 3-7:

$$\textbf{Equation 3-8}$$
$$E_t = E_0\exp(j\omega t)$$

Similarly, the current responses are as in equation 3-8:

$$\textbf{Equation 3-9}$$
$$I_t = I_0\exp(j\omega t)$$

Then the impedance for the simple circuit is described as a complex number as follows:

$$Z(\omega) = \frac{E}{I} = Z_0\exp(j\emptyset) = Z_0(\cos\emptyset + j\cos\emptyset) \qquad \textbf{Equation 3-10}$$

So, the impedance can be directly expressed in two ways in electrochemical impedance spectroscopy:

a)   In Cartesian coordinators (Nyquist Plot)

Impedance $\qquad\qquad\qquad |Z| = a - jb \qquad\qquad$ **Equation 3-11**

Resistive component of impedance $\quad a = R\cos\Phi$

The imaginary component of impedance $\quad b = R\sin\Phi$

b) In polar coordinates (Bode Plot)

Modulus of impedance $\qquad\quad R = |Z| = \sqrt{a^2 + b^2} \qquad$ **Equation 3-12**

 Phase angle $\theta \qquad\qquad\qquad \theta = \tan^{-1}(-b/a)$

Resistance and capacitance values are measured at these frequencies so that these quantities can provide information on corrosion rate, diffusion, and coating performance.

Normally, the coating system unit contents, capacitive, and resistant properties of an electrical interface produce what call a "Time-Constant". The plotting responses of a time constant on exhibit:

- in Nyquist plot shows as semicircles,

- in the Bode phase diagram shows an inflection

- In the Bode IZI magnitude, the plot indicates negative values on slopes

Various factors and processes generate multiple time constants on the same test electrode [108]. Some examples of simple EIS will be discussed to illustrate how the EIS technique will be used.

3.1.3 Equivalent circuits

The equivalent circuit usually refers to the theoretical circuit that adopts all electrical properties of a given real circuit of corrosion electrical response. Typically, looking for an equivalent circuit simplifies the calculation on a broader scale, which can be the simplest form of a more complex circuit to aid analysis [111] there are many simplified equivalent circuits that widely used in corrosion and coating, here are some of the famous models that used in coatings.

3.1.3.1 Full Randle's cell for a bare metal

It is one of the most common cell models. The equivalent circuit consists of a solution resistance, a double-layer capacitance, a polarization resistance and a Warburg element. The double-layer capacitance is in parallel with the layer resistance, and Warburg element is an equivalent electrical circuit component that models the diffusion process. This diffusion can be in the coating or the oxides film. Additionally, this cell is considered the preliminary point for additional more complicated models of corroded systems [109]. The equivalent circuit of a full Randles cell is shown in
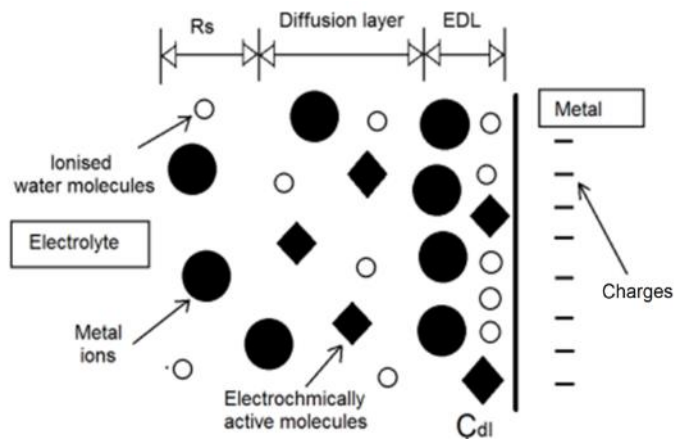
Figure 3-2 Electrical double layer for Randle's cell
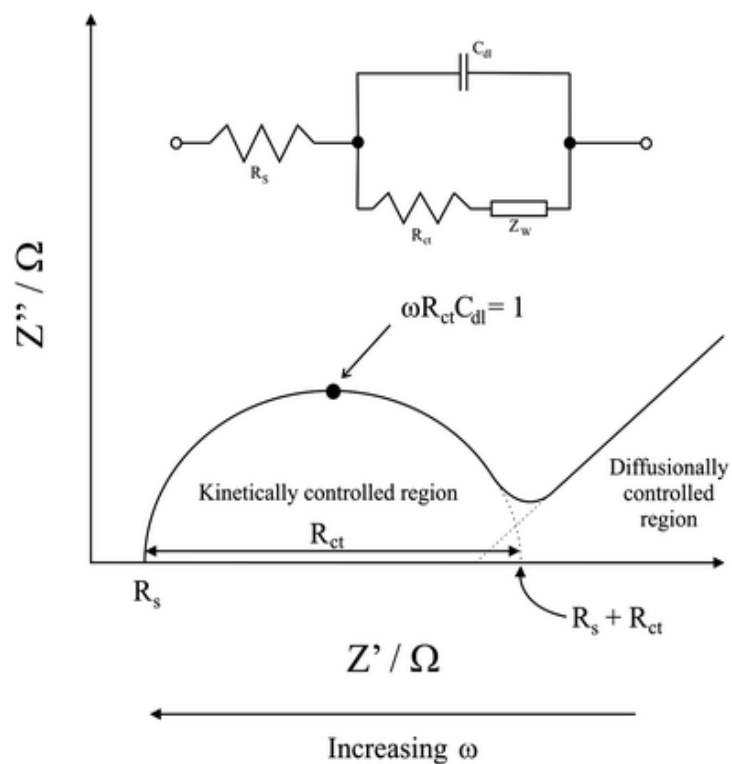
Figure 3-3 The Schematic Nyquist plot and modelling diagram for full Randle's Cell [112]

Figure **3-3** shows the Nyquist plot for a typical full Randles cell. The parameters in this plot were measured at the working electrode undergoing uniform corrosion. The Nyquist plot for a simplified Randle's cell is a semicircle. By reading the real impedance value at the high-frequency intercept, the solution resistance can be found. At the low-frequency intercept is a summation of the solution resistance and the polarization resistance. The diameter of the semicircle is, consequently, equal to the polarization impedance. [109].

The simplified Randles cell can be applied to bare metal corrosion behaviour in an electrolyte. Metal immersed in the solution creates an electrical double layer (EDL) interface with the electrolyte medium, and the corresponding of this EDL is via the simplified Randle's cell as shown in Figure **3-2**. This circuit will be represented as one "time constant" circuit in Bode and Nyquist plots. [107]

3.1.3.2 The equivalent circuit for the coated metal

All coatings in the actual environment have more complicated impedance tendencies when compared with the capacitive behaviour based on the simplified Randle's cell. After a short immersion in water, the coating system penetrates and generates a new two time-constants; the first one related to the coating solution interface . and the second one is related to the coating barrier properties with long immersion the liquid/metal interface layer created from oxides under the coating which reflecting the diffusion process on the metallic surface this element called Warburg element, In this time frame, corrosion could occur at this liquid/metal interface. Figure **3-4** shows the simple equivalent circuit described here[109].
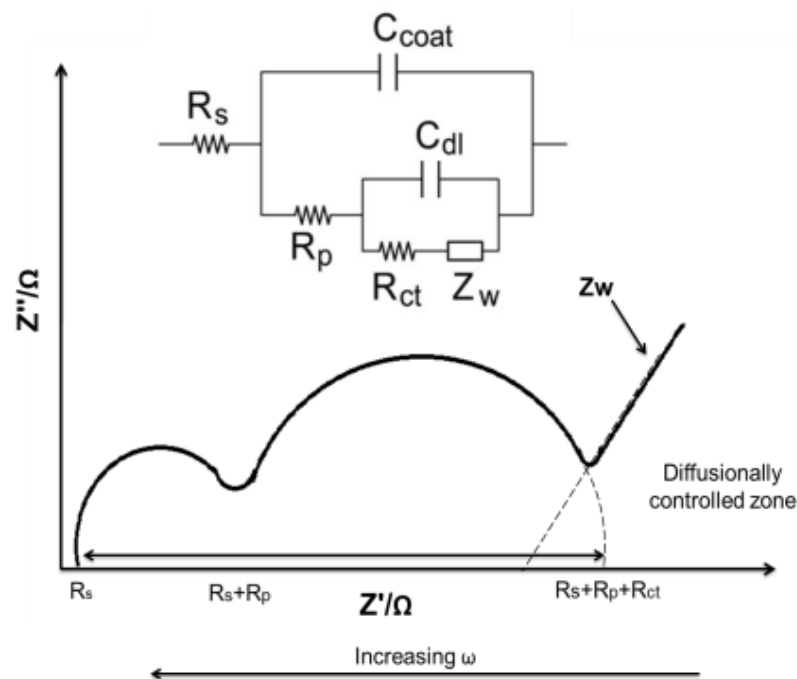
Figure 3-4The schematic Nyquist plot and modelling diagram for the coated metal[112]

C_{ct} refers to the total coating capacitance. This value is much smaller than a typical electrical double layer capacitance. Units are in pF, nF or μF. The R_p refers to the pore resistance, which is the resistance of ion-conducting routes that grows in the coating.

Routes are possibly not necessarily filled with the electrolyte, which is sometimes is affected by conductive elements in the coating matrix.

On the metallic side of the pores, the area of the coating starts delaminating and flaws are filled with the solution present. The diffused electrolyte solution inside the coating could be more different from the electrolyte solution outside the coating. The interface between this electrical flaw of the solution and the bare metal is demonstrated as a double-layer capacitor in parallel with a kinetically controlled charge-transfer response with two time-constants [107],[109]. Figure **3-4** shows the Nyquist plot for this simulated equivalent circuit of the coated metal (note that there are two perfect time constants with diffusion element). [109],[110].

3.1.4 Open Circuit Potential (OCP)

It is considered as one of the essential non-distractive and necessary measurements in any electrochemistry test, including the dynamic and static. When the workpiece is immersed in an electrolyte solution, the created potential of the metal is a function of the natural reaction of the metal and the oxidising force of the solution. The primary target of potential measurements is to quantify the measured potential of the metal samples without affecting the reactions on the metal samples surface. It is essential to measure the potential by using stable reference electrode so as a result, any changes that occur in the measured amount can be attributed to changes on the sample and solution interface [107], [113]. The reference electrode is very critical, as it affects the validity of potential measurements on the sample, known as a working electrode (WE)[114], [115].

There are many other names for open circuit potential, including the equilibrium potential, the resting potential, or the corrosion potential, and it can be defined as the change of potential logged in time, also as the measured potential of where the smallest current passing by anodic reactions equal to that in cathodic reactions [114]. Figure 3-5 shows a schematic simple open circuit potential cell.
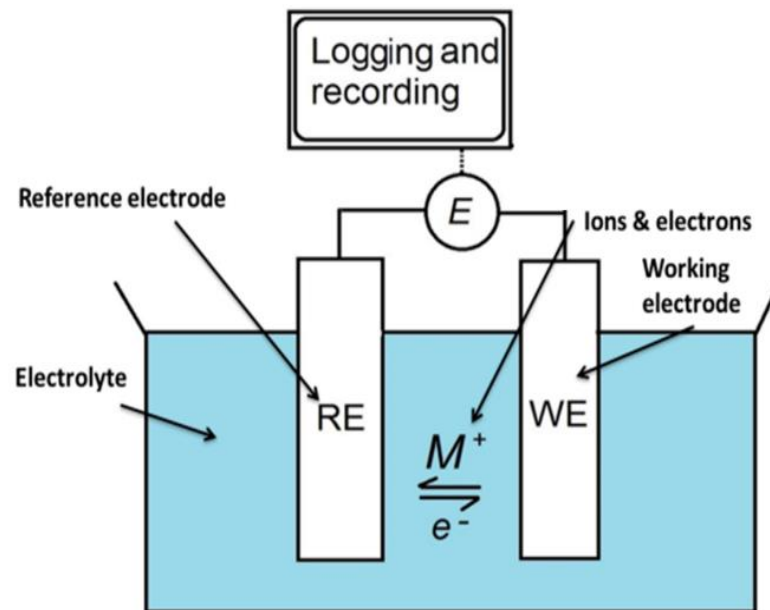
Figure 3-5 schematic simple open circuit potential cell

3.1.5 Potentiodynamic polarisations scanning (PDPS)

This technique is based on DC polarisation, Potentiodynamic polarisations scanning (PDPS) is another technique for the electrochemical corrosion measurement. PDPS helps to recognise the potential region over which the specimen stays passive or active. Moreover, the corrosion rate in the passive region, the pitting potential, and the ability of the metal substrate to spontaneously passivate in the particular electrolyte. However, the test is considered a destructive test for a coating so it can only be performed once [107]. This method will be used in this project. The schematic diagram shows a topical polarization curve, as seen in Figure 3-6.
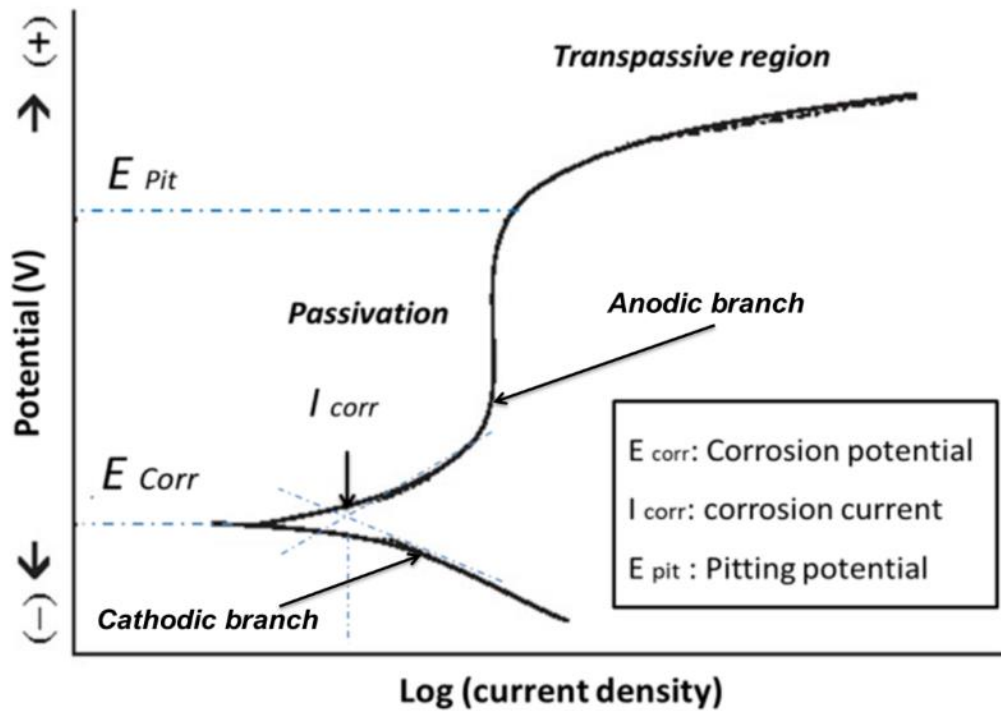
Figure 3-6 Schematic potentiodynamic polarisation diagram[116]

3.1.6 Experimental part in using the electrochemical testing technique

In this research project, electrochemical tests were performed on the coatings to assess their corrosion resistance. Experiments were conducted in Sheffield Hallam University (SHU) in Material and Engineering Research Institute (MERI) labs. By using a Princeton Applied Research PARSTAT 2273 with three-electrode cell; Figure 3-7 shows the electrochemical testing cell, containing the substrate as the working electrode, a saturated calomel electrode (SCE) reference electrode and platinum as the counter electrode. The corrosion behaviour of the uncoated and sol-gel coated aluminium alloy was evaluated using potentiodynamic polarization scans and electrochemical impedance spectroscopy (EIS). The EIS test specimens were prepared by masking the samples with a beeswax-colophony resin mixture, leaving an exposed area of 1.0 cm^2 in the centre of the sample. All electrochemical tests were carried out at room temperature (25° C +/- 2° C) and in aerated 3.5 % w/v NaCl. Before the PDPS test, the electrode potential was monitored for approximately 1 hour in the solution until it stabilised. Then the sample was polarised at a scan rate of 1.667 mVs^{-1} from the initial potential of -250 mV (vs OCP) to +750 mV (vs SCE); The EIS measurements were recorded between 100 kHz to 10 MHz with a sinusoidal AC RMS value of 10 mV [107], [109].
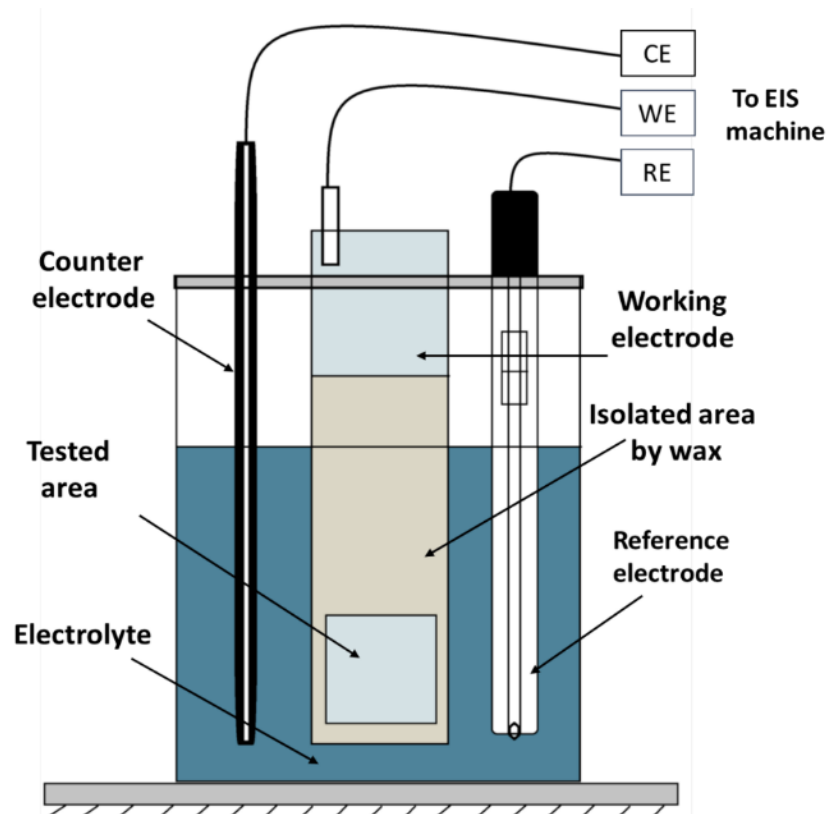
Figure 3-7 Shows schematic electrochemical testing cell

3.2 Surface and morphology characterisation techniques

3.2.1 Scanning electron microscopy (SEM)

The first use of electron beam in microscopy has been reported in the Symposium on New Methods for Particle Size Determination in the Subsieve Range at the ASTM Washington Spring American Meeting was in 1932 by Borries and Ruska [117]. In addition, the first identifying of the scanning electron microscope by the name was by Zworykin in his prototype microscopy in 1942 [118]. However, the real issue with this prototype was a low resolution, and as a result, SEM development continued, until in the 1950s at the University of Cambridge, through projects at Charles Oatley's laboratory [119], followed by the first commercial scanning microscope produced by Cambridge Instruments Ltd in 1965. SEM is considered as a relatively rapid, non-destructive, and inexpensive method to the analyse surfaces. High-resolution topographical images can be obtained by focusing an electron beam on the surface of the sample and then measuring the resulting secondary or backscattered electrons with a suitable detector[119].

As an SEM uses a high-energy beam of electrons to illuminate the specimen and produce a very highly magnified image, it has much greater resolution than a light-powered/optical microscope because electrons have a much shorter wavelength than visible light[119], [120].
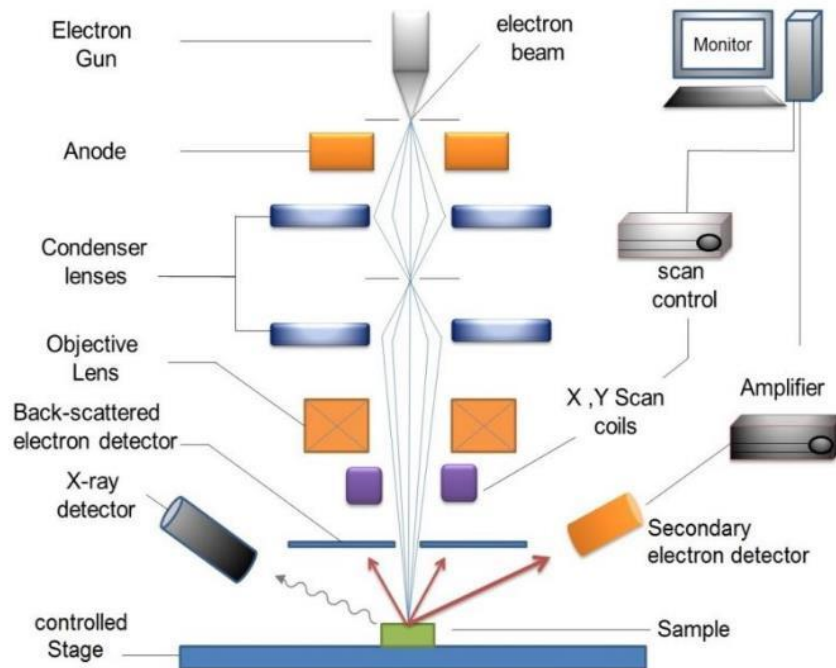
Figure 3-8 Schematic contents and Mechanism of scanning electron microscopy

Figure 3-8 shows how a beam of electrons is generated at the top of the microscope by the electron gun. Then the electron beam follows a vertical path through the condenser lens, which is sometimes under a vacuum. The beam travels through electromagnetic lenses; these lenses focus the beam down, concentrating them on the sample.

There are two types of formed electron interaction between the sample and the primary beam. The first one generates what is known as the secondary electrons, and these are generally formed on the surface, and the other one produces backscattered electrons, that generated deeper inside the tested material and usually accompanied by X-rays and heat.

Once the electron beam collides the sample, electrons and X-rays are ejected from the sample, as shown in Figure **3-9.** Detectors start collecting these backscattered electrons, secondary electrons, and X-rays and convert them into signals interpreted on a computer screen [121]. The SEM may also be fitted with an Energy Dispersive X-Ray (EDX) analyser, which is used to provide elemental identification and quantitative compositional information of samples.
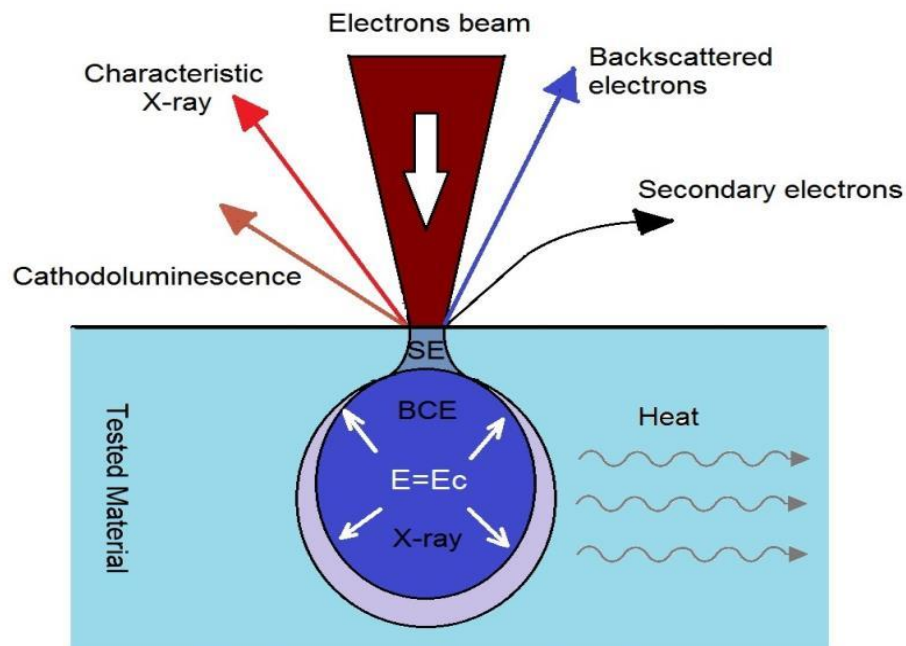
Figure 3-9 Mechanism of electron beam teardrop- shape, adapted from [121]

SEM and EDX will be used to obtain information about the sample such as external morphology, chemical composition, coating thickness and the presence of microcracks in the coating. In this PhD project, an FEI-QUANTA 650 scanning electron microscope (SEM), with an X-MAX 80 mm^2 energy-dispersive X-ray (EDX) spectrometer (Oxford Instruments), was used to analyse the morphology and chemical composition of coated samples and tests were performed at Sheffield Hallam University in MERI labs.

3.2.2 Atomic Force Microscopy (AFM)

AFM is usually used to indent the surface morphology and topography typically in high-resolution tapping mode, which permits nano-indentation to be performed, measuring the mechanical properties of tested samples[122]. The basic principle of AFM involves a fine tip being scanned across the surface of the sample to measure surface morphology and properties to construct a 3D image of the surface. The theory of AFM comes from the effect of atomic vibration effect on the nano-size probe which will reflect the concentrated laser beam on the top of the tip at the end of the cantilever "acts as the probe". A sharp probe will be scanned over the surface of the sample during the AFM scanning process. In this scanning, the cantilever will vibrate from the effect of surface atoms. Then the receiver will collect the reflected laser beam light from the cantilever and process it to draw the topography of the surface.

The high-resolution of the images can be between 1 nm to 200 µm [123]. Figure 3-10 shows the schematic of the atomic force microscope. In this study, the AFM was used is Bruker multi-mode eight on tapping mode with nano-indentation properties and tests were performed at Sheffield Hallam University in MERI labs [124].
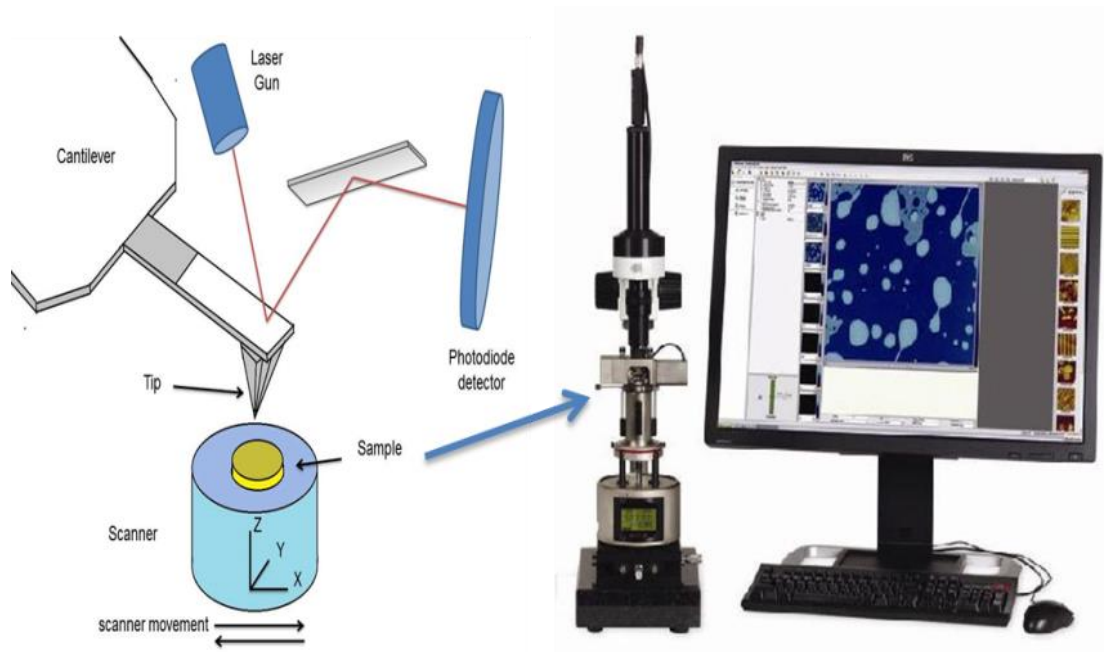
Figure 3-10 schematics of atomic forces microscope

3.2.3 Infinite Focus microscope (IFM)

IFM is a recent development in microscopy and can be considered as contactless optical 3D microscope which overcomes the low depth of field of the optical microscope by vertical scanning, and which can raster across the surface of the tested material to combine the desirable high resolution with topographical profile and depth in large field area [125]. It can achieve high and precise measurements with high repeatability and a vertical resolution reaching 10 nm. Figure 3-11 shows a schematic drawing of a 3D Infinite Focus microscope.
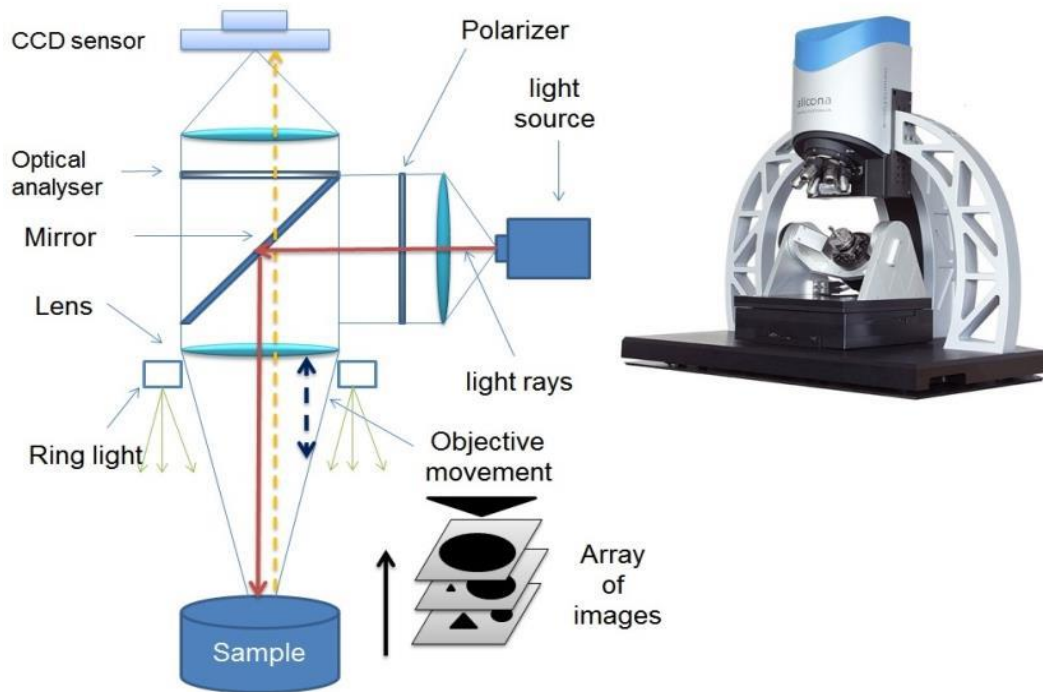
Figure 3-11 Schematic drawing of 3D Infinite Focus microscope

Nevertheless, the primary function of the IFM is not only to take images, but it can also be used for reverse engineering with a variety of software function which can analyse the captured images from standard dimensional analysis to surface roughness. The software packages include profile, roughness, surface texture and 2D and 3D image analysis [125]. The Infinite Focus G5 was used for all samples and tests were performed at Sheffield Hallam University in MERI labs.

3.3 Contact angle goniometer (CA)

Contact angle goniometer can be used to measure the angle at the edge of the liquid drop on a solid surface, where a three-phase liquid–vapour-solid interface meets on a surface. The mechanism of measuring the wettability of hard surfaces by contact of liquid is according to Young's equation as shown in Equation 3-13 and Figure 3-12, wherein the solid–vapour interfacial energy is defined as by γ_{SG} the solid liquid interfacial energy by γ_{SL}, and the liquid–vapour interfacial energy by γ_{LG}, then the equilibrium contact angle θ_c is determined from these quantities as :

$$\gamma_{SG} - \gamma_{SL} - \gamma_{LG} \cos \theta c = 0 \qquad \textbf{Equation 3-13}$$
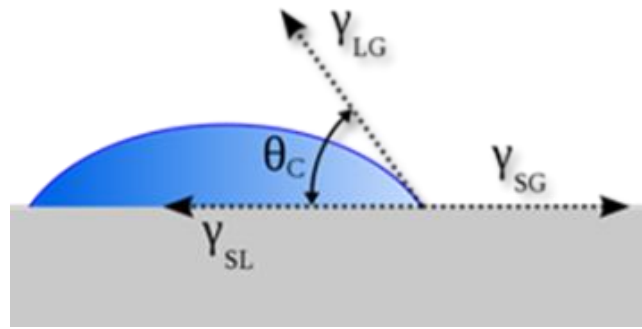
Figure 3-12 Contact angle of a liquid droplet wetted to a rigid solid surface

Contact angle measurements are sensitive to contamination. Tests are preferably performed under laboratory conditions with purified liquids and clean surfaces. If the liquid molecules are powerfully attracted to the solid molecules, then the liquid drop will entirely spread out on the surface, resulting in a contact angle approaching to 0°.

This is usually the case for the behaviour of water on ceramic or bare metals surfaces while the existence of contaminants or an oxide layer on the solid surface can slightly change the degree of the contact angle. If the water contact angle (WCA) is smaller than 90°, the surface has hydrophilic properties, and if WCA is greater than 90°, the surface has hydrophobic properties [126]. As shown in Figure 3-13. Hydrophobic surfaces are created by low surface energy; for example, fluorinated materials may have WCA as high as ~120°. The materials with nano-rough surfaces could obtain a WCA greater than 150° called super-hydrophobic surfaces.[127]–[129]

Figure 3-13 CA Goniometer, and hydrophobic & hydrophilic WCA drops

The hydrophobicity of all coated and non-coated samples was determined by performing water contact angle measurements using a Dataphysics OCA 15EC Goniometer, with deionised water (DI) used as the solvent [130]. Many analyses were performed across the

surface of each sample and the mean water contact angle value calculated by the Dataphysics OCA software.

The experiments were performed at Sheffield Hallam University in MERI labs, and it carried out on bare and coated samples using Contact Angle Goniometer Deionised water was used as the liquid, and the drop volume size was 1.5 µL, with the rate was 0.5 µl /sec. The contact angle was calculated by the software package.

3.4 Fourier-transform infrared spectroscopy FTIR

Infrared (IR) spectroscopy is one of the conventionally used methods for chemical analysing mostly the organic compounds. The theory behind this equipment is based on the stretching and bending of atoms bonds vibrations, so when the IR beam hit on the sample, the IR energy will make atoms vibrate to the vibrational frequency of the bonds of the atoms on the molecule and this molecule will absorb this IR radiation [131]. The absorbed IR waves will be converted and logged in the instrument processer into frequencies, resulting in creating a spectrum by frequency of responded molecules and represented into absorption and transmission.

This spectrum will be as fingerprint and determine chemical functional groups in the tested sample. Furthermore, the test is non-destructive, and the peak size in this spectrum can provide information about the presence and number of constituents inside the sample. IR spectroscopy can deliver the results in term of transmittance (T) or absorbance (A). The relationship between absorbance and transmittance is as follows: absorbance (A) is the base 10 logarithm of the reciprocal of the transmittance (T). The infrared radiation wavelength range that used in measurement from 0.78 to 1000 μm stated from the red light that can be visible for eyes to the microwave region, respectively. However, usually infrared presented in most instruments' measurement with wavenumber instead of a wavelength which started from (13,000 to 10 cm^{-1}). The range that must be used and can provide enough information is called the mid-IR-range of (4000 to 400 cm^{-1}). Wavenumber can be identified as a function of a wave per length unit as per the following Equation:

$$\textit{Wavenumber } (v) = \frac{1}{\lambda(\textit{in } \mu m)} \times 10^4 \qquad \textbf{Equation 3-14}$$

Where λ is the wavelength

Fourier transform IR spectroscopy is now used due to the high speed of data acquisition. Instead of applying each IR frequency sequentially, all frequencies will be applied together in FTIR spectroscopy and the frequency-specific data extracted.

The gathered information regarding the chemical composition or rehydration of the sol-gel coatings was obtained at Sheffield Hallam University MERI labs by using a Thermo Nicolet NEXUS-FT-IR Fourier transform infrared (FTIR) spectrometer coupled to a Graseby single reflection diamond ATR cell[131]. Samples were prepared by putting a dried film of sol-gel directly onto the ATR crystal and spectra were collected as a function of wave absorption, and tests were performed at Sheffield Hallam University in MERI labs.

3.5 Thickness measuring

Eddy current testing is a non-destructive testing (NDT) which is widely used to measure coating and paint thickness in the aerospace and automotive industries on both ferritic and non-ferritic metals. The phenomenon of electromagnetic induction is behind the functioning of this technique. In the measuring probe, the AC current flows through a small wire coil generating the magnetic field, so when this generated magnetic field is brought close to the metallic material, the circular flow of electrons occurs. This is known as eddy current, moving in swirling stream. The eddy current flows through the metal will generate its magnetic field, which will interact with a probe coil magnetic field in mutual inductance. The changes in the thickness of a coating or the presence of surface cracks will disturb the amplitude pattern of the eddy current magnetic field, which will be affecting the movement of the electrons in the coil by changing the current impedance and phase angle inside the coil. These changes can be used by the processing tool to identify changes in the thickness of the test piece. An Elcometer 456 B Coating Thickness Gauge was used at MERI labs for measuring the coating thickness in with SEM cross-sections for confirming the results.

3.6 Mechanical properties testing techniques

3.6.1 Adhesion pull-off Test

Adhesion of any coating is considered one of the most significant properties, especially when it needs to be evaluated for its performance, reliability and durability to suit the desired application. The strength of the adhesion of the coating with the substrate will be presented in the adhesion resistance and strength.

The primary use of the pull-off adhesion test is to determine the vertical forces that a given surface area can bear before a plug of material is detached. Pull-off will happen on the weakest part of the system, which comprises the test fittings, adhesive, coating system, and the substrate.

In this study, an Elcometer 108 hydraulic pressure dial gauge pull off tester was used at MERI labs, as shown in Figure 3-14, to measure the adhesion of the coating systems on the aluminium alloys 2024 T3 as per ASTM D4541[132].
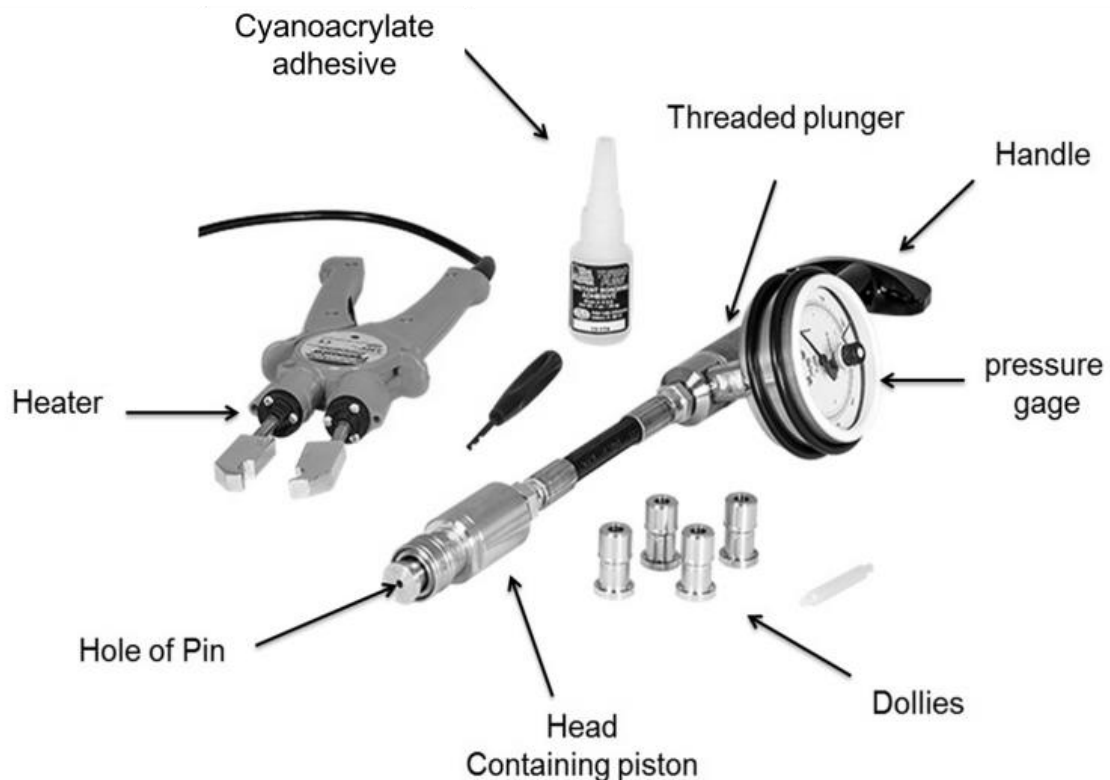
Figure 3-14 Elcometer 108 the hydraulic pressure dial gage pull off tester [132]

3.6.2 Cross-Cutting / hatching test

In this test, the method is based on measuring the resistance of cross-hatched coatings to separation from a substrate by using adhesive tape after an angled lattice pattern is cut by using the cutting tool manually into the coating until penetrating through to the metallic substrate.

The cross-hatching test was performed at Sheffield Hallam University in MERI labs and evaluated according to the standard practice code ASTM D3359-17 as per to schematic indicating classification results in Figure 3-15 this classification based on the estimating of the amount of coating separation from the coated sample [133], [134].

CLASSIFICATION OF ADHESION TEST RESULTS		
CLASSIFICATION	PERCENT AREA REMOVED	SURFACE OF CROSS-CUT AREA FROM WHICH FLAKING HAS OCCURRED FOR SIX PARALLEL CUTS AND ADHESION RANGE BY PERCENT
5B	0% None	
4B	Less than 5%	
3B	5 – 15%	
2B	15 – 35%	
1B	35 – 65%	
0B	Greater than 65%	
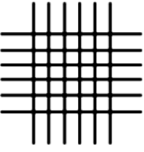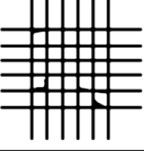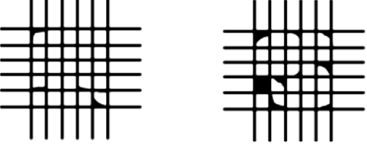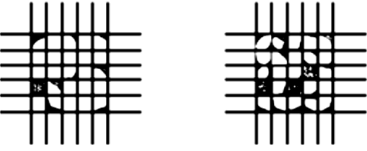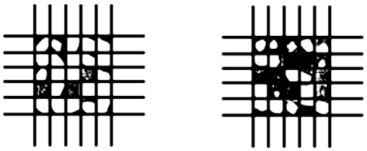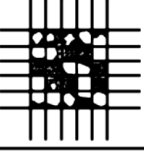
Figure 3-15 Method of cross-cut adhesion Test Results [134]

3.6.3 Hardness measurements

Hardness is defined as the property of resisting plastic deformation; this is determined by indenter penetration. The method to assess hardness is to measure the depth or area of an indentation left by an indenter of a specific geometry, so with a known force, applied for a specific time.

There are two main classifications of hardness measurement, relating to the test force: macro hardness with as applied load of higher than 9.807 N (1 kgf), and microhardness the applied load in the range of 9.807×10^{-3} to 9.807 N (1 to 1000 gf). Besides, there are many standard testing; these are included Vickers or Knoop scales, Brinell, and Rockwell. For practical and calibration reasons, each of these methods is distributed into a range of scales [135].

In this project the DURAMIN-40 AC3 automatic micro/macro universal hardness tester was used, the tester with load ranges of; 1 gf – 62.5 kgf, it can measure Vickers, Knoop and Brinell hardness methods as shown in Figure 3-16.

Figure 3-16 Duramin-40 Semi-automatic micro/macro hardness tester [136]

The Vickers hardness test was used in this project to evaluate coating hardness with an applied load between 10 to 50 gf by using a diamond pyramid indenter. This indenter is square-based with a penetration angle of 136 degrees between opposite faces as is shown in Figure 3-17.
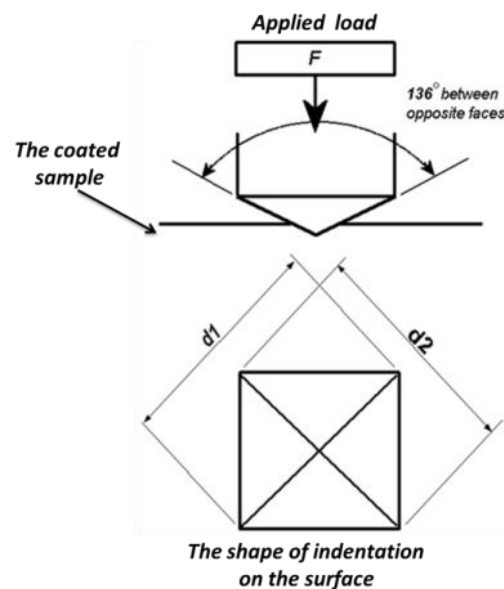
Figure 3-17 Vickers hardness indenter and shape of the indent on the surface[136]

The area of the indentation was used to determine the Vickers hardness values according to the following:

$$HV = \frac{2F sin(\frac{136}{2})}{d^2}$$

$HV = 1.854 \ \frac{2F}{d^2}$ approximately   **Equation 3-15**

Where:

F .... is the applied force

d^2 *.... Is d₁xd₂*

3.6.4 AFM Nano-indentation

The first application of atomic force microscopy (AFM) was to analyse the attraction forces between sample surfaces and an AFM tip, hence scanning the topography of the material at nanometer resolution levels and focusing on phase contrasts in selected regions of the sample. Afterwards, when the contact-mode AFM was used, it becomes possible to quantify the surface mechanical properties of the sample. This requires determination and analysis of the interdependence of the force applied to the tip and the indentation depth, represented in the so-called force-distance curve. In a simple analysis, this curve provides access to several critical micromechanical parameters: maximum indentation (the indentation depth depends on the stiffness of the region investigated when a constant force is applied as a set point), adhesion between the cantilever and the sample, and elastic/plastic deformation energies [137]. To find the relation in the force curve, the relationship between the cantilever displacement Z, and it is deflection d will be correlated.

Usually, the hardened surface is regarded as infinitely stiff when compared with the contacting cantilever and as a result, will be not able to indent at all. Consequently, the force curve will show one slope, which means the deflection matches the cantilever displacement.

The deflection sensitivity, which is reflected as a relation between photodiode voltage and the cantilever's deflection can be calibrated by extremely harder surface such as silicon crystal. Furthermore, it can be used as a reference control for the soft and elastic surface

force curves. Thus the relation of the difference between the two deflections axis will the depth indentation $\boldsymbol{\delta}$ [138]. as shown in below

$$\delta \ = \ z \ - \ d \qquad\qquad \textbf{Equation 3-16}$$

Thus, the offset of the displacement z_0 and the deflection d_0 before the contact can be determined

$$\delta = (Z - Z_0) - (d - d_0) \qquad \textbf{Equation 3-17}$$

Moreover, the indentation forces can be easily determined by Hooke's law to deflect cantilever, where (k) is the spring constant of the cantilever and (d) is the new deflection position, and d_0 is the control deflection position from the hard surface.

$$F \ = \ k \,(d \ - \ d_0) \qquad\qquad \textbf{Equation 3-18}$$

Applying the fitting of the force-indentation curve to the Sneddon models depends on the tip-cantilever shape. If it was conical, it could generate quantitative data on Young's modulus E of the tested surface.

The Indentation function in an AFM can fit various indentation models to measured force curves, allowing Young's modulus to be computed for the tested samples. The following Figure 3-18 shows the Sneddon model.
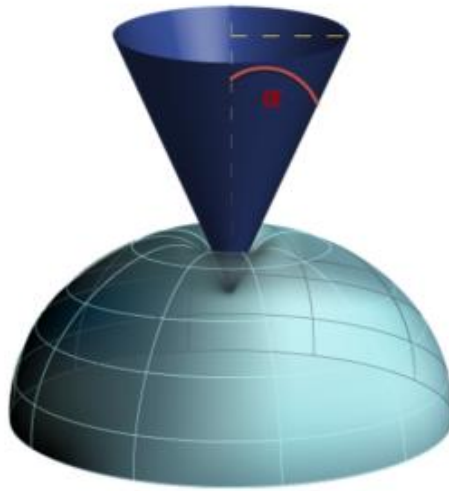
Figure 3-18 Contact between a cone and an elastic half-space[124]

$$F = \frac{2}{\pi} \frac{E}{(1-v^2)} \tan(\alpha) \, \delta^2 \quad \textit{Sneddon model} \qquad \textbf{Equation 3-19}$$

Whereas

F = force (from force curve)

E = Young's modulus (fit parameter)

ν = Poisson's ratio (sample dependent, typically 0.2 - 0.5)

α = half-angle of the indenter

δ = indentation

In this study, AFM nano-indentation was used to determining Young's modules for the sol-gel thin film.

3.7 Experimental Work

3.7.1 Materials and chemicals

All material and chemicals used in this work are analytical grades. All experiments are performed under ambient environment without removing any dissolved oxygen. All glassware is cleaned with acetone and deionised water.

3.7.2 Substrate preparation

Aluminium alloy AA2024-T3, Type AR Q-panels samples, with a size of 102 mm × 25 mm × 1.6 mm were used as the testing substrates. Chemical compositions of the substrate are given in Table **3-1** [139]. The as-received panels were soap washed and rinsed with deionised water, then washed with acetone to remove inorganic impurities such as oil, grease and fatty residues from the surface. they were then placed in an ultrasonic bath for 5 min for additional cleaning with an alkaline-based solution. After that, they were washed with deionised water and dried by nitrogen. The panels were placed in a desiccator for the test is not more than couple days.

Table 3-1 Composition of Aluminum Alloy AA2024-T3 as balance[139]

Element	Si	Fe	Cu	Mn	Mg	Cr	Zn	Ti	Other Elements
Wt. (%)	0.50	0.50	3.8–4.9	0.30–0.9	1.2–1.8	0.10	0.25	0.15	0.05-0.15

3.7.3 Pre-treating the aluminum alloy AA2024-T3 with corrosion inhibitors

Pre-treated samples were prepared by direct spraying as three faces of a solution of the of benzimidazole (BZI) and/or oleic acid (OA) on the surface of AA2024-T3 substrates, and then left hanging to dry for one day to allow it to create a film on the surface then expose in 3.5% w/v NaCl to investigate the protection from corrosion.

3.7.4 Sol-gels preparation

The Novel hybrid organic-inorganic sol-gel used in this study was synthesised from tetraethyl orthosilicate silane (TEOS), and trimethoxymethylsilane (MTMS) purchased from Sigma-Aldrich. These precursors were mixed in isopropanol by dropwise additions of deionised water (DI) at the molar ratio of 18: 14: 17: 220 respectively. The sol-gel was then enhanced with polysiloxane (PSES) solution, which was obtained by adding 12 mol% of (–OH) terminated polysiloxane polymer into the hybrid sol-gel [140].

The first way to enhance the corrosion protection was by increasing the hydrophobicity of coating, which is done by adding a fluorinated functional group to the sol-gel matrix.

The Novel modified fluorinated hybrid sol-gel, labelled as F-SBX, was prepared by adding 1.5 vol.% of 1H,1H,2H,2H-perfluorodecyltriethoxysilane (PFOTS) from Sigma-Aldrich into the original SBX sol-gel formulation. Dropwise additions of nitric acid 65-70% ACS Reagent grade (HNO_3) from Sigma Aldrich were made as a catalyst for the hydrolysing and condensation reactions. The formulation was then stirred for 24 hours.

The other way to enhance the sol-gel by adding VCI corrosion inhibitors of benzimidazole and/or oliec acid to the base SBX sol-gel fourmula.

The base SBX sol-gel formula was then mixed with benzimidazole (BZI) $C_7H_6N_2$ as a corrosion inhibitor to be applied on aluminium alloys. Firstly of all, the benzimidazole was dissolved in ethanol C_2H_5OH with ratio 1:1 w/v in order to mix and stir it with base SBX sol-gel with 3.5 v/v. % BZI that work with the sol-gel formula without affecting cross-linking, adhesion or mechanical properties of the coatings on aluminium alloys 2024-T3.

Also, the SBX sol-gel formula was mixed with oleic acid (OA) $C_{18}H_{34}O_2$ as a corrosion inhibitor; the mixing was with 0.1 v/v. % that combined with the sol-gel formula without affecting the cross-linking, adhesion and mechanical properties of the coatings on aluminium alloys 2024-T3. Then both inhibitors BZI and OA with sol-gel were applied as double layer system to determine the effect of protection on AA2024-T3.

All these coatings will be investigated and evaluated as monolayer coated system. However, the bilayer of benzimidazole and oleic acid sol-gel trail system will be investigated.

3.7.5 Film Deposition

The coating was applied to the pre-cleaned aluminium alloy substrates by spray coating application. The distance from the gun to the substrate was maintained at approximately 15 cm, and the coating was built up over three passes. After deposition, the coatings were left in ambient air for 10 min before being thermally treated at 80°C for 4 hours, as shown in Figure 3-19. Also, Table 3-2 shows sample codes used to identify samples.
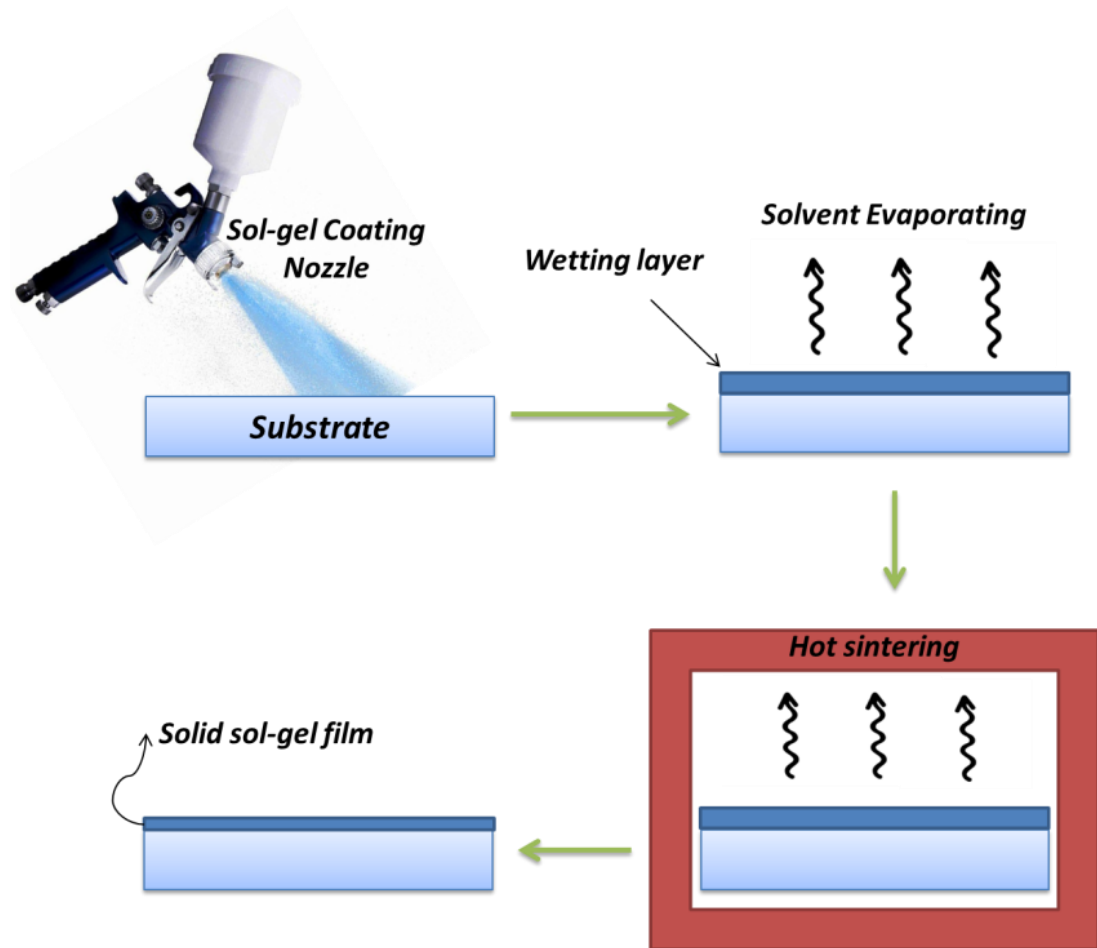
Figure 3-19 the sol-gel film deposition process

Table 3-2 Samples identification table

No.	Identifier	Base Composite Sol-gel formula	Benzimidazole BZI	Oleic acid OA	PFOTS	Curing Temperature (in 4 hours)
1-	*Bare -AA2024*	-	-	-	-	-
2-	*BZI-Bare-AA2024*	-	Yes	-	-	-
3-	*OA-Bare -AA2024*	-	-	Yes	-	-
4-	*BZI-OA-Bare-AA2024*	-	Yes	Yes	-	-
5-	*SBX-80 sol-gel*	TOES+MTMS	-	-	-	80º C
6-	*F-SBX-80 sol-gel*	TOES+MTMS+PFOTS	-	-	1.5 vol.%	80º C
7-	*ZBI- SBX -80 sol-gel*	TOES+MTMS	3.5 vol. %	-	-	80º C
8-	*OA- SBX-80 sol-gel*	TOES+MTMS	-	0.1 vol. %	-	80º C
9-	*BZI-OA-SBX-80 sol-gel*	TOES+MTMS	3.5 vol. %	0.1 vol. %	-	80º C

Chapter 4- Study the Effect of Applying Benzimidazole and/or Oleic-Oil Corrosion Inhibitors Directly on The Surface of Aluminium Alloys 2024-T3 Substrates

Overview

This chapter will present and investigate the corrosion protection that is provided by direct deposition of inhibitors on the surface of substrates with evaluating the film adsorption properties on bare aluminium alloy AA2024-T3. There will be no involvement of any sol-gel coatings in this chapter. The applied film-forming corrosion inhibitors were as benzimidazole (BZI) and oleic acid (OA). The corrosion mechanism and protection performance of bare and pre-treated aluminium alloy AA 2024-T3 by benzimidazole and/or oleic acid will be investigated in 3.5% w/v NaCl by using potentiodynamic polarization (PDPS), electrochemical impedance spectroscopy (EIS), infinite focus microscopy (IFM), scanning electron microscopy (SEM) and energy-dispersive X-ray spectroscopy (EDX). The test samples were treated and coated on one side then dried for one day, and the edges were waxed, leaving 2 cm^2 of the desired test area. Table 4-1 below gives the sample identification codes used:

Table 4-1 Samples identification table

No.	Identifier	Base Composite Sol-gel formula	Benzimidazole BZI	Oleic acid OA
1-	*Bare -AA2024*	Nil	-	-
2-	*BZI-Bare AA2024*	Nil	yes	
3-	*OA-Bare AA2024*	Nil	-	yes
4-	*BZI-OA-Bare AA2024*	Nil	yes	yes

4.1 Potentiodynamic polarization scanning (PDPS)

The corrosion and corrosion protection for the bare and treated AA2024-T3 samples potentiodynamic polarisation was investigated in 3.5% NaCl solution. The anodic and the cathodic behaviour was measured between -250 mV and 750 mV against the open circuit potential (OCP) of the tested sample. As shown in Figure 4-1, the bare AA2024-T3 sample has corrosion current $6.9 \times 10^{-6} \text{A/cm}^2$. The anodic branch of the uncoated sample shows the continuous active dissolution of the metal while the cathodic branch exhibits diffusion control. The corrosion current density (I_{corr}) of the pre-treated benzimidazole sample BZI-Bare-AA2024 is about one order of magnitude lower than the untreated bare-AA2024 sample with the result at about $5.1 \times 10^{-7} \text{A/cm}^2$, while the oleic acid-treated sample is one and a half orders of magnitude lower than the bare AA2024 with a current density

about $2.5 \times 10^{-8} A/cm^2$. The Third sample of mixed oleic with benzimidazole OA-BZI-Bare AA2024 exhibits a corrosion current that is lower than the other individual treated samples and the bare AA2024 by two and a half orders of magnitude lower than the bare AA2024 sample at approximately $0.8 \times 10^{-9} A/cm^2$.
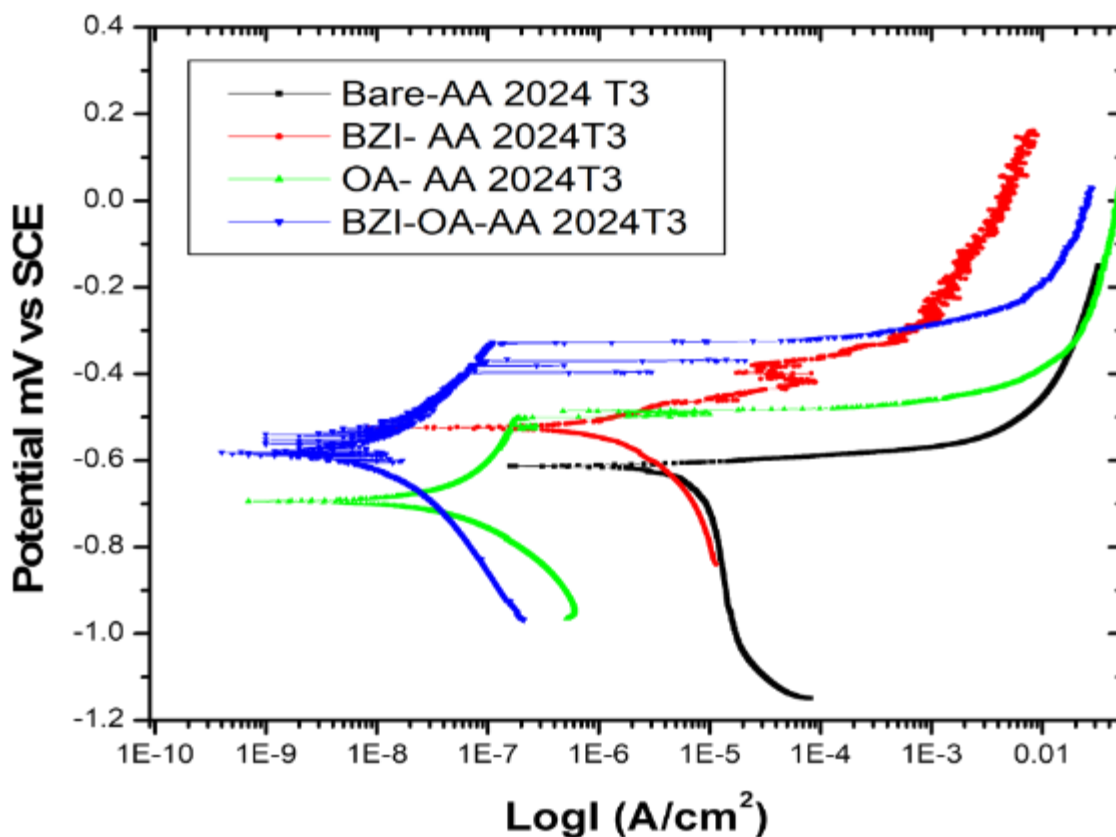
Figure 4-1 PDPS Polarization curves for the bare and Pre-treated AA 2024-T3 samples in

3.5% NaCl after one hour of exposure

The corrosion potential of bare AA2024 was measured at -612 ± 2 mV (SCE), while the BZI-Bare AA2024, OA-Bare AA2024, OA-BZI-bare AA2024 treated samples were measured at -565 ± 2 mV (SCE), -660 ± 2 mV (SCE), and -640 ± 2 mV (SCE) respectively.

The cathodic branches showed different diffusion control on all treated samples. The pitting potential of BZI bare AA2024 and The OA bare AA2024 was about -500 mV suggested that the pitting may here be commenced. The mixed inhibitors sample BZI-OA AA2024 at -300 mV exhibited the pitting potential higher than other samples. The cathodic

branch of BZI treated sample was stabilised with one order of magnitude lower than the Bare and OA-Bare AA2024. Table 4-2 showed the summarised PDPS polarisation data:

Table 4-2 PDPS polarisation data for four samples

Sample	E_{corr}[mV](Vs SCE)	I_{corr} [A/cm^2]	Average OCP mV vs SCE
Bare-AA2024	-612 ± 2	6.9×10^{-6}	610
BZI-Bare-AA2024	-565 ± 2	5.1×10^{-7}	615
OA-Bare-AA2024	-660 ± 2	2.5×10^{-8}	710
OA-BZI-Bare-AA2024	-640 ± 2	0.8×10^{-8}	718

4.2 Study the effect of long immersion on the Bare-AA2024 sample in 3.5% NaCl solution

In order to understand the corrosion behaviour, electrochemical impedance spectroscopy (EIS) is more appropriate than polarisation techniques for corrosion behaviour analysis. The tests were run for 144 hours in 3.5% NaCl solution. The experiments were repeated at least 5 times for each sample for good testing practice, to ensure that the results over repeated. Surface morphology changes over the testing period and after impedance testing was also logged.

The EIS impedance data for the Bare-AA2024 sample run-in period of the 144 hrs of immersion test are shown in Figure 4-2.

Starting from one hour of immersion a low impedance, of about 3 ohm.cm^2 was observed at high frequencies between 10^3 and 10^5 Hz. This is attributed to surface interface and solution resistance. Furthermore, it slightly decreased to about 2.6 ohm.cm^2 after 144hr immersion. At low frequency from 0.1 to 0.01 Hz the impedance generally decreased from the first hour to 144 hrs.

Furthermore, the phase angle θ, shown in Figure 4-3 exhibited two time-constants in the first hour of immersion. This is might as a result of the oxide layer created on the sample from the preparation process[141]. However, from 24 hrs until 144 hrs it showed one time-constant which shifted from around 100Hz to around 10Hz.
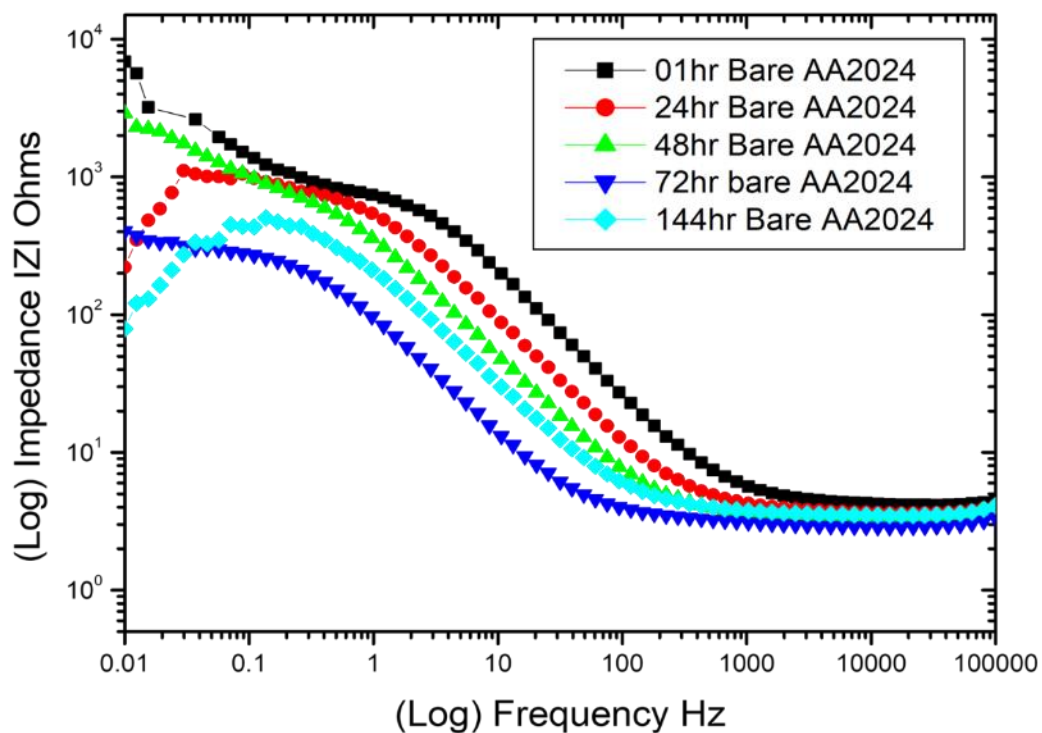
Figure 4-2 Impedance behaviour of Bare-AA2024 in 3.5% NaCl
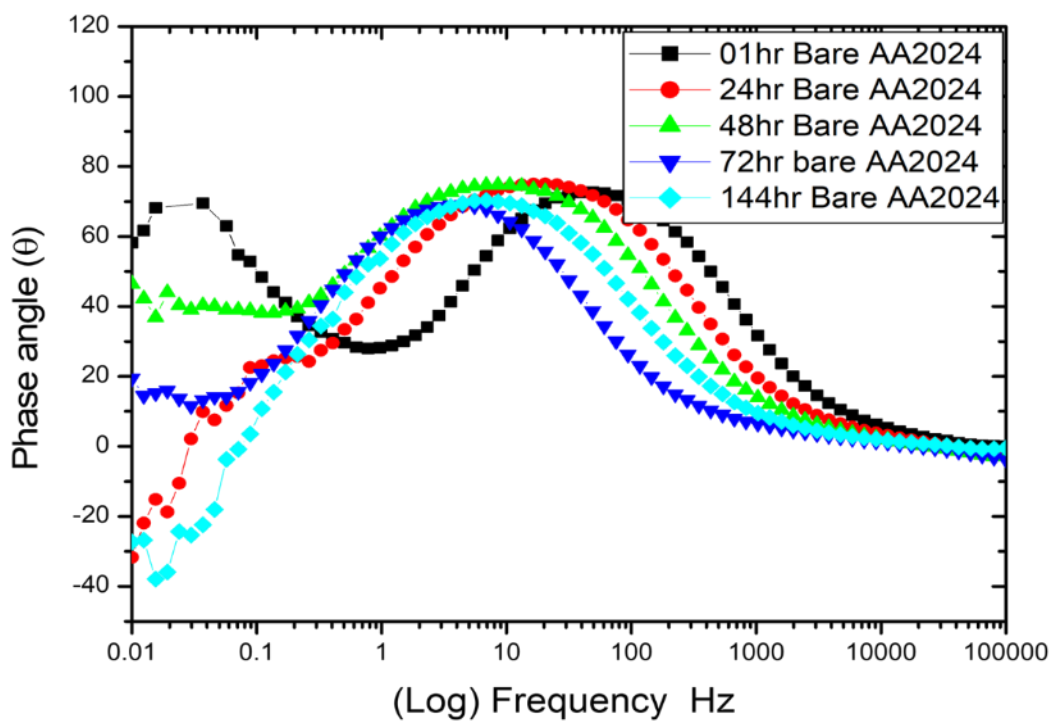
Figure 4-3 Phase angle response of Bare-AA2024 in 3.5% NaCl

4.2.1 Surface morphology and elements confirmation of Bare-2024 sample

This behaviour was accompanied by the appearance of general and pitting corrosion changing the substrate to a darker colour from 24 hrs of immersion until the end of the test. The surface examination was exhibiting heavy corrosion over the entire exposed area with individual pits being observed, as seen in Figure 4-4
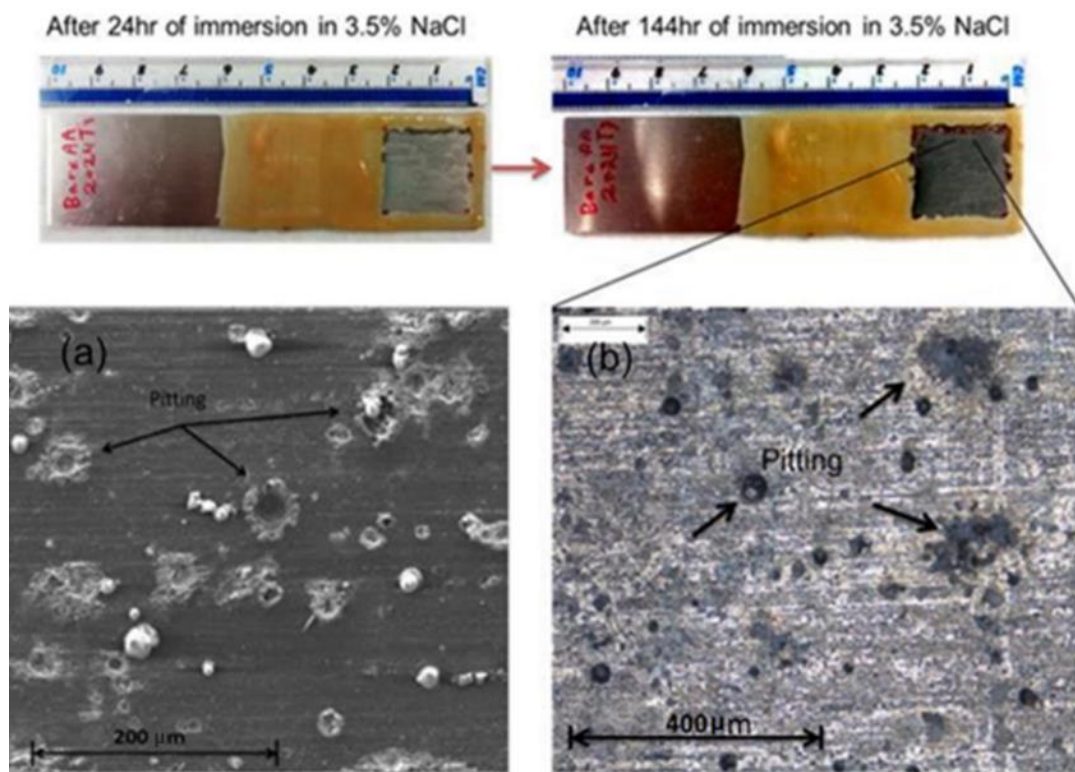
Figure 4-4 Shows the Bare-AA2024 sample after immersed in 3.5% NaCl solution after 144hrs with (a) SEM image and (b) IFM image showed excessive pitting corrosion

Figure 4-5 showed that the analysing of the EDX spectrum and mapping imaging for the Bare-AA2024 after 144 hrs is highly oxidised, as demonstrated by the green mapping of oxygen element, also on the EDX spectrum for the bare sample it can be seen a high peak of oxygen at 5.2 Kev which reflects the creation of aluminium oxides. Furthermore, the localised high chloride concentrating levels is shown in the blue chloride map was evidence of extensive pitting corrosion damage that has come from aluminium chloride.
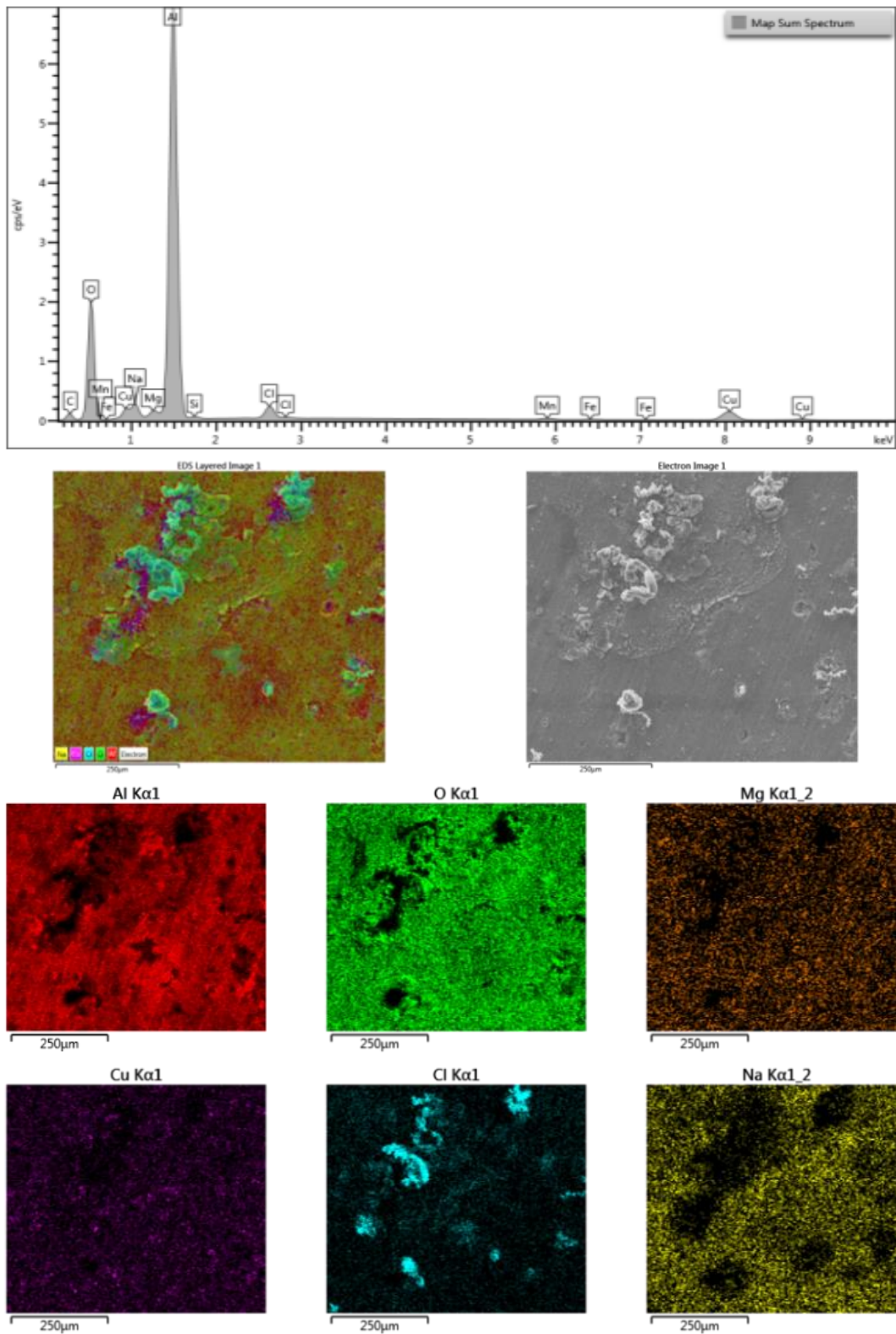
Figure 4-5 EDX spectrum and mapping images for Bare-AA2024 sample after 144hr in 3.5% NaCl solution

4.2.2 ATR-FTIR for Bare-AA2024 chemical composition confirmation

The information from Fourier transform infra-red (FTIR) spectroscopy is presented in Figure 4-6 for the Bare-AA2024 samples before and after immersion. The spectra show essential information and the results which indicate bonding between inorganic groups in the AA2024 sample.
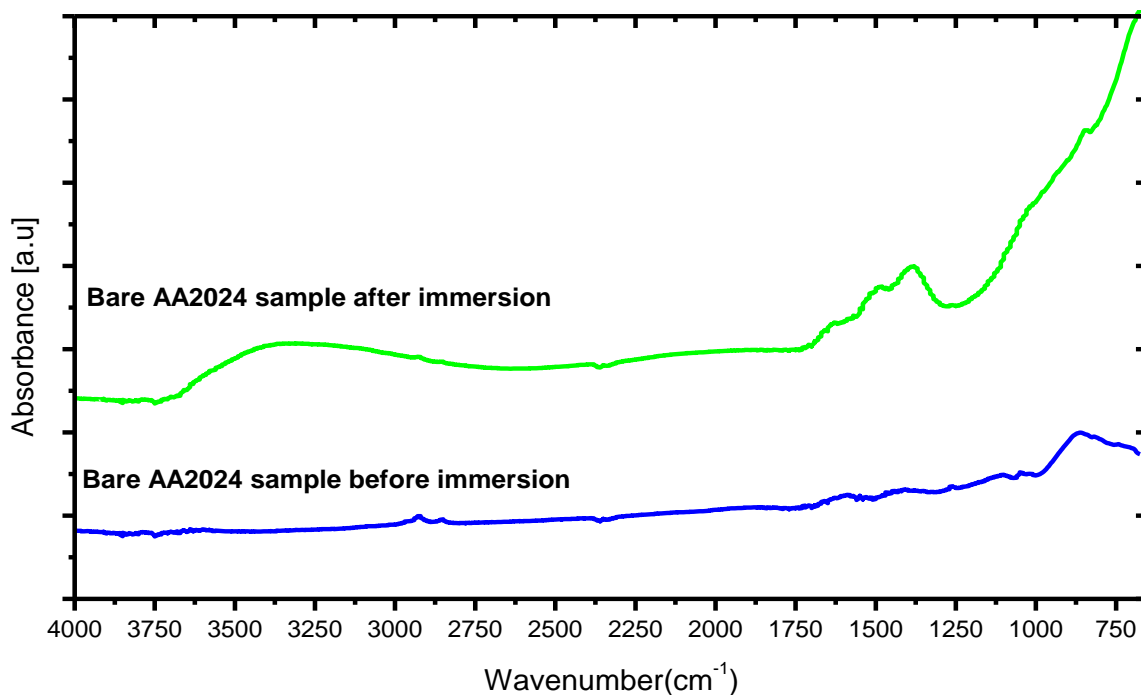
Figure 4-6 ATR spectrum for Bare-AA2024 sample before and after immersion in 3.5% NaCl solution

The OH and single O-M bonds are clearly presented on the spectrum after immersion. From this, the broad OH- stretch appears in the region between 3000 and 3400 cm^{-1} attributed to aluminium hydroxide Al-OH and the remained H$_2$O in the corroded areas. Additionally to that the peaks of the active group at 1150 cm^{-1} till the shoulder at 1045 cm^{-1} are respectively assigned to asymmetric and symmetric (δ Al–OH), bending vibrations of loose O-H of which related to boehmite γ-AlO (OH), the band peaks at 880 cm^{-1} is assigned to raised peak stretch of O-H (δ OH). The raised peaks of the groups 740 and 650 cm-^{1} are respectively assigned to vibrations and stretching of symmetric and asymmetric of aluminium-oxygen (δ Al–O) [142].

4.3 Study the corrosion protection by spraying oleic oil (OA) on the surface of AA2024 sample in 3.5% NaCl solution

The fatty acids can be used as a protective film to prevent air and humidity causing corrosion on metal sheets, so the primary purpose in pre-treating the AA2024-T3 with oleic acid is to create a barrier film on samples [143][144].

From the impedance data for the OA-Bare-AA2024 substrate, as is shown in Figure 4-7, one hour of immersion reveals moderate impedance values, starting at about $8 \text{ ohms.} \text{cm}^{-2}$. This is attributed to surface interface solution resistance at high frequency between 10^5 to 10^3 Hz, then starting to rise gradually with a slight slope to reach a higher magnitude about $1.2 \times 10^5 \text{ ohms.} \text{cm}^{-2}$ in the low frequencies between 1.0 to 0.01 Hz.

However, at high frequencies, the impedance decreased to approximately $4 \text{ ohms.} \text{cm}^{-2}$ after 24 hrs of the immersion period acting as an un-treated bare sample. Generally, at low frequencies from 0.1 to 0.01 Hz, the impedance dramatically decreased from the first hour to 144hr to reach about $4.1 \times 10^2 \text{ ohms.} \text{cm}^{-2}$.

Additionally, the phase angle θ, Figure 4-8, showed two time-constants in the first immersion hour, the first between 10^5 to 10^3 Hz and the second between 10 to 1.0 Hz. These come from the aluminium oxide with oleic film layer created by the sample pre-treatment process by OA. However, from 24 hrs until 144 hrs the sample showed one time-constant which shifted from 100 Hz to 10 Hz.
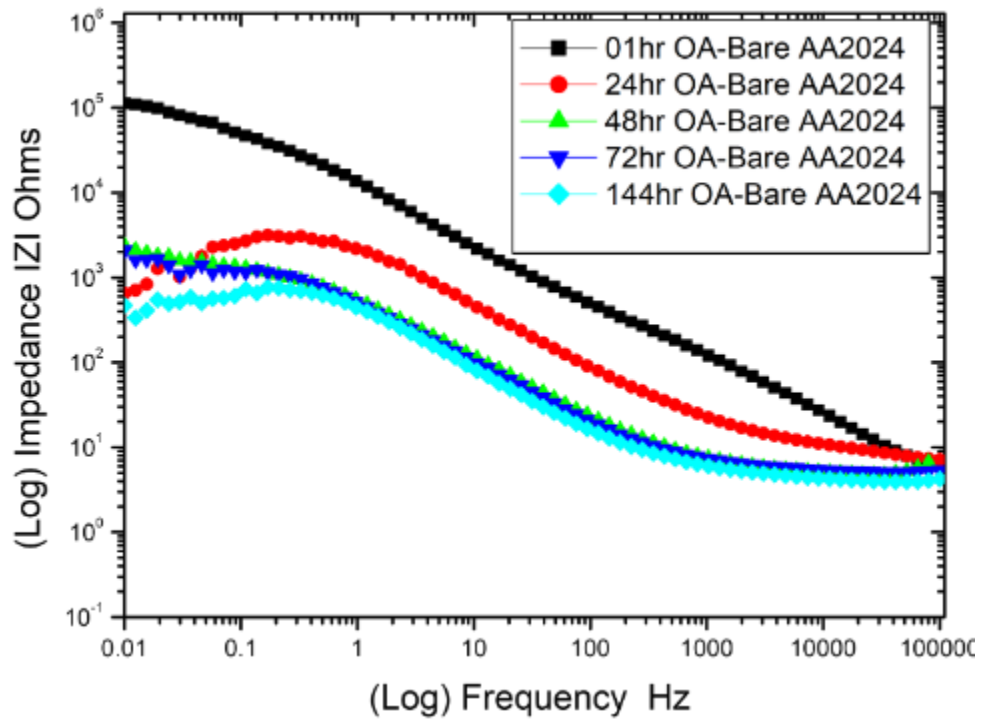
Figure 4-7 Impedance behaviour of OA-Bare-AA2024 in 3.5% NaCl solution
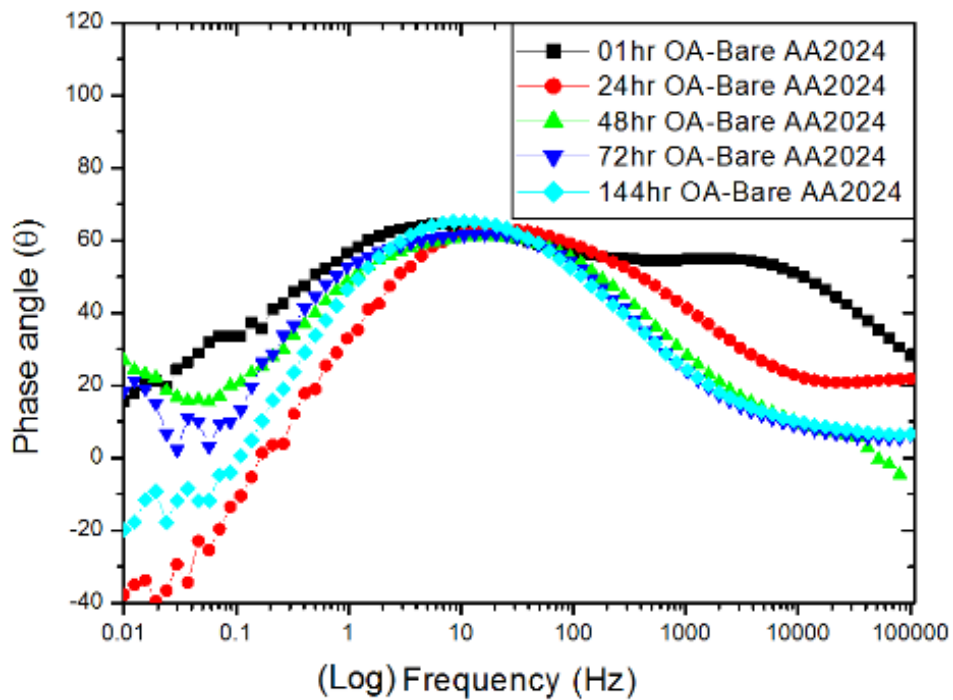
Figure 4-8 Phase angle response of OA-bare AA2024 in 3.5% NaCl solution

4.3.1 Surface morphology and elements confirmation of OA-Bare-2024 sample

This behaviour was accompanied by the appearance of general and pitting corrosion changing the substrate to some darker and some brighter colour areas after the 24 hrs of immersion. Then at the end of the test (144 hrs), when the oleic acid protection failed, and

the sample started to be generally corroded. The surface examination exhibits randomly distributed corrosion over the exposed area with individual pitting being observed as shown Figure 4-9.
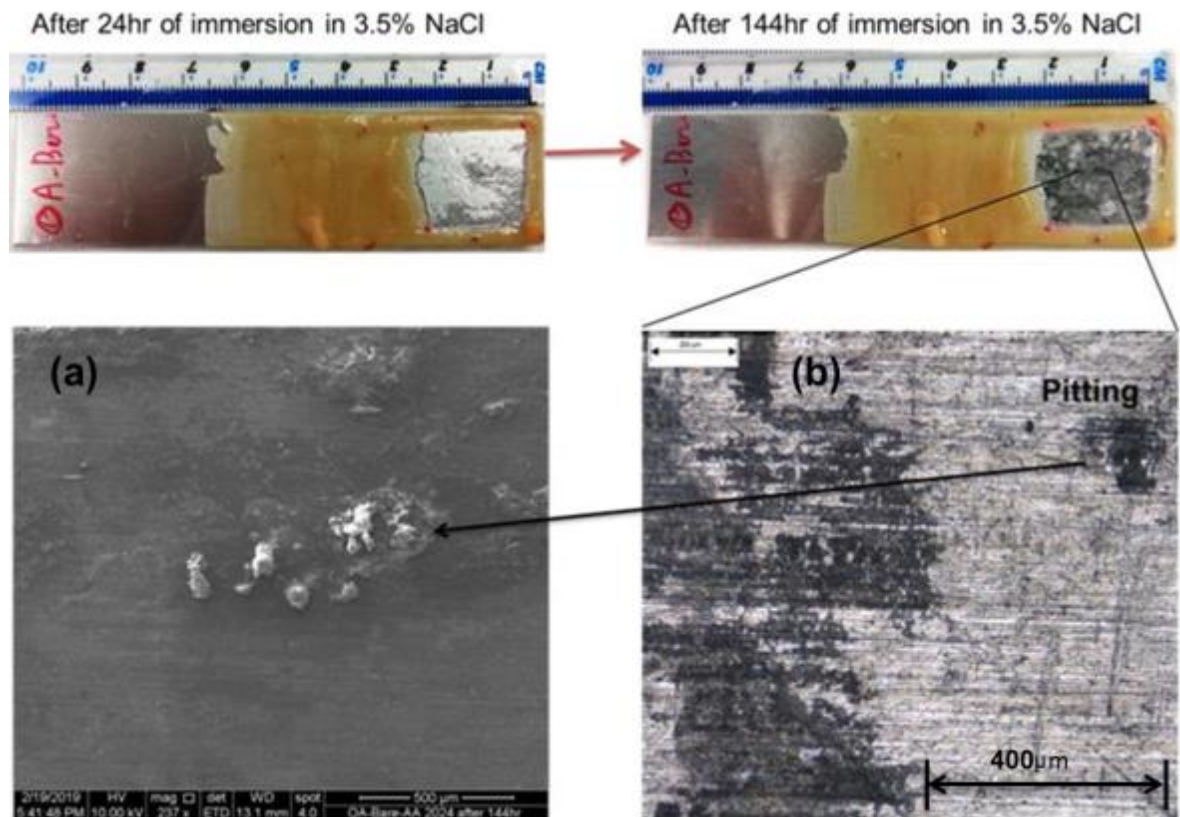
Figure 4-9 Shows the Oa-Bare AA2024 sample after immersed in 3.5% NaCl solution with (a) SEM image and (b) IFM image shows pitting corrosion

Figure 4-10 The analyses of the EDX spectrum and mapping imaging for the oleic acid pre-treated sample OA-Bare-AA2024 after 144 hrs (as showed in Figure 4-9 (b)) revealed the moderate oxidative rate on the coated sample on the EDX spectrum at the peak 5.2 Kev, also on the green oxygen map there was a non-even distributing of oxygen element, which reflects the creation of non-uniformly dispersed aluminium oxides. On the other hand, the localised chloride level is still high at the yellow map, also shown in the image as a white colour as evidence of pitting corrosion pits that have come from aluminium chloride but less than the bare AA 2024 sample. The oxygen concentration map in Figure 4-10 shows more reaction than that in Figure 4-5, supporting the theory that oleic acid had provided partial protection to the surface.
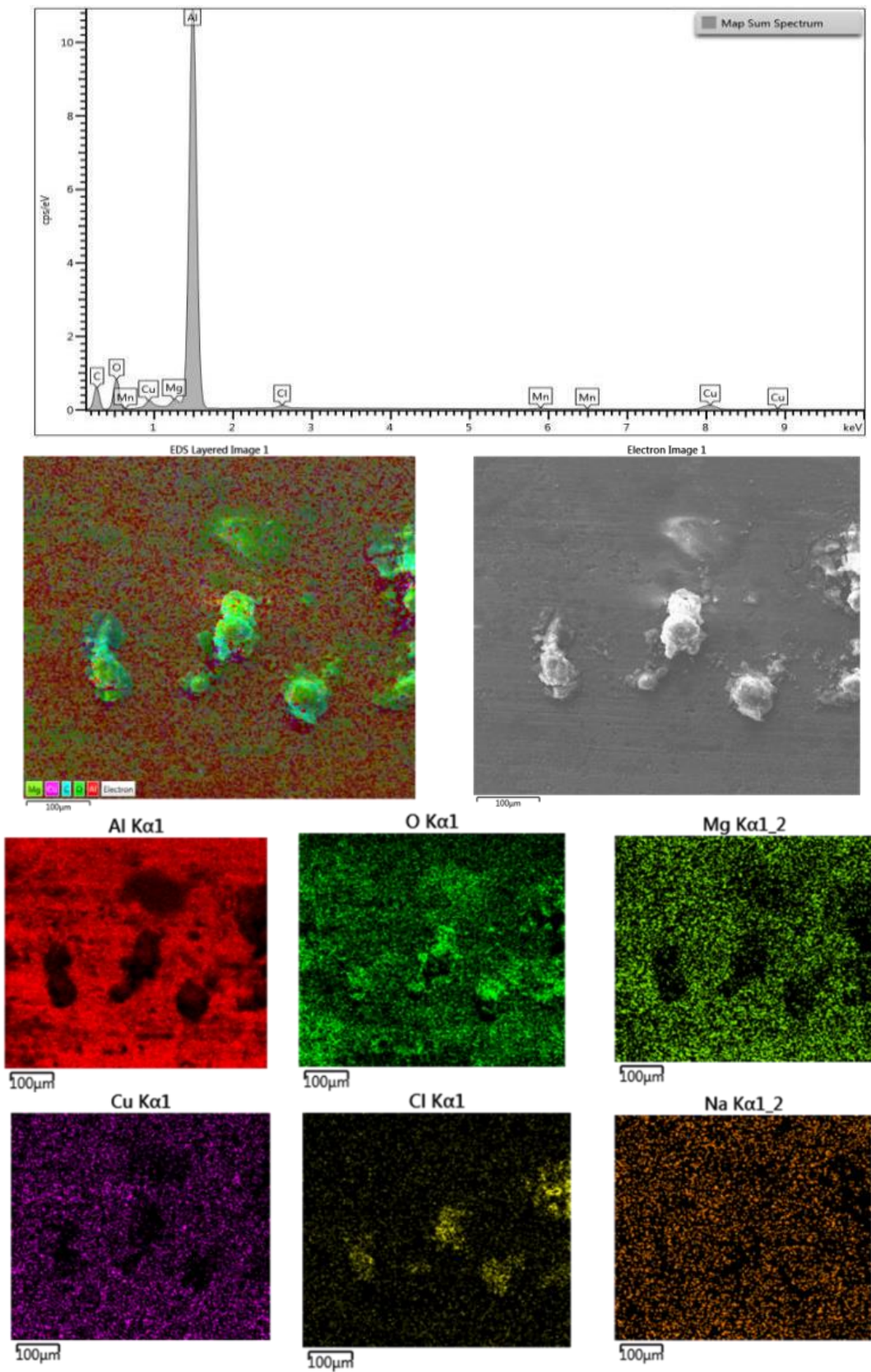
Figure 4-10 EDX spectrum and mapping images for OA-Bare-AA2024 sample 144 hrs in

3.5% NaCl solution

4.3.2 ATR-FTIR for OA-Bare-AA2024 chemical composition and adsorption confirmation

FTIR was used to confirm the film adsorption of Oleic acid on the surface of bare-AA2024 substrate, FTIR analysis of fresh oleic acid was carried out as a control and is presented in Figure 4-11. Numerous vibration modes are characteristic of the oleic acid molecule. Also, these peaks and stretches can be observed and remain on the OA-Bare-AA2024 sample after immersion.

The alkyl group presents two main contributions at 2926 cm^{-1} and 2850 cm^{-1} representative of CH_3 and CH_2 stretching respectively. Additional peaks of CH_2 at 1460 cm^{-1} and 1300 cm^{-1} [145]. The carbonyl function C=O as showed in a peak at 1710 cm^{-1}, however, After applying the oleic acid on AA2024 samples, this peak at 1710 cm-1 started to decrease in intensity, and after immersion started to disappear, replaced with a new peak at 1585 cm^{-1} representing of Al-O-C group-specific vibrations. This new peak is attributed to the Bridging reaction of the carboxylic group with Al atoms [20], [78], [146].

In addition, the C=C band is characterised by a weak peak group at 3007 cm^{-1}. Although there was a trace of adsorption of oleic acid after 144 hrs of immersion, the corrosion taking place due to the loss of active groups such as C=O and Al-O-C as a result of this the OH- stretching appears at the region between 3000 and 3400 cm^{-1} attributed from Aluminium hydroxide Al-OH and the retained water H_2O in the corroded areas[147].
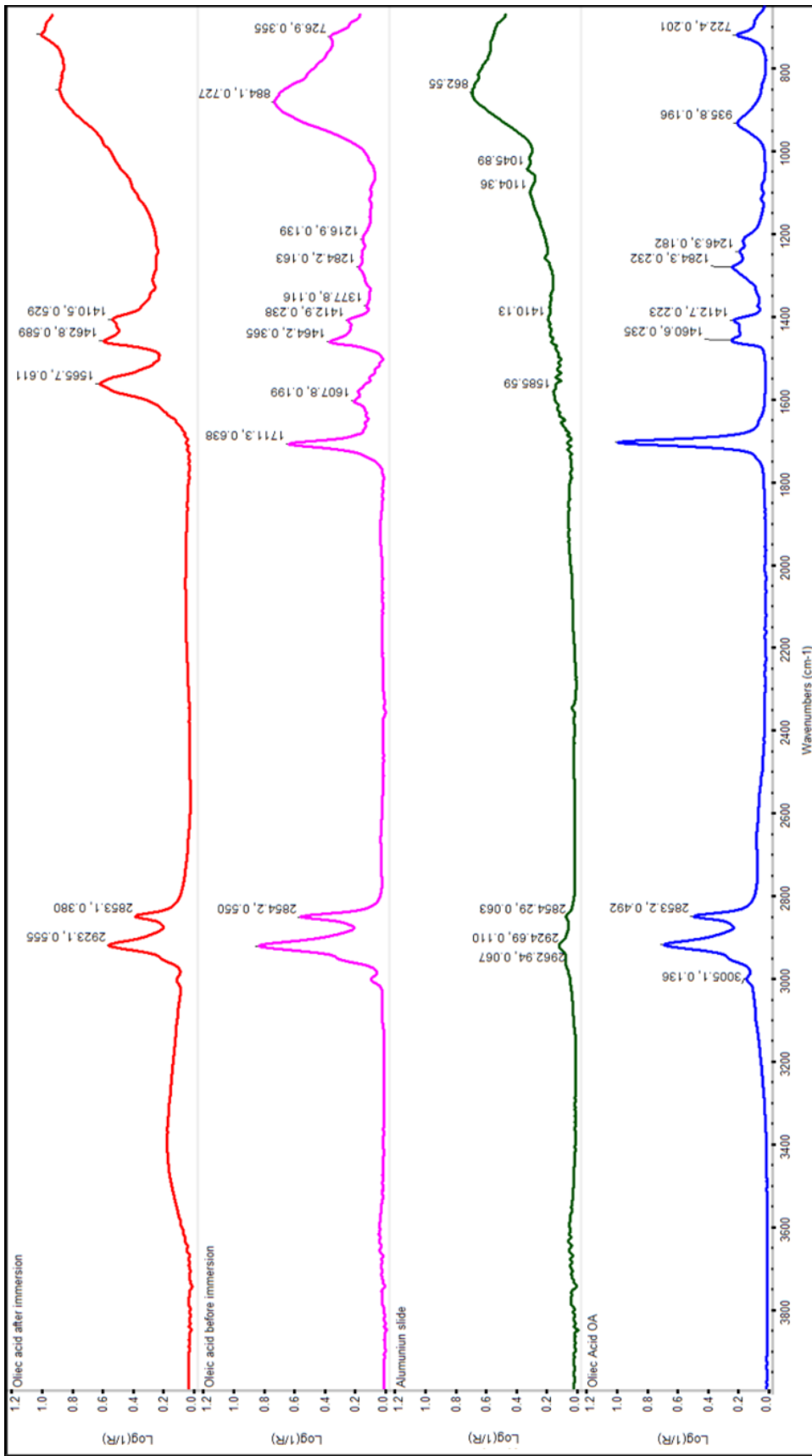
Figure 4-11 ATR spectrum for OA- Bare AA2024-T3 sample before and after immersion in 3.5%NaCl solution

4.4 Study the corrosion protection by spraying benzimidazole (BZI) on the surface of AA2024 sample in 3.5% NaCl solution

Benzimidazole is a film-forming corrosion inhibitor was also studied in this test by deposition from the solution on the aluminium alloy AA2024 substrate and left to dry to provide the opportunity to create a film that protects the alloy from oxidation.

From the impedance data for the BZI-Bare-AA2024 substrate as is shown in Figure 4-12, the EIS results in one hour of immersion expose nominal impedance, starting at about 8 ohms.cm^{-2} that might be attributed to surface interface solution resistance at high frequency between 10^5 to 10^3 Hz, then starting rising with slightly sloping to reach the higher magnitude in the low frequencies between 1.0 to 0.01 Hz with value about $3.3 \times 10^5 \text{ ohms.cm}^{-2}$, which is higher by two orders of magnitude than the Bare-AA2024-T3 sample.

After 24 hrs. of the immersion period, it continues to behave similarly as a coated sample, which shows a degree of protection. At low frequencies from 0.1 to 0.01 Hz, the impedance decreased dramatically from the first hour to 144hr to reach about $2.0 \times 10^5 \text{ ohms.cm}^{-2}$. This suggests the possibility of creating a film of benzimidazole on the substrate to save the AA2024-T3 alloy from direct corrosion. Furthermore, the phase angle θ Figure 4-13 showed one big time-constant in the first immersion hour, between 10^3 to 0.1Hz, these are attributed to the created BZI film layer which came from the sample treatment process.

However, from 24 hrs until 144 hrs two time-constants were observed, the first time constant started from 10^5 to 10^3 Hz and the second one began from 10 to 0.1 Hz, and this two time-constants could be attributed to the integration of BZI film and the aluminium oxide film on the substrate.
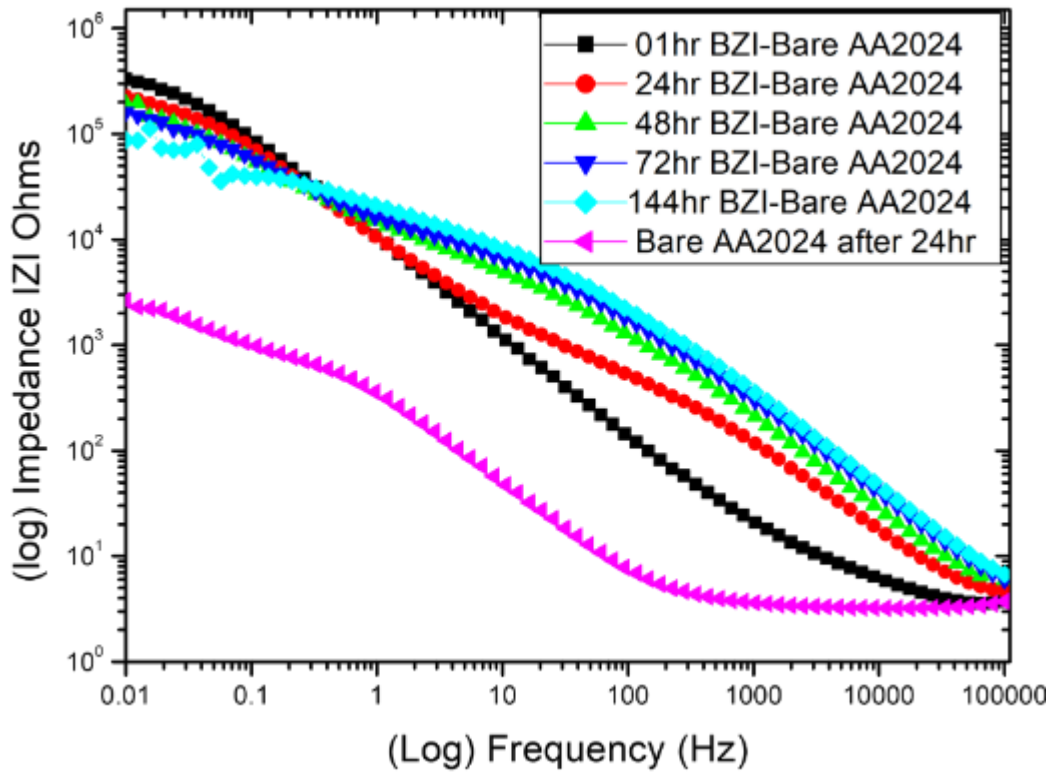
Figure 4-12 Impedance behaviour of BZI-Bare-AA2024 in 3.5% NaCl solution
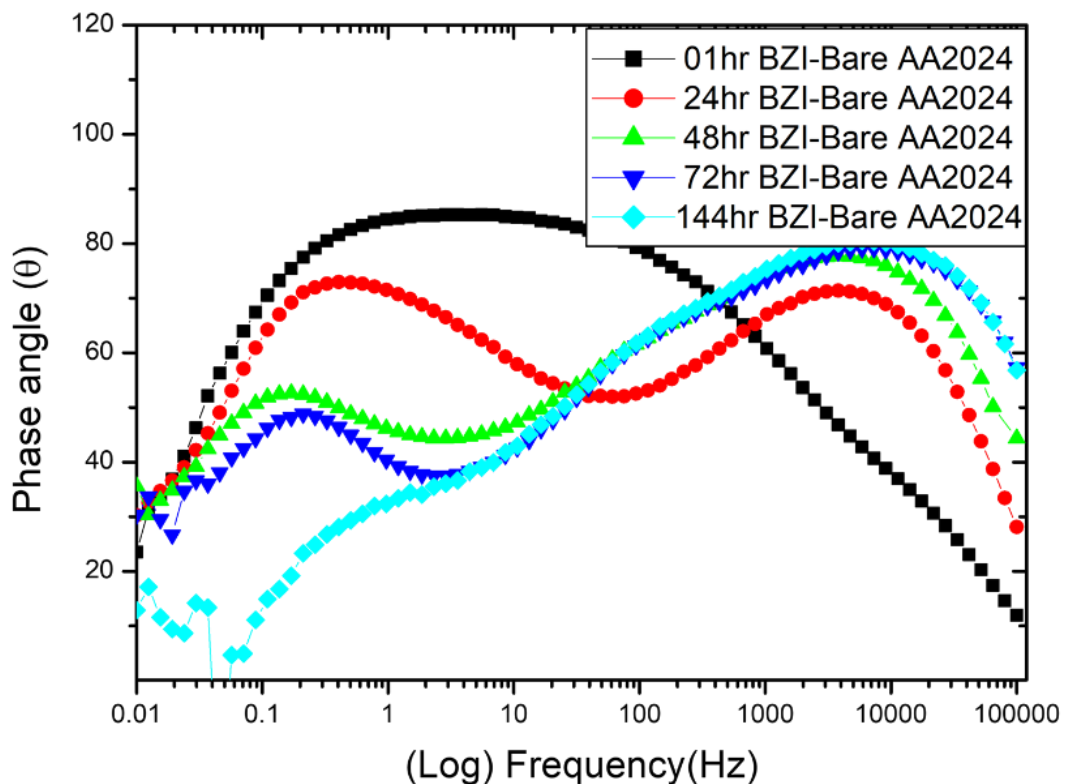
Figure 4-13 Phase angle response of BZI-Bare-AA2024 in 3.5% NaCl solution

4.4.1 Surface morphology and elements confirmation of BZI-Bare-2024 sample

There was no visual appearance of corrosion during the test period, and the substrate stayed in a bright colour from 24 hrs until 144 hrs of immersion. The surface examination exhibited visible a BZI film created on the surface as showed Figure 4-14.
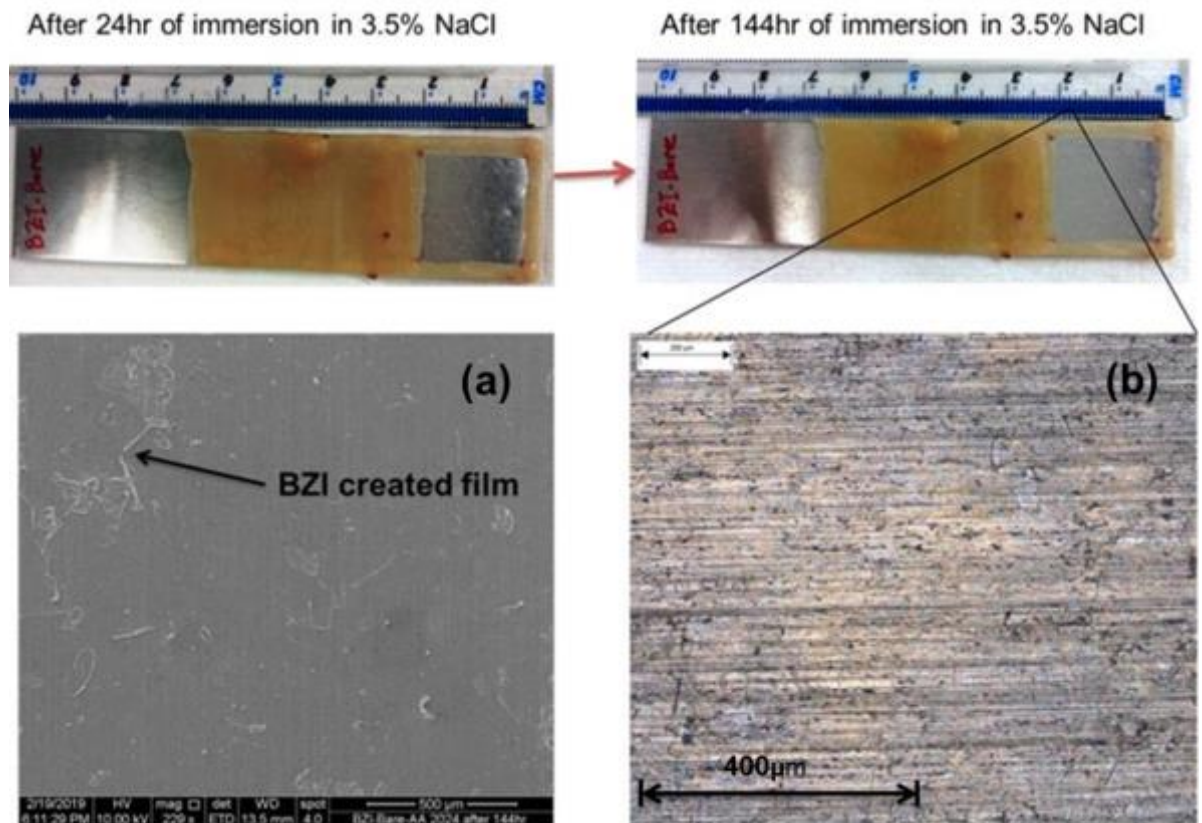
Figure 4-14 Shows the BZI-Bare AA2024 sample after immersed in 3.5% NaCl solution with (a) SEM image and (b) IFM image with no creation of corrosion

The EDX spectrum and mapping of BZI-Bare-AA2024 confirmed there was lower oxidative rate on the surface of BZI-bare-AA2024 sample after 144 hrs as it can be seen from the peak 5.2Kev and the purple map of oxygen and was even-distributed on the surface, but the intensity was small when compared to the bare sample this reflecting that there is a uniform distributing of aluminium oxides. Also, there was a no-chloride level indicated. There was no sign for pitting on the BZI pre-treated sample. The nitrogen significantly was homogeneously distributed which exhibits the film-forming on the surface coming from benzimidazole as it showed in Figure 4-15.
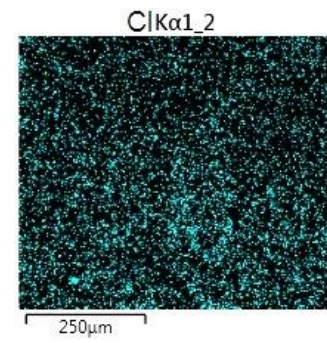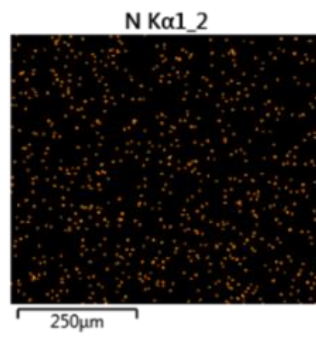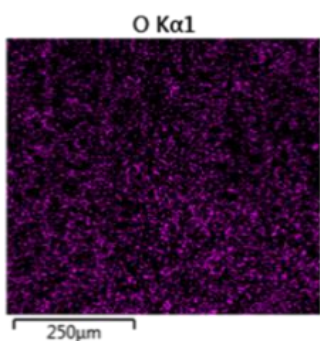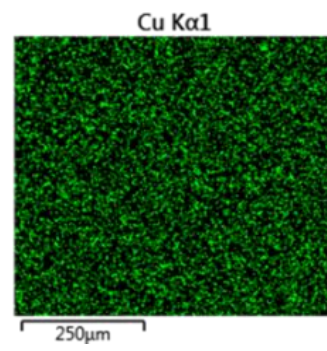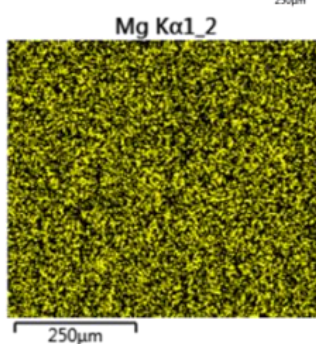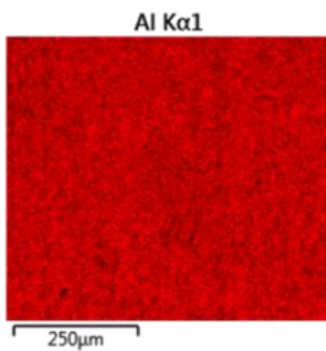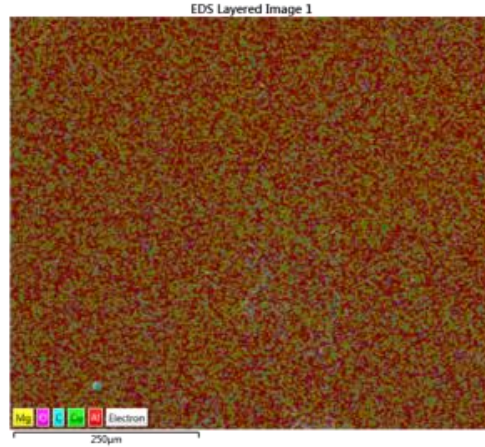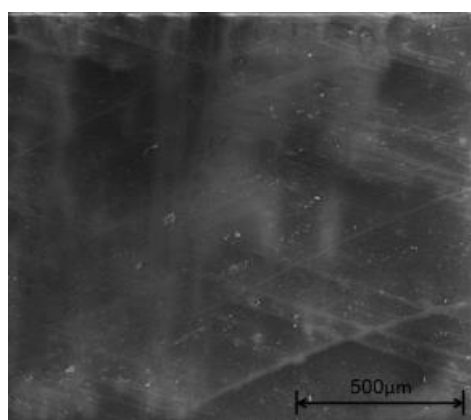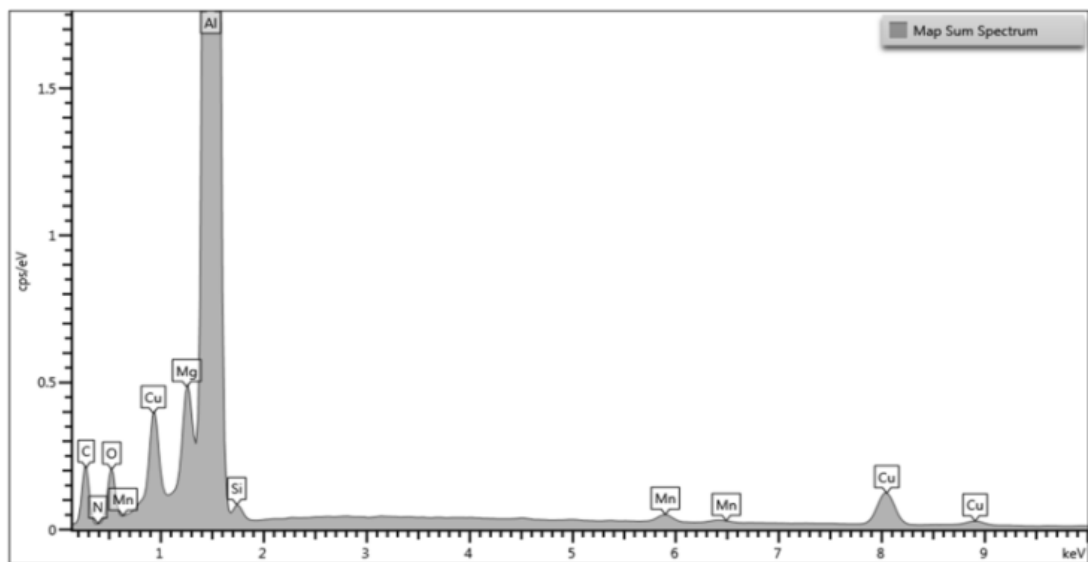
Figure 4-15 EDX spectrum and mapping images for BZI-Bare-AA2024 sample 144 hrs in 3.5% NaCl solution
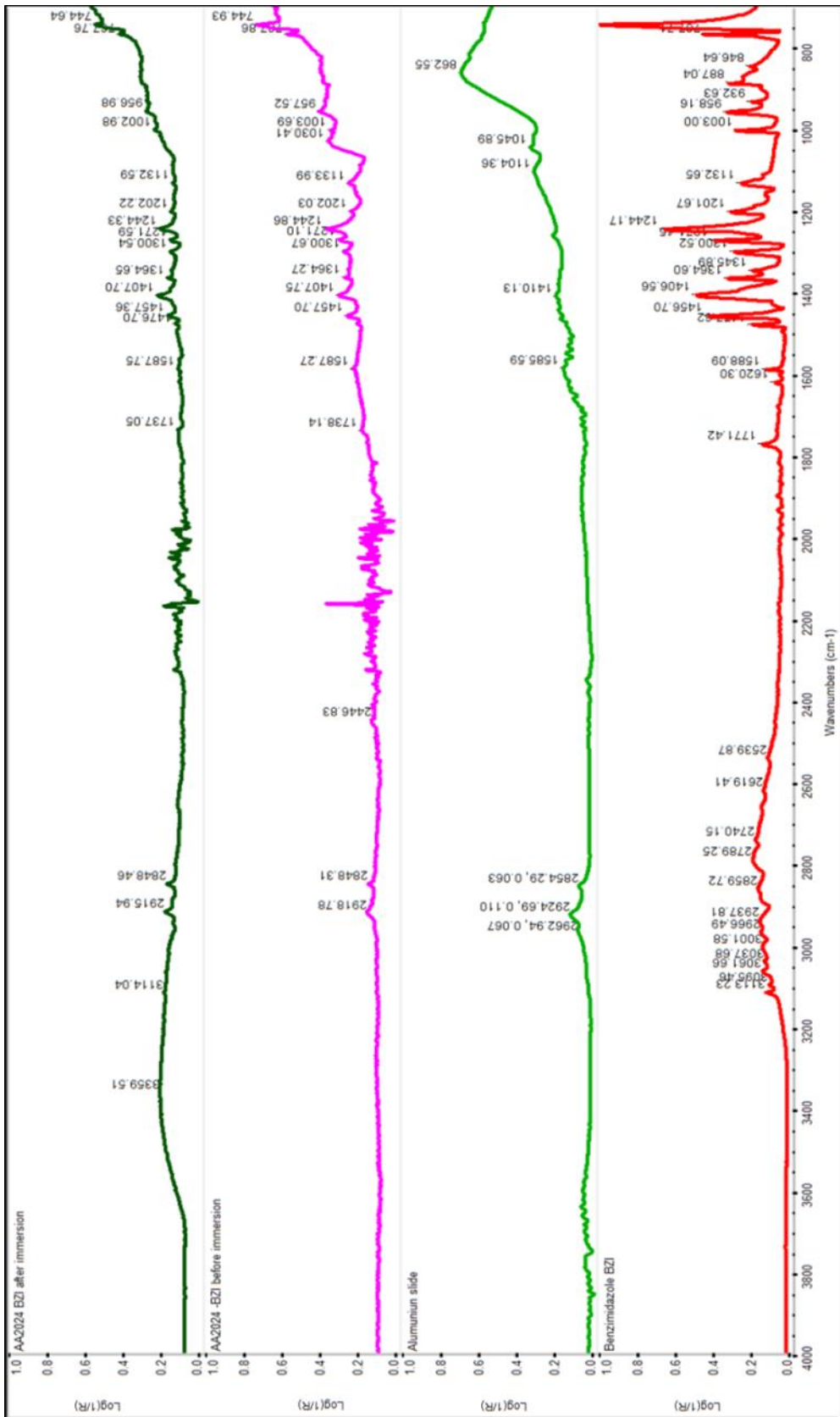
Figure 4-16 ATR spectrum for BZI-Bare AA2024 sample before and after immersion in 3.5%NaCl solution

4.4.2 ATR-FTIR for BZI-bare AA2024-T3 chemical composition and adsorption confirmation

FTIR data confirm the presence of the film adsorption of Benzimidazole (BZI) on the surface of Bare-AA2024 before and after immersion. The Benzimidazole FTIR is carried out as a control and is presented in Figure 4-16. Numerous vibration modes are characteristic of the BZI molecule. Also, these peaks and stretches can be observed and remain on the BZI-Bare-AA2024 sample after treatment. The imine C=N stretching is present at 1588 cm-1, and additional carbon double bond C=C stretching peaks are confirmed at 1478 cm-1, 1459 cm-1 and 1410 cm-1 respectively.

Likewise, the fingerprint of the aromatic amine stretching C-N can be detected at 1365, 1348 and 1302 cm^{-1} respectively, confirms the benzimidazole presence on the substrate. These stretching peaks keep their position even after long immersion, which might be attributed to the BZI reacting with a metallic surface. The C-H out-of-plane bending is characterized by a weak group of peaks at 958,885,769 and 750 cm^{-1}[145], [148].

Although there was a trace of adsorption of Benzimidazole after 144hr of immersion, hydration taking place due to diffusion action, and as a result of this OH- stretching appears at low intensity in the region between 3000 and 3400 cm^{-1} attributed to aluminium hydroxide Al-OH film and the remained propagated H_2O in the interfacial and oxidised layer [142], [147], [148].

4.5 Study the corrosion protection of the Pre-treated bare AA2024 samples with 1:1 v/v oleic oil/benzimidazole

The nature of oleic acid is working as a weak film-forming inhibitor and physical blocker, and the benzimidazole is working as a strong film-forming inhibitor. The mixture of both inhibitors in 1:1 v/v and depositing on the test AA2024-T3 substrate. Then the mixture was left to dry for one day.

From the Impedance data for the OA-BZI-Bare-AA2024 substrate shown in Figure 4-17, the EIS results in the first hour of immersion reveal nominal impedance, starting at about 24 $ohms.cm^{-2}$ at high frequency which reflects the solution resistance between 10^5 to 10^3 Hz, then starting to rise with a slight slope to reach the higher magnitude in the low frequencies between 1.0 to 0.01 Hz with a value of about 3.2×10^5 $ohms.cm^{-2}$, behaving in a similar manner to the BZI-Bare-AA2024 pre-treated substrates. With exposure, the low frequencies impedance decreased to about 11 $ohms.cm^{-2}$in after 24hr and continues to behave like a coated sample which showed a degree of protection. Generally, at low frequencies from 0.1 to 0.01 Hz, the impedance decreased from the first hour to reach at 144hr about 1.2×10^4 $ohms.cm^{-2}$. This showed that the mixture of OA and BZI could create a film on the substrate saving the AA2024-T3 from the direct corrosion, although not as effectively as BZI treated samples.

Furthermore, the phase angle θ (Figure 4-18) showed two time-constants in the first immersion hour, the first between 10^5 to 10^4 Hz and the second from 10 to 0.1 Hz and these come from the created a film layer from treatment process of BZI-OA mixture on the sample. However, from 24hr till 144hr showed two time-constants. The first one started from 10^5 to 10^3 Hz and the second one began from 10 to 0.1 Hz and this two time-constant attests to the presence of the OA-BZI film and the aluminium oxide film created on the substrate.
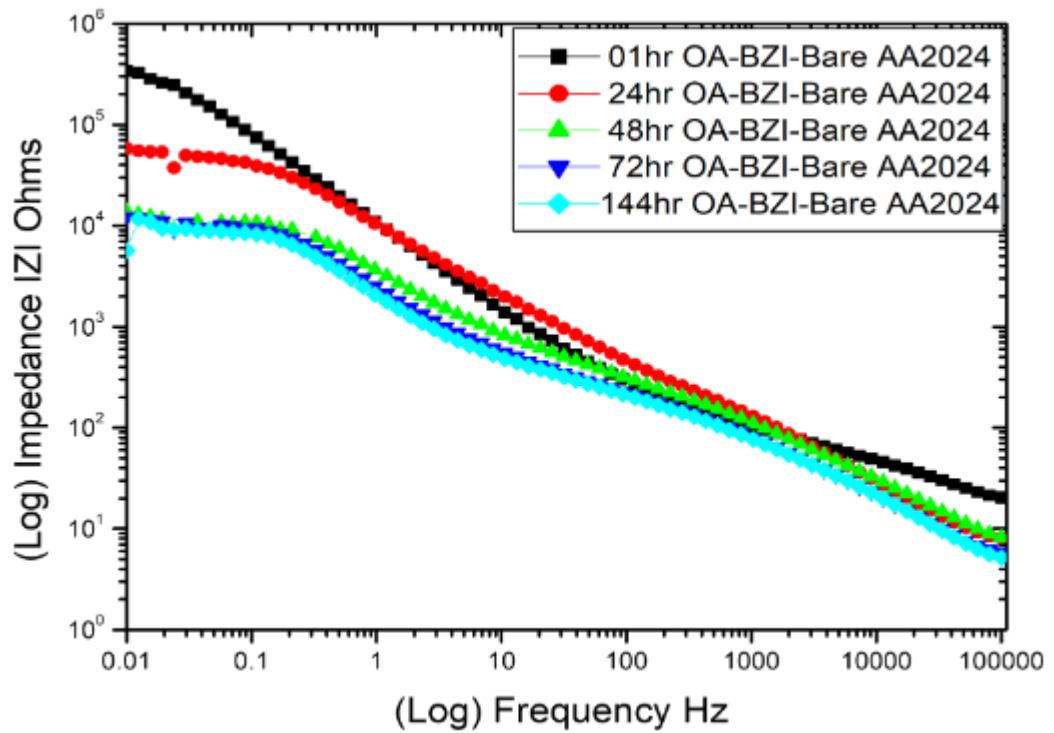
Figure 4-17 Impedance behaviour of OA- BZI-Bare-AA2024 in 3.5% NaCl solution
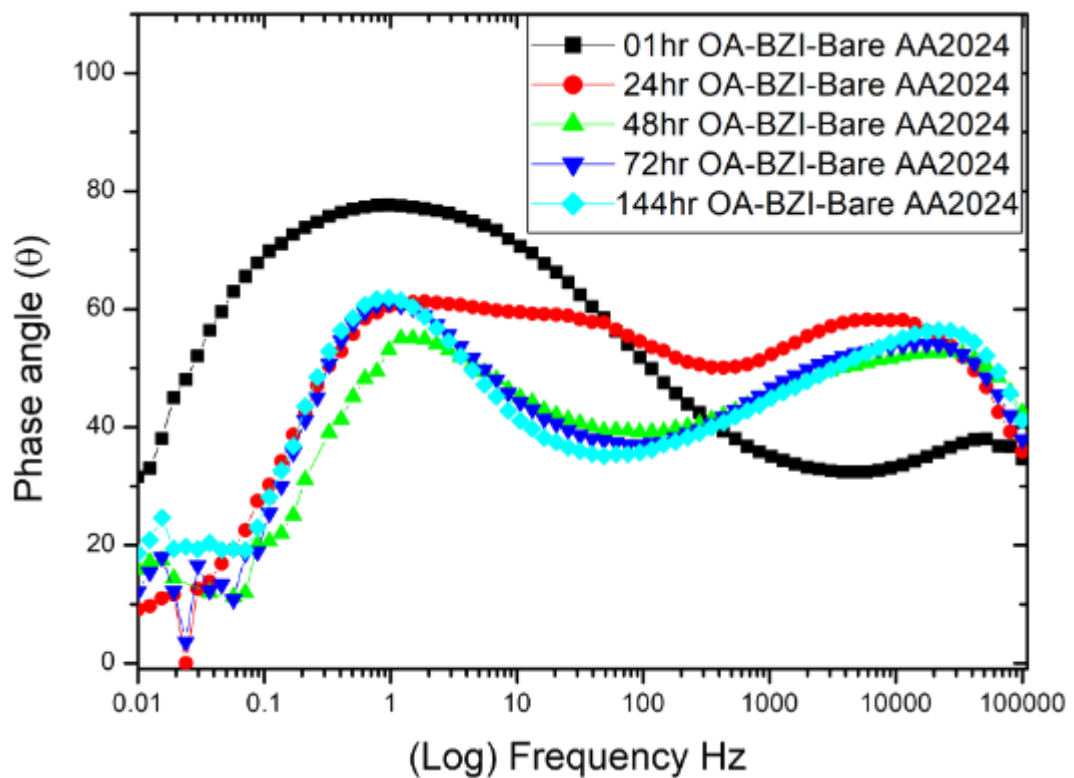
Figure 4-18 Phase angle response of OA-BZI-bare AA2024 in 3.5% NaCl solution

4.5.1 Surface morphology and elements confirmation of OA-BZI-Bare-2024 sample

The corrosion performances of OA-BZI-Bare-AA2024 coated sample within 144 hrs were accompanied by the appearance of light corrosion. The substrate stayed a bright colour for 24 hrs. However, after 144 hrs immersion, the corrosion started to be observed on the surface visibly, and by SEM and IFM imaging The surface changes exhibited, as shown in Figure 4-19.
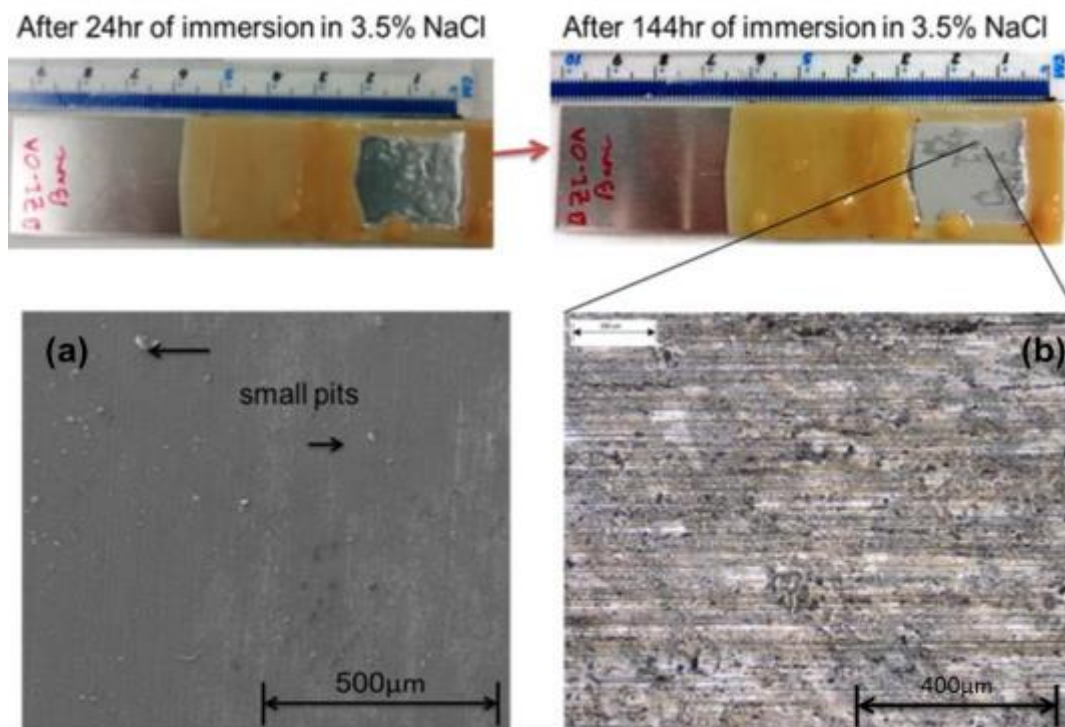
Figure 4-19 Shows the OA-BZI-Bare AA2024 sample after immersed in 3.5% NaCl solution with (a) SEM image and (b) IFM image shows small pitting corrosion

The EDX mapping and spectrum of the OA-BZI-Bare-AA2024 sample after 144 hrs revealed a lower oxidative rate and this could be seen on the purple map of oxygen and in the oxygen peak intensity at 5.2 Kev at the spectrum. With an insignificant chloride level apparent in line with indication benign sign of less aggressive corrosion (i.e. Oxide formation) when it compared to the bare AA 2024 as it showed in Figure 4-20.
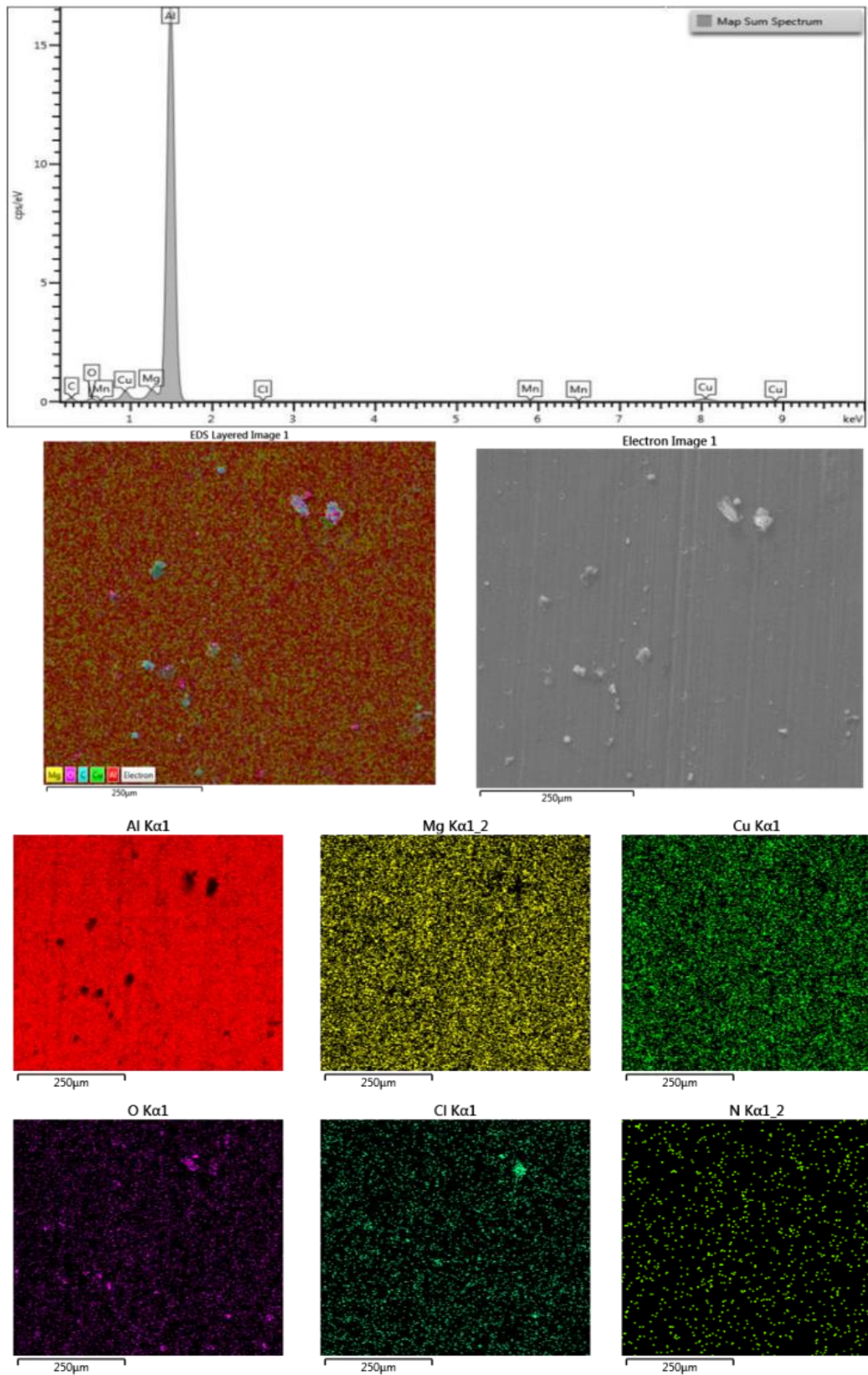
Figure 4-20 EDX spectrum and mapping images for OA-BZI-Bare-AA2024 sample 144hr in 3.5% NaCl solution

4.5.2 ATR-FTIR for OA-BZI-Bare-AA2024 chemical composition and adsorption confirmation

The information from the FTIR spectroscopy of the mixed BZI / OA pretreated substrate confirms the adsorption of benzimidazole and oleic acid on the metal surface. Generally, the presence of BZI can be observed by the amines fingerprint in the wavenumber range 1700 to 650 cm^{-1} on strong the fingerprint of the aromatic amines stretching C-N which can be detected at 1365, 1348 and 1302 cm^{-1} respectively which can be used to confirm the presence of benzimidazole on the surface of the substrate even after immersion.

Likewise, the OA fingerprint can be detected by the presence of the alkyl group with two main contributions at 2926 cm^{-1} and 2850 cm^{-1} representative of CH3 and CH2 stretching respectively. Also the carboxylic function group C=O is shown by the peak at 1710 cm^{-1}.

After applying the coating this peak at 1710 cm^{-1} started to decrease in intensity, and after 144 hrs of immersion started to disappear, replaced with a new peak at 1585 cm^{-1} representing Al-O-C group-specific vibrations. Besides, the C=C band is characterized by a small peak group in 3007 cm^{-1}[142], [147]–[149].
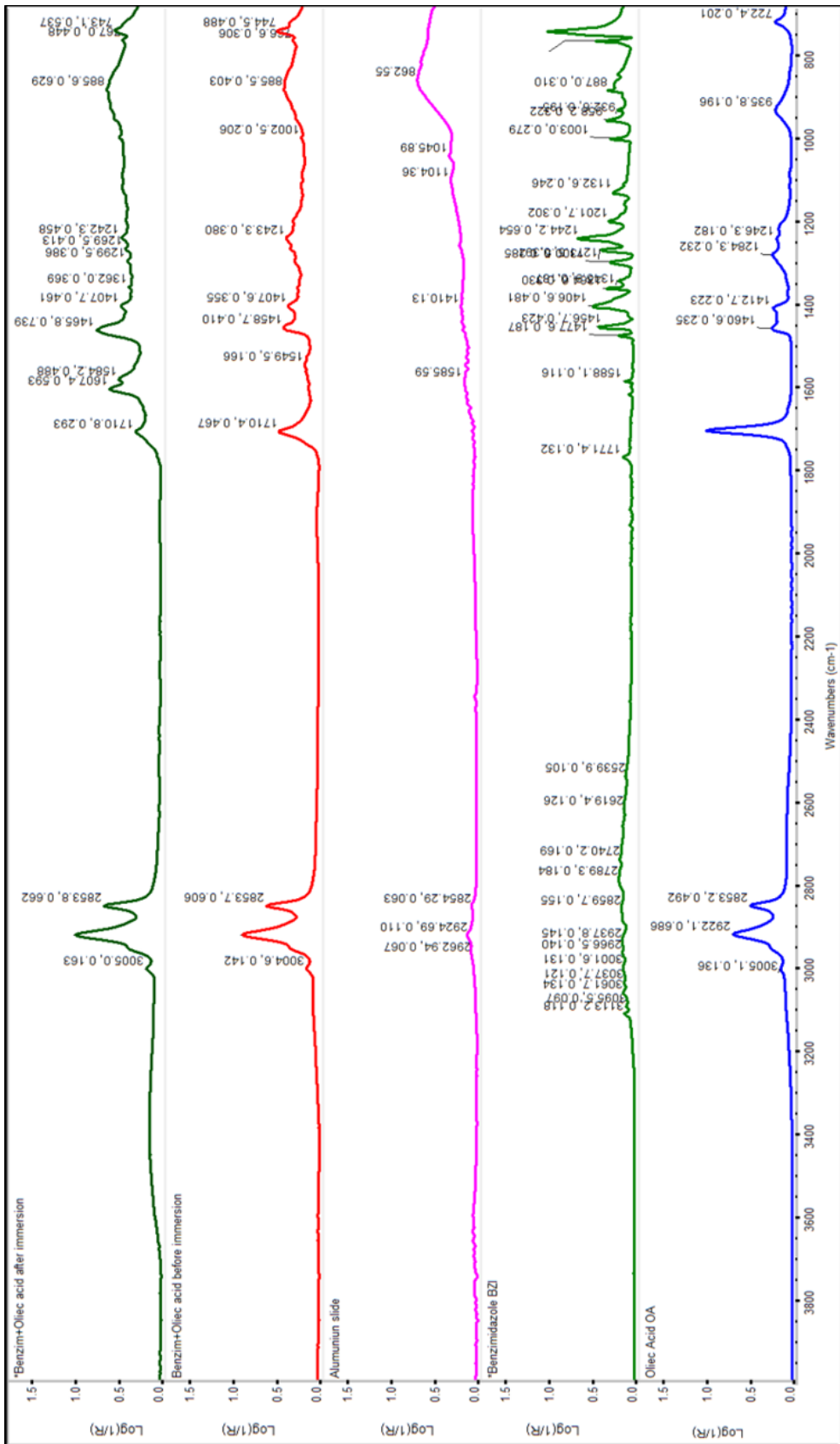
Figure 4-21 ATR FTIR spectrum for OA-BZI- Bare-AA2024 sample before and after immersion in 3.5%NaCl solution

4.6 Analysing of the corrosion protection performance on all pre-treated AA2024-T3 Substrates

As exhibited for all samples in Figure 4-22 and Figure 4-23, after 24 hours, at low frequencies from 10^5 to 10^3 Hz, the impedance magnitude was decreased by approximately one order of magnitude for the BZI-Bare-AA2024 samples compared to the OA-BZI-Bare-AA2024 samples. However, the OA-Bare-AA2024 samples and Bare-AA2024 samples revealed a lower impedance compared to BZI, OA-BZI sample, respectively.

Also, after 24 hours at frequencies between 10^2 to 10^5 Hz, the impedance curve for the BZI-Bare-AA2024 sample reveals pure capacitive behaviour which knowen as time-constant element (Q).

The impedance slowly increased from at about 1.32×10^5 ohms. cm^{-2} in the middle range of the frequencies and finally reached the point where the rate of increase of impedance is low at the low frequencies (0.1 to 0.01 Hz). Likewise, the EIS measurement of OA-BZI-Bare-AA2024 samples with values about 1.0×10^4 ohms. cm^{-2} .

A notable drop in impedance after 144 hrs for the OA-BZI-Bare-AA2024 sample was observed at about 0.9×10^4 ohms. cm^{-2}. On the other hand, at this exposure time, OA-BZI-Bare AA2024 still shown higher impedance compared to the OA-Bare-AA2024 and Bare-AA2024 substrates. Also, Bare and OA pre-treated samples show very low impedance which presented low protection from the pre-treating of oleic acid as well non-treated sample, with a value of less than 4.8×10^2 ohms. cm^{-2} , 1.32×10^2 ohms. cm^{-2} respectively.

The EIS data analysis found that the BZI and OA-BZI treatments were capable of providing moderate corrosion protection to the AA2024 substrate, even after 144 hrs immersion.
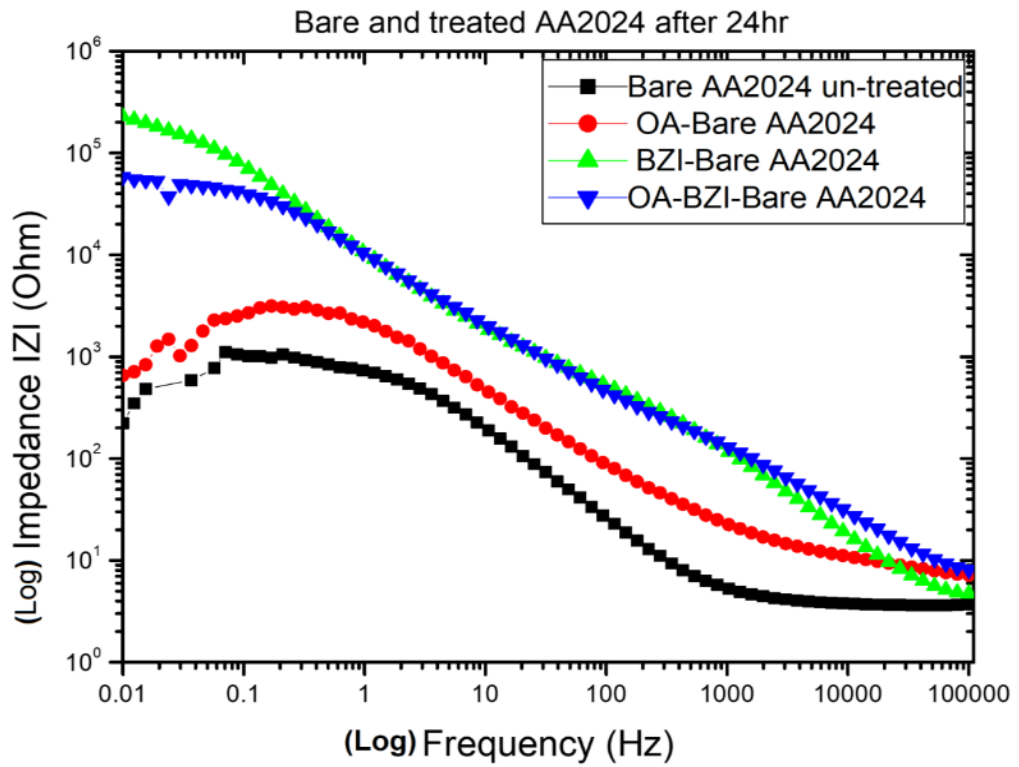
Figure 4-22 Bare and treated samples after 24hr in 3.5% NaCl solution
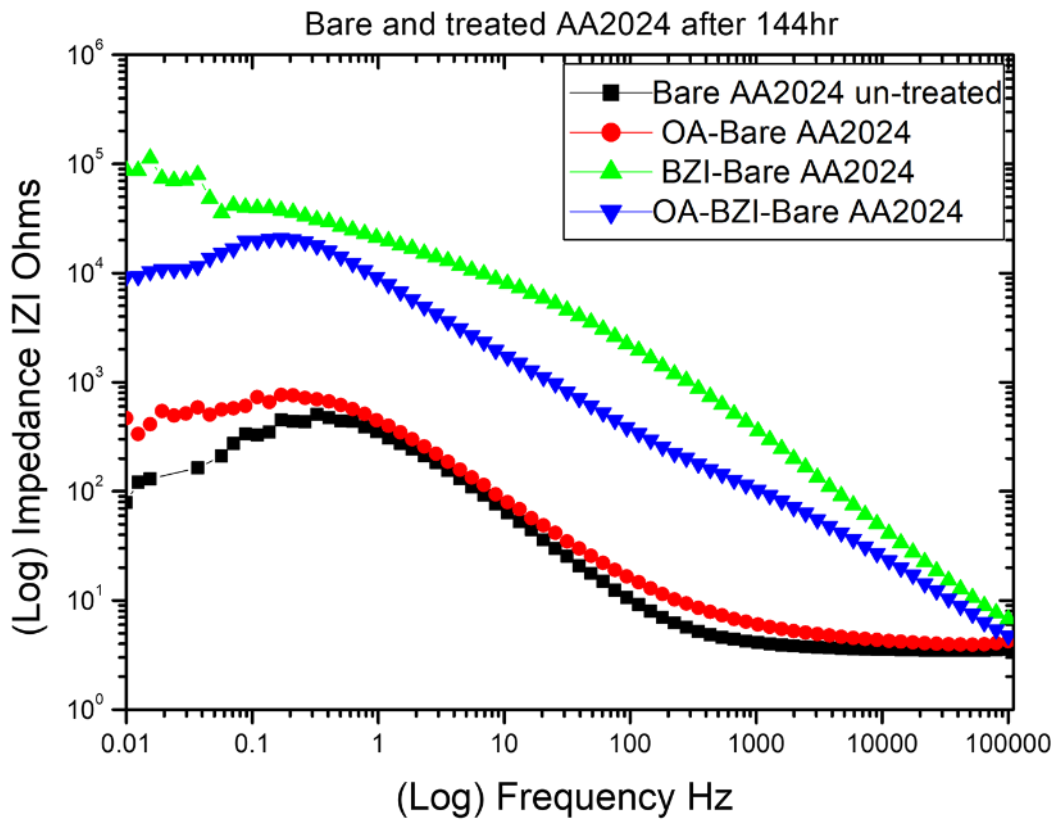
Figure 4-23 Bare and treated samples after 144 hrs in 3.5% NaCl solution

4.6.1 Investigate the corrosion protection behaviour for on bare and treated samples by using equivalent circuits fitting and modelling

Figure 4-24 shows Nyquist plots for bare and treated samples with BZI/OA, (a) tested samples after 24 hrs and (b) tested samples after 144 hrs. These data were used for fitting data to obtain the suggested equivalent circuits by using ZSimpwin electrochemical impedance spectroscopy (EIS) data analysis software
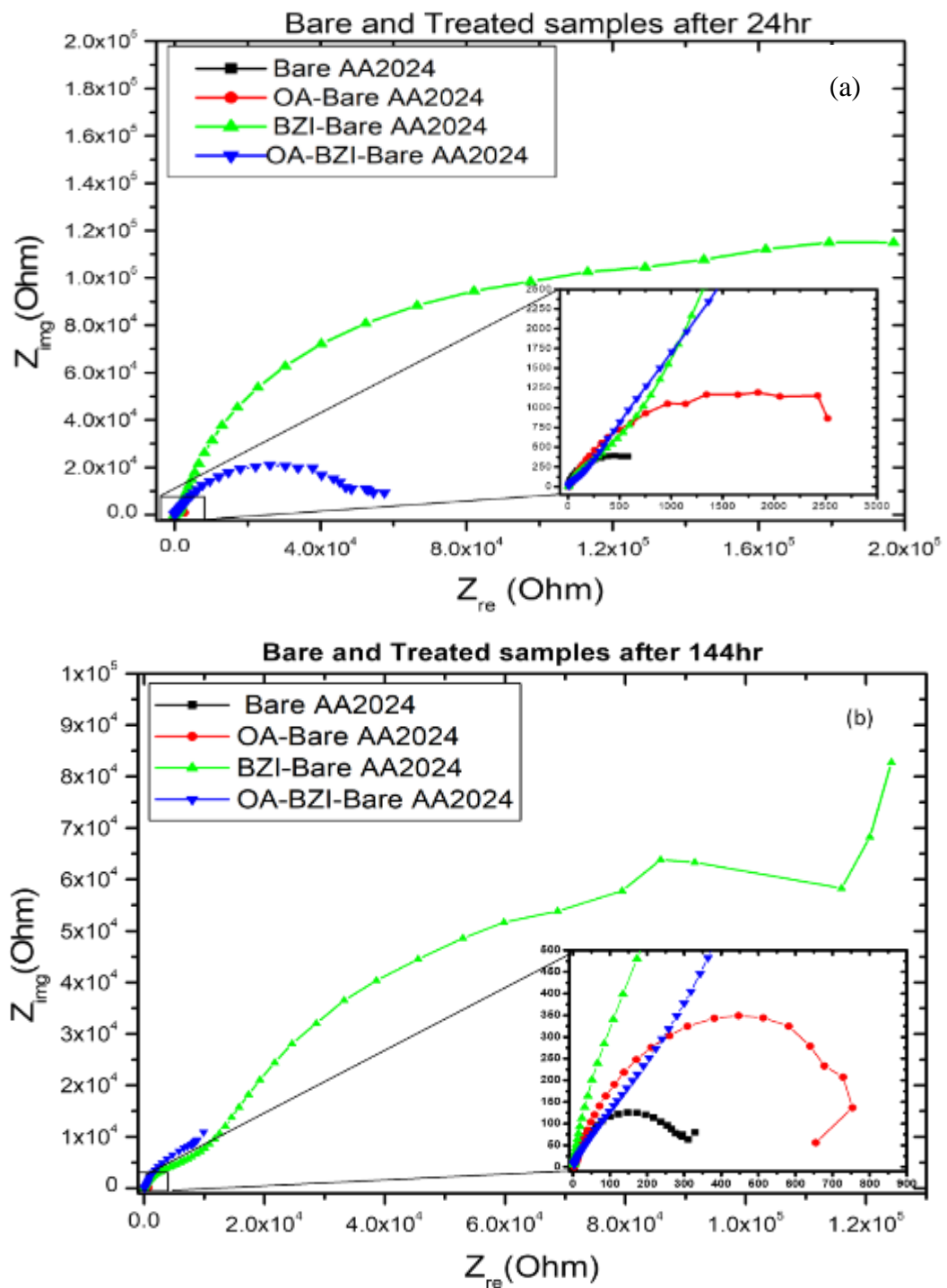
Figure 4-24 Nyquist plots for Bare and pre-treated samples in (a) 24 hrs, and (b) 144 hrs

The fitting plots for bare sample Figure 4-25 and treated samples were given in Figure **4-26** Figure **4-27**, Figure **4-28** for OA-Bare-AA2024, BZI-Bare-AA2024 and OA-BZI-Bare-AA2024 respectively.
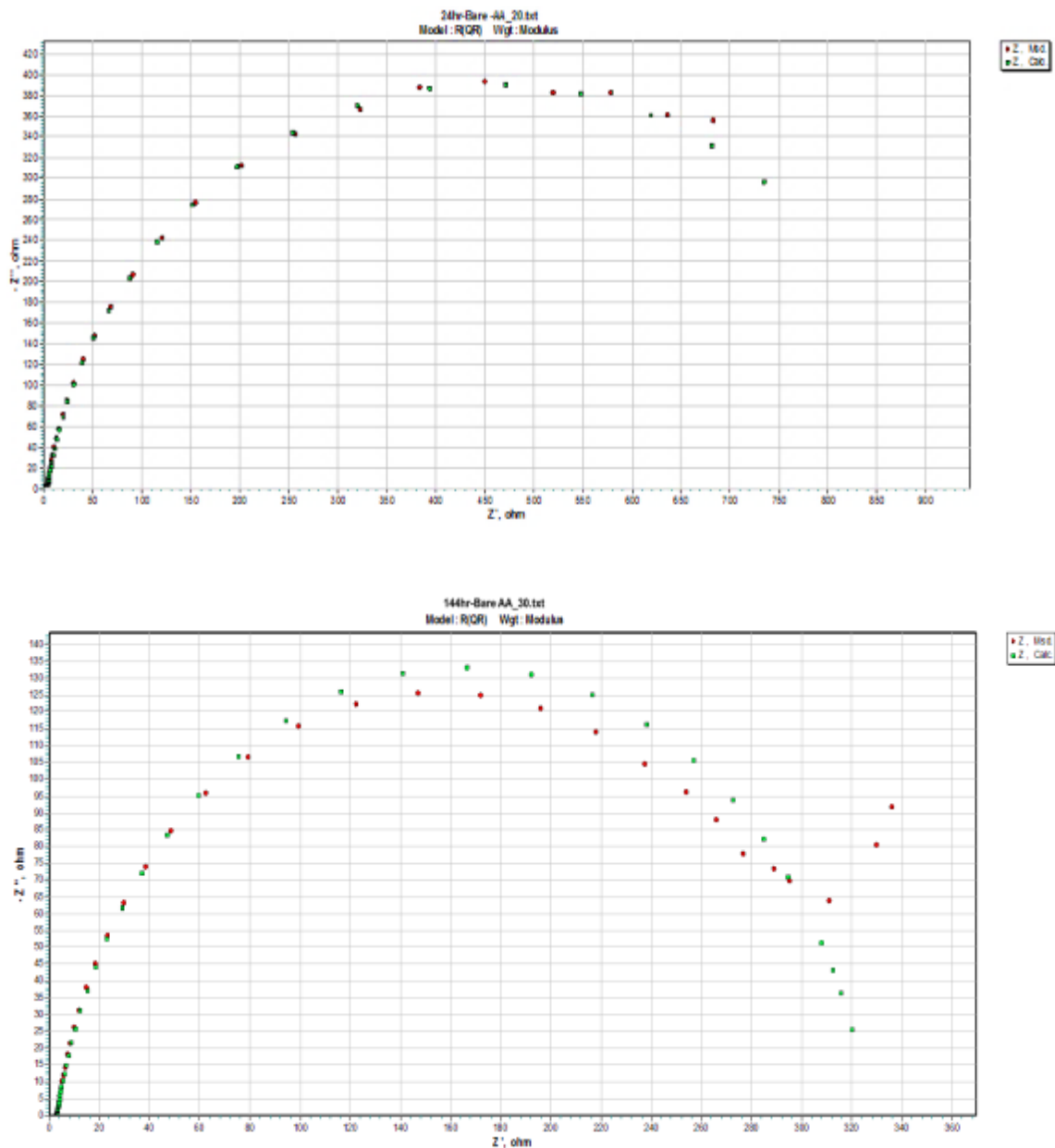
Figure 4-25 EIS Fitted data for Bare-AA2024 sample in 24hr and 144 hrs immersed in 3.5%NaCl solution

The equivalent circuit model was established from the EIS Nyquist plots. In these equivalent circuits, a constant phase element Q is used instead of an ideal capacitor C to

account for current leakage in the capacitor and frequency dispersion effect of the alternating current signals [107], [109], [150].
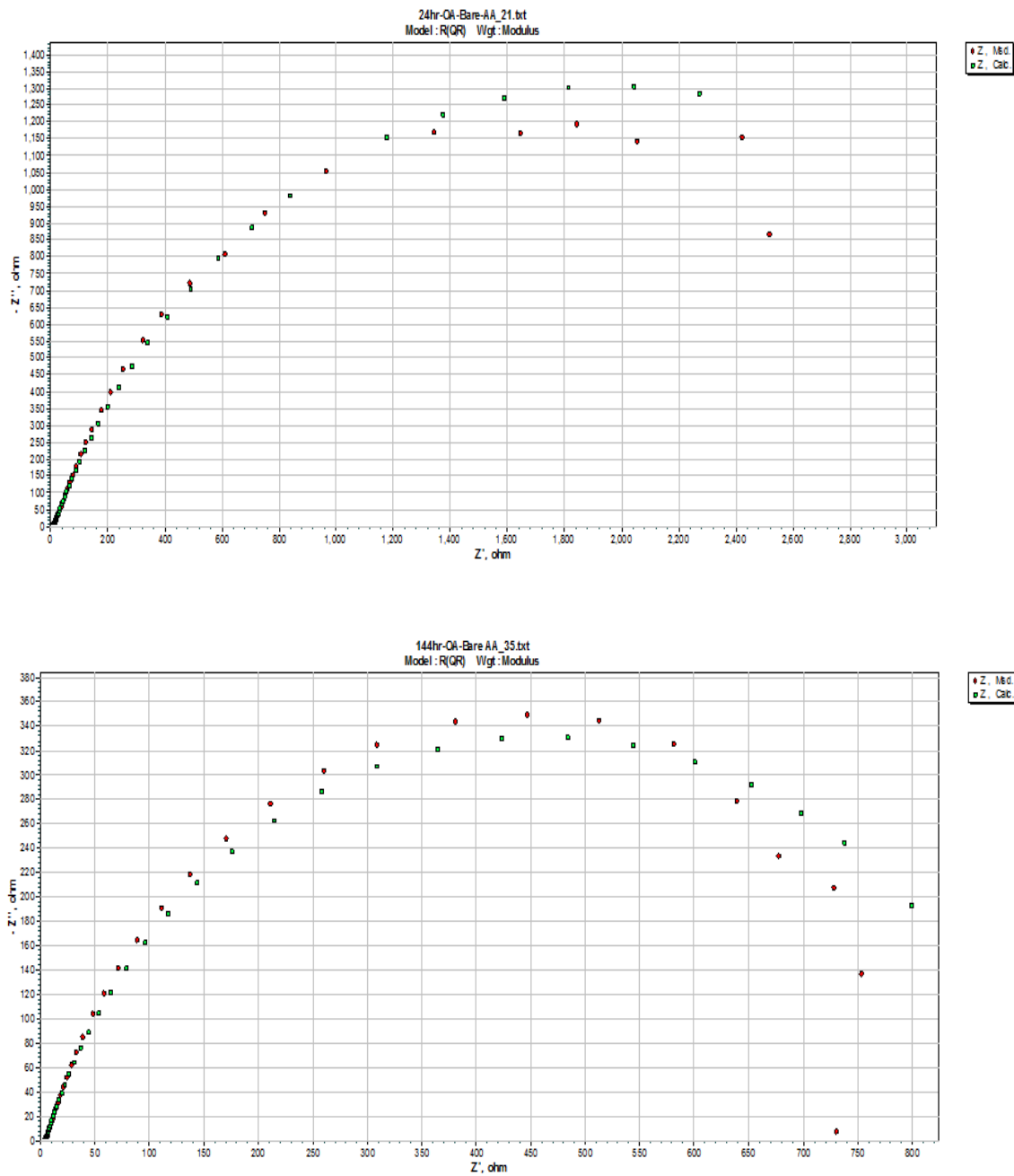
Figure 4-26 EIS Fitted data for OA-Bare-AA2024 sample in 24hr and 144 hrs immersed in 3.5%NaCl solution
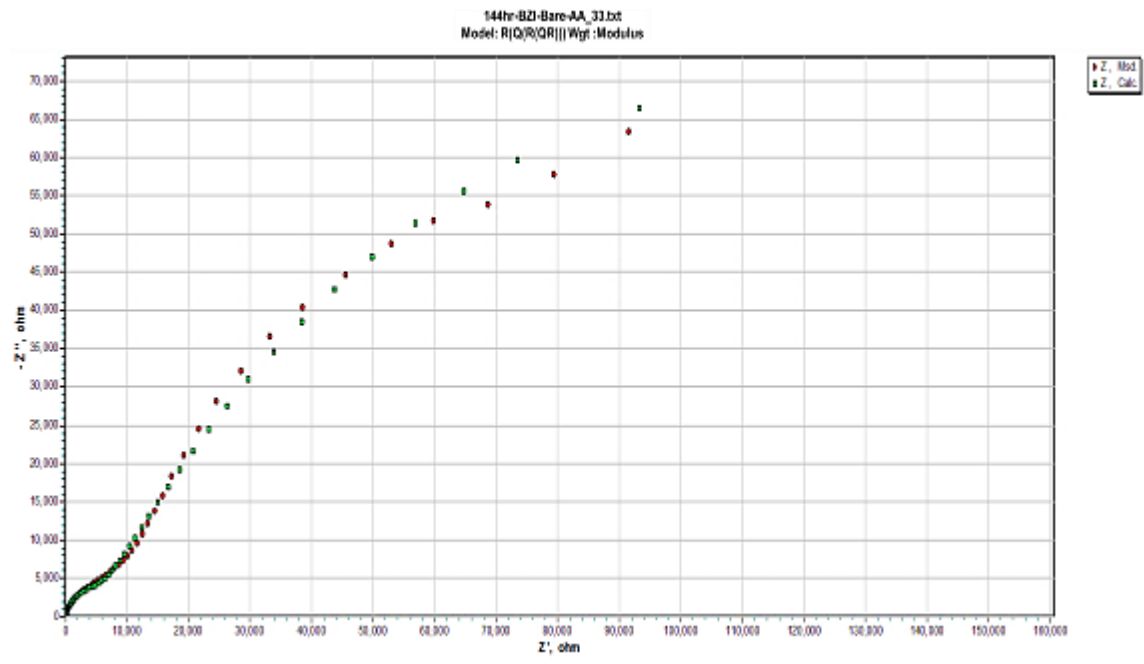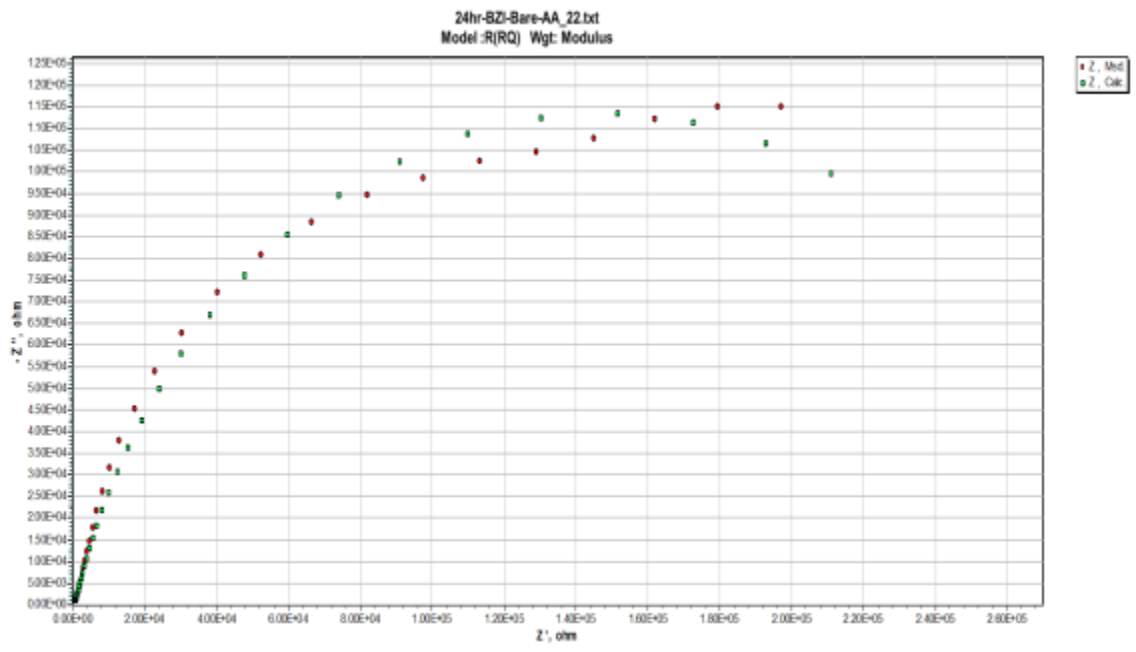
Figure 4-27 EIS Fitted data for BZI-Bare-AA2024 sample in 24hr and 144 hrs immersed in 3.5%NaCl solution
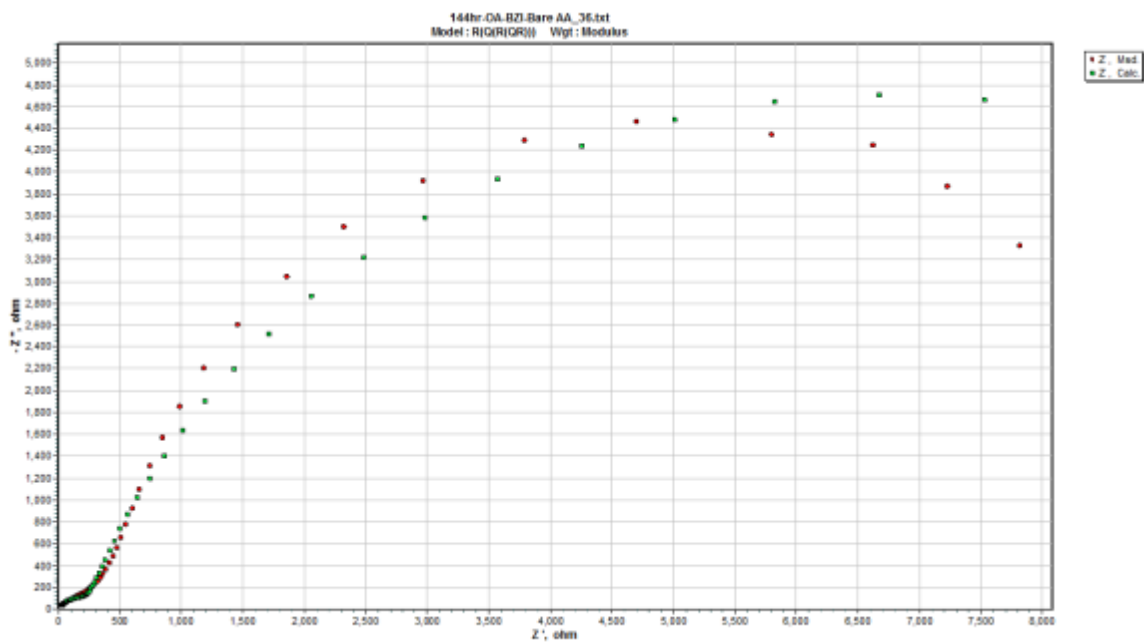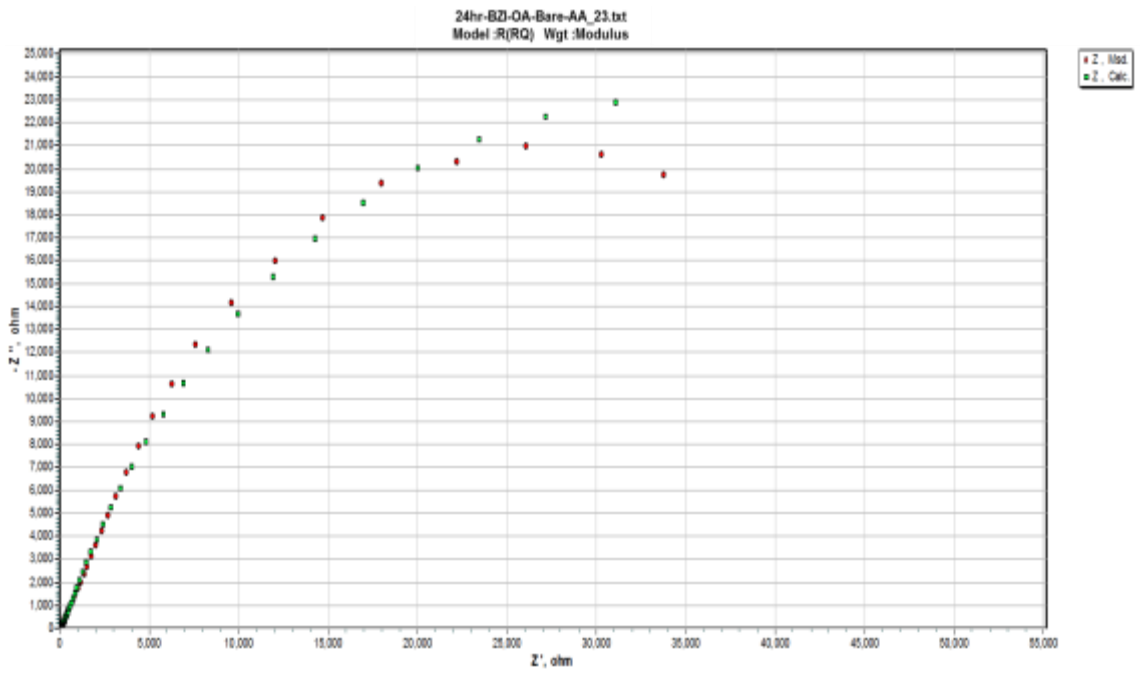
Figure 4-28 EIS Fitted data for OA-BZI-Bare-AA2024 sample in 24hr and 144 hrs immersed in 3.5%NaCl solution

Table 4-3 and Table 4-4 below list the fitted results obtained from EIS Nyquist plot for the bare and treated samples in 24hr and 144hr immersion in 3.5 wt. % NaCl solution, respectively. The elements used for the equivalent circuits were: solution resistance (R_s), created film layer resistance (R_{FL}) for Oleic acid (OA) or Benzimidazole (BZI), then film constant phase elements (Q_{FL}), intermediate oxide layer resistance (R_{iL}), intermediate oxide passive layer capacitance (Q_{iL}) [151].

Table 4-3 The fitted data obtained from EIS spectra for Bare and treated samples after 24hr in 3.5 wt. % NaCl solution.

Simulation of immersion time after 24 (hr)				
Element	Bare AA2024	OA-Bare AA2024	BZI-Bare AA2024	OA-BZI-Bare AA2024
Circuit	*R(QR)*	*R(RQ)*	*R(RQ)*	*R(RQ)*
R_s	3.85	3.035	3.115	4.465
Q_{FL}	-	8.672E-5	4.977E-6	7.981E-6
n	-	0.8	0.848	0.765
R_{FL}	-	1.032E3	1.96E5	7.919E4
Q_{iL}	2.517E-5	-	-	-
n	0.81	-	-	-
R_{iL}	905.100	-	-	-

Table 4-4 The fitted data obtained from EIS spectra for Bare and treated samples after 144hr in 3.5 wt. % NaCl solution.

Simulation of immersion time after 144 (hr)					
Sample	Element	Bare AA2024	OA-Bare AA2024	BZI-Bare AA2024	OA-BZI- Bare AA2024
	Circuit	*R(QR)*	*R(QR)*	*R(Q(R(QR)))*	*R(Q(R(QR)))*
	R_s	3.065	4.288	3.180	4.257
	Q_{FL}	-	-	2.062E-6	2.050E-5
	n	-	-	0.848	0.712
	R_{FL}	-	-	7.382E3	2.96E2
	Q_{iL}	1.916E-03	4.082E-04	2.081E-5	8.434E-5
	n	0.882	0.800	0.648	0.810
	R_{iL}	306.500	913.7	1.495E5	1.305E4

In the first 24 hours of immersion, the four samples illustrate different behaviour. Starting with Bare-AA2024-T3 sample as shown in Figure 4-29(A) revealed a one time-constant with two resistance and one-time constants this equivalent. The R_{IL} comes from aluminium oxidation film creation within 24 hrs at about 905 ohms.cm^{-2}. After 144 hours of immersion as shown in (B), the Bare-AA2024 samples kept the one-time constant circuit, but with reducing in R_{IL} with about 306 ohms.cm^{-2} and this as result of some pitting on the surface [152], [153].

(A) Bare-AA2024 after 24 hrs in 3.5% NaCl

(B) Bare-AA2024 after 144 hrs in 3.5% NaCl
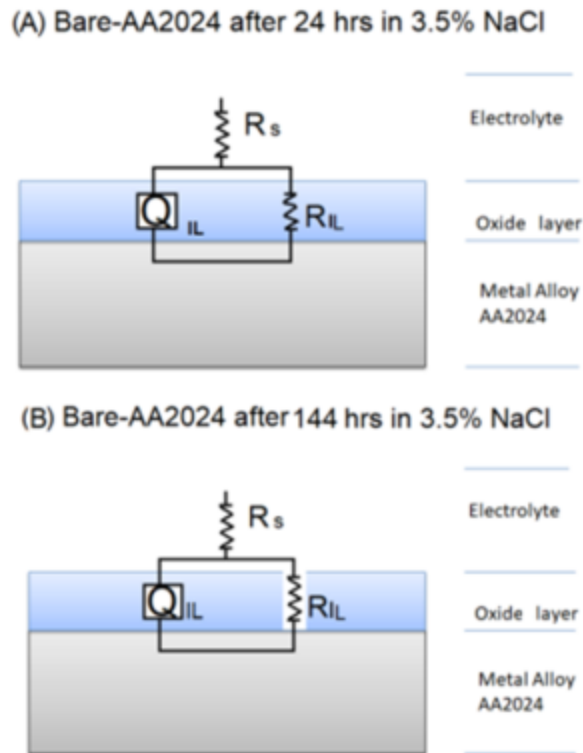
Figure 4-29 the equivalent circuit for Bare AA2024-T3 sample

The BZI-Bare-AA2024 and OA-Bare-AA2024 samples illustrate the same behaviour with two resistances and one time-constant respectively, the R_{FL} is the resistance from created film on the surface from film-forming inhibitors of benzimidazole (BZI) and/or oleic acid (OA) as shown in Figure 4-31 (C) and Figure 4-30 (E) it shows that the R_{FL} of BZI on Aluminium surface is the highest at about 1.962×10^5 ohms.cm^{-2}.

However, after 144 hrs the behaviour of both pre-treating methods was changed, while BZI-Bare-AA2024 samples changed to two time-constants with three resistances arising from the film protection on the substrate in line with the creation of oxide film under BZI film as shown in Figure 4-31 (D). The other sample of OA-Bare-AA2024 Figure 4-30 (F) revealed a one-time constant which presenting that the created oleic acid film has been removed, and replaced by oxide layer of aluminium and the protection started to fail on the surface [152].

(E) OA-Bare-AA2024 after 24 hrs in 3.5 NaCl

Electrolyte

R_S

Q_{FL} R_{FL}

OA layer

Metal Alloy AA2024

(F) OA-Bare-AA2024 after 144 hrs in 3.5 NaCl

Electrolyte

R_S

Q_{FL} R_{FL}

OA layer

Metal Alloy AA2024
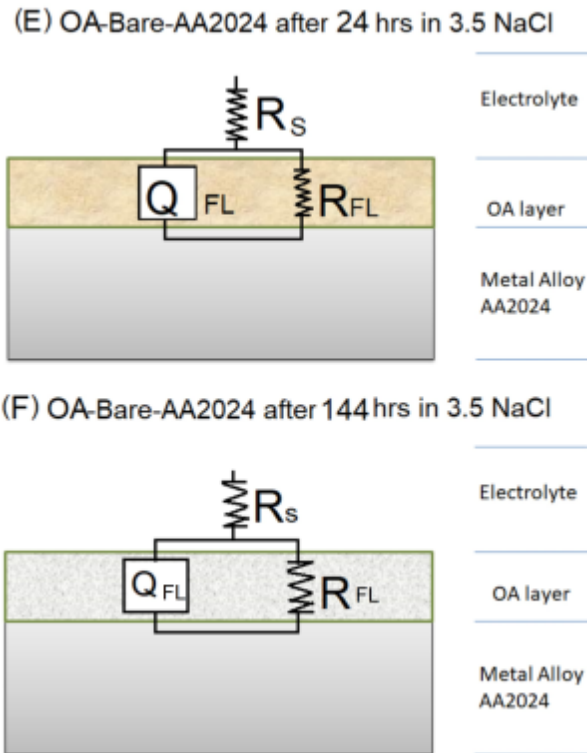
Figure 4-30 the equivalent circuit for oleic oil-treated AA2024-T3 sample

Electrolyte

R_S

Q_{FL} R_{FL}

BZI layer

Metal Alloy AA2024

(D) BZI-Bare-AA2024 after144hrs in 3.5 NaCl

Electrolyte

R_S

Q_{FL} R_{FL}

Q_{IL} R_{IL}

BZI layer

Oxide Layer

Metal Alloy AA2024
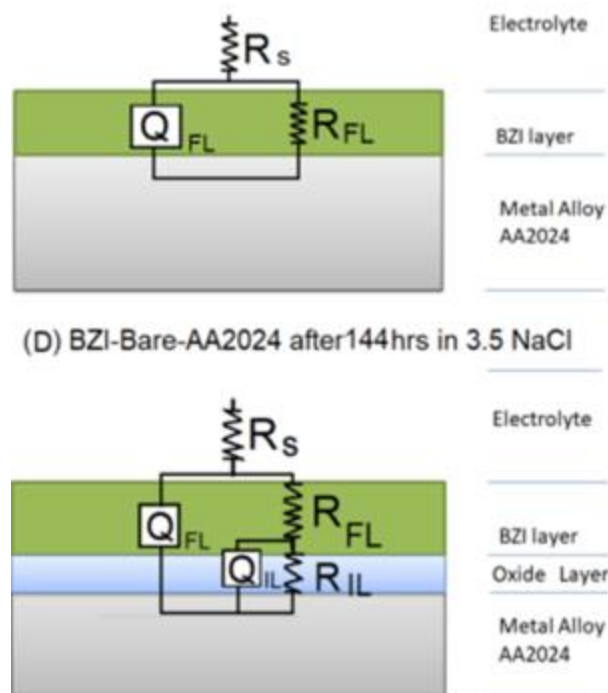
Figure 4-31 the equivalent circuit for benzimidazole-treated AA2024-T3 sample

In Figure 4-32, for OA-BZI-Bare-AA2024 sample, after 24 hours is shown in Figure 4-32 (G) similar behaviour with presenting one time-constant as a result of film creation on the

surface which is reflected the presence of R_{FL} of the mixed solution of BZI and OA with the value of 7.92×10^4 ohms.cm^{-2}. However, the protection of the first film was lost, after 144 hrs as showed in Figure 4 28 (H) started to exhibit a two time constant with three resistances, which may as result of removing the oleic acid from the mixture as its adsorption might weaker than the BZI on the metal surface attributed to relatively strong nitrogen bonds in BZI to metallic surface[154], [155].
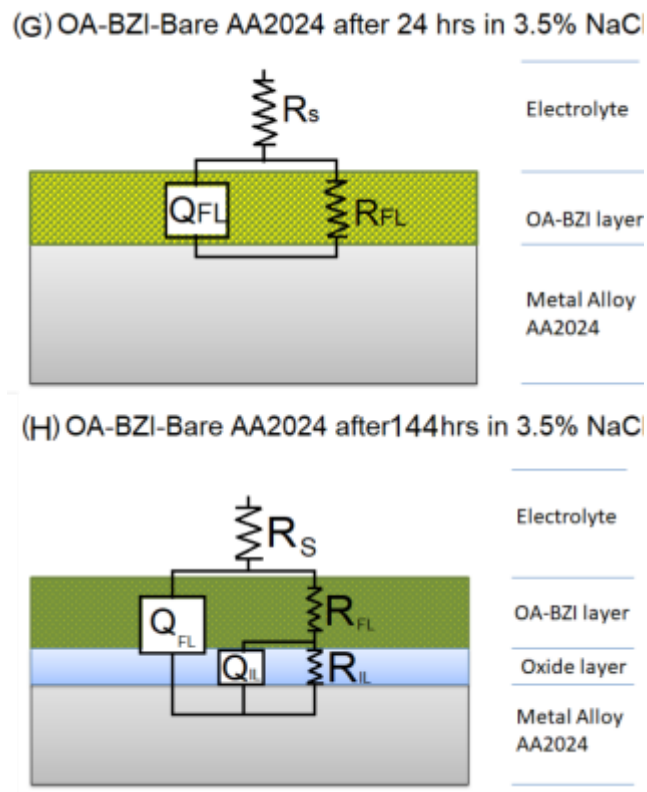
Figure 4-32 the equivalent circuit for OA-BZI-treated AA2024-T3 sample

The protection by oleic acid and benzimidazole results from different mechanisms. While the oleic acid protection is based on barrier protection which provides a type of hydrophobicity property reducing the diffusion only. The corrosion protection of benzimidazole is working as an active film-forming inhibitor by direct adsorption on the surface metal creating film stopping the galvanic effect from copper-based intermetallic particles. [156]

4.7 Fourth Chapter Summary

From the results bare aluminium and inhibitors treated samples; it is apparent that the Bare-AA2024 is vulnerable to corrosion in the aggressive environment and easy to corrode as the pitting and general corrosion takes place.

The pre-treating process by film-forming inhibitors on aluminium alloys surface can protect the bare metal for up to six days in 3.5% v/v NaCl solution.

The oleic acid acts as a barrier but is not lasting for longer than 48 hrs. Benzimidazole lasts for longer than oleic and mixture inhibitors of both by more than one week. However, the BZI film did not completely stop the diffusion from the metallic surface in the high positive polarisation area.

Mixing inhibitors 1:1 v/v of benzimidazole and oleic acid performs to combine the advantages of both protection mechanisms. However, the long term performance of this pre-treatment in an aggressive medium was not sufficient and needed further investigation.

Chapter 5- Study of Using Hybrid Organic-Inorganic Sol-Gel Coatings for Corrosion Protection on Aluminium Alloy 2024-T3 Substrate

Overview

In this results and discussion Chapter, two suggested sets of sol-gel coating will be presented and investigated. The first part discusses the corrosion protection by organic - inorganic hybrid sol-gel coatings (named as SBX) on AA2024-T3 alloys. This sol-gel was prepared from tetraethyl orthosilicate silane (TEOS) and triethoxymethylsilane (MTMS) precursors as performance control samples. The second part will present and discuss the corrosion protection and other properties of hybrid fluorinated sol-gel coatings (named as F-SBX) by introducing as additive of the fluorinated precursor 1H,1H,2H,2H-Perfluorodecyltriethoxy silane (PFOTS) precursor which could be used in top coating applications. The two formula preparations were described in the experimental chapter in section 3.7.4 .

The corrosion protection performances of organic-inorganic hybrid sol-gel coating on bare aluminium alloy AA2024-T3 and sol-gel coated samples have been investigated by using the Potentiodynamic polarisation scanning (PDPS), electrochemical impedance spectroscopy measurements (EIS), both in 3.5% w/v NaCl solution, infinite focus microscopy (IFM), scanning electron microscopy (SEM) and Energy-dispersive X-ray spectroscopy (EDX) analyses, water contact angle (WCA). The samples were coated by sol-gel with one side then dried for 4 hours at 80°C, as mentioned in the experimental chapter in section 3.7.4 coded as SBX and F-SBX then waxed with leaving 2 cm^2 of the desired tested area. All electrochemical and other tests were repeated five times with present the same behaviour. Table 5-1 shows samples identification.

Table 5-1 Samples identification table

No.	Identifier	The base of Sol-gel	PFOTS v/v%	Curing Temperature
1-	**SBX-80**	TEOS+MTMS+PSX	Nil	80°C
2-	**F-SBX-80**	TEOS+MTMS+PSX	1.5%	80°C
3-	**Bare-AA2024**	Nil	Nil	Nil

5.1 Potentiodynamic polarisation scanning (PDPS)

Potentiodynamic polarisation scanning was used to investigate the corrosion and corrosion protection for bare and the sol-gel coated AA2024-T3 samples in a chloride level of 3.5% NaCl. The anodic and the cathodic curves were measured between -250 mV and 750 mV

against the open circuit potential (OCP) of the tested sample. Polarisation curves of two sol-gels coated and the bare samples are shown in Figure 5-1, Where their anticorrosion behaviour is compared. Primarily, both coated samples displayed excellent initial performances, as barrier properties when compared to the bare AA2024 T3 sample.
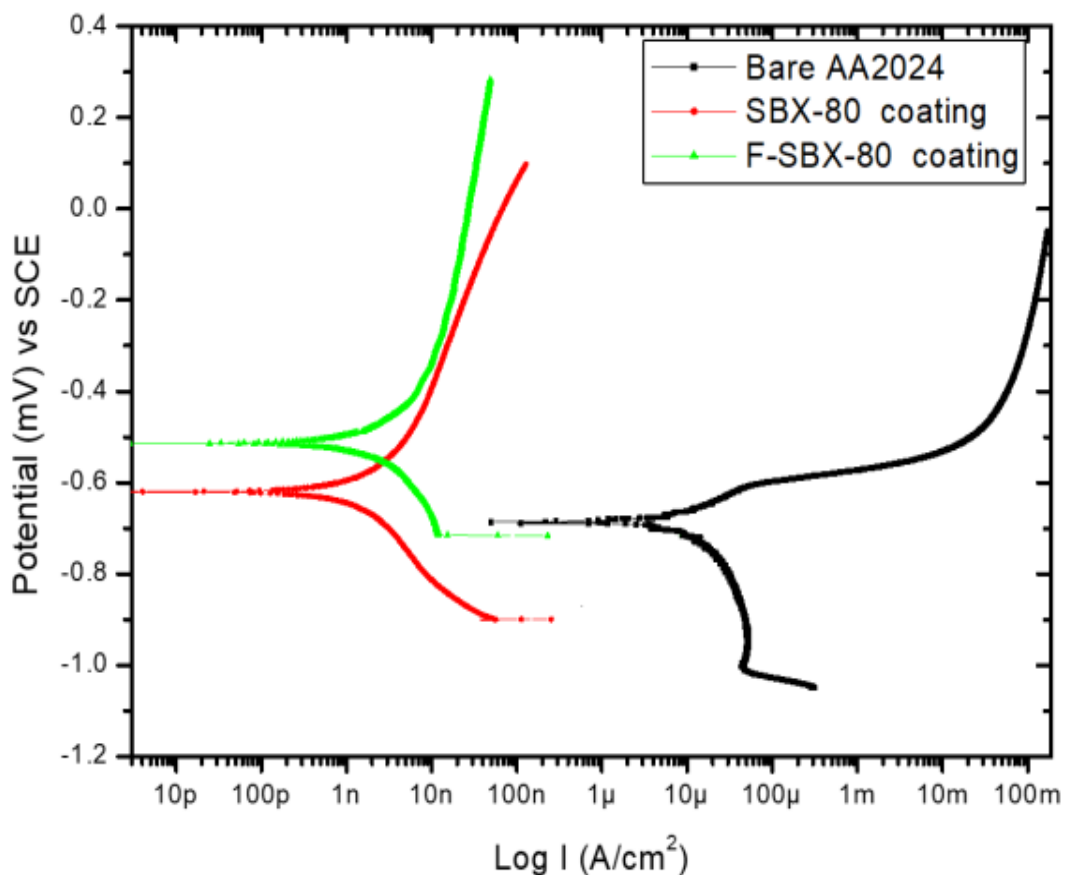
Figure 5-1 Polarization curves for the bare and sol-gel coated samples in 3.5% NaCl solution in one hour of exposure

Corrosion potential (E_{corr}) and corrosion current density (I_{corr}) were obtained, as shown in Table 5-2 by extrapolation of cathodic and anodic curves using the Tafel extrapolation method. The current density on the cathodic branch is reduced by approximately four magnitudes for all sol-gel coated samples compared to the bare sample. The anodic polarisation current was changed due to the kind of additive above the OCP. F-SBX-80 initially reduced the anodic current by seven orders of magnitudes. SBX-80 samples had an anodic current reduced by about six orders of magnitudes when compared to the bare sample of AA 2024.

Corrosion current densities of both sol-gel coated samples were estimated at $1.02 \times 10^{-9} A/cm^2$, $1.22 \times 10^{-9} A/cm^2$ for SBX-80 and F-SBX-80 sol-gels respectively, compared to $7.10 \times 10^{-6} A/cm^2$ of the bare AA2024 T3 alloy. The results suggest that corrosion protection offered by both sol-gel coatings SBX and F-SBX was attributed to barrier protection properties of the sol-gel coatings. Corrosion potential increased for the sol-gel coated Al alloys in comparative with the bare sample.

The shift in E_{corr} indicates that the anode is inhibited to a greater degree than the cathode in F-SBX formula which exhibited sort of active protection, and this is attributed to the fluorine-carbon atoms bridging to the substrate [107], [150].

Table 5-2 PDPS polarisation data for bare and Sol-gel coated samples

Sample	E_{corr} [mV vs SCE]	I_{corr} [A/cm^2]	OCP [mV vs SCE]
Bare-AA 2024	-662 ± 2	7.10×10^{-6}	-640
SBX-80 coating	-608 ± 2	1.02×10^{-9}	-708
F-SBX-80 coating	-521 ± 2	1.22×10^{-9}	-658

5.2 The hybrid organic-inorganic Sol-Gel Formula SBX as a base Coating

The need for a new formula of sol-gel is taking place as the sol-gel technology one of the eco-friendly coating techniques and can provide the metal alloys proper protection from corrosion and the surrounded environments.

The basis of this formula was mentioned in the experimental chapter section 3.7.4 ; however, the main precursors here were only used tetraethyl-orthosilicate silane (TEOS) and triethoxymethylsilane (MTMS) then hydrolysed by water in the presence of nitric acid as catalyst and afterwards applying it on the AA2024 T3 sample with dried in 80°C, and the sol-gel formula was named by (SBX).

5.2.1 Surface morphology and elements scanning of SBX-80 sol-gel coating before testing

In general, the surface of SBX-coating on the substrate was even and smooth, and the SEM and EDX images and spectroscopy confirm the chemical element of the sol-gel formula on the AA 2024 sample. Also, the cross-section showed that the thickness of the coating is 17 ± 2 µm. Figure 5-2 and Figure 5-3 showed the SEM and EDX image of the substrate chemical composition and adhesion index [134].
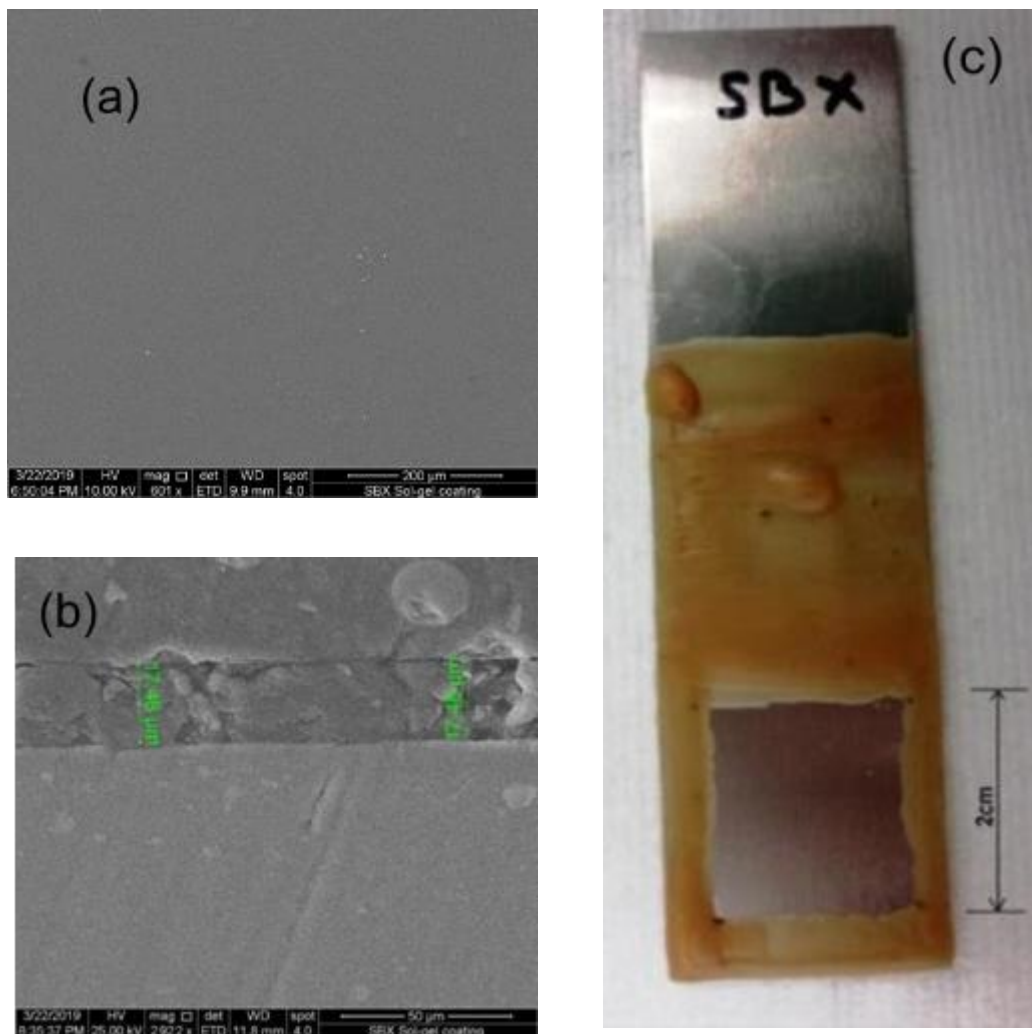
Figure 5-2 (a) SEM image of surface morphology, (b) SEM image of cross-section and (c) SBX-80 coating waxed sample
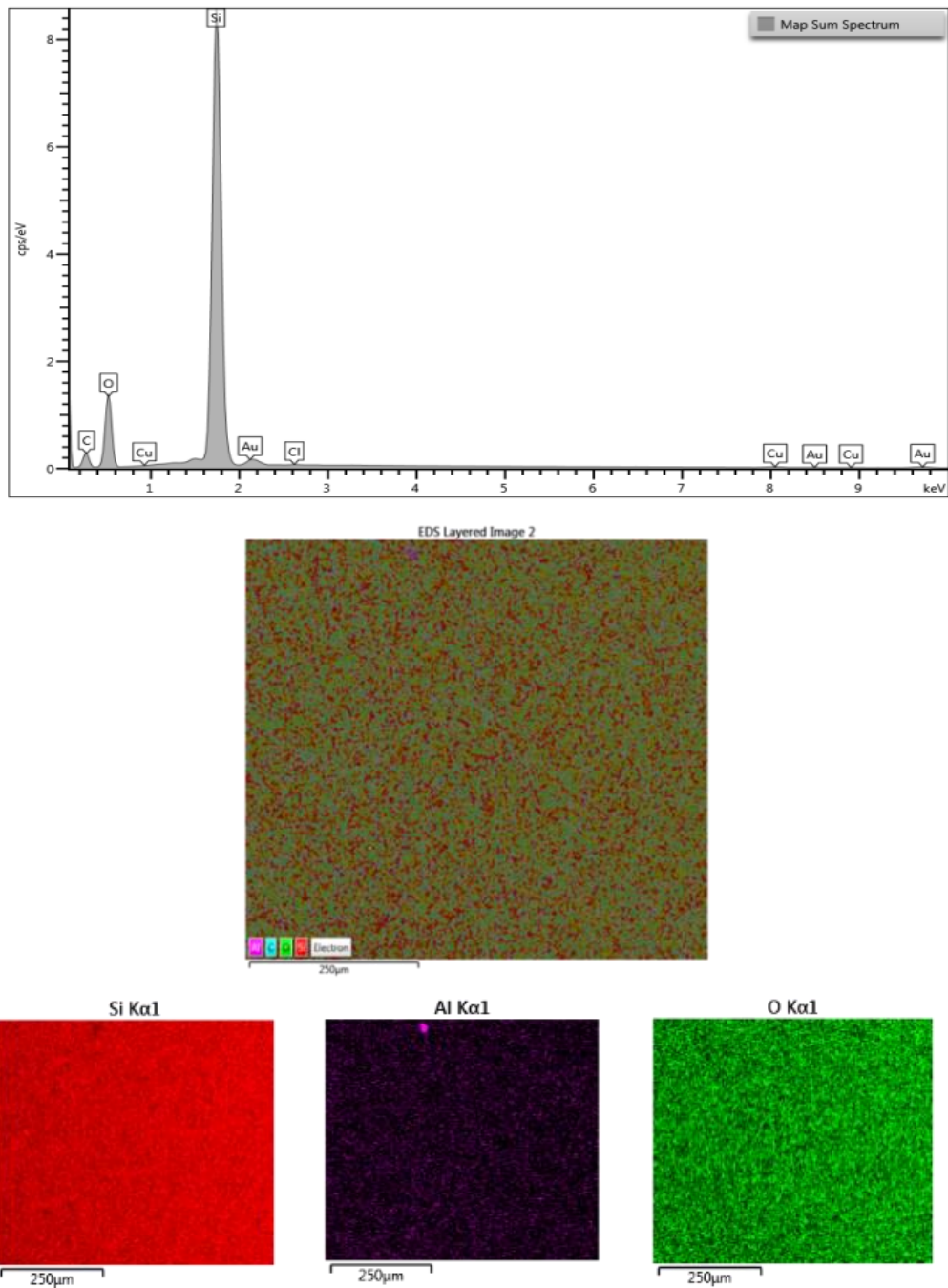
Figure 5-3 EDX mapping and spectroscopy for SBX-80 sol-gel coating before testing

5.2.2 Analysing ATR-FTIR for SBX-80 sol-gel chemical composition before testing

The information from the FTIR data of the SBX on the coated substrate confirms the Hybrid coating of SBX-80 Sol-gel formula bonding on AA2024 substrate as a dried gel on the AA2024 surface. From Figure **5-4**, the confirmation of chemical composition can be seen as the following. The TEOS, MTMS precursors and Deionised water were put as a control in the next graph.
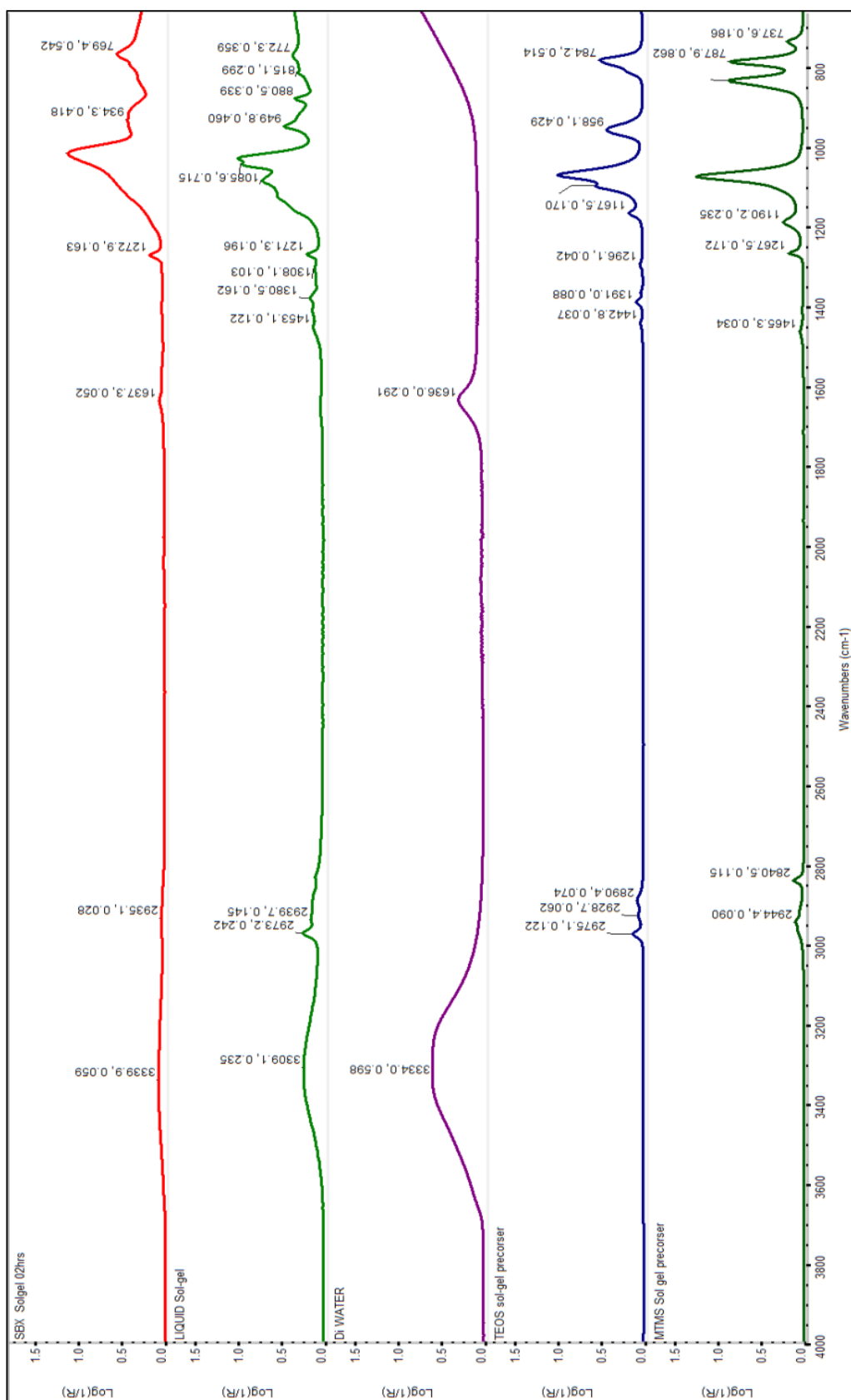
Figure 5-4 ATR spectrum for precursors and SBX-80 sol-gel on the AA2024-T3 substrates

The stretching peaks on the liquid SBX sol-gel at about 2956, 2902 and 2845 cm^{-1} respectively attributed to C-H stretching bond for CH$_2$ and CH$_3$, and as identified by changes of the TEOS and MTMS precursors. Similarly, the peaks between 1248 and 1290 cm^{-1} attributed to the bending of C-H.

The peak at 3800 to 3020cm^{-1} associated with OH- stretching, also the weak peak at 1648 cm^{-1} attributed to O-H bending can be seen on liquid SBX sol-gel as a sign of hydrolysing of both precursors and this peak decreased in intensity after the sol-gel dried as it in xerogel SBX coating on the substrate[82], [157].

The indication of SI-O- reactions can be defined at low wavenumbers on both liquid sol-gel and xerogel, at about peak 1028cm^{-1} attributed to cyclic SI-O which shifted after drying to 1098cm^{-1} attributed to linear Si-O, the hybrid part Si-C-R of sol-gel can be seen at 846 cm^{-1} attributed to bending of Si-C, and this can also be seen on the organic precursor MTMS at the same frequencies [145], [157].

5.2.3 The Electrochemical Impedance Spectroscopy (EIS) for the Base SBX-80 Sol-Gel Coating

The test was run for about two weeks with repeated for more than five times in a 3.5% NaCl solution. The results for the SBX-80 sol-gel coated samples were obtained in this chapter and compared to bare AA2024 sample.

The impedance data for the SBX-80 coated substrate, as is shown in Figure 5-5, illustrates the general behaviour of this coating as a corrosion barrier coating or as a base coating. The EIS results in the first hour of immersion exhibit reasonable impedance, starting at about 1.7×10^3 ohms. cm^{-2} at high frequency which reflects the solution resistance between 10^5 to 10^3 Hz, starting rising with slightly sloping to with general capacitor behaviour attributed to coating resistance then levelled off at about 1.1×10^5 ohms. cm^{-2} then again reach the higher magnitude in the low frequencies between 1.0 to 0.01 Hz with value about 7.8×10^5 ohms. cm^{-2} .

In 24 hrs of the immersion, the coating resistance started to decrease, probably due to the diffusion and oxidisation on the metal surface. However, the drop of the impedance at high frequencies is less than one magnitude which means the coating resistances is still working and provide moderate protection.

The impedance is decreased to reach 1.2×10^3 ohms. cm^{-2} in the high frequency and continues to behave as a coated sample which showed low protection to reach after 336 hrs about 5.2×10^2 ohms. cm^{-2}. At low frequency from 0.1 to 0.01 Hz the impedance decreased from the first hour 7.8×10^5 ohms. cm^{-2} after 336 hrs to reach about 1.1×10^5 ohms. cm^{-2}. That might reveal although there was some loss of performances, there was a possibility of keeping the barrier properties to protect AA2024 alloy from direct corrosion.

Furthermore, the phase angle θ Figure 5-6 showed two time-constants in the first immersion hour, the first between 10^3 to 0.1 Hz and the second one between 10 to 0.01Hz. These come from the created oxidised film layer which came from direct diffusion. Likewise, from 48 till 336 hrs these two time-constants with creating a small new one from the underneath oxidation, first one started from 10^5 to 10^3 Hz and the second one began from 10 to 0.1 Hz and this two-time-constants attributed to the same aluminium oxide film formed on the substrate [150].
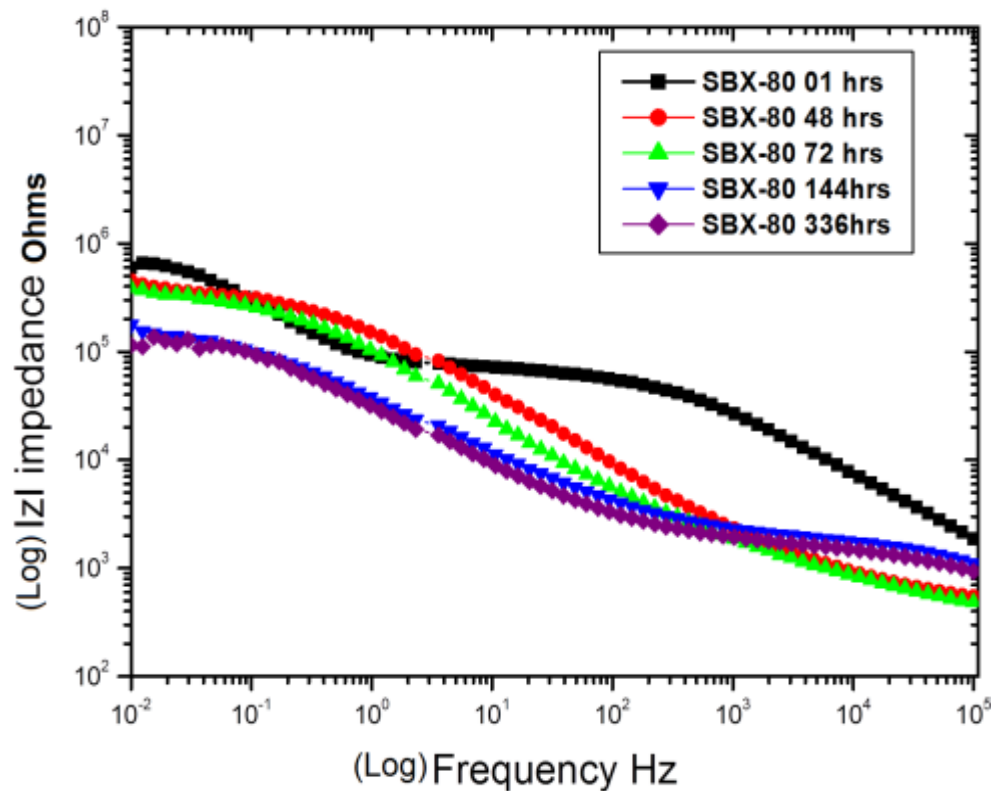
Figure 5-5 Impedance behaviour of SBX-80 sol-gel coating in 3.5% NaCl solution
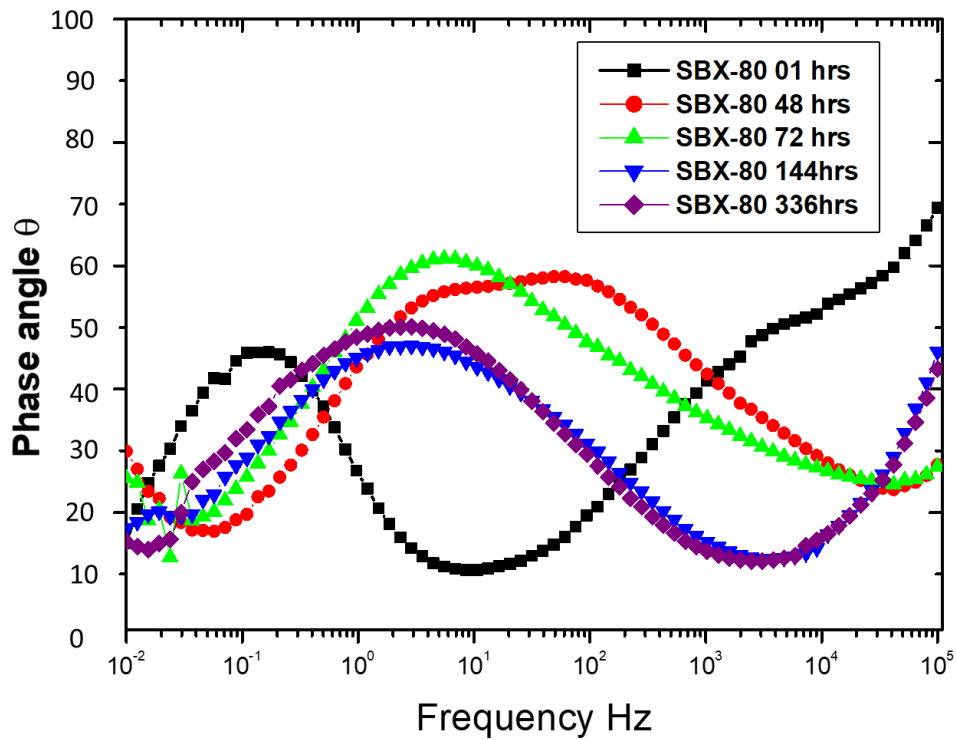
Figure 5-6 Phase angle response of SBX sol-gel coated sample in 3.5% NaCl solution

In Figure 5-7, The protection behaviour of SBX-80 sol-gel coating was accompanied by the appearance of light corrosion. The coated substrate stayed clear until 336 hrs. After the 360 hrs of immersion, some pitting corrosion started and it can be seen under the sol-gel with some film cracking.

However, the SBX-80 sol-gel coating still on the surface with some of the cracks and this due to drying of the interfacial layer at the period of morphology testing. The surface morphology examination exhibits the SBX-80 sol-gel coating still existing even after 360 hrs despite some indication of damage.
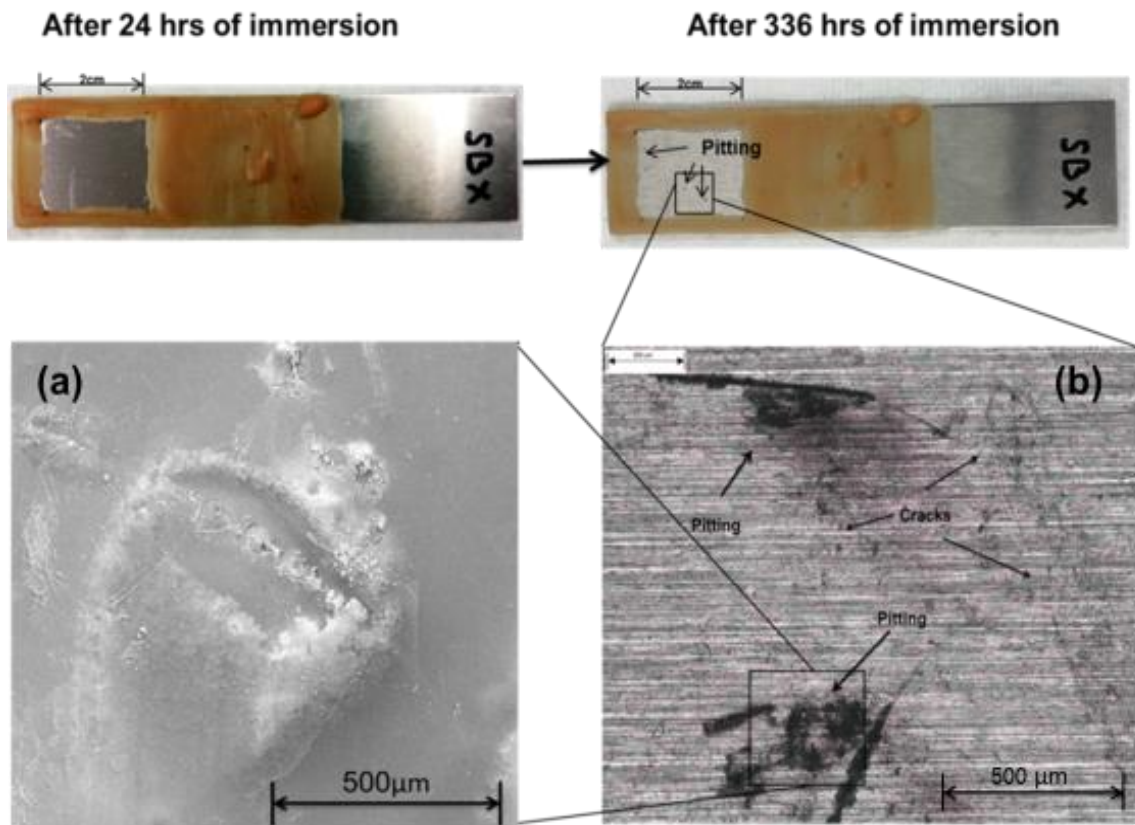
Figure 5-7 Shows the SBX Sol-gel substrate after 336 hrs of immersion (a) SEM image and (b) IFM image showed some cracks and pitting corrosion under the coating

Figure 5-8 shows the EDX mapping and spectrum images for SBX-80 hybrid organic-inorganic sol-gel coated sample after 336 hrs of immersion in 3.5% NaCl solution, which is revealed some pitting and cracks but with very insignificant oxidation rate when it compared to the Bare AA 2024 sample.

The carbon elements mapping related to the organic part of the sol-gel. The minor chloride level on the sol-gel coating surface includes some indication for pitting corrosion. The silicon element at 6.2 Kev and on the green map still mostly uniformly distributed, which reflects the sol-gel coating existing on the surface of the substrate.
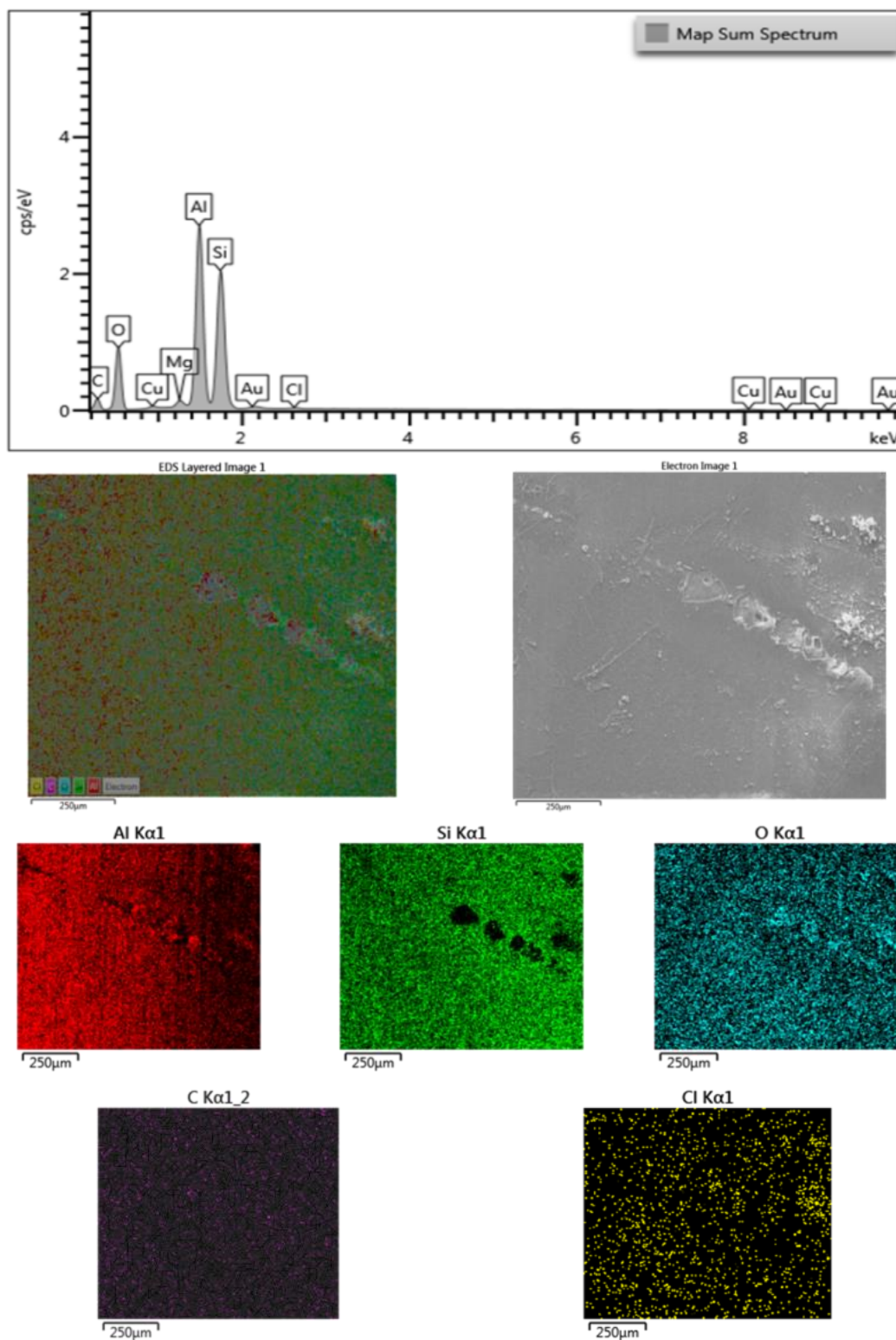
Figure 5-8 EDX spectrum and mapping images for SBX Sol-gel coated sample 336 hrs in

3.5% NaCl solution

5.3 The Fluorinated Sol-Gel modified Formula F-SBX-80 as enhanced Top Coating

As one of the weaknesses of the SBX sol-gel alone is the porosity which is a common issue in any sol-gel formula leading to the ionic and electrolyte diffusion to the aluminium alloy metal surface, and this will allow creating an oxidising film that reducing the adhesion, especially after the long immersion releasing the residual stresses and sometimes forming cracks on the coating film. Pitting may form under the coating, which all will make the sol-gel coating less durable in the case to be used as a top-coating without the presence of inhibitors [158]–[160]. Therefore, to enhance the sol-gel coating, there are some techniques, one of them by increasing the hydrophobicity. In this second part of sol-gel will be investigating the improvement on the SBX hybrid organic-inorganic sol-gel formula by adding 1.5% v/v ratio of the fluorinated precursor 1H,1H,2H,2H-Perfluorodecyltriethoxy silane (PFOTS), then applying the same techniques of spraying and curing in 80°C. The new formula will be labelled as F-SBX-80.

5.3.1 Surface morphology and elements confirmation of modified F-SBX-80 sol-gel coating non tested sample

The surface of F-SBX coating on the substrate was even and a smooth surface similar to SBX formula; additionally, this coating has hydrophobic properties which will be mentioned later.

Using the SEM and EDX images and spectroscopy can confirm the chemical element of the sol-gel formula which was coated on the AA 2024-T3 sample such as Si, C, O and the small detected amount of Fluorine (F) at 6.4 KeV, which reflecting the real percentage of additive less than 1.5% v/v. Besides, it is noticeable that the cross-section that showed in Figure 5-9 that the thickness of the coating is 18 μm ± 2. Figure 5-10 illustrates the EDX mapping and spectrum images of non-tested F-SBX sample confirming the chemical elements of sol-gel coating and aluminium alloy.
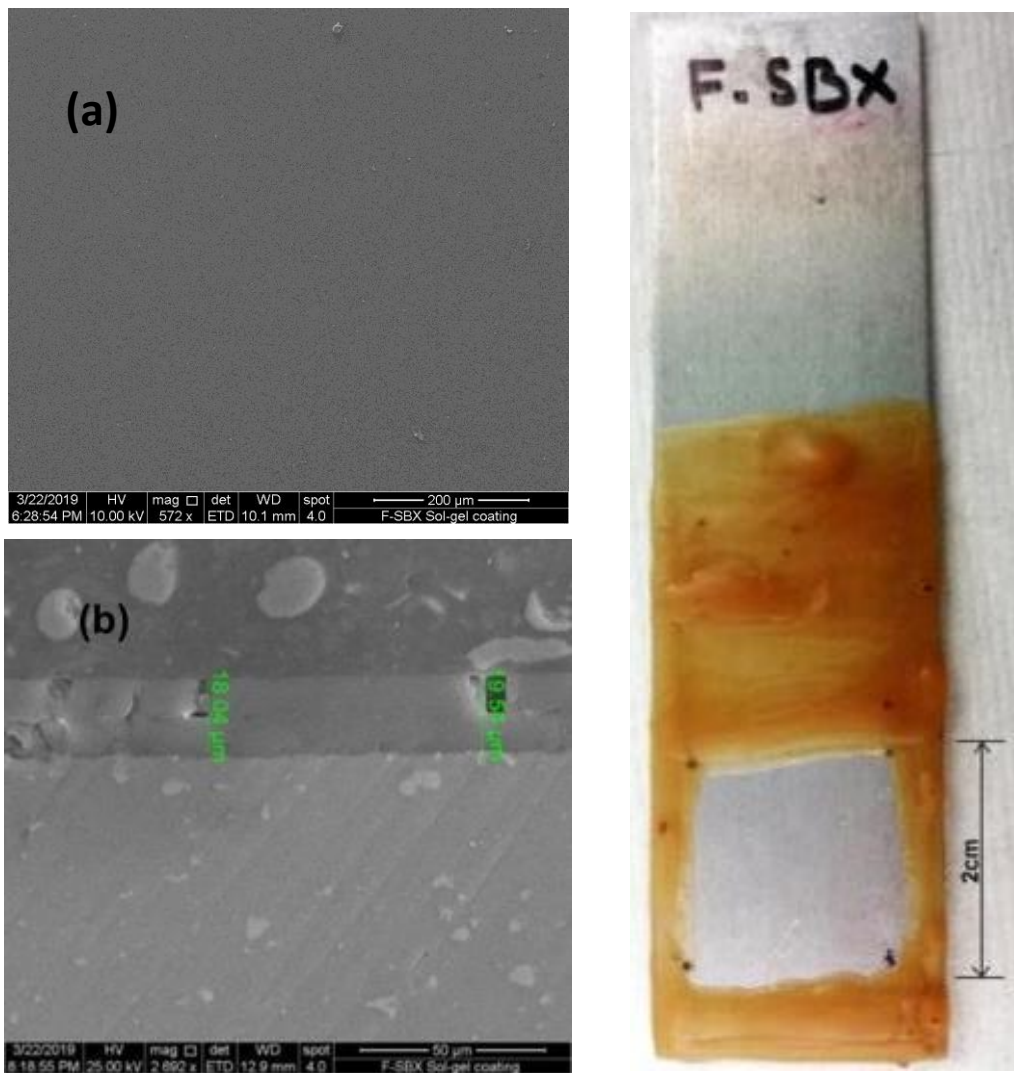
Figure 5-9 Shows the F-SBX-80 coating waxed sample (a) SEM image of surface morphology, (b) SEM image of the cross-section
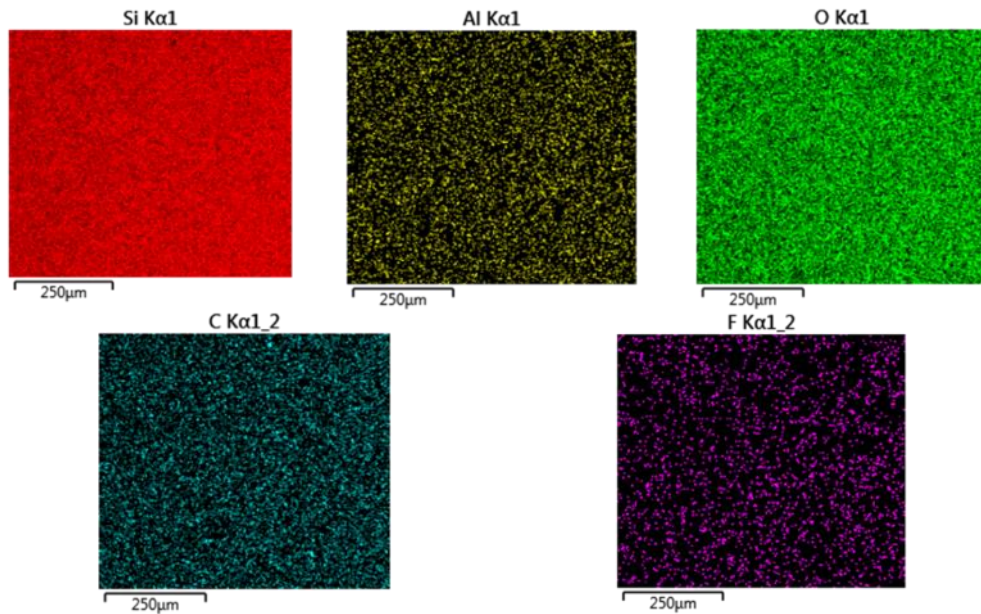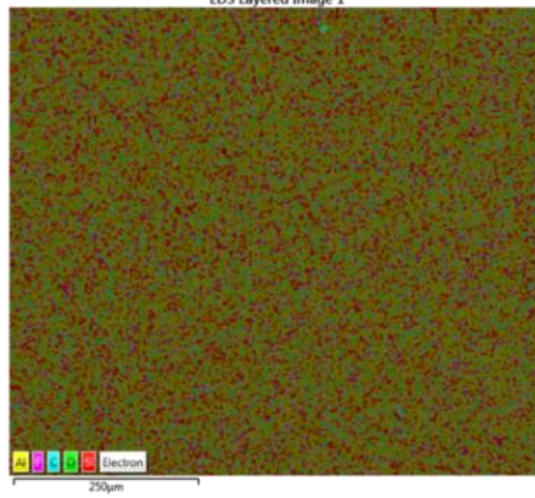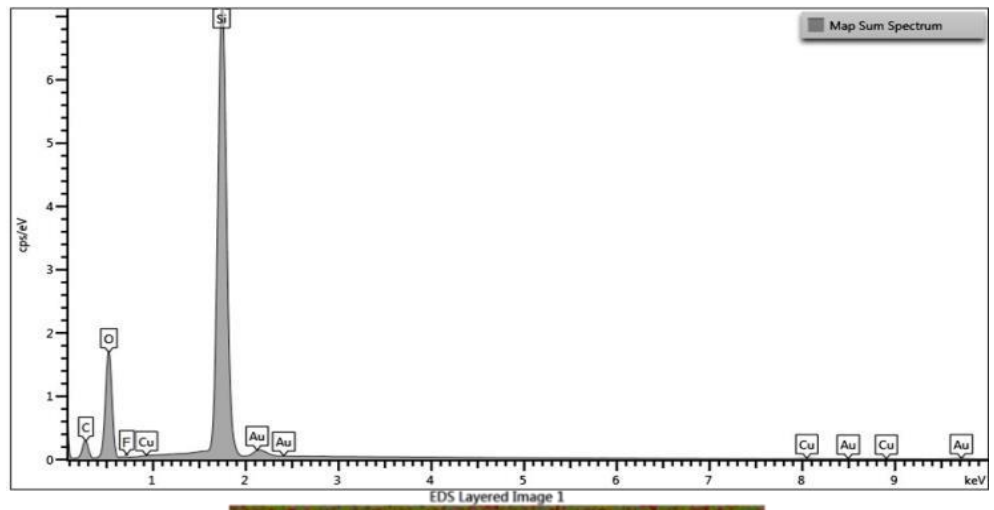
Figure 5-10 EDX mapping and spectroscopy for F-SBX-80 coating

5.3.2 Analysing ATR-FTIR results of F-SBX-80 sol-gel chemical composition

The information from the FTIR spectroscopy of the F-SBX on the coated substrate confirms the modified hybrid coating of F-SBX-80 Sol-gel formula bonding on AA2024 substrate as a dried gel on the metal surface. From Figure 5-12, the confirmation of chemical composition can be seen as the following the TEOS, MTMS, PFOTS and Deionised water were put as a control to see the changes in the new formula of F-SBX sol-gel.

Likewise, the FTIR of F-SBX-80 sol-gel has the broad fingerprint peaks similar to the basic formula SBX as mentioned previously in section 5.2.2   as apparent in the comparison FTIR as shown in Figure **5-4**.

The successful incorporation of the fluorinated precursor into the sol-gel was confirmed by comparing the infrared spectrum obtained from the F-SBX coating to the unmodified SBX-80.

The zoomed-in Figure 5-11, shows the presence of the C-F bonds can be confirmed by examining the IR spectral range between 1400-900 cm^{-1} indication of bending peaks of the C-F and C-F2 bonds which can also be detected by the presence of bands at 1140 and 1250 cm^{-1} is provided by the presence of the groups highlighted in the spectrum [150], [161].
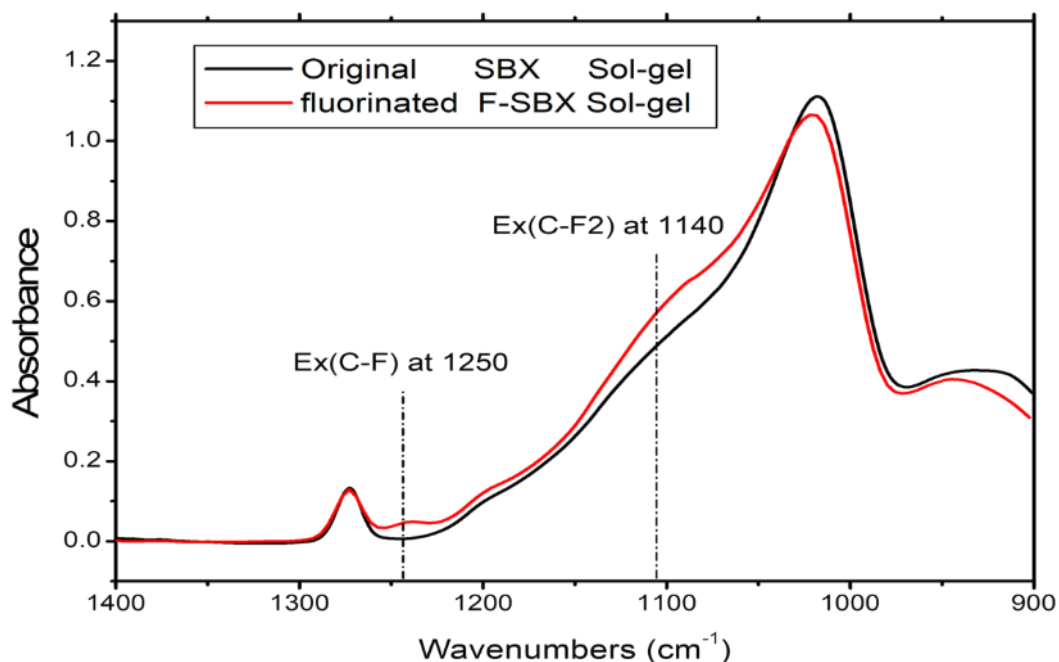
Figure 5-11 The zoomed-in FTIR spectra showing the effect of PFOTS addition to the unmodified SBX-80 sol-gel
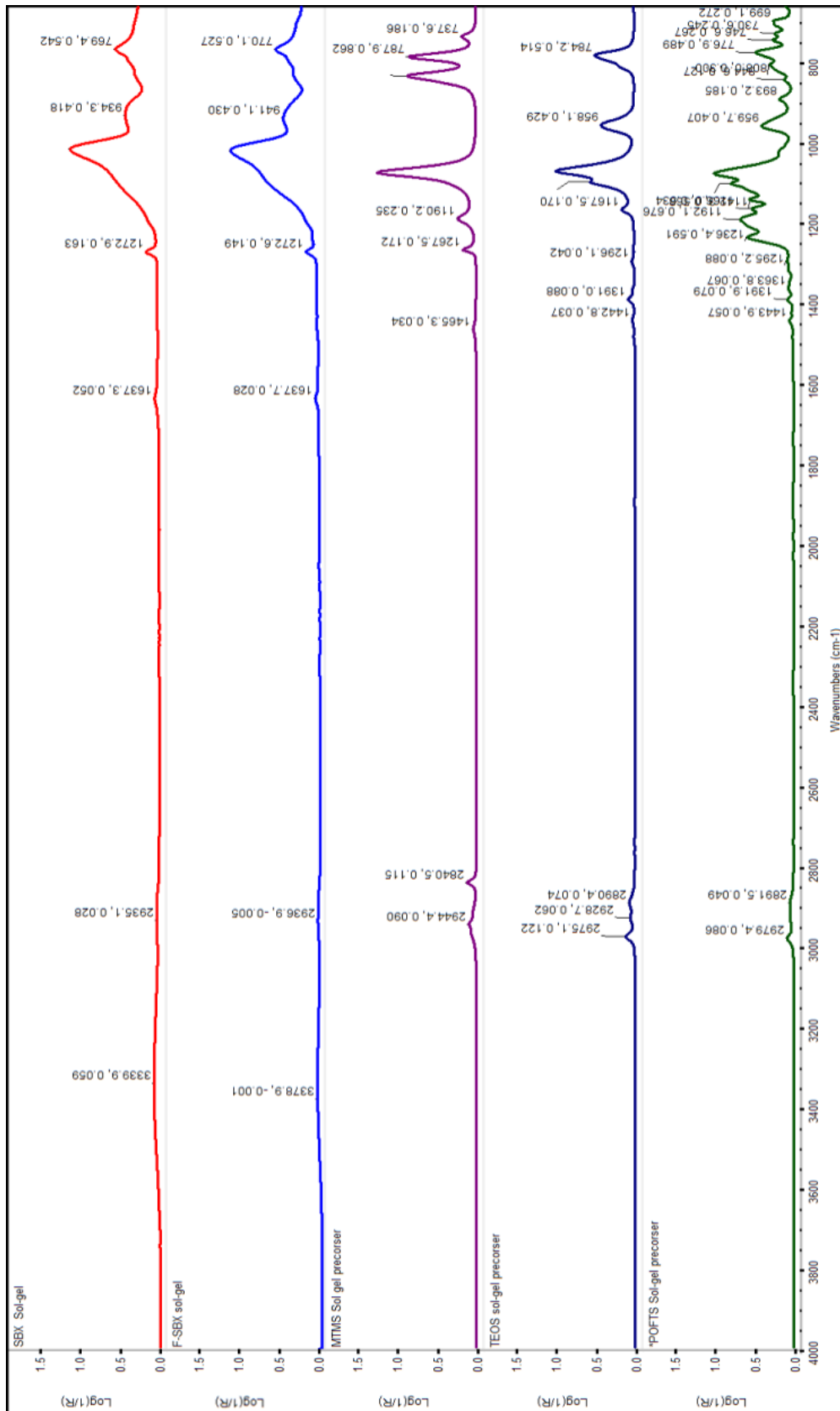
Figure 5-12 ATR-FTIR spectrum for precursors and F-SBX sol-gel on the AA2024 substrates

5.3.3 The water contact angle of SBX And F-SBX coatings

Figure 5-13 shows the WCA droplets on both coating systems presented by the typical bar chart mean values. In Figure 5-14 (a) the results of measured water contact angle (WCA) of the original SBX-80 coating was $67° \pm 2$, and as shown in (b) the WCA measurement on the modified F-SBX-80 Sol-gel coating was to change it to $118° \pm 2$. The higher water contact angle recorded for the F-SBX-80 shows that its wettability is lower than that of the SBX-80 as a result of increased hydrophobicity of the fluorinated F-SBX-80 coating [162].
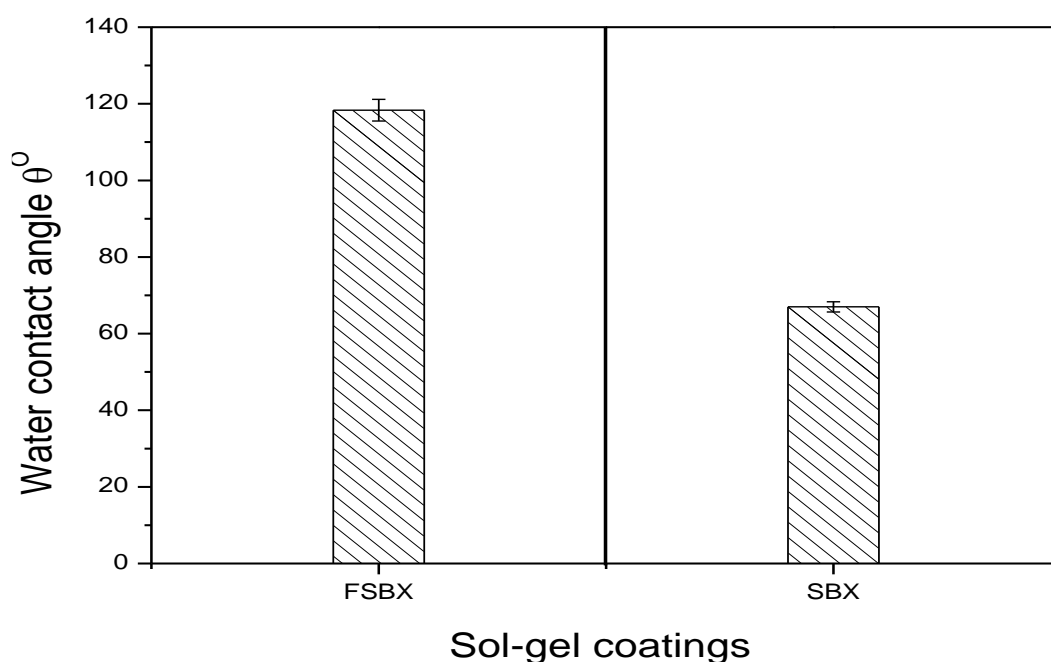
Figure 5-13 Bar chart showing mean values of WCA of F-SBX-80 and SBX-80 coatings
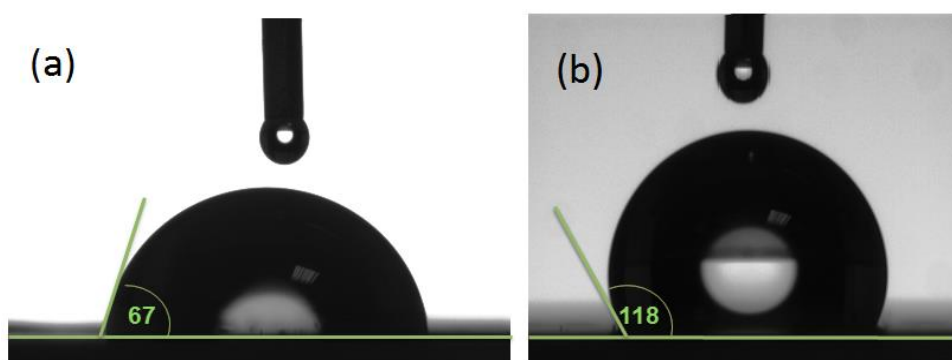
Figure 5-14 Optical images showing water droplets on (a) SBX-80 and (b) the modified F-SBX-80 sol-gel coatings

5.3.4 The topography of samples by atomic force microscopy (AFM)

Figure **5-15** shows the surface topography difference between SBX and F-SBX coating systems. AFM reveals the homogeneous for both coatings. However, the fluorinated functional group in PFOTS ($-CH_2CH_2(CF_2)_7CF_3$), has changed the surface morphology of modified sol-gel from the nearly smooth surface as shown in SBX-80 to the slightly rough surface with spherical humps as shown in F-SBX-80. These changes might have a role in increasing the hydrophobicity of F-SBX coating. The surface roughness Rz of SBX and F-SBX coatings is 4.8, 10.4 nm respectively.
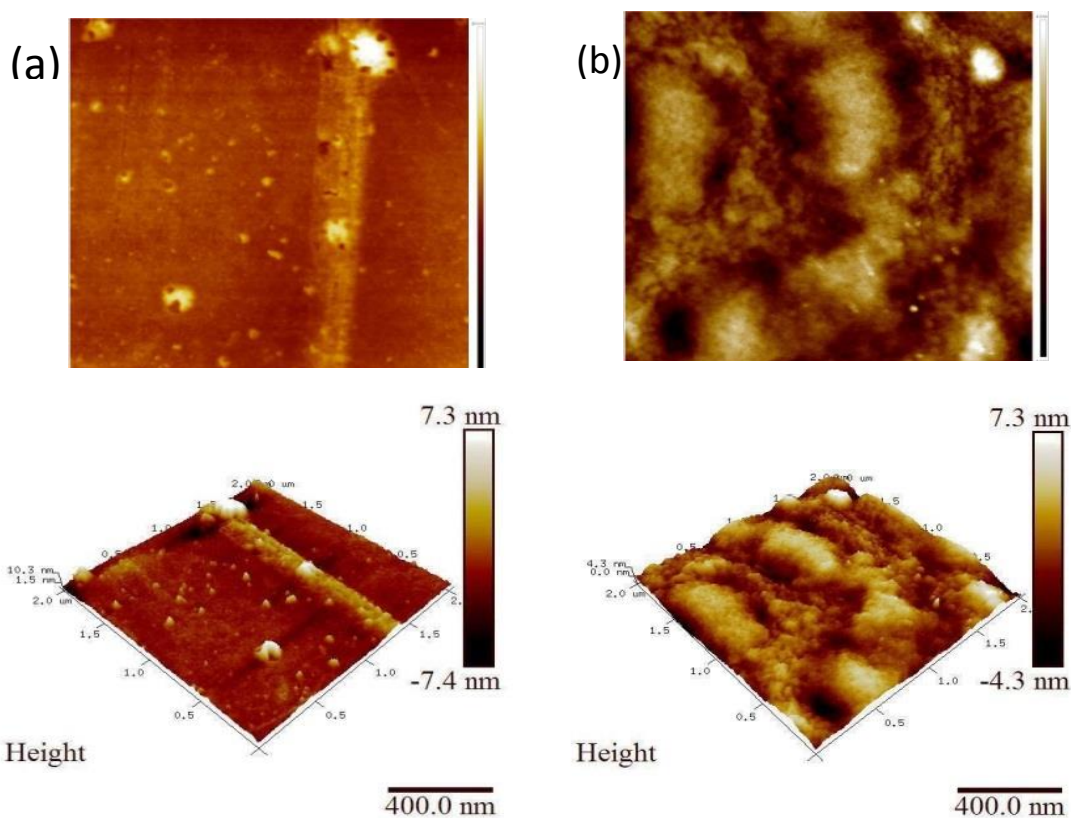
Figure 5-15 AFM images, showing the difference in morphology between (a) SBX and (b) F-SBX sol-gel surface

5.3.5 The Electrochemical impedance spectroscopy (EIS) for the fluorinated F-SBX-80 Sol-Gel coatings

Figure 5-16 and Figure 5-17 show impedance magnitude and phase angle plots for F-SBX-80. From the Impedance data for the F-SBX-80 coated substrates, as is shown in Figure 5-16, the general behaviour of the coating as a corrosion barrier coating can be detected from the EIS results. So, in the first hour of immersion exhibits reasonable impedance, starting at high frequency between 105 to 103 Hz in about 2.0×10^3 ohms. cm^{-2}, rising with sloping, showing coating capacitative behaviour. This was attributed to solution/coating interfacial resistance R_s. The higher magnitude was attributed to coating resistance Rct in the low frequencies between 10 to 10^{-2} Hz with value about 3.2×10^6 ohms. cm^{-2} .

At 48 hrs of immersion, it seems that the coating resistance started to be slightly decreased due to the normal diffusion and oxidisation of the metal surface but still considered in the same range when it compared to SBX coating. However, the drop of the impedance at higher frequencies is less than one magnitude which means the overall coating resistance is still working and providing good protection. Generally, it is decreased after 48 hrs of immersion to about 1.5×10^3 ohms.cm^{-2} in the range of high frequency which showed a low of protection to reach after 336 hrs about 1.2×10^3 ohms.cm^{-2}.

At low frequency from 10 to 0.01 Hz the impedance slightly decreased from the first hour to 336 hrs to reach about 1.02×10^6 ohms.cm^{-2} .This demonstrated the possibility of long-term protection of AA2024-T3 alloy from the direct corrosion.

Corrospondlly, the phase angle θ Figure 5-17 showed two time-constants. The first immersion hour was between 10^5 to 10^3 Hz and the second one between 10 to 0 .01Hz and these time-constants may be attributed from the created interfacial oxide layer. Likewise, from 48hr till 336hr kept the main two time-constants. The first one started from 10^5 to 10^3 Hz and the second one began from 10 to 0.1 Hz. These two time-constants are attributed to the same aluminium oxide film formed on the substrate [150].
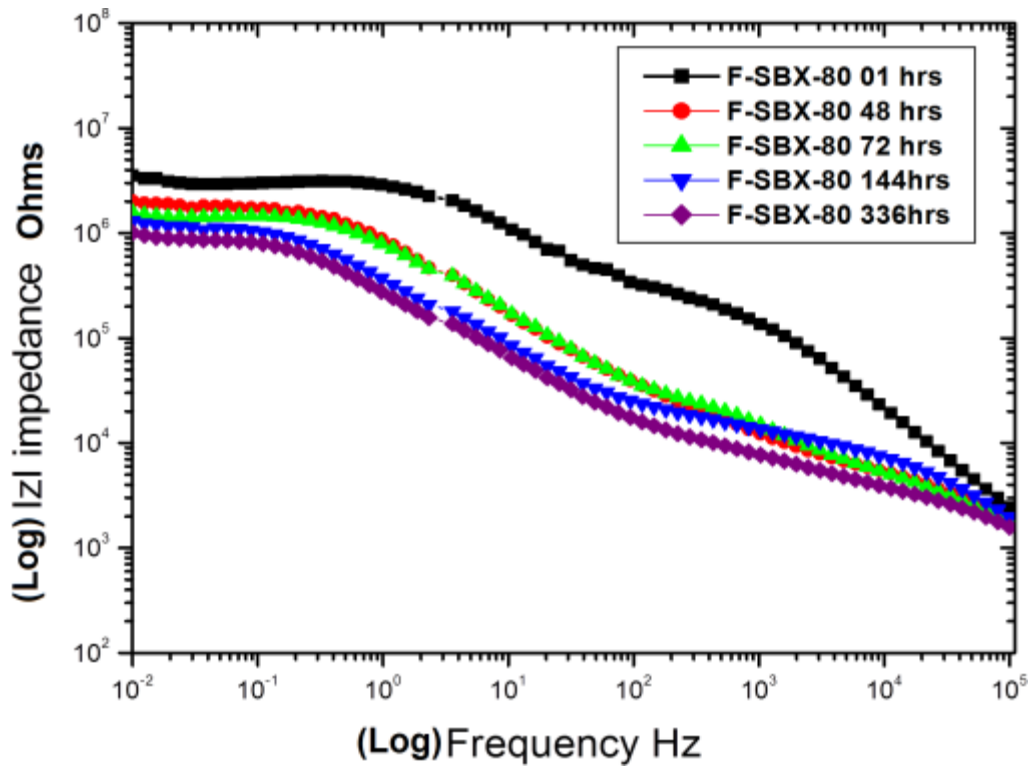
Figure 5-16 Impedance behaviour of F-SBX-80 sol-gel coating in 3.5% NaCl
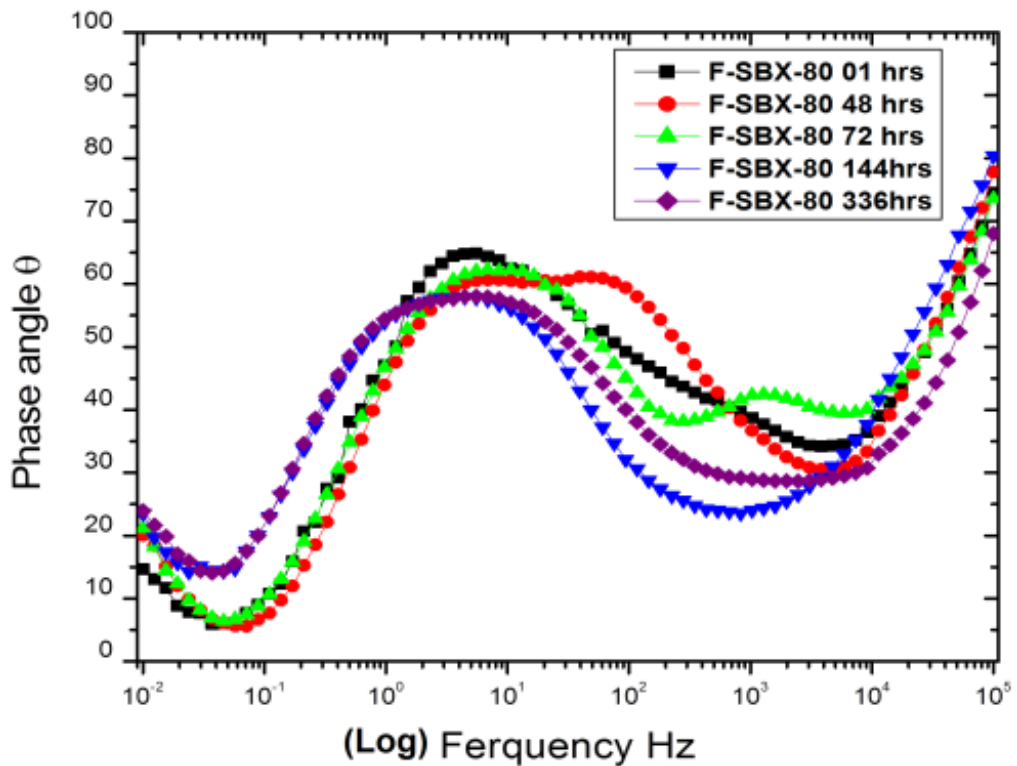
Figure 5-17 Phase angle response of F-SBX-80 sol-gel coated sample in 3.5% NaCl

This behaviour of protection of F-SBX sol-gel coating after 336 hrs in the period of the immersion was accompanied by the appearing of even surface substrate with no cracks until 360 hrs without pitting or corrosion under the coating film. After the 360 hrs of immersion, the surface examination exhibited that the F-SBX sol-gel coating is still providing and capable of keeping protection longer than the SBX coating, as it appears in Figure 5-18
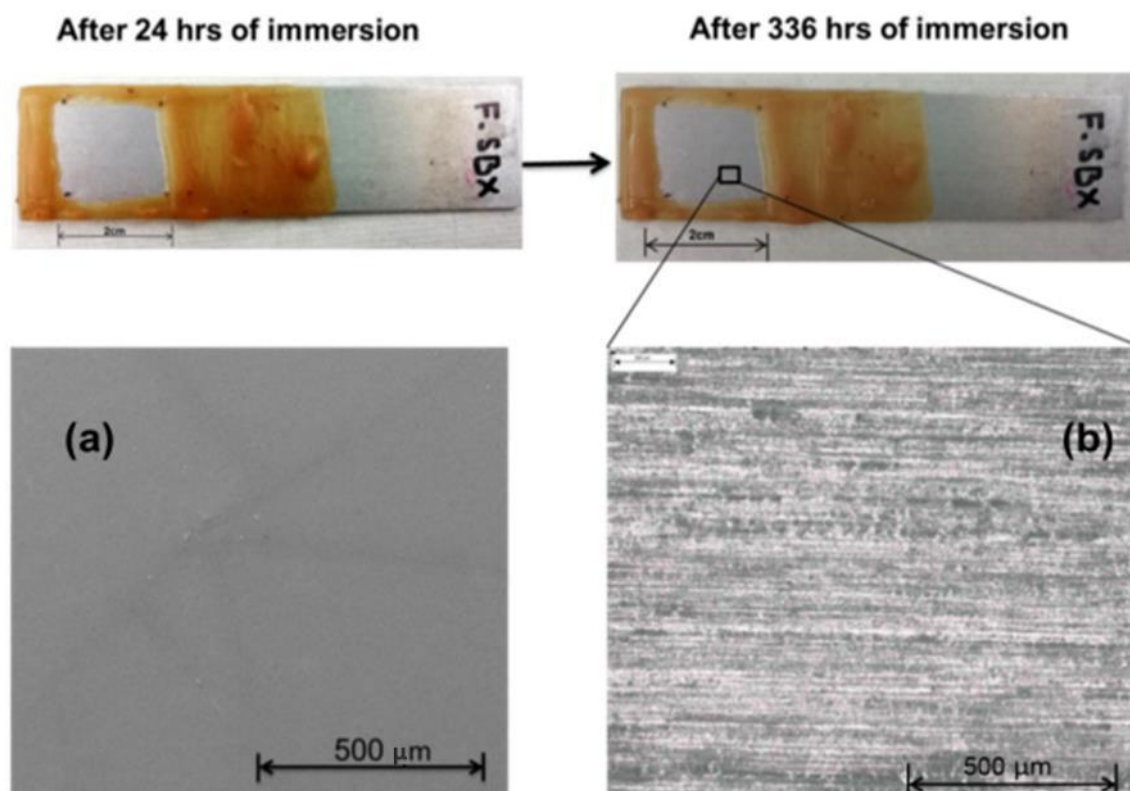
Figure 5-18 Shows no sign of cracks or pitting corrosion on the F-SBX Sol-gel coated sample after 336 hrs (a) SEM image and (b) IFM image

The EDX spectrum and mapping images of the tested F-SBX samples after 360 hrs confirmed that the F-SBX sol-gel coating on AA2024-T3 sample is still providing a good film on the surface of AA2024 substrate without the appearance of cracks and corrosion keeping the same chemical elements with insignificant change from the no-tested F-SBX sample, similarly when it compared to the changes in SBX and bare AA2024-T3 sample at the same testing period as is shown in Figure 5-19.
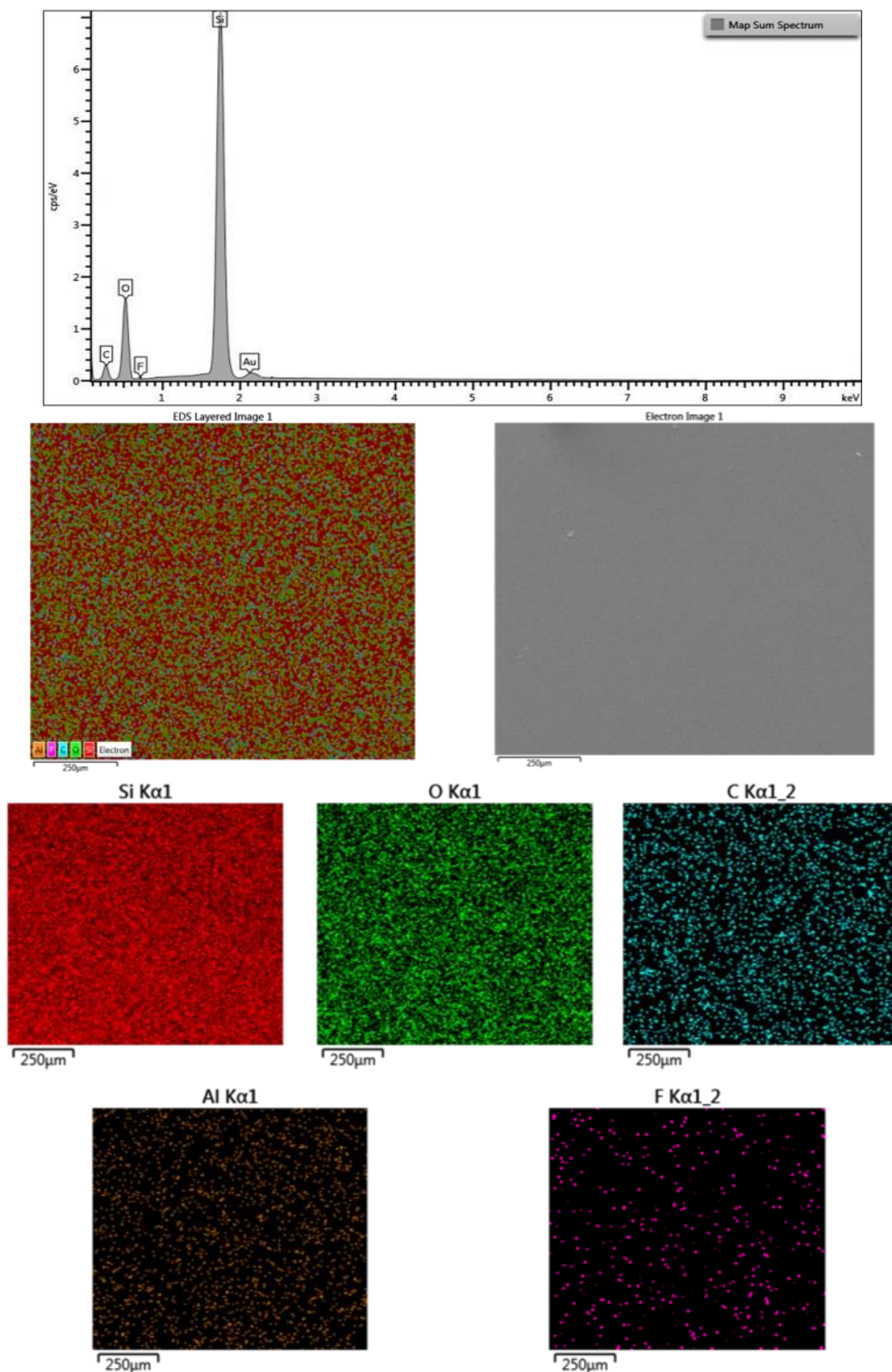
Figure 5-19 EDX spectrum and mapping images for F-SBX Sol-gel coated sample after

336 hrs in 3.5% NaCl solution

5.4 Analysing the enhancement on corrosion protection of F-SBX-80 and SBX-80 coated samples regarding bare AA2024-T3 samples

From Figure 5-20, the overall impedance was increased by approximately one order of magnitude for the F-SBX-80 coated samples compared to the SBX-80 samples, with impedance values of 4.1×10^6 and 6.8×10^5 ohms.m$^{-2,}$ respectively.
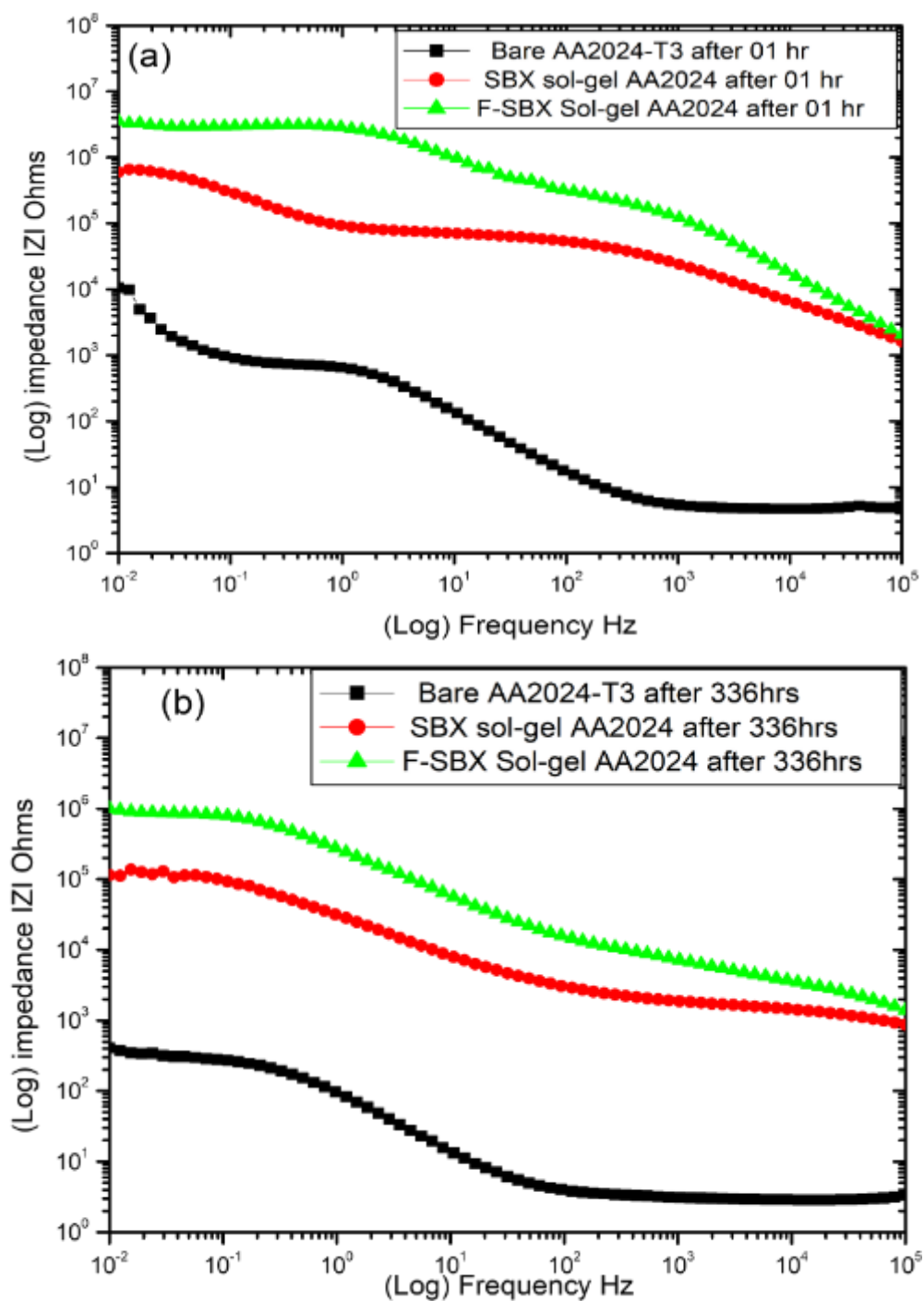
Figure 5-20 Impedance magnitude plots for F-SBX-80, SBX-80 and Bare-AA2024 samples

(a) in the first hour, and (b) after 336 hrs
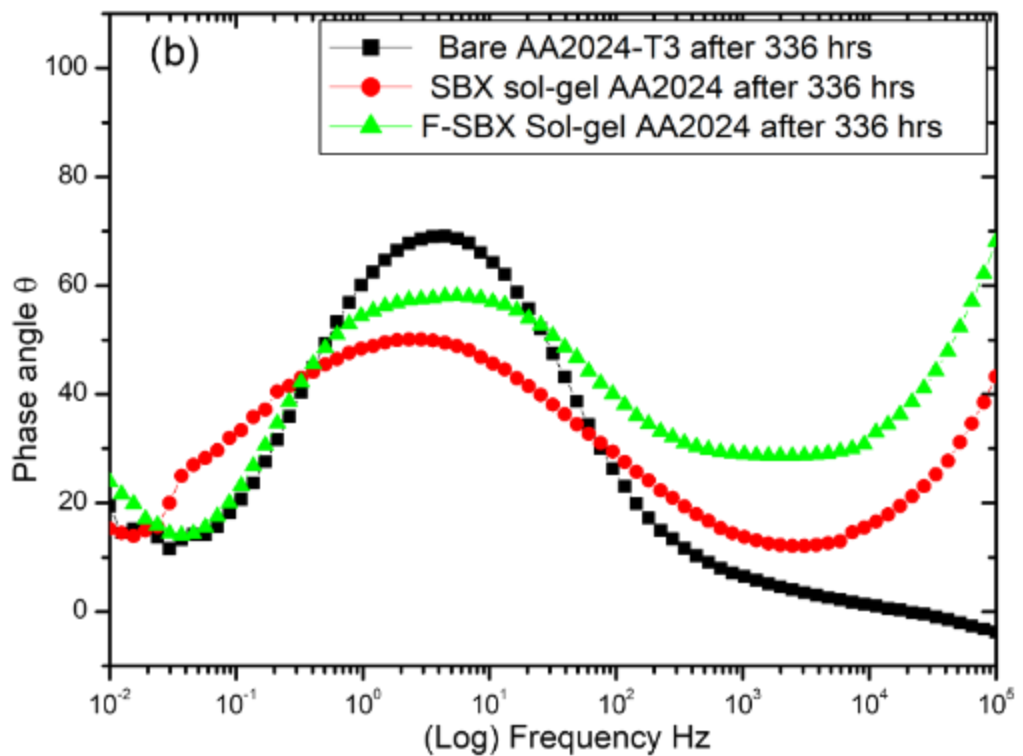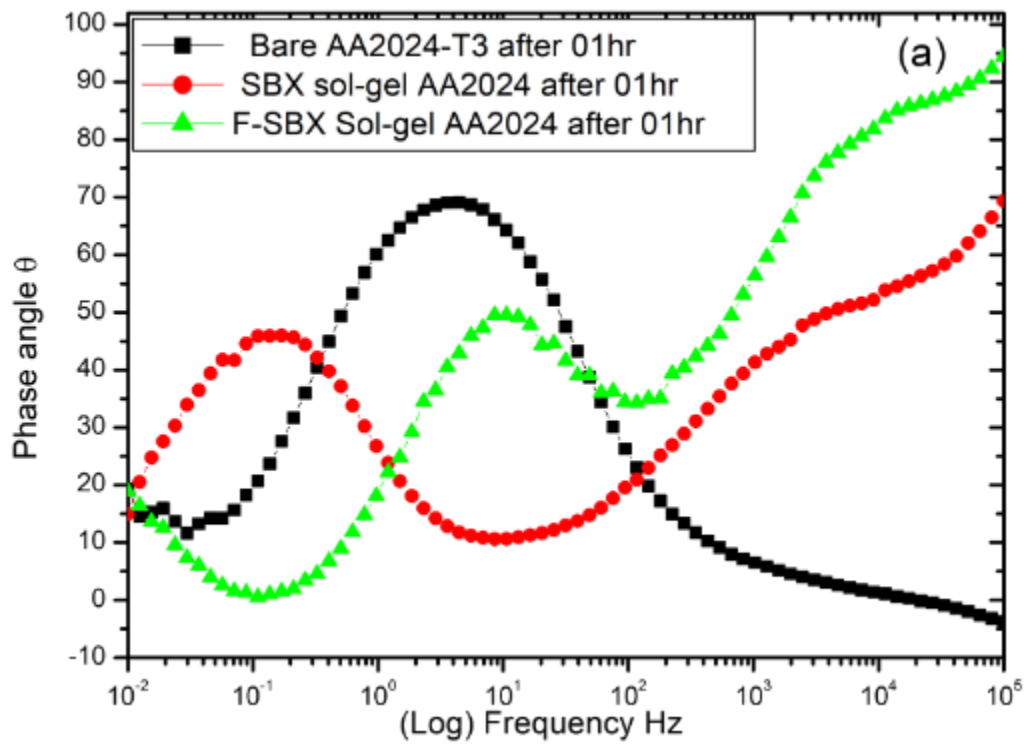
Figure 5-21 phase angle plots for F-SBX-80, SBX-80 and Bare-AA2024 samples

(a) in the first hour, and (b) after 336 hrs

After one hour the impedance curve for the F-SBX-80 sample reveals capacitive behaviour between frequencies 10^3 to 10^5 Hz, then the impedance slowly increased from about 6.0×10^5 ohms. cm^{-2} in the middle range of the frequencies and finally levelled-off at the same point in the low frequencies from 1.0 to 0.001 Hz.

Likewise, in the EIS measurements of the SBX-80 coated sample; a noticeable drop in impedance was detected to about 1.0×10^5 ohms. cm^{-2} after 14 days. The SBX coating is still revealed higher impedance compared to the bare AA2024-T3 substrate.

The phase angle plots in Figure 5-21 is acquired on the first day for both coating systems show that the F-SBX-80 and SBX-80 coated sample exhibit two semi-circles. After 48 hrs of immersion, the phase angle plot for the SBX-80 coated samples kept the presence of two time-constants. As well as, the F-SBX-80 coated samples also kept two time-constants until the 14th day of the test. The increased Rct values obtained from F-SBX are consistent with anodic inhibition obtained through a fluorine-influenced interface [150].

5.4.1 Investigating the corrosion protection behaviour for both SBX-80 and F-SBX-80 sol-gel coatings by using equivalent circuits and fitting and modelling

Figure 5-22 shows Nyquist plots for both SBX and F-SBX coatings in 01hr to 336 hrs. These plots were used to obtain and fitting the data to some models of equivalent circuits by using ZSimpwin electrochemical impedance spectroscopy (EIS) data analysis software.
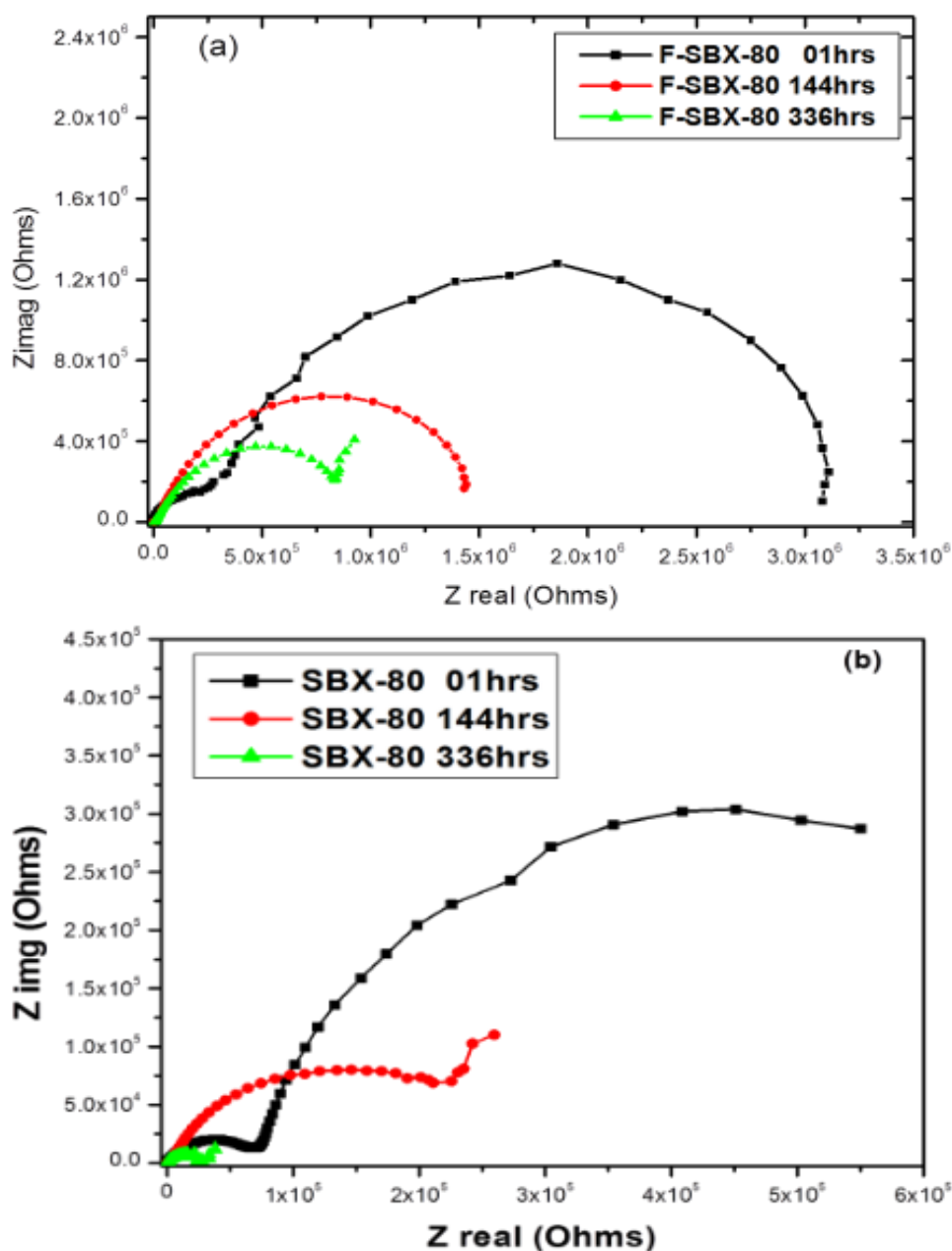
Figure 5-22 Nyquist plots for (a) F-SBX and (b) SBX sol-gel coatings

The fitting plots for F-SBX-80 and SBX-80 sol-gel for 01 hr, 48 hrs and 144 hrs EIS data were showed in Figure 5-23 and Figure 5-24, respectively.
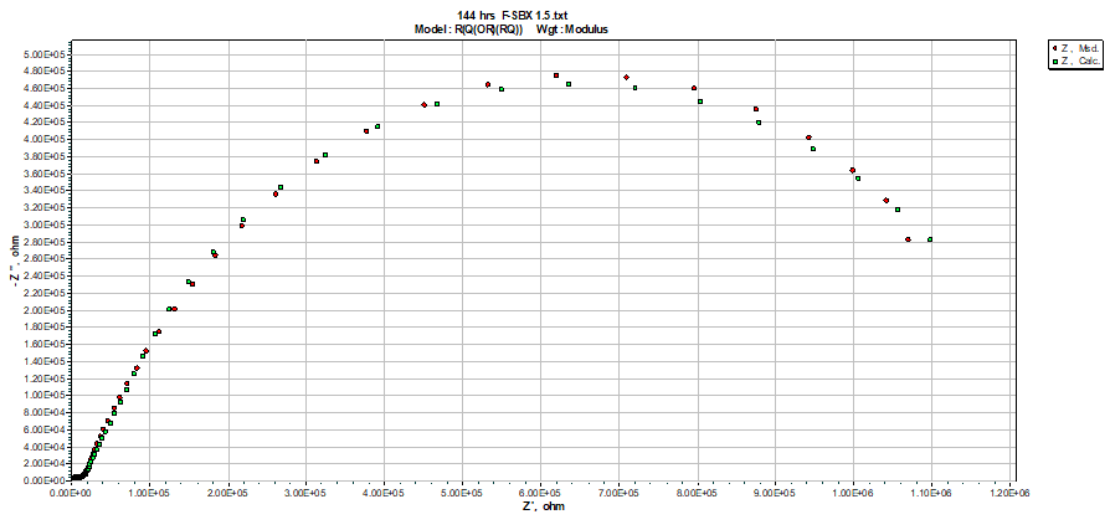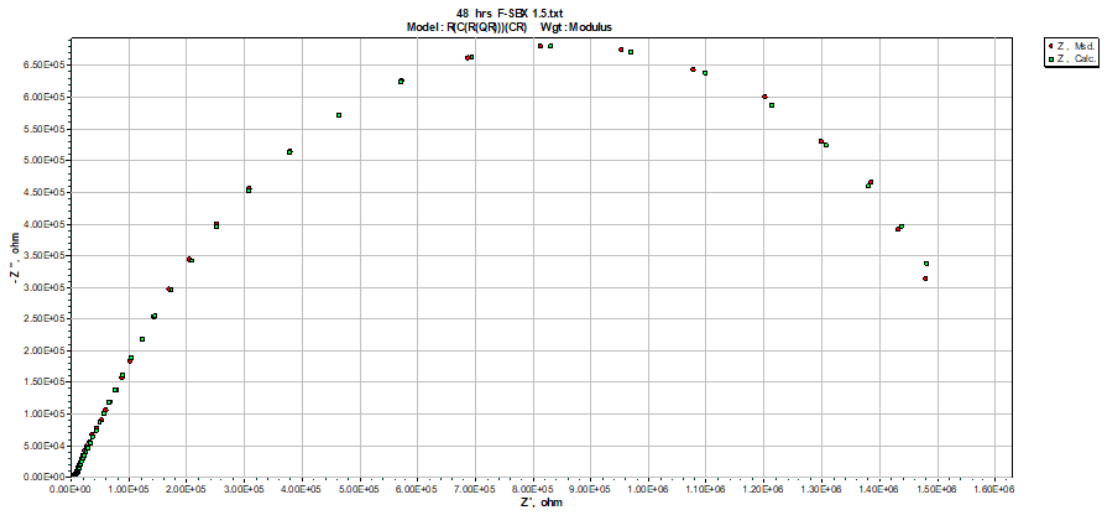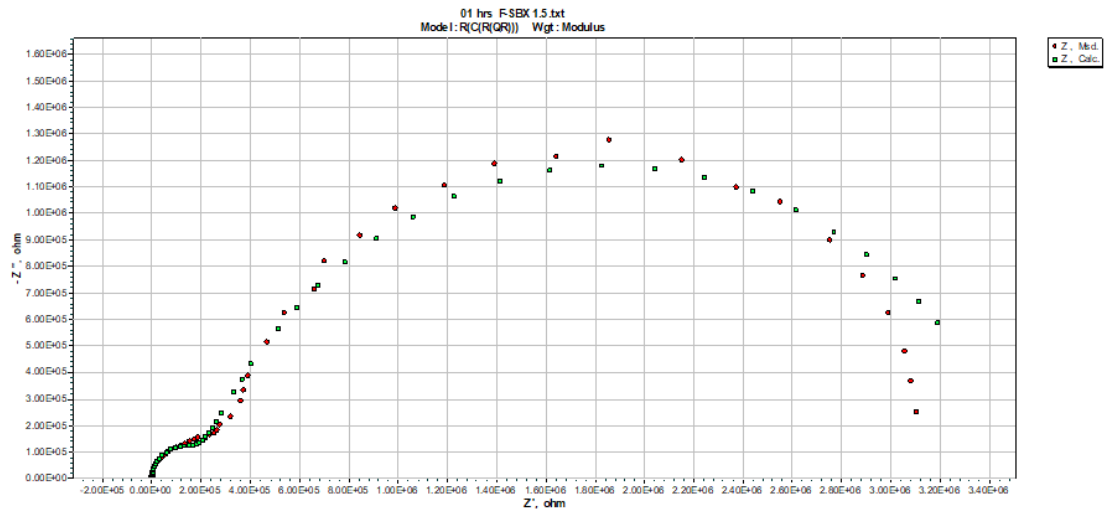
Figure 5-23 EIS data fitting for F-SBX-80 coating in 01hr, 48hrs and 144hrs
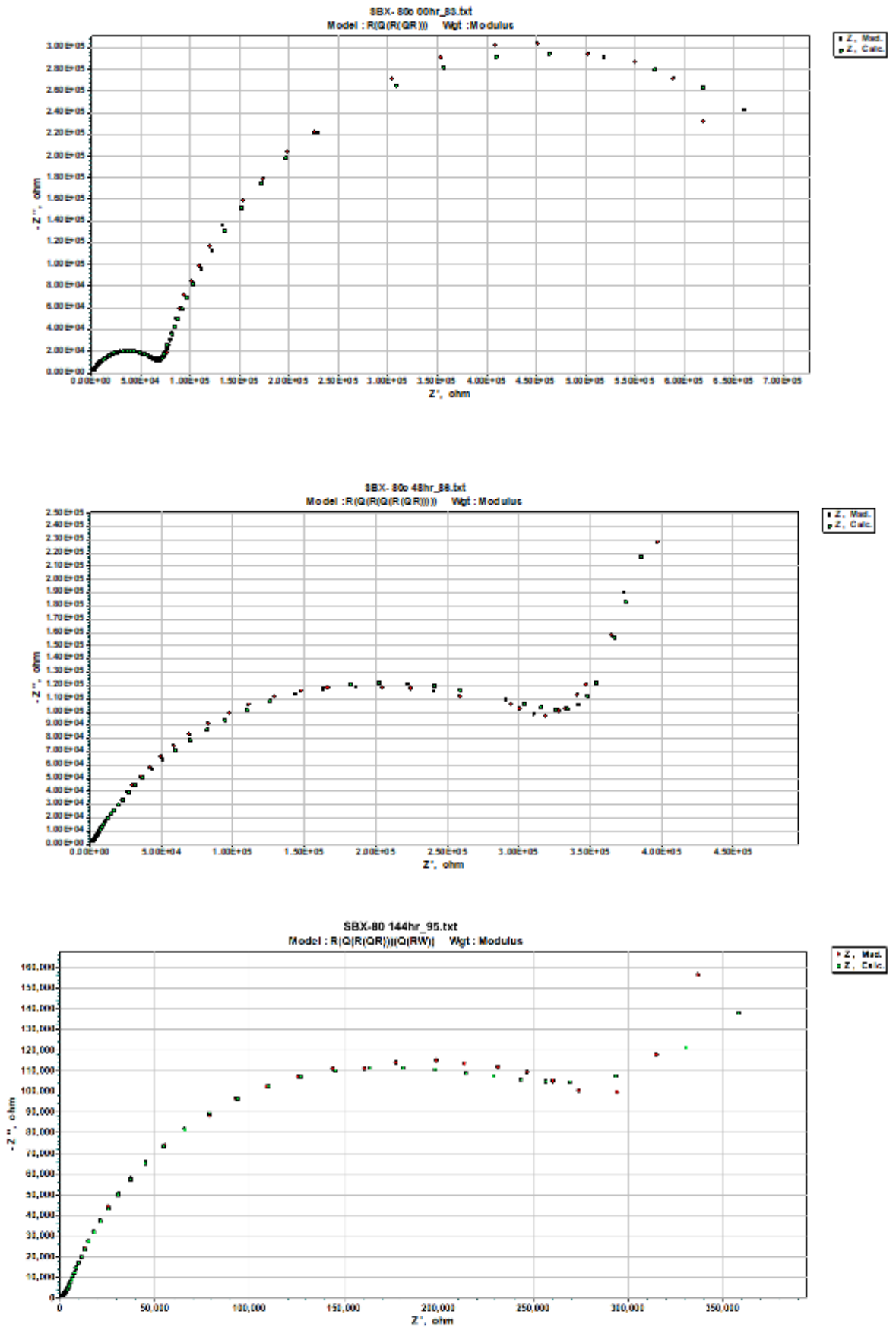
Figure 5-24 EIS data fitting for SBX-80 coating in 01hr, 48hrs and 144hrs

Table 5-4 and Table **5-3** below demonstrate the fitted data obtained from EIS spectra for the SBX-80 and the F-SBX-80 sol-gel coating after various immersion times in 3.5% w/v NaCl solution. The equivalent circuits were used to simulate the corrosion mechanism on the coated sample in 01 hr, 48hrs and 144 hrs. In these circuits, a time-constant element (Q), was used instead of an ideal capacitor C, to account for current leakage in the capacitor and/or frequency dispersion effect of the alternating current signals [107], [109].The suggested equivalent circuits for each of the EIS plots in 01hr, 48hrs and 144hrs were provided in Figure 5-26 and Figure 5-25.

Table 5-3 The fitted data obtained from EIS spectra for the F-SBX sol-gel coating after various immersion times in 3.5 wt. % NaCl solution.

Sample	Element	immersion time (h)		
		01	48	144
	Circuit	R(Q(R(QR)))	R(Q(RO)(QR))	R(Q(RO)(RQ))
	R_s	10	18	45
	Q_{ct}	8.913E-10	9.326E-10	1.915E-9
	n	1	1	0.900
	R_{ct}	2.220E6	6.522E04	3.776E4
	O_{ct}	-	2.823E-7	4.866E-7
	B	-	0.469	0.618
	Q_{iL}	3.800E-8	1.103E-7	3.592E-7
	n	0.772	0.803	0.800
	R_{iL}	3.319E6	9.675E5	2.136E4

Table 5-4 The fitted data obtained from EIS spectra for the SBX sol-gel coating after various immersion times in 3.5% w/v NaCl solution.

Sample	Element	immersion time (h)		
		01	48	144
	Circuit	R(Q(R(QR)))	R(Q(R(Q(RW))))	R(Q(R(Q(RW))))
	R_s	100	205	195
	Q_{ct}	1.085E-7	2.059E-7	6.1181E-6
	n	0.649	0.800	0.752
	R_{ct}	7.294E4	817	110
	Q_{iL}	4.934E-6	1.236E-6	9.815E-6
	n	0.827	0.800	0.818
	R_{iL}	7.790E5	3.504E6	1.475E5
	W_{iL}	-	2.317E-5	8.084E-5

The elements used for the equivalent circuits were: solution resistance (R_s), coating resistance (R_{ct}), coating constant phase elements (Q_{ct}), intermediate oxide layer resistance (R_{iL}), intermediate oxide layer capacitance (Q_{iL}), fininte Warburg-circuit element (O) and Warburg-circuit element (W) [151] as all mentioned in the experimental Chapter in section 3.1.3 .

At the first hour of immersion, both samples illustrate the same behaviour with three resistance and two time-constants respectively, as shown in Figure 5-26 (a) and (c). However, after 48 hours of immersion both coated samples SBX and F-SBX started behaving individually. SBX-80 coating results indicate that there are two time-constants. The first one arises in the high-frequency range and may be attributed to electrolyte diffusion resistance in the coating, the second one is due to barrier properties of the coating, the third one may be attributed to Warburg-circuit element (W) as result of diffusion on substrate surface as shown in Figure 5-26 (d). On the other hand, the F-SBX-80 coated sample kept two time-constants with a fininte Warburg-circuit element (O) as shown in Figure 5-26 (b). This (O) element is thought to originate from the hydrophobic nature of the fluorinated group (-$CH_2CH_2(CF_2)_7CF_3$), which prevents the diffusion of electrolyte into the fluorinated coating.
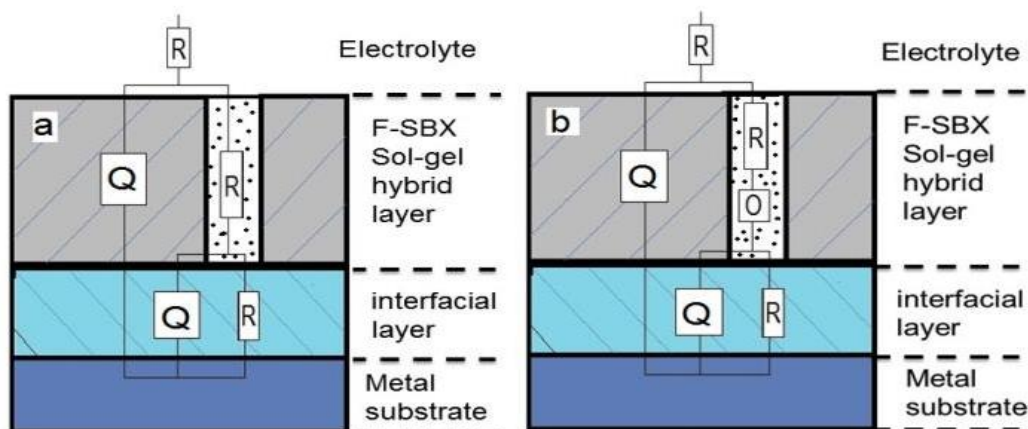
Figure 5-25 the modelling of F-SBX-80 (a) in the first hour, (b) after 144 hrs
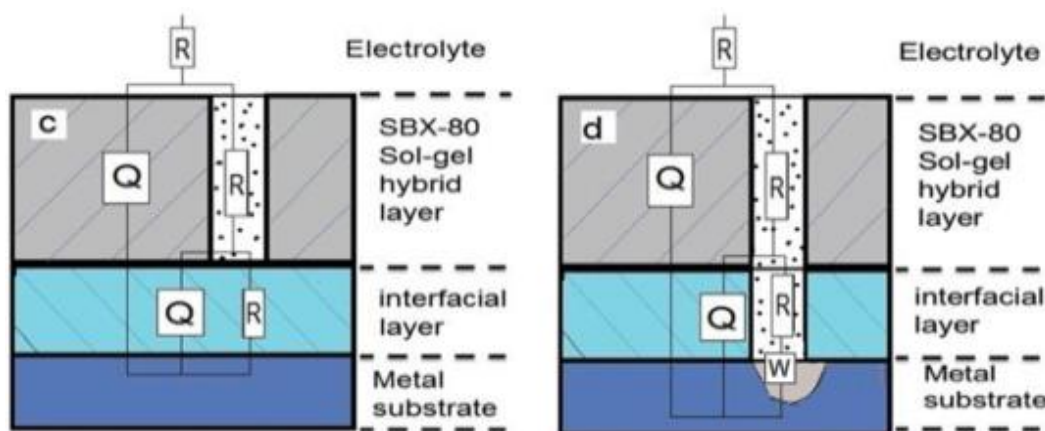
Figure 5-26 the modelling of SBX-80 (c) in the first hour, (d) after 144 hrs

As can be seen, the behaviour of SBX-80 coating initially subjugated by two semi-circles, which represent the resistance of the coating and interfacial layers. As immersion time increases, the resistive nature of the coating reflected the onset of degradation.
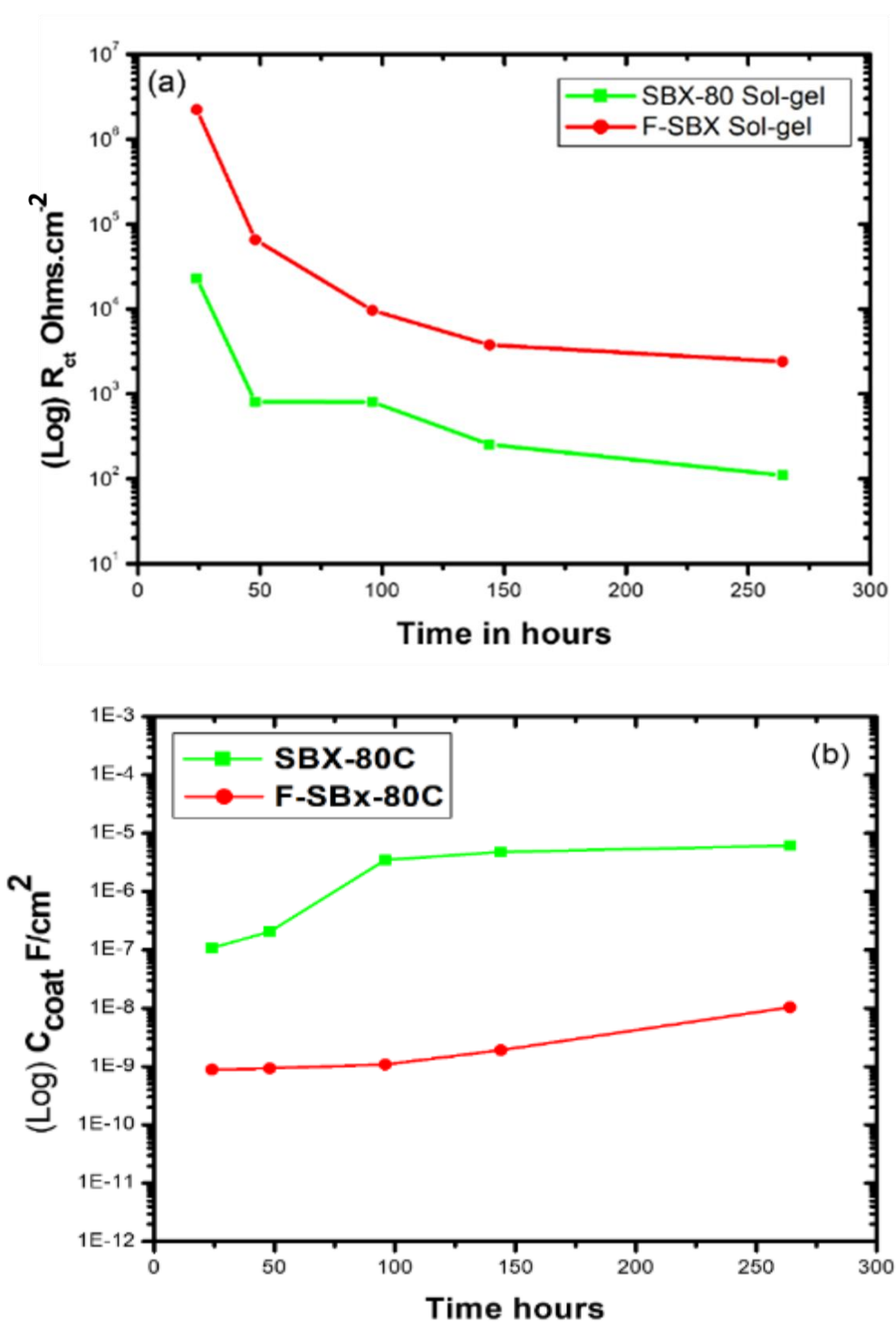
Figure 5-27 Graphs showing (a) Coating Resistance (R_{ct}) and (b) Coating constant phase elements (C_{ct}) for both SBX-80 and F-SBX-80 sol-gel Coatings

The deterioration of the corrosion protective characteristic of the coatings was studied between 24 and 336 hours in immersion, as shown in Figure 5-27.

A value of R_{ct} of F-SBX at the first hour of immersion started from an initial amount of 2.22×10^6 ohms.cm^{-2} then after 48 hrs was dropped to 6.8×10^4 ohms.cm^{-2}, then it was relatively dropped after 96 hrs to reach about 4.0×10^3 ohms.cm^{-2} at the end of the test. These resistances have a corresponding coating constant phase element (Q_{ct}) with capacitance behaviour of 1.08×10^{-7} and 8.91×10^{-10} F.cm^{-2} for SBX-80 and F-SBX-80 respectively after one hour of immersion. Due to the degradation of coating, the SBX-80 coating capacitance increases after 144 hrs of immersion to 4.7×10^{-6} F.cm^{-2} [103]. On the other hand, the F-SBX-80 showed levelling off in the same magnitude about 2.6×10^{-9} F.cm^{-2}.

The coating resistance (R_{ct}) of the SBX-80 coating in the First hour of immersion, was about 7.3×10^4 ohms.cm^{-2} is approximately one order of magnitude less than the F-SBX-80 sol-gel coating; it indicates that the SBX-80 coating samples still have a satisfactory coating resistance. However, after 48 hours, the coating resistance of the SBX-80 coating decreased markedly to 8.0×10^2 ohms.cm^{-2}, before continuing to decline throughout the remainder of the test to reach 1.1×10^2 ohms.cm^{-2}. As exposure time increase, the reduction is due to the microcracking and diffusion of the SBX sol-gel coating.

5.4.2 The Effect of prolonged water exposure on both coating films

FTIR technique was used for comparing the response of rehydration of SBX-80 and F-SBX-80 sol-gel films in an aqueous environment (3.5% v/v NaCl solution) for five days to assess the relative water uptake of both.

The evaluation was made by examining the differences in the OH stretching region between 3000 and 3400 cm^{-1}. Figure 5-28 (a) shows a noticeable change in the OH stretch after immersion for the unmodified SBX-80 coating, which can be attributed to water uptake.

By comparison, Figure 5-28 (b) shows that insignificant changes were observed in this region in the case of the fluorinated F-SBX-80 coating. This suggests that there was minimal water uptake by the fluorinated coating which related to the hydrophobic properties of this coating.
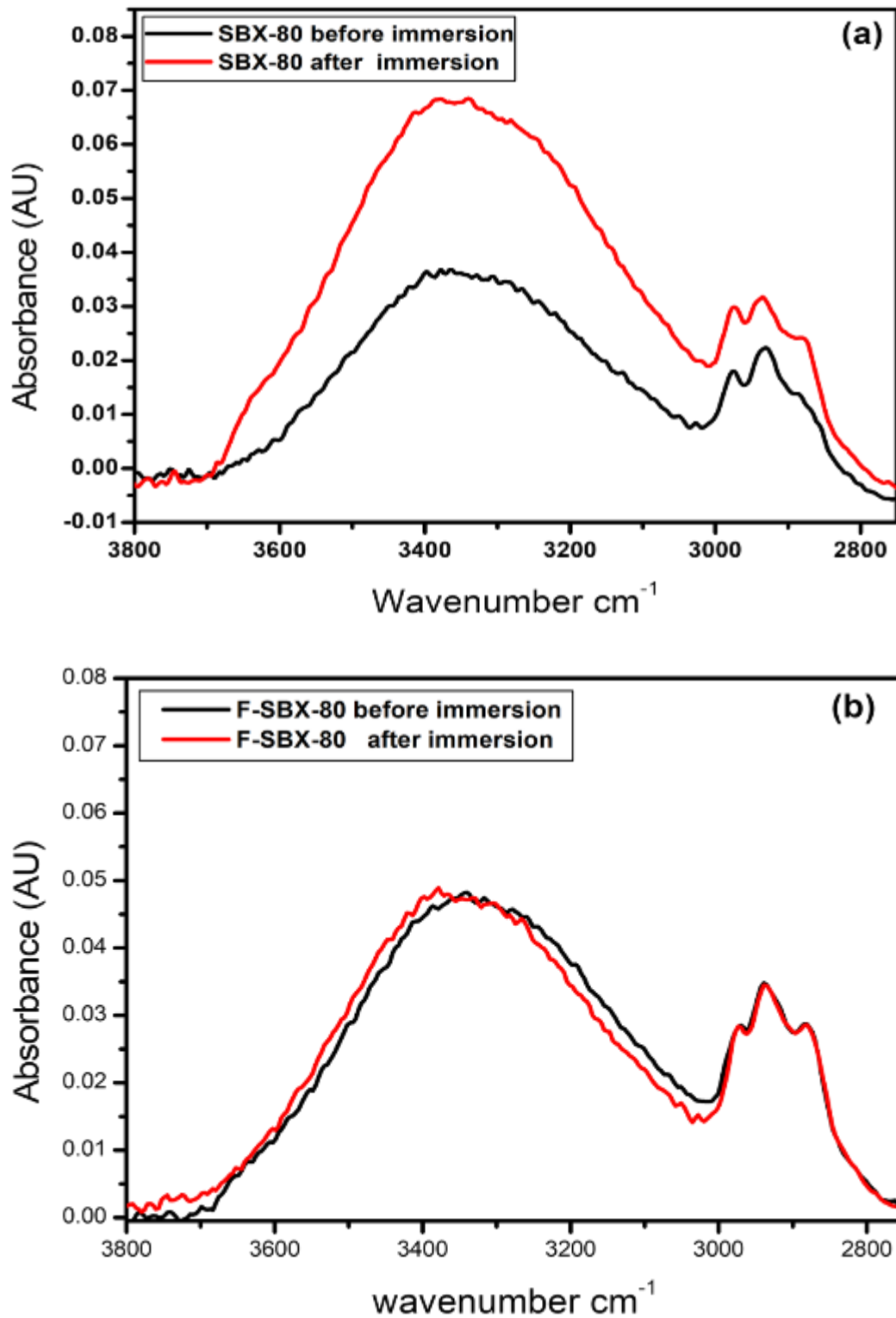
Figure 5-28 ATR-FTIR spectra showing the change in the OH stretch region before and after water immersion for (a) SBX-80 and (b) F-SBX-80 coatings

5.4.3 Crack Growth observations after Long Immersion

Both sol-gel coated samples SBX-80, and F-SBX-80 demonstrated an ability to provide corrosion protection to the aluminium alloy substrate. Visual examination of samples

immediately after immersion showed no apparent degradation or damage to the coating. After longer immersion times (greater than five days), Figure 5-29 (a) and (b) exhibited the SBX-80 coating was susceptible to the formation of microcracks when dried in ambient atmospheric conditions. The cracks were observed to be around 1-8 µm wide on the surface. Exposure of the aluminium alloy substrate as a result of coating cracking has the potential to detrimentally affect the subsequent corrosion protection, having implications for situations where wet/dry cycling is experienced. By comparison, the F-SBX-80 coating showed excellent resistance to cracking under similar circumstances, as shown in Figure 5-29 (c) and (d). The contact angle measurements showed that the F-SBX-80 was more hydrophobic than the SBX-80, while the FTIR confirmed that the unmodified sol-gel had a higher propensity for water uptake. The presence of water in the film could lead to swelling and loss of coating-substrate adhesion, leading to the cracking observed in the case of the SBX-80.
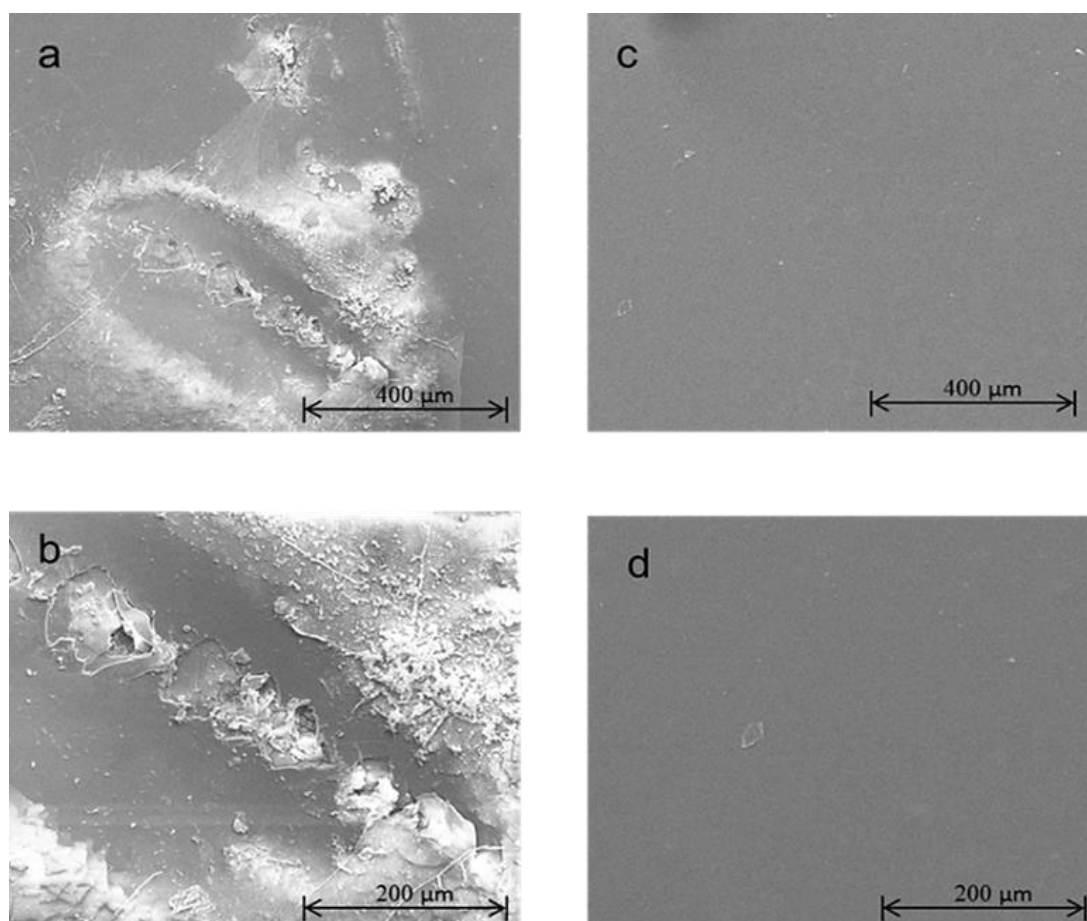
Figure 5-29 Secondary electron SEM micrographs of the immersion effect on both coatings (a), (b) SBX-80 and (c), (d) F-SBX-80

5.5 Fifth Chapter Summary

Both organic-inorganic hybrid sol-gel coatings SBX and F-SBX provide good protection on the aluminium alloy AA2024-T3 in 3.5% NaCl solution.

It is noticeable; the fluorinated additive (PFOTS) increased hydrophobicity and also was enhanced the corrosion protection of the base formula SBX sol-gel, by reducing the possibilities of diffusion in the electrolyte in pores of the coating to the metal surface.

This technique was making sol-gel coating more durable and easier to use as a monolayer or as a top coating with easy-cleaning properties. The mechanical and crack resistance was enhanced for the modified fluorinated coating. However, the protection from these sol-gel formulae alone is not enough in the long run, and it needs a combination of inhibitors to make it maintain longer.

Chapter 6- Study the Enhancement to Corrosion Protection By Adding Film-Forming Corrosion Inhibitors to SBX Organic-Inorganic Hybrid Sol-Gel Coating

<div align="center">**Overview**</div>

Three sets of results are presented and discussed. The first set investigates the corrosion protection of the hybrid organic-inorganic sol-gel coatings SBX formula containing benzimidazole (BZI) on AA2024-T3 alloy substrate. These modified coatings are labelled as BZI-SBX 80 sol-gel.

The second will present results and discussion around the corrosion protection of coatings produced by adding oleic acid (OA) to the same SBX formula, then applying it on AA2024-T3. This coating is labelled as OA-SBX 80 sol-gel.

The third part will present the results of double-layer sol-gel coatings, first one sol-gel with benzimidazole and the second one with the oleic acid and applied on AA2024-T3 alloys. This coating is labelled as BZI-OA-SBX 80 sol-gel.

The corrosion protection performance of organic-inorganic hybrid sol-gel coating with inhibitors when applied to aluminium alloy 2024-T3 substrates was investigated using Potentiodynamic polarisation (PDPS), electrochemical impedance spectroscopy (EIS), infinite focus microscopy (IFM), scanning electron microscopy (SEM) with Energy-dispersive X-ray spectroscopy (EDX) analysis and water contact angle (WCA). The test samples were coated with sol-gel on one side then dried for 4 hours at 80° C. The sample identification is given in Table 6-1

Table 6-1 Inhibitor-modified sample identification table

No.	Identifier	The base of Sol-gel	Benzimidazole BZI v/v%	Oleic acid OA v/v%
1-	**BZI-SBX-80**	TEOS+MTMS+PSX	3.5%	Nil
2-	**OA-SBX-80**	TEOS+MTMS+PSX	Nil	0.1%
3-	**OA-BZI-SBX-80**	TEOS+MTMS+PSX	3.5%	0.1%
4-	**Bare AA2024-T3**	Nil	Nil	Nil

6.1 Potentiodynamic polarization scanning (PDPS)

The potential dynamic polarisation-scanning test (PDPS) is performed on samples with three sets of sol-gel coatings modified with tow film-forming inhibitors of BZI and OA as mention above.

Polarisation curves of four sol-gel coated samples and a bare sample are shown in Figure 6-1; Generally, all coated samples displayed remarkable performance properties compared to the bare AA2024 sample.
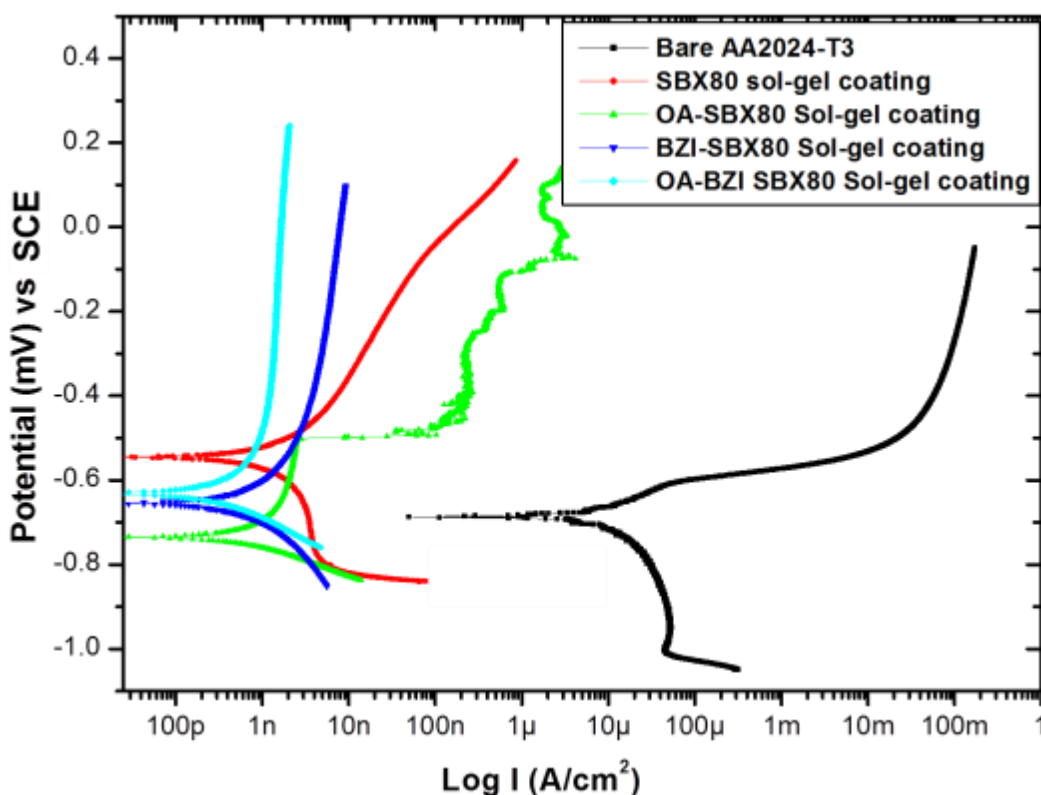
Figure 6-1 (**PDPS**) **Polarization curves for the bare and sol-gel coated samples with different organic inhibitors in 3.5% NaCl**

The corrosion potential (E_{corr}) and corrosion current density (I_{corr}) were obtained as shown in Figure 6-1 and Table 6-2 by extrapolation of cathodic and anodic curves using the Tafel extrapolation method.

Generally, the current density on the cathodic branch of Tafel curve for all sol-gel coated samples is reduced by more than four magnitudes when compared to the bare AA2024-T3.

Nevertheless, from the anodic polarisation curve, the behaviour of four types of coatings were distinct from each other. This is due to the type of inhibitors. Starting with the double-layer of benzimidazole sol-gel / oleic acid sol-gel system which is coded as BZI-OA-SBX-80 displayed the greater reduction, being eight orders of magnitude lower of current density.

The benzimidazole sol-gel only BZI-SBX-80 coated sample comes second, as it reduced by seven orders of magnitude to bare AA2024-T3 this is attributed to the surface-active and high electronegativity of benzimidazole [64].

On the other hand, the sol-gel with oleic acid inhibitor sample only OA-SBX-80 sol-gel showed less protection on the anodic branch, reveals the failure in protection in the potential of -502 mV due to the initiate of pitting and coating failure, this reducing is about four orders of magnitude less than the bare AA 2024-T3.

The SBX-80 sol-gel only showed a reduction in the anodic branch by about four and a half orders of magnitude less than the bare AA 2024-T3.

The information that obtained from the figure of Corrosion current densities of bare and sol-gel coated samples were reduced to $2.92 \times 10^{-10} \text{A/cm}^2$ for (BZI-OA-SBX80) , $5.98 \times 10^{-10} \text{A/cm}^2$ for (BZI-SBX-80), $9.8 \times 10^{-10} \text{A/cm}^2$ for (OA-SBX-80) and $1.1 \times 10^{-9} \text{A/cm}^2$ for (SBX-80) respectively, and as compared to $7.1 \times 10^{-6} \text{A/cm}^2$ of the bare AA2024-T3 alloy. The corrosion potential shifted to more positive values for coatings containing BZI and more negative values for those containing oleic acid.

The shift in E_{corr} indicates that the anodic is inhibited to a greater degree than the cathode in BZI-OA-SBX 80 and BZI -SBX 80 sol-gel mixture. This can be attributed to the benzimidazole nitrogen active atoms bridging to the substrate surface [64], [67]. Also, can be attributed to oleic acid can clog pores by increasing the hydrophobicity in the filled pores which contribute to a reduction in the electrolyte diffusion to the surface of the substrate [76], [77].

Table 6-2 PDPS polarisation data for bare and Sol-gel coated samples with inhibitors

Sample	E_{corr}[mV](Vs SCE)	I_{corr} [A/cm^2]	OCP [mV] (Vs SCE)
Bare-AA2024-T3	-662 ± 2	7.10×10^{-6}	-650
SBX-80 Sol-gel	-608 ± 2	1.10×10^{-9}	-708
OA-SBX-80 sol-gel	-735 ± 2	9.60×10^{-10}	-672
BZI-SBX-80 Sol-gel	-651 ± 2	5.98×10^{-10}	-482
BZI-OA-SBX-80 sol-gel	-647 ± 2	2.92×10^{-10}	-509

6.2 The Effect of Adding the Benzimidazole only to the base organic-inorganic hybrid SBX Sol-Gel coating

In common issue with many sol-gels formulas, the drawback of using the SBX sol-gel alone is porosity [100], [163], [164], leading to ionic and electrolytic diffusion to the metal surface, which will make the sol-gel coating less durable if it is used as a single layer coating system without the presence of inhibitors. Therefore, enhancement was attempted to the base SBX-80 sol-gel coating by adding an organic corrosion inhibitor, benzimidazole (BZI). The modification was done on the SBX-80 formula by adding 3.5% v/v ratio of solution from1:1 Benzimidazole (BZI) in ethanol to the base SBX formula and this modified formula is coded as BZI-SBX-80 sol-gel.

6.2.1 Surface morphology and elements of modified BZI-SBX-80 sol-gel coating

The surface of BZI-SBX-80 sol-gel coating on the substrate was consistent and smooth, similar to the unmodified base SBX formula as shown in Figure 6-2 (a). As well as shown in Figure 6-2 (b) in the cross-section SEM image the thickness of the coating is about 16 µm ±2.
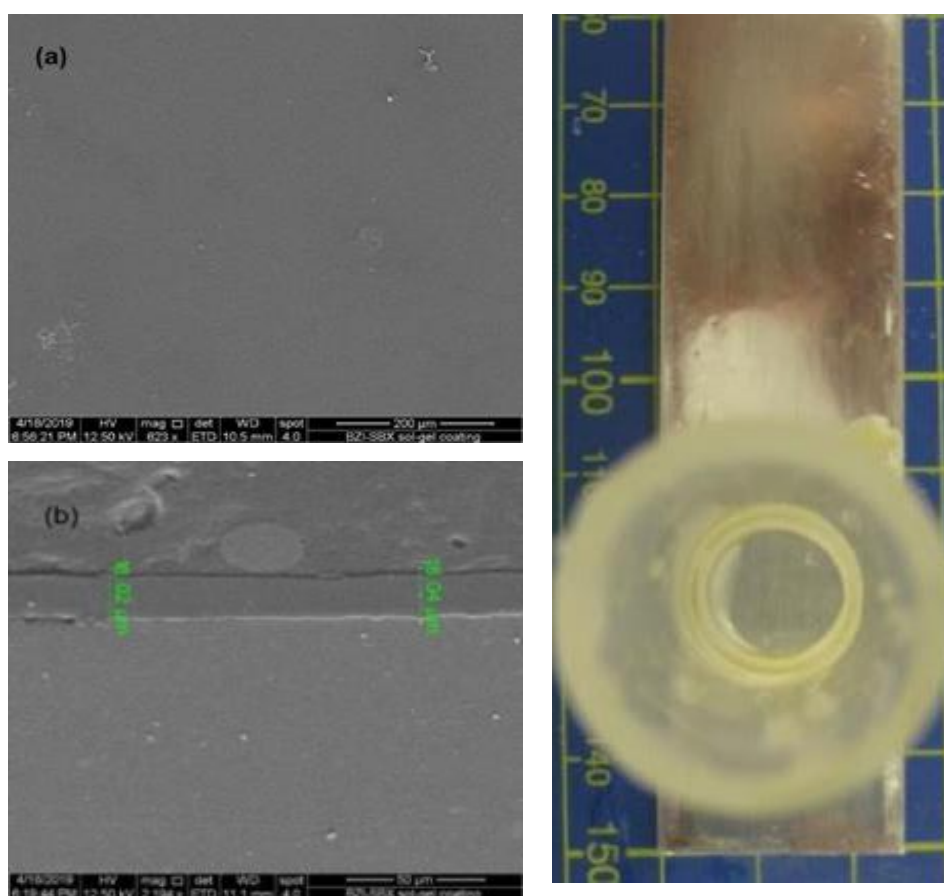
Figure 6-2 (a) surface morphology and (b) cross-section SEM images BZI-SBX-80 sol-gel sample

The EDX images and spectra in images of Figure 6-3 verifying the elemental composition of the sol-gel formula when coated on the AA 2024-T3 sample this showed silicon (Si), carbon (C), oxygen (O) and an amount of Nitrogen (N) reflects the small percentage of benzimidazole inhibitor in sol-gel these elements were homogeneously distributed on the coating surface.
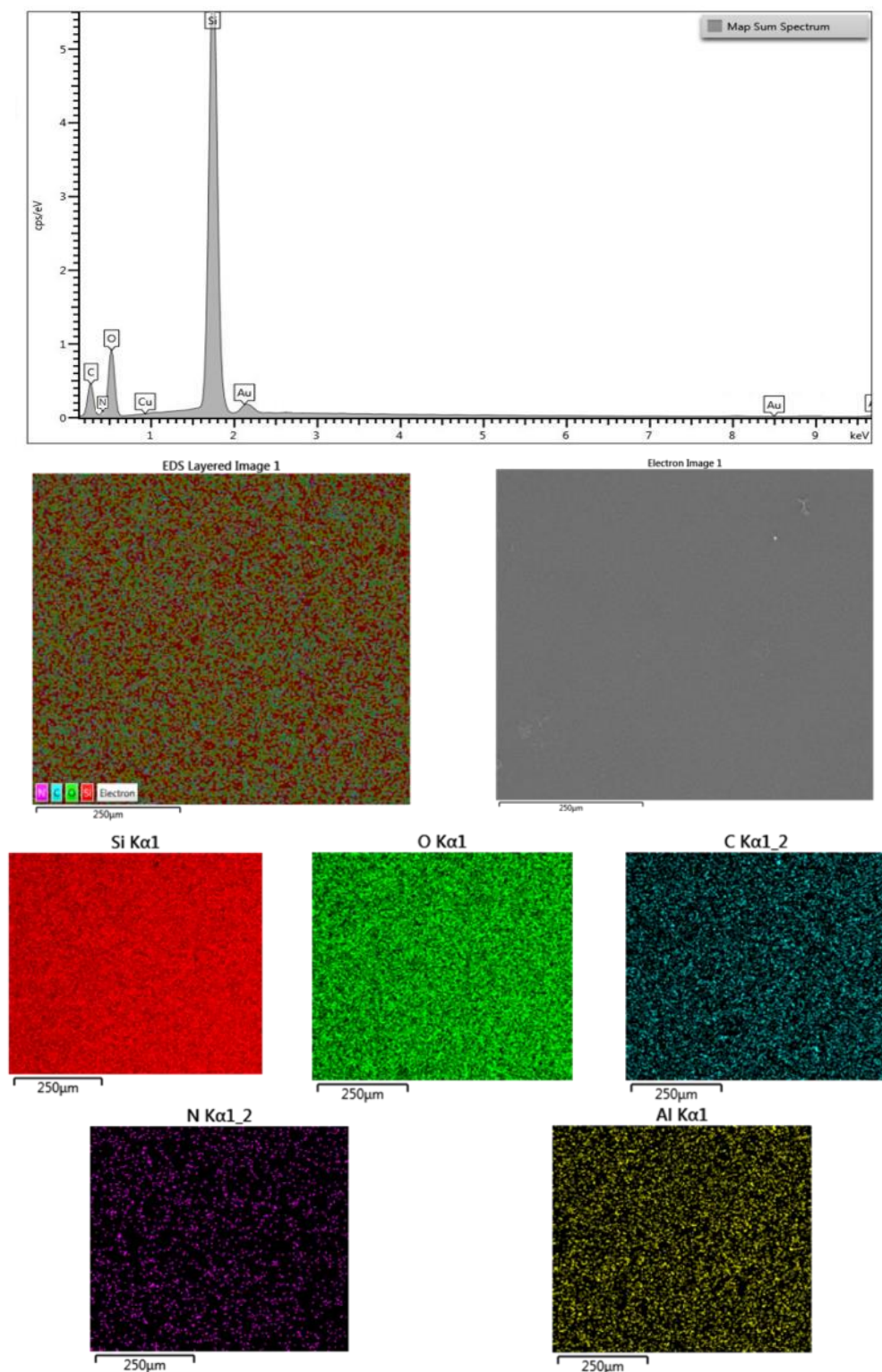
Figure 6-3 EDX mapping and spectroscopy for BZI-SBX-80 coating

6.2.2 Analysing ATR-FTIR for BZI-SBX-80 sol-gel chemical composition

The information from the FTIR spectroscopy of the dried BZI-SBX-80 sol-gel coated on the AA2024-T3 substrate demonstrates the organic-inorganic hybrid sol-gel coating of BZI-SBX-80 was attached to the AA2024-T3 substrate.

Figure 6-4, show the chemical composition for the SBX-80 sol-gel formula as mentioned in chapter 5 section 5.2.2   and the benzimidazole (BZI). The FTIR of BZI-SBX-80 sol-gel has the broad fingerprint peaks similar to the basic SBX formula as mentioned previously as shown in Figure 6-4.

Successful incorporation of the organic BZI inhibitor into the SBX sol-gel formula was confirmed by comparing the infrared spectrum obtained from the BZI-SBX-80 coating to the unmodified SBX-80. This is enlarged in Figure 6-5.

The spectrum of the BZI-modified coating, several peaks are seen relating to the BZI molecule. These peaks can be observed and remain in the BZI-SBX-80 sol-gel coated sample. They are as follows: weak imine C=N stretching presents at 1564.5 cm^{-1}, and carbon double bond C=C stretching peaks at about 1477 cm^{-1}, 1458 cm^{-1} and 1408 cm^{-1} respectively.

Similarly, the fingerprint of the aromatic amines stretching C-N can be detected at 1364 and 1300 cm^{-1} respectively, which can be used to confirm the benzimidazole presence in the sol-gel formula. The C-H out-of-plane bending is characterized by peaks in 768 and 745 cm^{-1}[148].
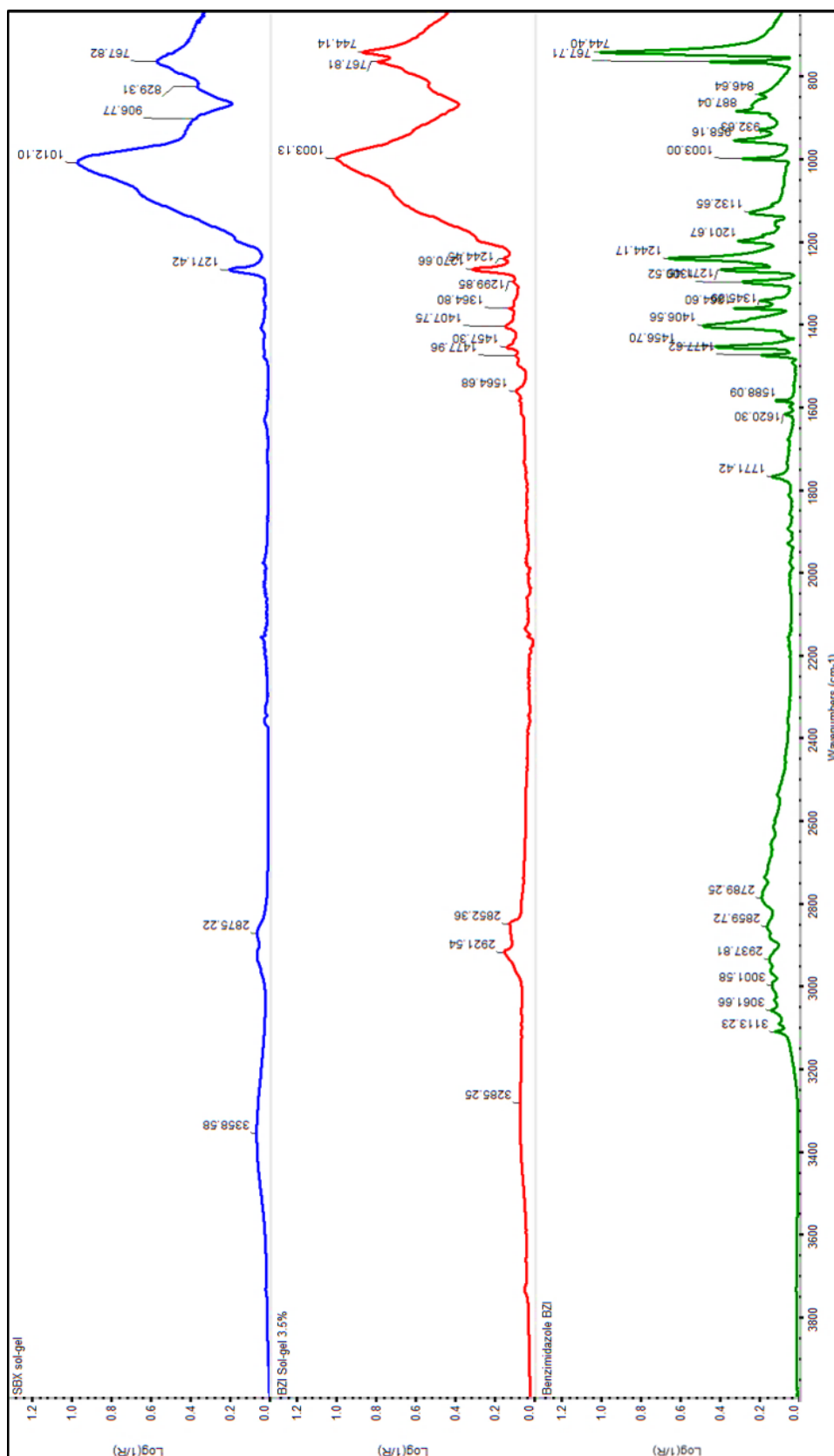
Figure 6-4 ATR spectrum for BZI-SBX-80 and SBX-80 sol-gel coating on the AA2024 substrates
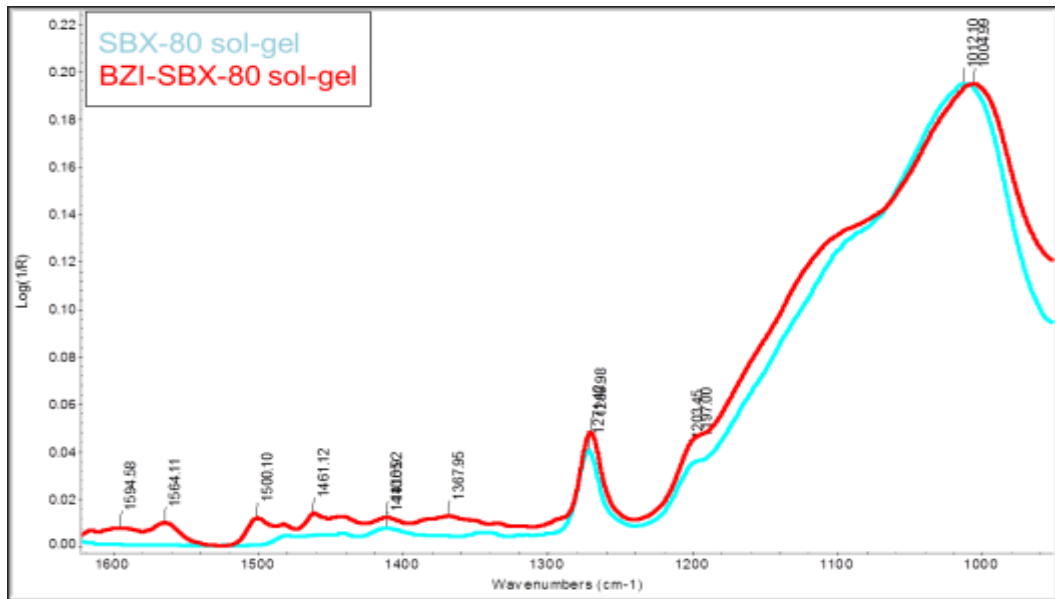
Figure 6-5 FTIR spectra showing the effect of BZI adding to the SBX-80 sol-gel

6.2.3 Water Contact Angle Of SBX And BZI-SBX Coatings

Figure 6-6 shows the mean water contact angle of 8 runs of SBX and ZBI-SBX sol-gel coated systems. In Figure 6-7 the results of the measured water contact angle (WCA) of the original SBX-80 coating was $67° \pm 2$, and as shown in (b) the measured WCA on modified BZI-SBX-80 Sol-gel coating was $88° \pm 4$. The higher water contact angle recorded for the BZI-SBX-80 shows that its wettability is lower than that of the original SBX-80. This is a result of the decrease in hydrophilicity (wettability) of coating from benzimidazole dispersed in the SBX-80 sol-gel coating [162].
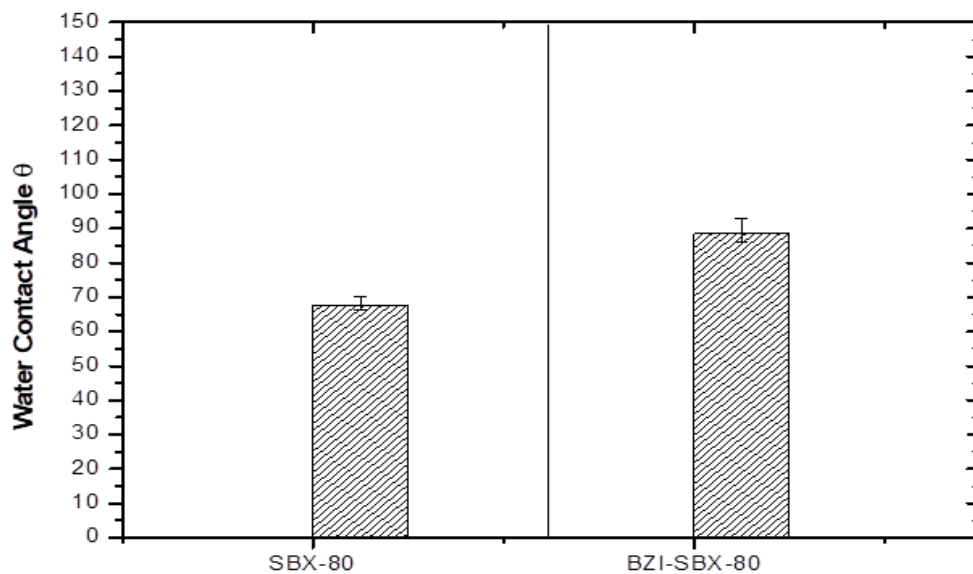
Figure 6-6 Bar chart showing mean values of WCA of BZI-SBX-80 and SBX-80 coatings
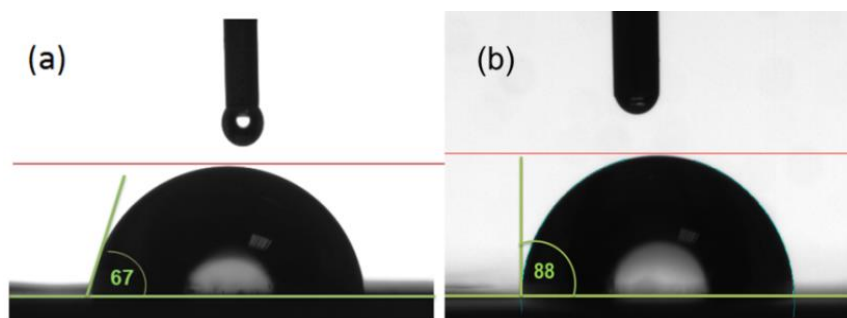
Figure 6-7 Optical images showing water droplets on (a) SBX-80 and (b) modified BZI-SBX-80 coatings

6.2.4 Electrochemical Impedance Spectroscopy (EIS) for the BZI Modified Coating

These tests were performed over a period of 14 days. Figure 6-8 and Figure 6-9 show impedance magnitude and phase angle plots for BZI-SBX-80 samples. The impedance data of the BZI-SBX-80 sol-gel coated substrates, shows the general behaviour of the coating as a good corrosion inhibitor coating.

The first hour of immersion exhibit reasonable impedance at high frequency between 10^5 to 10^3 Hz, starting at about 2.0×10^3 ohms. cm^{-2} reflecting the solution surface interface resistance, as it goes lower in frequency, the impedances started rising with slop reflecting capacitative behaviour which attributed to coating impedance, then at low frequencies between 10 to 0.01 Hz levelled-off to reach the highest magnitude with a value of about 5.9×10^7 ohms. cm^{-2} **.**

After 48 hrs immersion, the coating resistance started to be decreased possibly due to inhibitor consumption to the slow diffusion and oxidisation on the metal surface, yet it's still remained in the same range [165]. The drop of the impedance at higher frequencies was less than one order of magnitude, which means the overall coating resistance is still providing resistive barrier when is compared to the SBX sol-gel only.

In 72 hrs the impedance was more decreased in the low frequencies between 10^5 to 10^3 Hz to about 2.1×10^6 ohms. cm^{-2} behave similarly as a coated sample which kept the protection to drop after 336 hrs about 1.2×10^6 ohms. cm^{-2} .

At low frequencies from 10^1 to 10^{-2} Hz, the impedance decreased from the first hour to 360 hrs to reach 1.02×10^6 ohms. cm^{-2} , which might be the benzimidazole film working as a barrier as direct physical protection on AA2024–T3 from direct corrosion.

Correspondingly, the phase angle θ (Figure 6-9) showed one time-constant in the first immersion hour, between 10^5 to 10^1 Hz this comes from the coating capacitative

behaviour. After 48 until 360 hrs the data exhibited two time-constants, the first one from 10^5 to 10 Hz. The second one began from 10 to 0.01 Hz and this two-time-constant behaviour can be attributed to the creation of aluminium oxide film on the substrate [41].
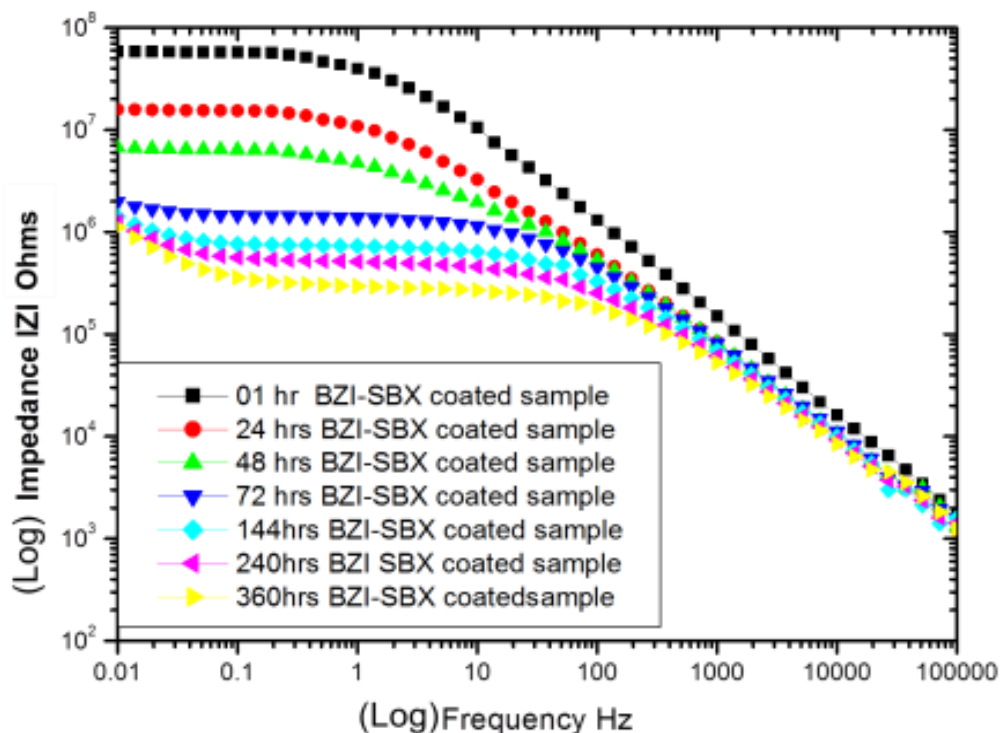
Figure 6-8 Impedance behaviour of BZI-SBX sol-gel coating in 3.5% NaCl
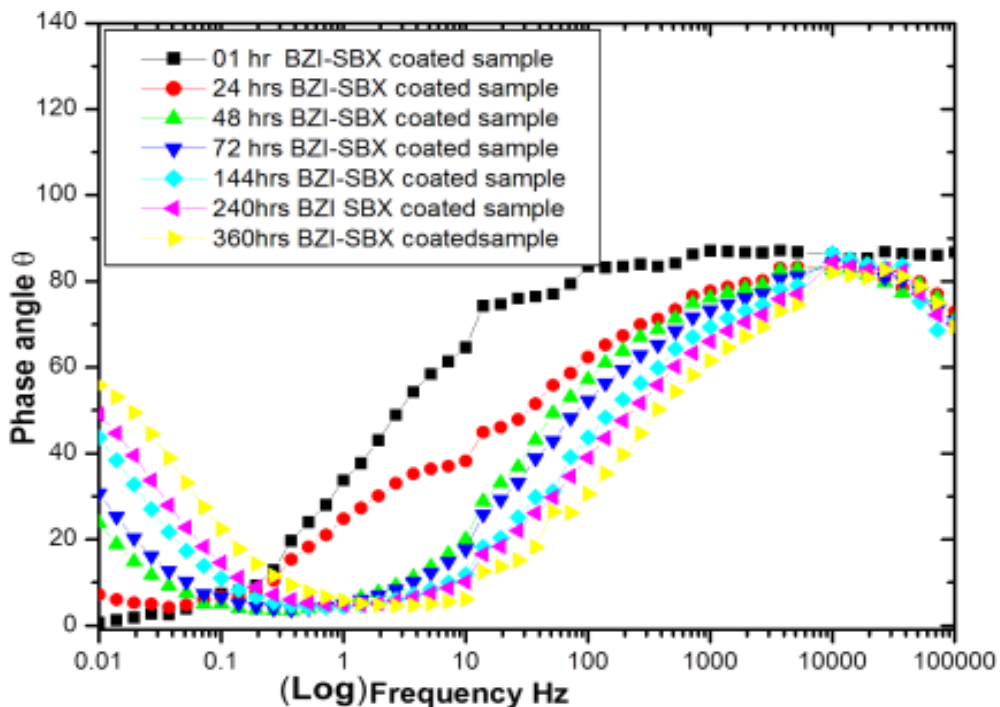
Figure 6-9 Phase angle response of BZI-SBX sol-gel coated sample in 3.5% NaCl

This behaviour protection of BZI-SBX-80 coating was accompanied by the appearance of a smooth and homogeneous coating surface on the substrate. The surface stayed free from visible evidence of corrosion and cracks free for more than 360 hrs. In addition to that, after 400 hrs immersion surface visual examination and showed it is still intact and capable of protection for longer than the sol-gel SBX only, as shown in Figure 6-10
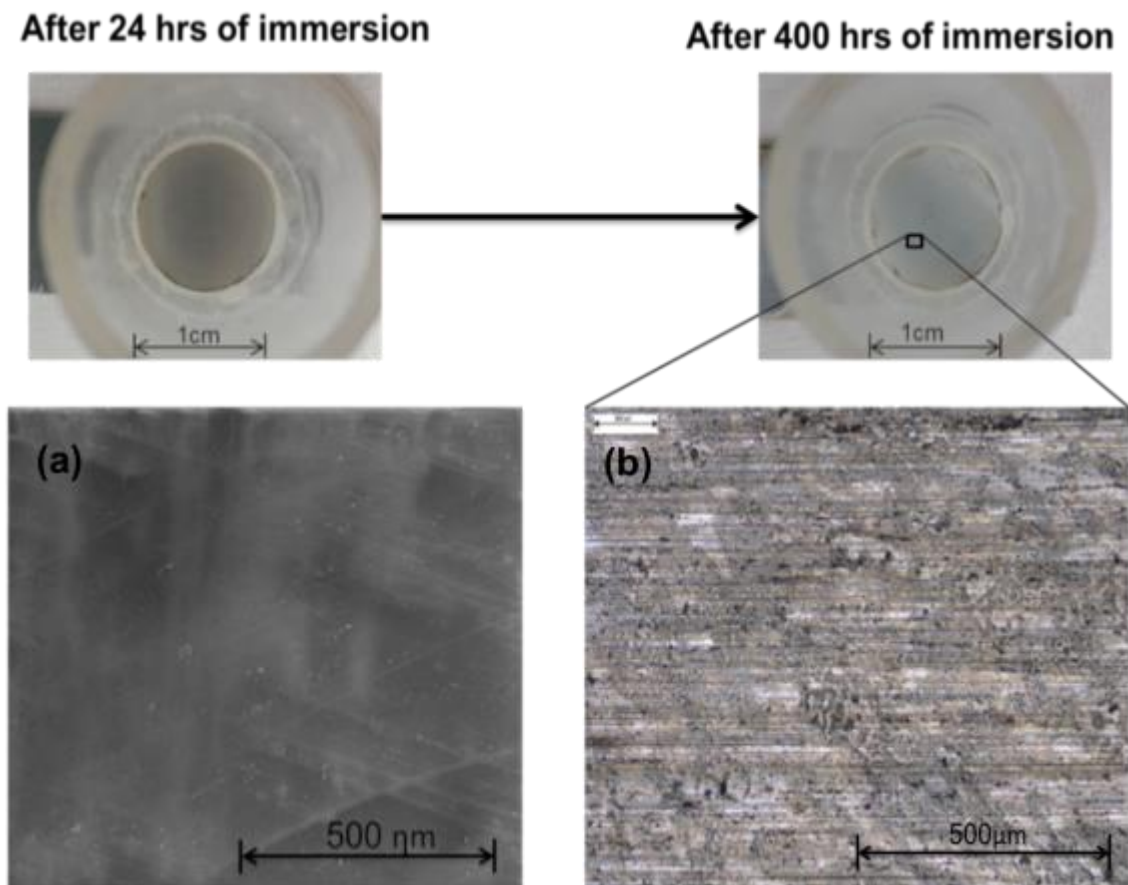
Figure 6-10 Shows (a) SEM image and (b) IFM image of the BZI-SBX-80 coated samples immersed in 3.5% NaCl solution with no creation of corrosion

The trace of the benzimidazole after 400 hrs of testing in 3.5% NaCl on the surface of AA2024-T3 substrate was checked by using the EDX technique. The BZI-SBX sol-gel coating was removed completely by adhesion pull-off test until left the surface clean from any sol-gel coating as in SEM that shown Figure 6-11.
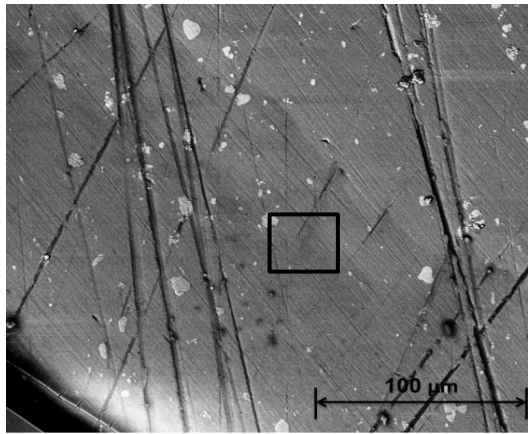
Figure 6-11 SEM image of the surface after removing the BZI-SBX-80 coating

Then by using EDX analysis, as shown in Figure 6-12, the spectrum showed a very small trace of nitrogen which reflects the presences of an azole group on the surface. By zooming-in, the spectrum from 0.1 to 2.0 KeV it shows the peak shoulder confirmed the nitrogen at about 0.4 KeV by element weight percentage of 1.0 ~1.1 wt.% [166].
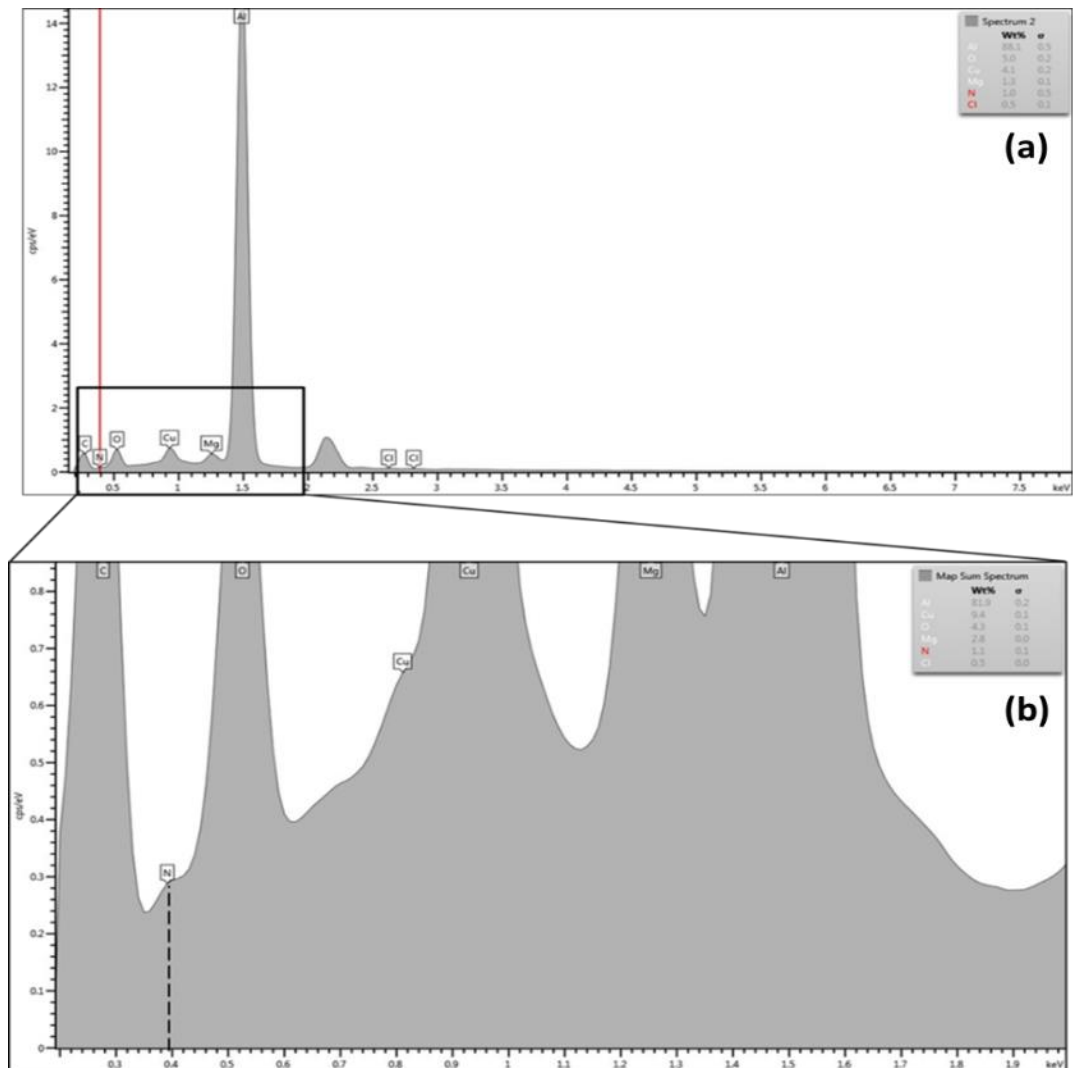
Figure 6-12 (a) EDX spectrum, (b) zoomed spectrum showing the trace of nitrogen
adsorption on the AA2024-T3 after 400 hrs of immersion

6.3 The Effect of Adding: Oleic acid (OA) to the base organic-inorganic hybrid Sol-Gel coating

Another way to enhance the SBX Sol-gel coating is by introducing an inhibitor such as oleic acid. There are two benefits of oleic-oil. Firstly, it can work as a film-forming inhibitor. Secondly, it can block the porosity of the sol-gel to reduce oxygen transmission rates and diffusion [167].

The SBX-80 sol-gel coating can be enhanced by adding a small ratio of about 0.1 % v/v of oleic acid (OA) to the SBX-80 formula. This modified formula will be coded as OA-SBX-80 sol-gel.

The testing method was to expose the rounded area of $1cm^2$ in 3.5% NaCl solutions for 360hrs and repeated for more than five times.

6.3.1 Surface morphology and elements confirmation of modified OA-SBX-80 sol-gel Coating

The general appearance of the surface of OA-SBX-80 sol-gel coated sample was even and smoothed with the entrance of rounded encapsulated oleic acid inside the film as it showed in Figure 6-13 there was also trace of oily wettability on the surface of the sol-gel coating.

Furthermore, it is noticeable that from the SEM image of the cross-section showed that the thickness of this OA-SBX-80 coating is 18 μm ± 2.
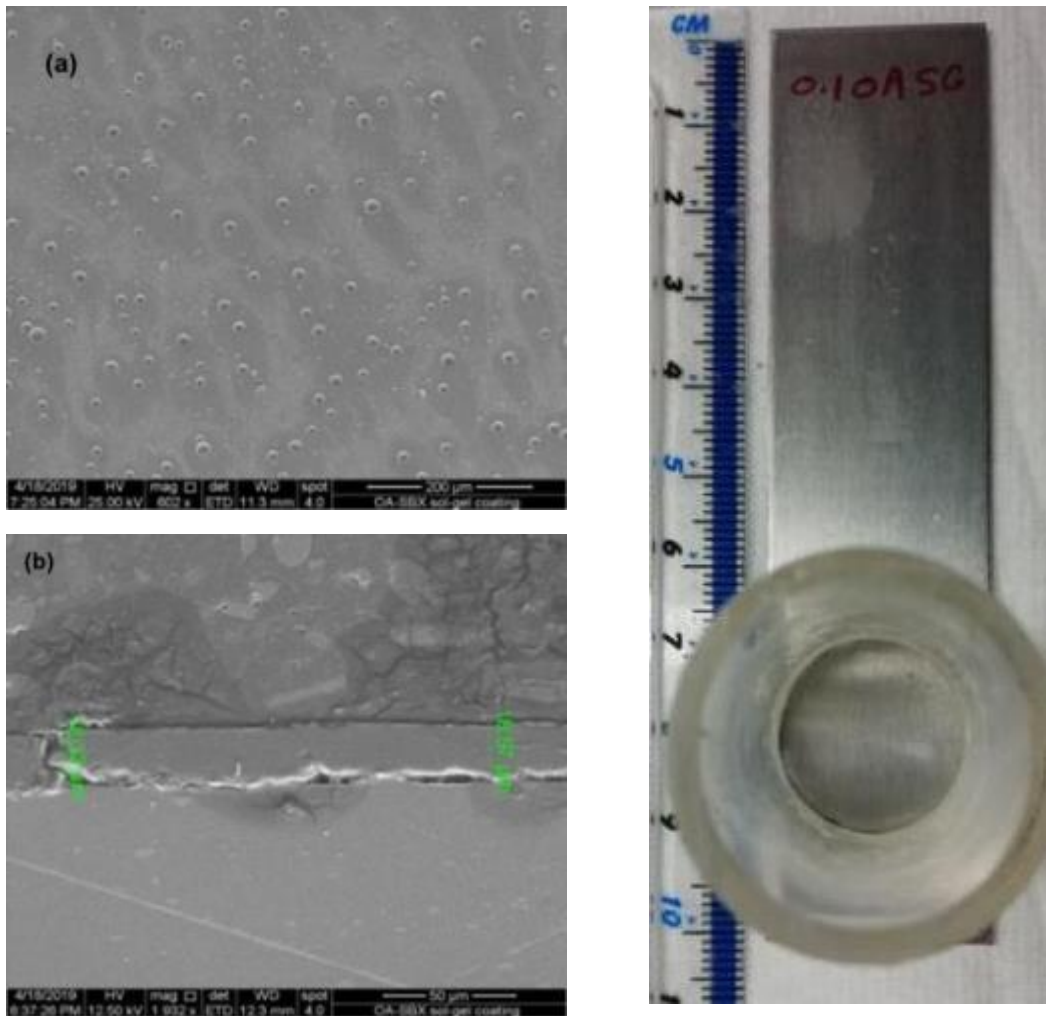
Figure 6-13 Shows the OA-SBX-80 coating (a) SEM image of surface morphology,

(b)SEM image of the cross-section

By using the SEM and EDX spectroscopy can verify the chemical elements of the sol-gel formula on AA 2024-T3 including silicon, carbon, and oxygen. These elements were homogeneously distributed on the surface of the coating. Figure 6-14 EDX spectrum and mapping of the substrate for elements compositions of sol-gel.
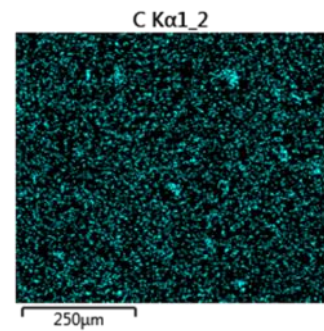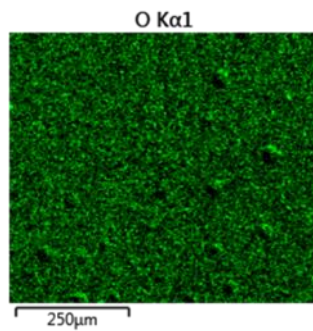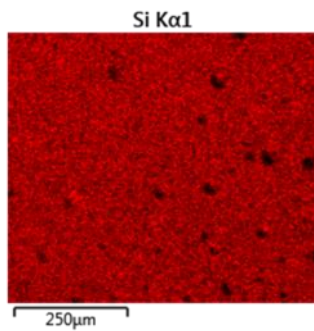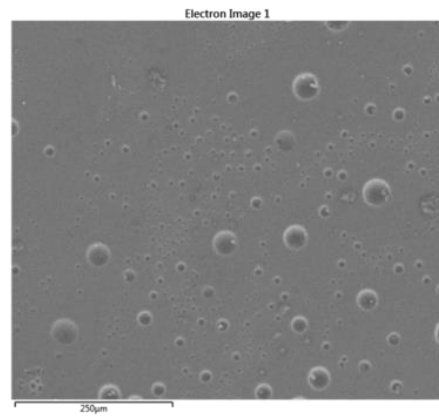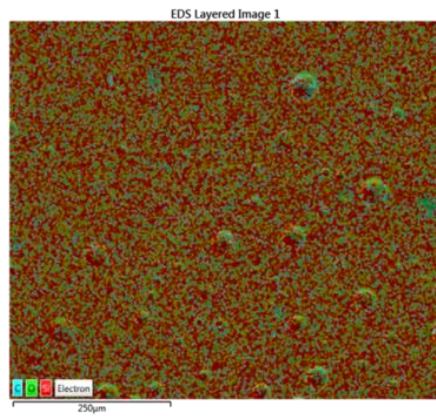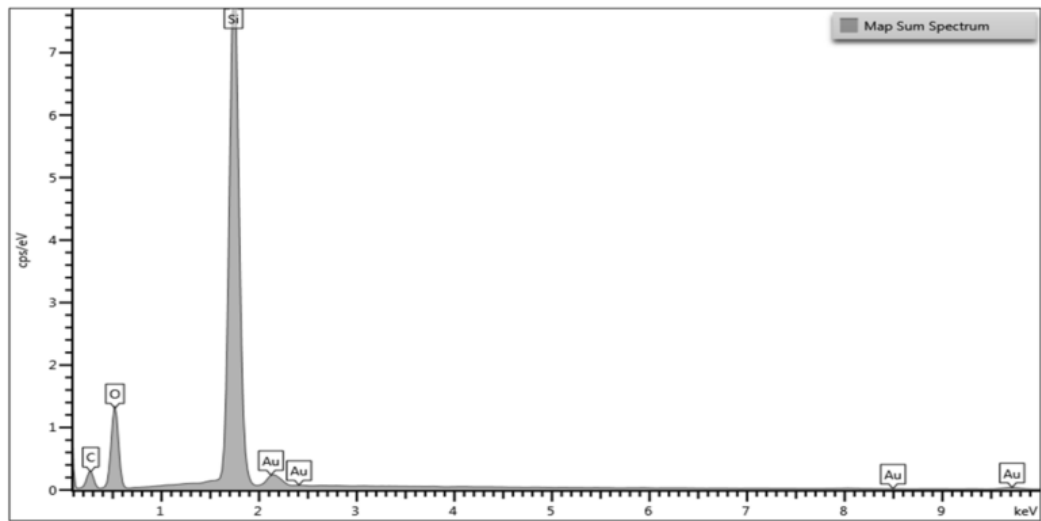
Figure 6-14 EDX mapping and spectrum for OA-SBX-80 coating

6.3.2 Analysing ATR-FTIR for OA-SBX-80 sol-gel chemical composition

The information from the FTIR spectroscopy of the oleic acid encapsulated sol-gel coating OA-SBX-80 on the substrate of AA2024-T3 confirms the organic-inorganic hybrid sol-gel coating of OA-SBX-80 well attached on AA2024-T3 substrate. From Figure 6-15 the chemical composition can be seen for the SBX-80 sol-gel formula and the oleic acid modified coating.

The spectrum obtained from the OA-SBX-80 sol-gel formula has the broad fingerprint peaks similar to the basic formula SBX sol-gel as mentioned previously in chapter 5 section 5.2.2 as is shown in Figure **5-4**.

However, successful incorporation of adding oleic acid (OA) into the base formula of SBX-80 sol-gel was confirmed by comparing the infrared spectrum obtained from the OA-SBX-80 coating to the unmodified SBX-80.

The alkyl group present two main contributions at 2925 cm^{-1} and 2856 cm^{-1} representative of CH_3 and CH_2 stretching respectively. Additional peaks are characteristic of the confirmation of CH_2 at 1460 cm^{-1} and 1300 cm^{-1}. As expected The carbonyl function C=O is shows by a peak at 1707 cm^{-1} [142], [145], [147].
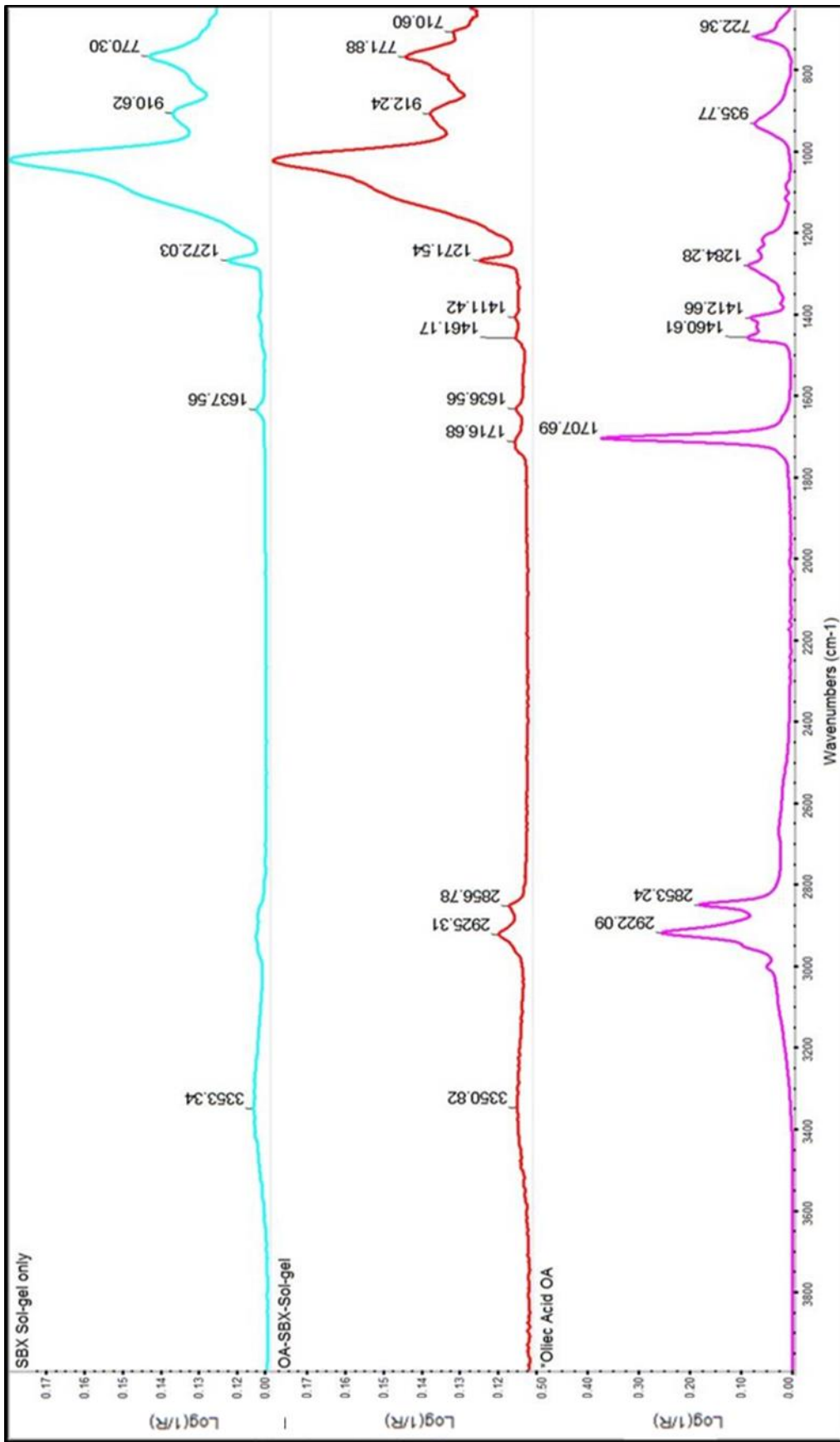
Figure 6-15 ATR spectrum for OA-SBX-80 and SBX-80 sol-gel coating on the AA2024-T3 substrates

6.3.3 Water Contact Angle of SBX-80 And OA-SBX-80 Coatings

Figure 6-16 shows the water contact angle measurements on both SBX-80 sol-gel and OA-SBX-80 Sol-gel coating systems presented graphically as mean values of 8-time repeats to the experiment.

In Figure 6-17, the results of measured water contact angle (WCA) of the original SBX-80 coating was $67° \pm 2$, and as shown in (b) the result of WCA on modified OA-SBX-80 Sol-gel coating was $101° \pm 2$. The higher water contact angle recorded for the OA-SBX-80 shows that its wettability is lower than that of the original SBX-80 as a result of an increase in hydrophobicity attributed to oleic acid encapsulation in the SBX-80 sol-gel coating [162].
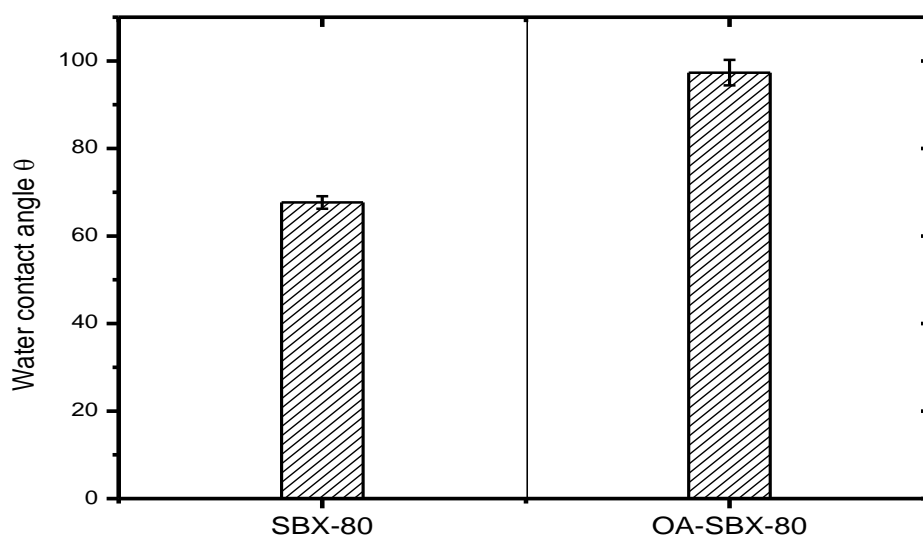
Figure 6-16 Water contact angle of both SBX-80 and OA-SBX-80 sol-gel
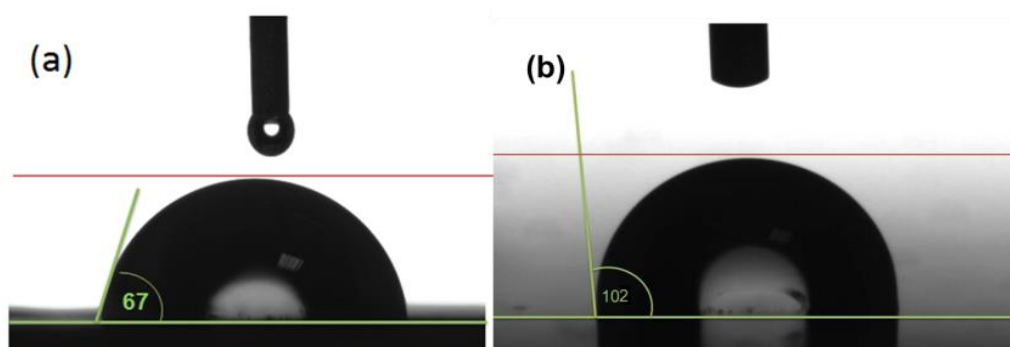
Figure 6-17 Optical images showing water droplets on (a) SBX-80 and (b) modified OA-SBX-80 sol-gel coating

6.3.4 Electrochemical Impedance Spectroscopy (EIS) for the Oleic Acid Modified Coating

Tests were performed for a period of 360 hrs. Figure 6-18 and Figure 6-19 show impedance magnitude and phase angle plots for OA-SBX-80 samples, respectively. The Impedance data of the OA-SBX-80 sol-gel coated substrates, as shown in Figure 6-18 suggest that the OA coating is performing as a durable corrosion inhibitor coating. The EIS results in the first hour of immersion exhibit high impedance, starting at about 4.7×10^2 ohms.cm^{-2} at a high frequency of 10^5, then starts to rise with the slope reflecting the general capacitative behaviour attributed to coating/solution interface impedance until it reaches the higher magnitude in the low frequencies between 10 to 0.01 Hz with a value of about 1.3×10^6 ohms.cm^{-2} .

After 48 hrs of the immersion, at high frequencies of 10^5 Hz, the coating impedance starts slightly decrease possibly due to the slow diffusion and oxidisation process to the alloy surface. However, still considered in the same range as the first-day immersion at about 3.7×10^2 ohms.cm^{-2}.

The drop of the impedance at frequencies between 10^3 to 10^0 Hz, was less than one order of magnitude from the first hour; however, the overall coating resistance suggests it is still providing excellent protection. After 120 hrs immersion at low frequencies, the impedance is decreased at about 0.9×10^6 ohms.cm^{-2} . It kept this protection behaviour with a small reductions in impedance until 360 hrs to reach 0.4×10^6 ohms.cm^{-2}. This persistent protection might be as a result of the bridging reaction of oleic acid on the surface working as a pores-blocker in the sol-gel coating matrix.

Correspondingly, the changes in the phase angle θ as shown in Figure 6-19, in the first immersion hour showed one time-constants. This comes from coating capacitor behaviour. After 240 hrs two time-constants started forming, the first one from 10^5 to 10^3 Hz, the second one from 10^2 to 10^{-2} Hz. These time-constants can be attributed to the creation of an aluminium oxide film formed and to oleic acid bridging on the substrate [150].
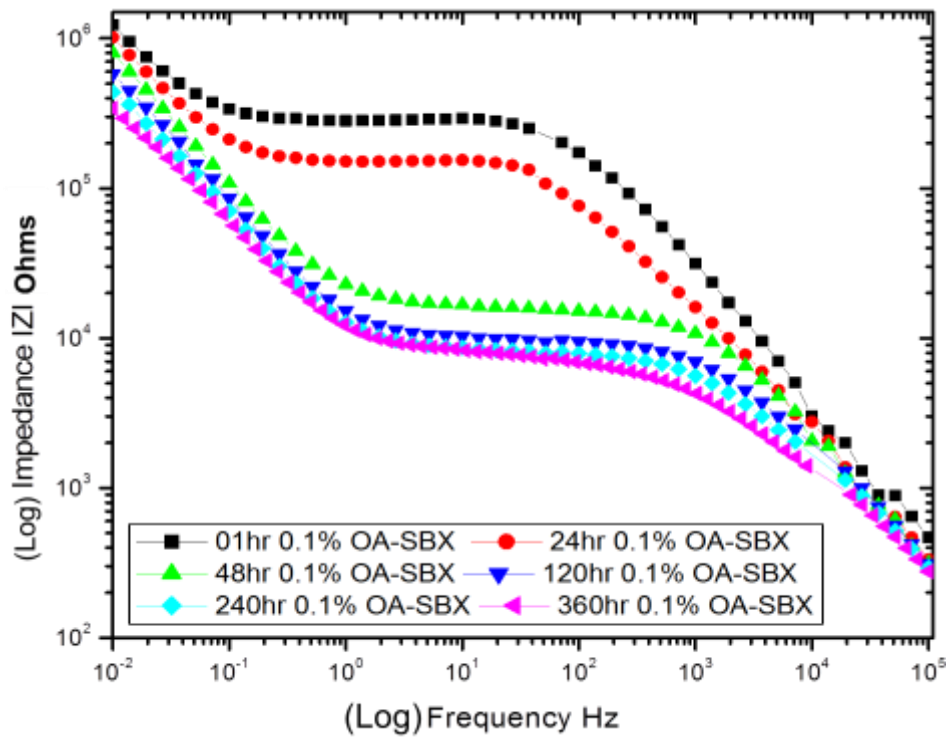
Figure 6-18 Impedance behaviour of OA-SBX-80 sol-gel coating in 3.5% NaCl
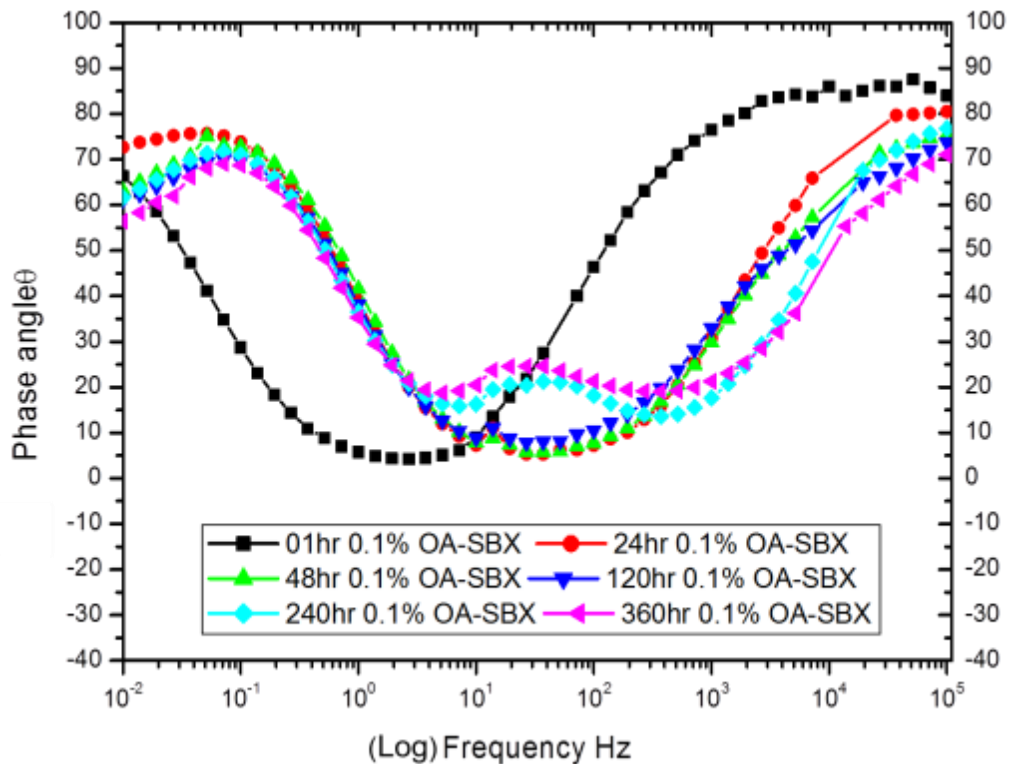
Figure 6-19 Phase angle response of OA-SBX-80 sol-gel coating in 3.5% NaCl

The protection behaviour of OA-SBX-80 sol-gel coating in the period of the test was accompanied by the appearance of a good appearance of the surface of the coating on the substrate, which stayed without cracks and corrosion for more than 480 hrs.

 After that, small OA-unfilled holes appeared but without any development of pitting until the end of the test. In addition to that, after 720 hrs immersion, the surface examination reveals the sol-gel coating still present and capable of keeping the protection, as it appears in Figure **6-20**.
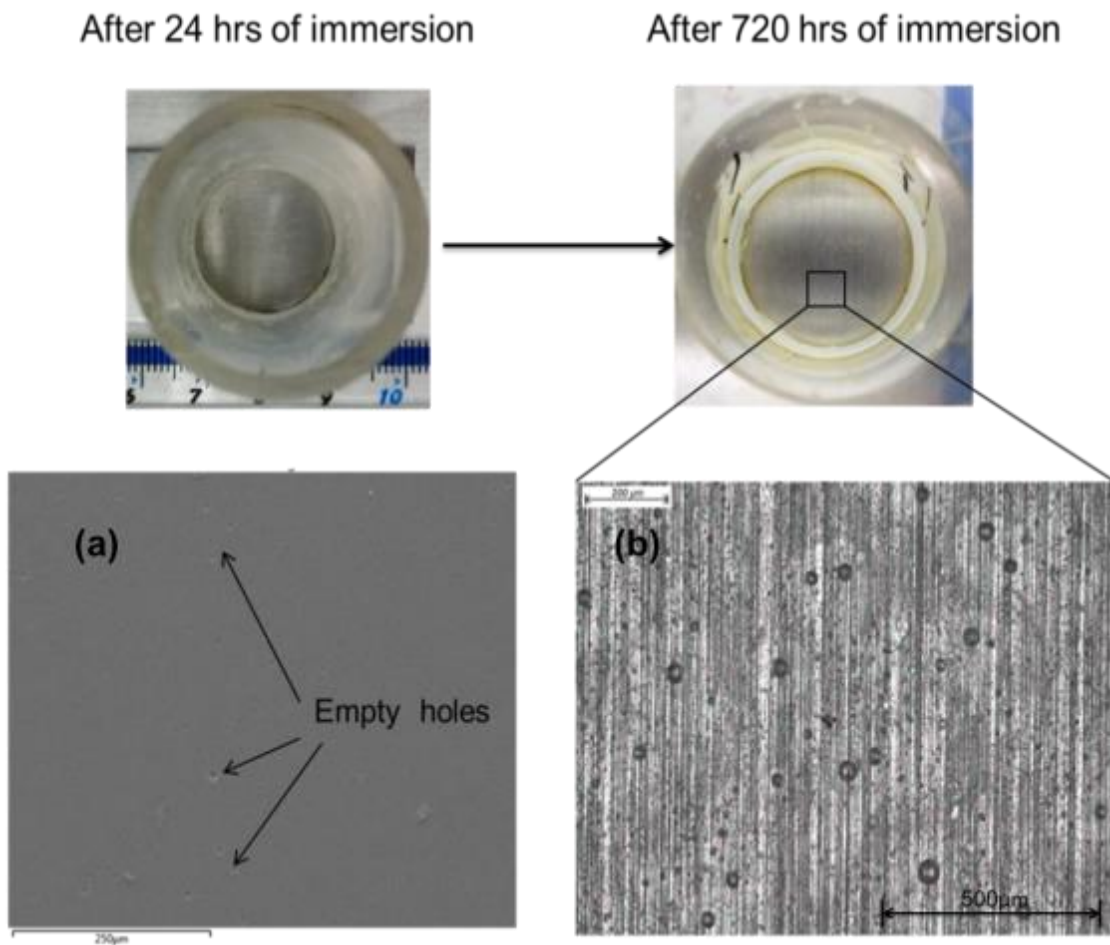
Figure 6-20 Shows (a) SEM image, and (b) IFM image of the OA-SBX-80 coated samples immersed in 3.5% NaCl solution with a sign of empty holes after 720hrs

6.4 Analysing the enhancement on corrosion protection by adding benzimidazole and/or oleic acid to the SBX-80 formula

As it is shown in Figure 6-21, after the first hour of immersion the overall impedance of BZI-SBX-80 at low frequencies was increased by approximately two orders of magnitude to the OA-SBX-80 and SBX-80 coated samples, with values of 5.9×10^7 ohms.cm^{-2} (BZI-SBX-80), compared to 1.28×10^6 ohms.cm^{-2} (OA-SBX-80) and 6.2×10^5 ohms.cm^{-2} (SBX-80).
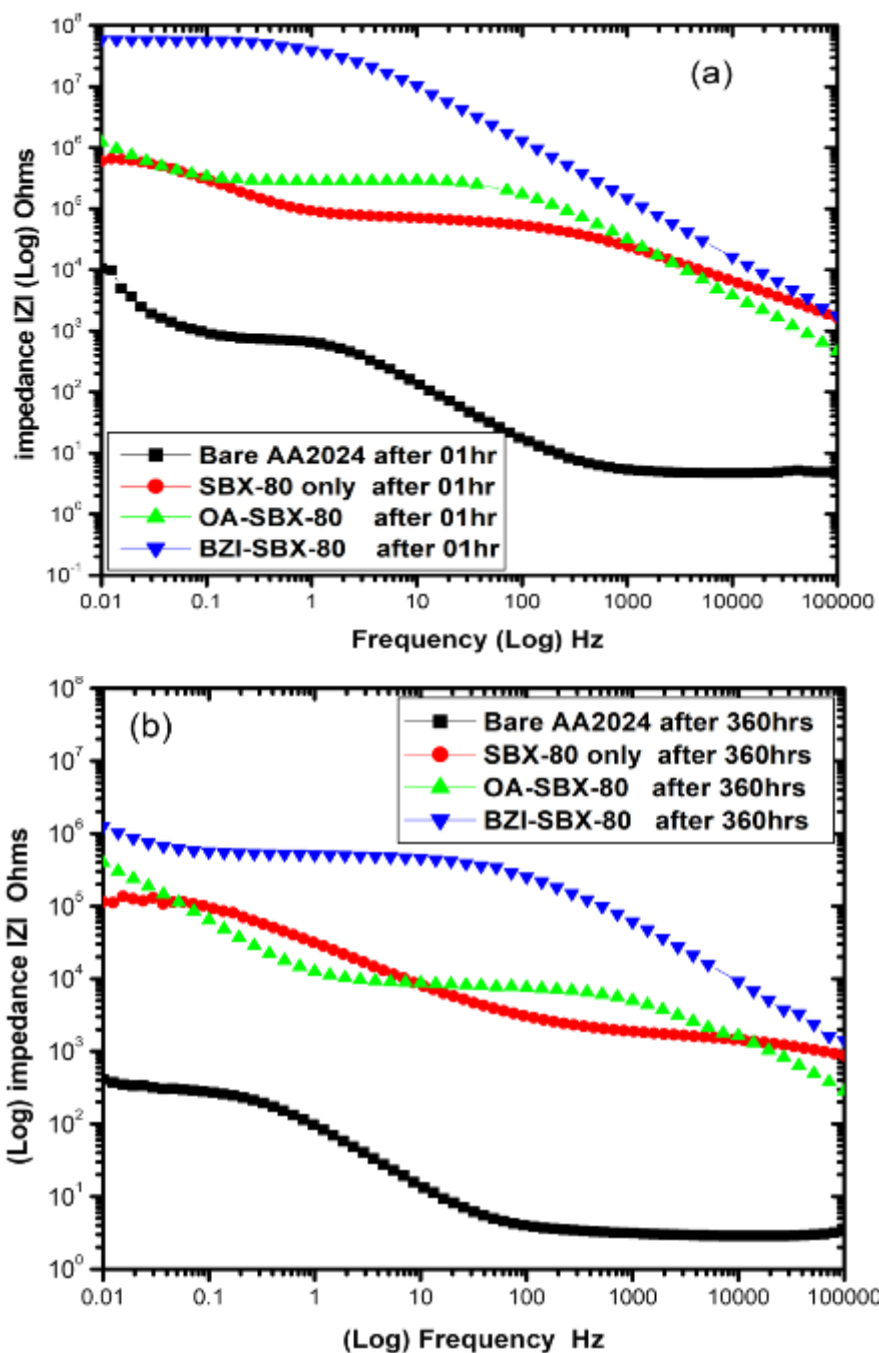
Figure 6-21 Impedance magnitude plots for BZI-SBX-80, OA-SBX-80, SBX-80 and Bare-AA2024 samples (a) in the first hour, and (b) after 360 hrs
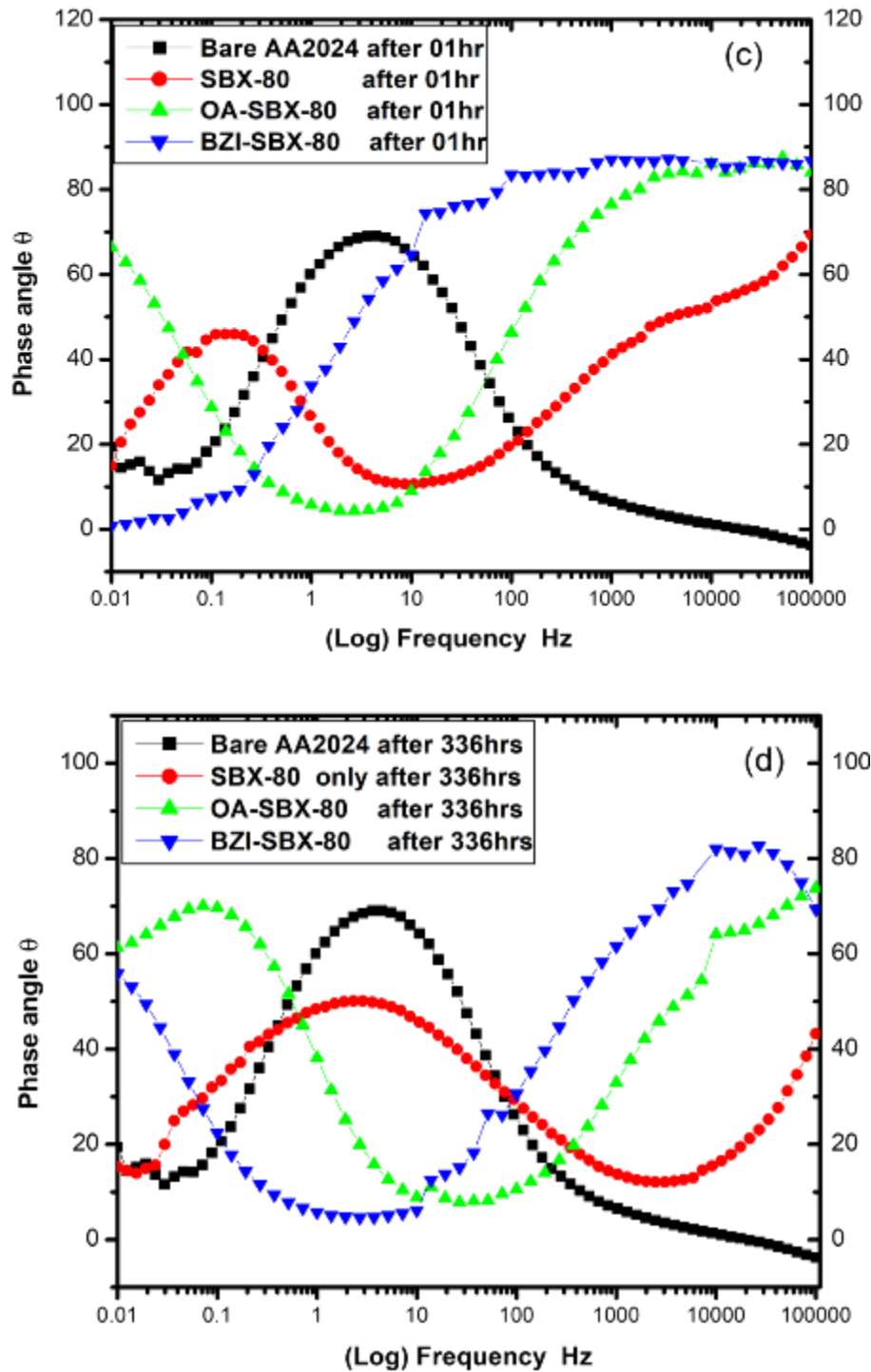
Figure 6-22 Phase angle plots for BZI-SBX-80, OA-SBX-80, SBX-80 and Bare-AA2024 samples (c) in the first hour, and (d) after 360 hrs

From Figure 6-21, in the first hour for the BZI-SBX-80 samples at frequencies between 1.0 to 10^5 Hz, the curve reveals capacitive behaviour, then the impedance slowly increased with slop to about 4.6×10^7 ohms.cm^{-2} in the middle range of the frequencies and finally

reached the point where the rate of increase impedance is small at the low frequencies which are 5.9×10^7 ohms.cm^{-2}.

After 360 hours, the BZI-SBX coated samples dropped about one and a half orders of magnitude; this is maybe due to the electrolyte diffusion and expansion of the pores in the coating matrix. However, this drop is not affecting the visible protection; suggesting the film of BZI has been created on the metal surface[64].

In Figure 6-21(b), a noticeable measured impedance was observed to the SBX-80 coated sample at about 1.0×10^5 ohms.cm^{-2} after 360hrs. However, the OA-SBX-80 sol-gel sample revealed visual corrosion protection starting with small impedance at 10^5 Hz of about 6.5×10^3 ohms.cm^{-2} which is lower than the SBX and BZI-SBX-80 coatings. This might be attributable to the coating resistance beginning to reduce due to the creation of rounded spheres of encapsulated oleic acid with the inibbitor acting slightly as a conducting material. The low frequencies impedance reaches of about 1.0×10^6 ohms.cm^{-2} , this impedance is considered higher than SBX-80 coating in the middle frequency range between 100 to 0.1 Hz. This may be attributed to the coating pores-blocking properties of the oleic acid. Then it is started to rise again from frequency 0.1 to 0.01 Hz to reach the overall magnitude of about 1.28×10^6 ohms.cm^{-2}.

The phase angle plots Figure 6-22 (a) and (b) on the first immersion hour for all coating systems, illustrate that the BZI-SBX-80, OA-SBX-80 and SBX-80 sol-gel coated samples exhibit different semi-circles response as the following:

The BZI-SBX-80 which showed one semi-circle on the first hour then moved to two semi-circles. This may be attributed to BZI film creation on the metal surface and limited oxide formation.

The OA-SBX and SBX-80 coatings system showed two semi-circles. Then after that, until 360 hrs, the phase angle plot for the BZI-SBX-80, and OA-SBX-80 coated samples indicated the presence of two time-constants. The SBX-80 coated samples exhibited two time-constants due to the creation of an oxide film until the 360 hrs of the test. It was found from the literature [64], [67], [68], that the BZI and its derivatives may be positioned in a parallel adsorption arrangement (film) close to the surface and resisting the electrolyte diffusion. Second, the oleic acid in sol-gel works as pores-blocking. This can work as a corrosion inhibitor to provide a barrier on the metal surface preventing the diffusion of charged ions [76], [77].

6.4.1 Investigating the corrosion protection behaviour for both BZI-SBX-80 and OA-SBX-80 sol-gel coatings by using equivalent circuits fitting and modelling

Figure **6-23** shows Nyquist plots for both BZI-SBX-80 and OA-SBX-80 coatings from 01hr to 360 hrs respectively. These plots were used for equivalent circuits modelling fitting by using ZSimpwin electrochemical impedance spectroscopy (EIS) data analysis software.
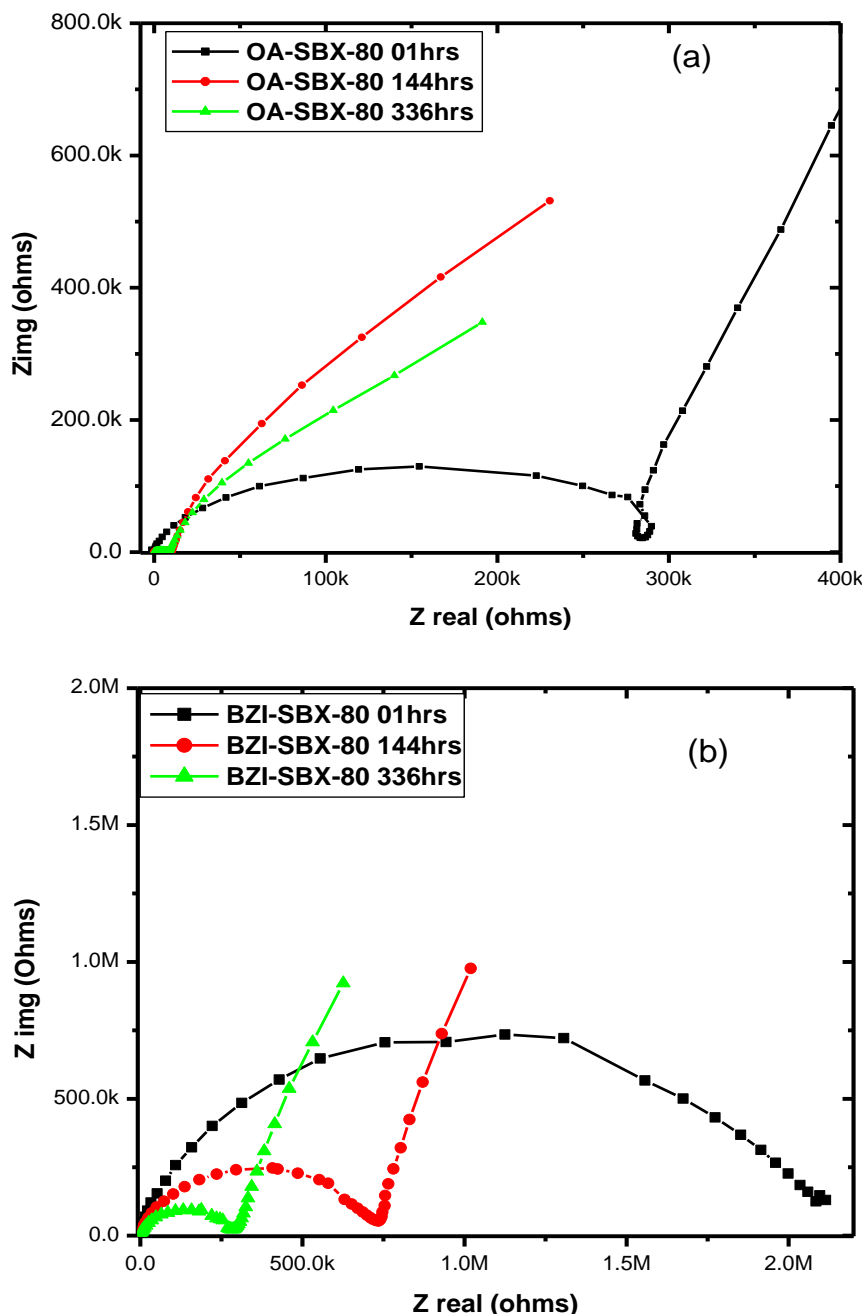
Figure 6-23 Nyquist plots for (a) OA-SBX and (b) BZI-SBX coatings

The fitted EIS data plots for OA-SBX-80 and BZI-SBX-80 sol-gels for 01 hr, 48 hrs and 144 hrs were given in Figure 6-24 and Figure **6-25** respectively. It showed the general fitted equivalent circuits with two time-constants for both coating system.
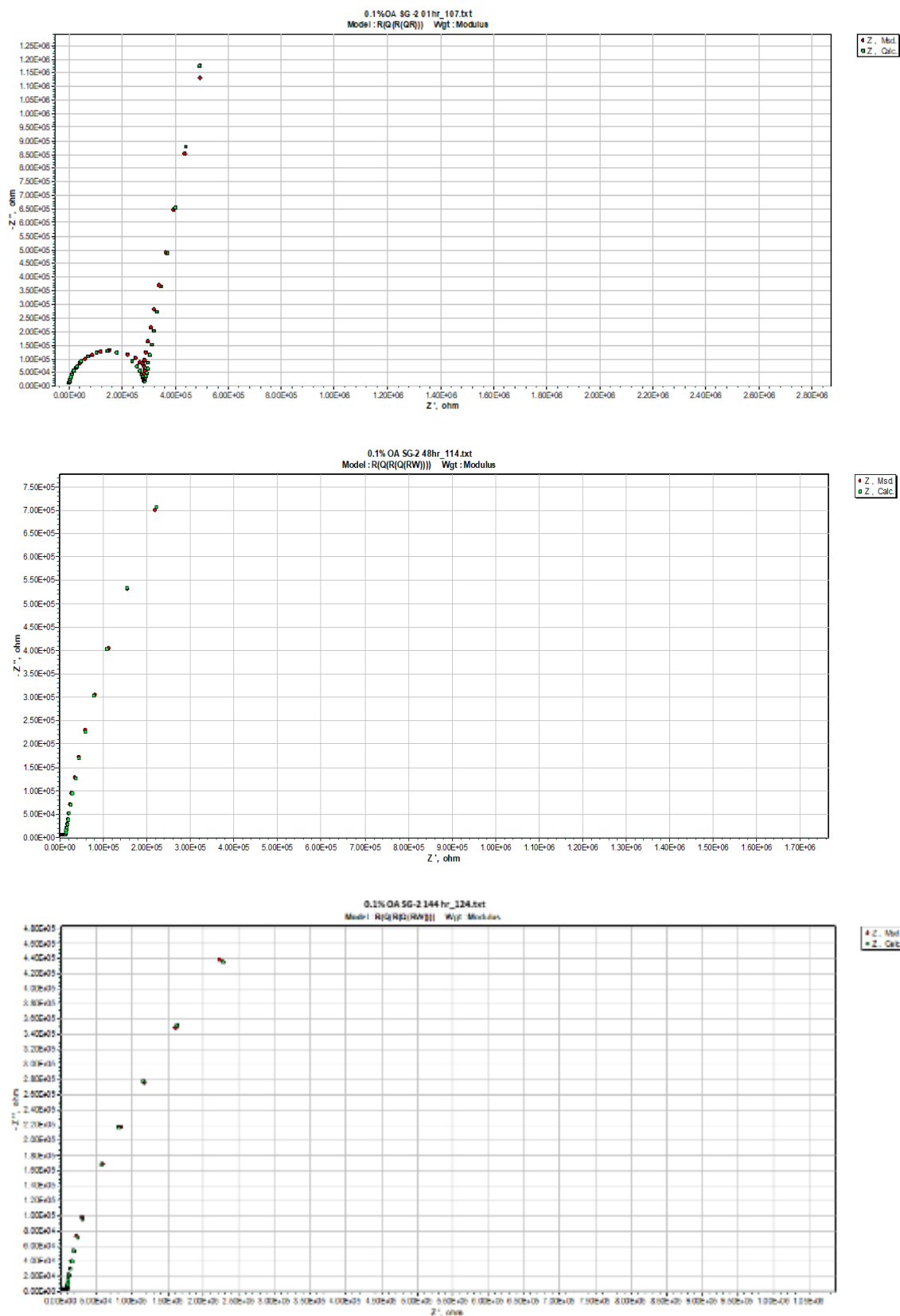
Figure 6-24 EIS data fitting for OA-SBX-80 in 01hr, 48hrs and 144hrs
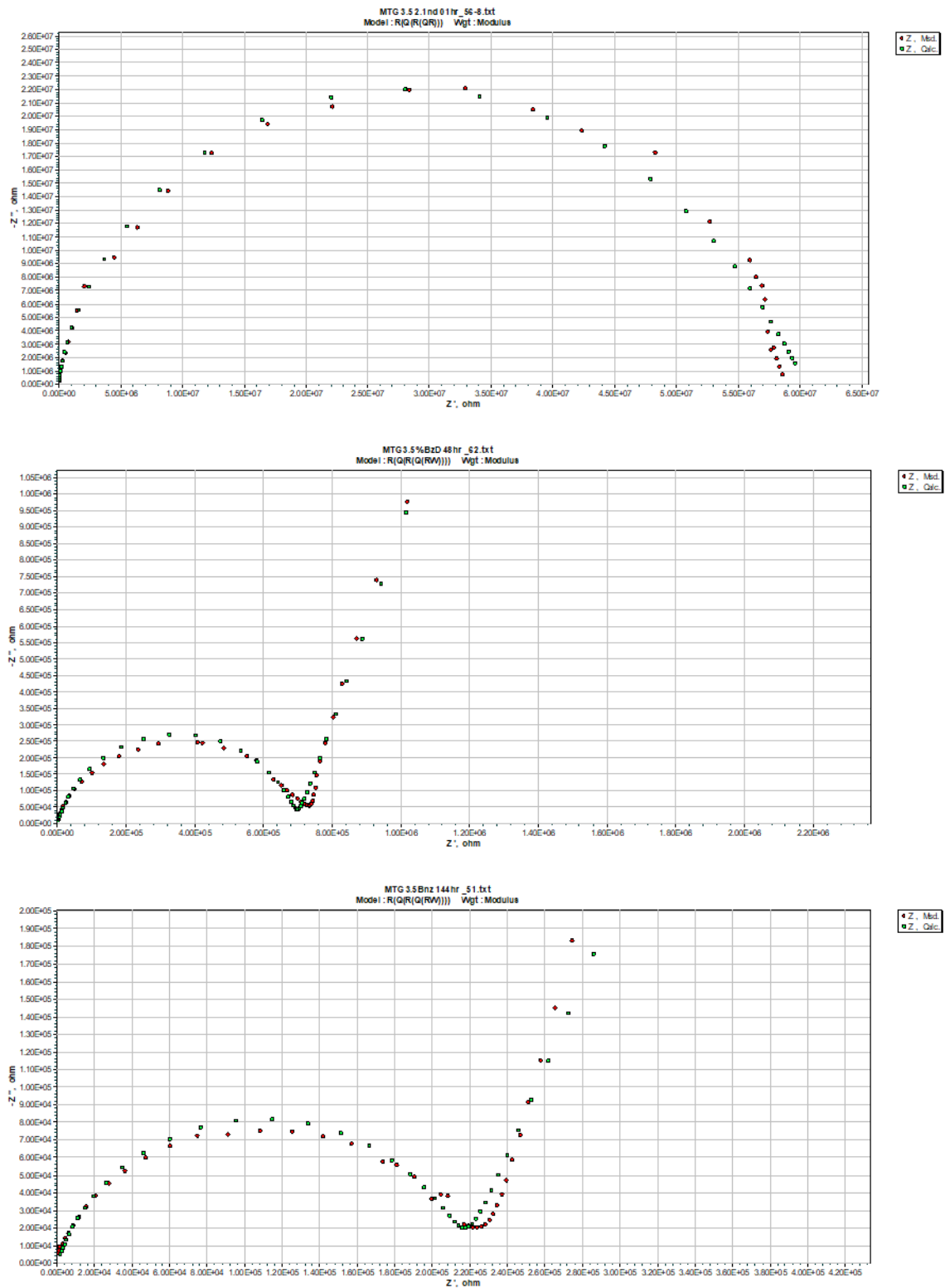
Figure 6-25 EIS data fitting for BZI-SBX-80 in 01hr, 48hrs and 144hrs

The time-constant element (Q), was used instead of an ideal capacitor C, to account for current leakage in the capacitor and/or frequency dispersion effect of the alternating current signals [107], [109]. The elements that used for modelling the equivalent circuits

here were: solution resistance (R_s), coating resistance (R_{ct}), coating constant phase elements (Q_{ct}), intermediate oxide layer resistance (R_{iL}), intermediate oxide layer capacitance (Q_{iL}), Warburg diffusion element (W)[151].

Table **6-3** and

Table 6-4 below shows the fitted data obtained from EIS spectra for the OA-SBX and the BZI-SBX sol-gel coatings after various immersion times in 3.5% w/v NaCl solution.

Table 6-3 The fitted data obtained from EIS spectra for the OA-SBX sol-gel coating after various immersion times in 3.5 wt. % NaCl solution.

Sample	Element	immersion time (hrs)		
		01	48	144
Circuit		R(Q(R(Q(RW))))	R(Q(R(Q(RW))))	R(Q(R(Q(RW))))
	R_s	102	205	195
	Q_{ct}	1.089E-8	2.155E-8	1.044E-7
	n	0.9138	0.888	0.772
	R_{ct}	2.878E5	1.232E4	8.770E3
	Q_{iL}	9.956E-6	1.577E-5	2.026E-5
	n	0.9296	0.897	0.916
	R_{iL}	1.667E6	5.688E6	8.594E5
	W_{iL}	4.554E-7	1.041E-6	6.716E-6

Table 6-4 The fitted data obtained from EIS spectra for the BZI-SBX sol-gel coating after various immersion times in 3.5 wt. % NaCl solution.

Sample	Element	immersion time (hrs)		
		01	48	144
Circuit		R(Q(R(QR)))	R(Q(R(Q(RW))))	R(Q(R(Q(RW))))
	R_s	105	110	201
	Q_{ct}	1.471E-9	4.549E-9	9.148E-9
	n	0.9626	0.887	0.8406
	R_{ct}	1.326E7	1.301E6	6.991E5
	Q_{iL}	3.453E-9	6.406E-8	9.016E-8
	n	0.800	0.650	0.800
	R_{iL}	4.697E7	5.885E5	1.778E3
	W_{iL}	-	4.349E-8	7.044E-10

The proposed equivalent circuits were used to simulate the corrosion mechanism on the coated sample in 01 hr, 48hrs and 144 hrs were provided in Figure 6-26 and Figure 6-27. At the first immersion hour, both OA-SBX and BZI-SBX sol-gel coated samples illustrate

the different behaviour with three resistance and two time-constants with Warburg diffusion element (W) for OA-SBX-80 and without Warburg diffusion element (W) in BZI-SBX-80. However, after 48 hours immersion till 144hrs, both coated samples, OA-SBX and BZI-SBX started behaving similarly with three resistance and two time-constants with Warburg diffusion element (W).

In the case of the OA-SBX-80 coating, The first time-constant arises in the high-frequency range and may be attributed to electrolyte coating resistance, the second one is due to barrier properties of the formed OA and oxides film on the interfacial layer (iL), and the Warburg diffusion element (W) was maybe attributed to the diffusion resistance on the interfacial layer on the substrate as shown in Figure 6-26 (a,b).

It is notable that after 144 hrs immersion, the oleic acid capsules in the coating matrix is started to be empty, that could lead to a reduction in the coating resistance Rct.
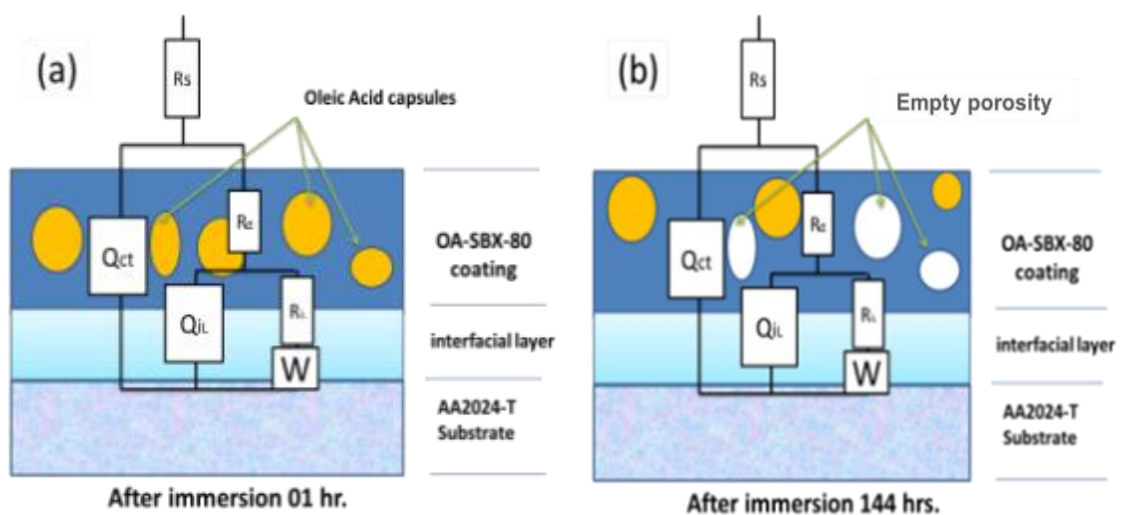
Figure 6-26 the equivalent circuits modelling of OA-SBX-80 (a) after 01hr, (b) after 144hrs

On the other hand, BZI-SBX-80 coated sample kept two time-constants as shown in Figure 6-27 (c and d). The interfacial active layer (R_{iL}) is assumed to originate from the adsorption of BZI with the metallic oxides on the metal surface. This layer shows high electro-negativity reducing the diffusion to the surface and electrolyte media [64], [67], [68].
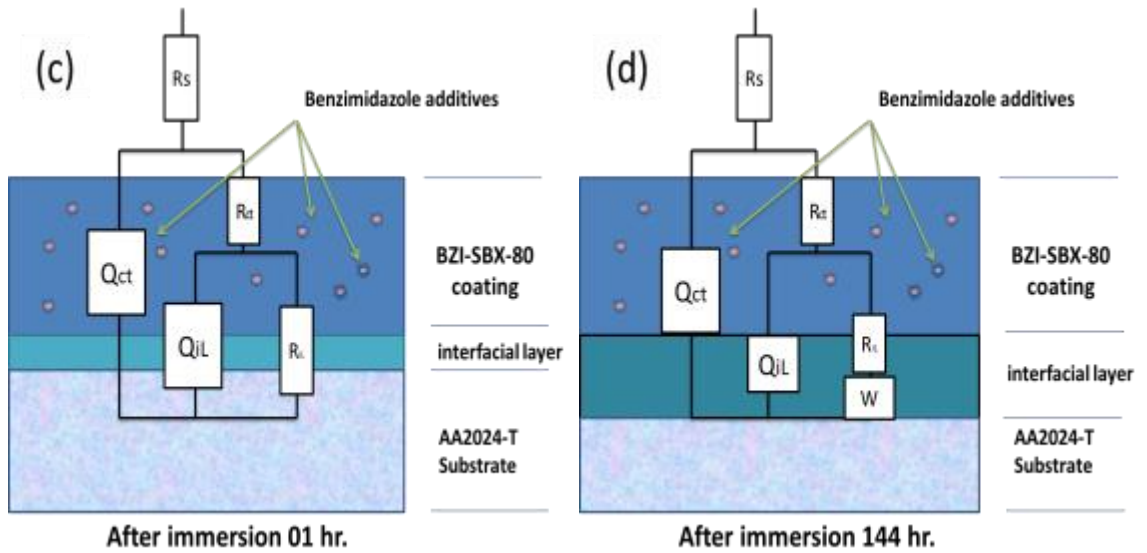
Figure 6-27 the equivalent circuits modelling of BZI-SBX-80 (a) after 01hr, (b) after 144hrs

Though of keeping the created BZI film on the surface working with sol-gel coating resistance after 48 hrs, it is thought that the BZI storage on the sol-gel matrix started to be consumed, which made the coating less resistive to diffusion.
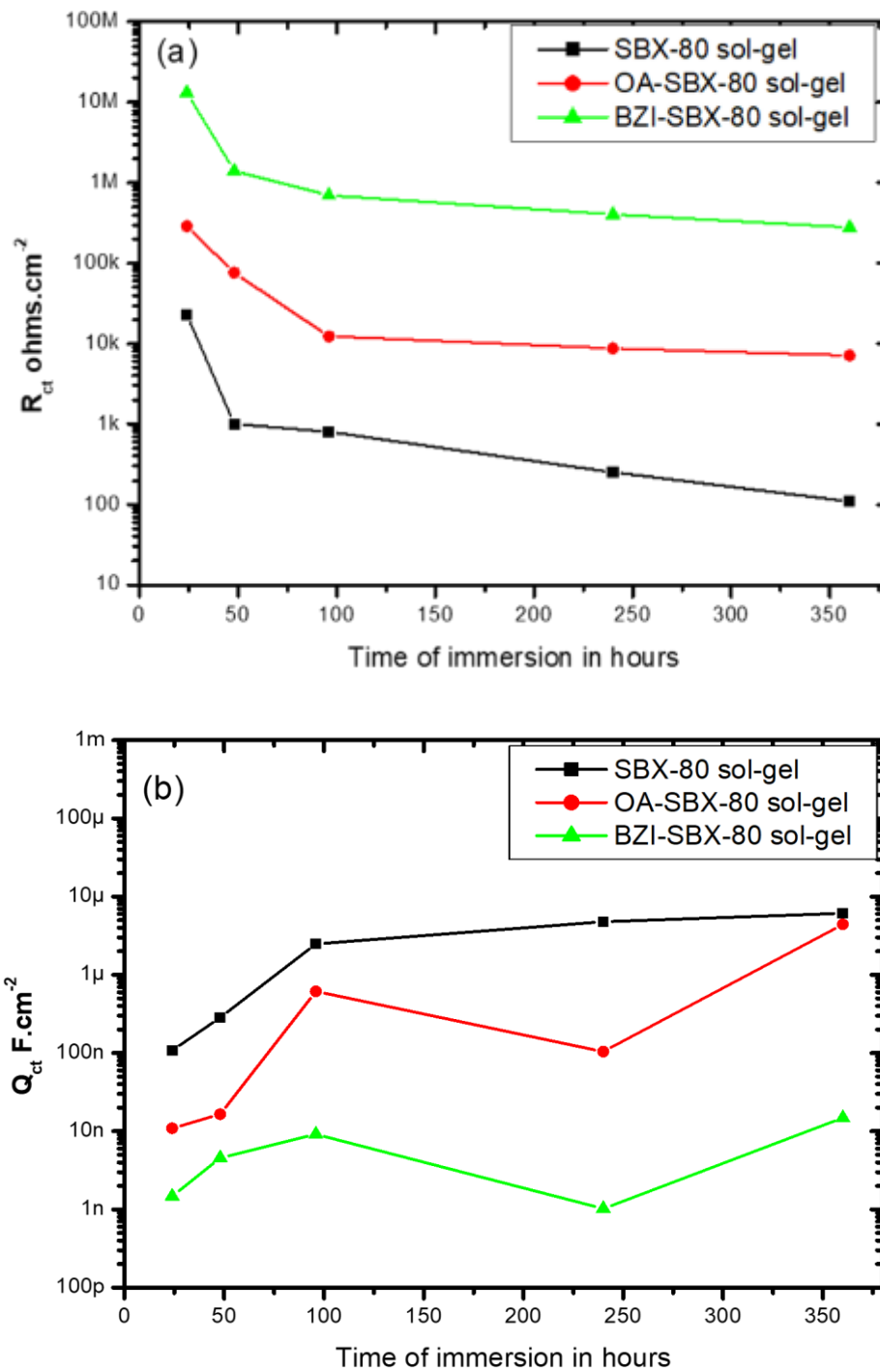
Figure 6-28 Graphs showing (a) Coating Resistance and (b) Coating constant phase for SBX, OA-SBX and BZI-SBX-80 Coatings

As immersion time increases, the reduction in the resistive nature of the coating reflected the onset of degradation. The degradation of the corrosion protection of coatings with and without inhibitors was studied between first to 360 hours of immersion, as shown in Figure **6-28**(a),(b). After one hour immersion, the coating resistance (R_{ct}) of the SBX-80 coating is about one order of magnitude less than the OA-SBX-80 coating and one and a half

orders of magnitude less than the BZI-SBX-80 coating, which indicates that the OA-SBX-80 and BZI-SBX-80 coated samples have a reasonable initial coating resistance.

After 48 hours, the resistance of the SBX-80 coating decreased markedly to 1.01×10^3 ohms.cm^{-2}, before continuing to decline throughout the remainder of the test. This reduction may be due to the weakening of the coating protection as exposure time increases.

After 48 hours the coating resistance of the OA-SBX-80 dropped from an initial value 2.8×10^5 ohms.cm^{-2} to 7.6×10^4 ohms.cm^{-2}. This after remained relatively constant for the remainder of the test period.

On BZI-SBX-80 sol-gel coated sample, the initial coating resistance value starting from 1.3×10^7 ohms.cm^{-2} then after 48 hours dropped to 1.4×10^6 ohms.cm^{-2} then after 96 hours stilled on 6.9×10^5 ohms.cm^{-2} the remainder of the test period.

The resistances of the coated systems have a corresponding coating constant phase element (Q_{ct}) with capacitative behaviour after the first hour of immersion by $1.07x10^{-7}$, $9.913x10^{-9}$ and $3.15x10^{-9}$ F.cm^{-2} for SBX-80, OA-SBX-80 and BZI-SBX-80 respectively.

This capacitative behaviour indicates increases the overall impedance of the coatings. However, due to degradation after 360 hrs of immersion, the SBX-80 and OA-SBX-80 coatings capacitance effect increases after 240 hrs of immersion to $4.771x10^{-6}$ and $1.04x10^{-7}$ F.cm^{-2} respectively for both SBX-80 and OASBX-80 coatings [18]. The BZI-SBX-80 coating showed levelling-off in the same magnitude about $9.15 \ x10^{-9}$ F.cm^{-2}. [103].

6.5 Duplex benzimidazole sol-gel and oleic acid OA-BZI-SBX-80 sol-gel coating System on aluminium alloy 2024-T3

As individual additives, Benzimidazole and oleic acid give good results that indicate an enhancement of the basic SBX sol-gel formula. However, the need to investigate the two inhibitor system arises from a desire to incorporate both the advantages of an active film of benzimidazole and pore-blocking of oleic acid that enhance the sol-gel stability and resist of the electrolyte diffusion to the metal surface.

Therefore, the improvement of primary SBX-80 sol-gel coating was done by adding both organic corrosion inhibitors of benzimidazole (BZI) on the top layer and oleic acid (OA) on the second layer with their previous tested ratios. The improvement was done on the SBX-80 formula by adding 3.5% v/v ratio of the solution of Benzimidazole (BZI) $C_7H_6N_2$ and small ratio of about 0.1 % v/v of oleic acid (OA), and applying them separately on the surface as shown in Figure 6-29. This modified coating system will be coded as OA-BZI-SBX-80 sol-gel as mentioned previously in the chapter 3 section 3.7.4 and in identifying Table 3-2 page 177 .
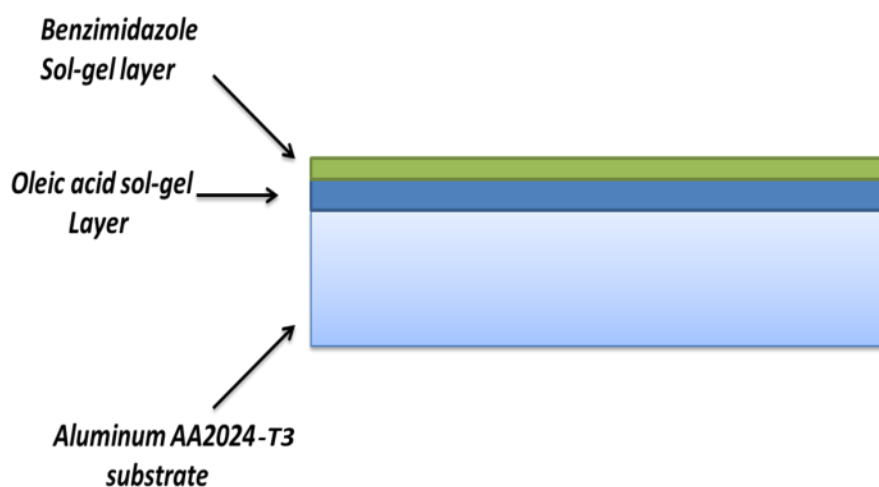
Figure 6-29 the double layer sol-gel coating system of BZI and OA

6.5.1 Surface morphology and elements of modified BZI-SBX-80 sol-gel coating

The general behaviour of the surface of OA-BZI-SBX-80 sol-gel coating on the substrate was even and smoothed as it shows in Figure 6-30 (a). It is noticeable that the cross-section as showed in Figure 6-30 (b) the thickness of the coating systems were about 10 ± 2 μm for each layer.
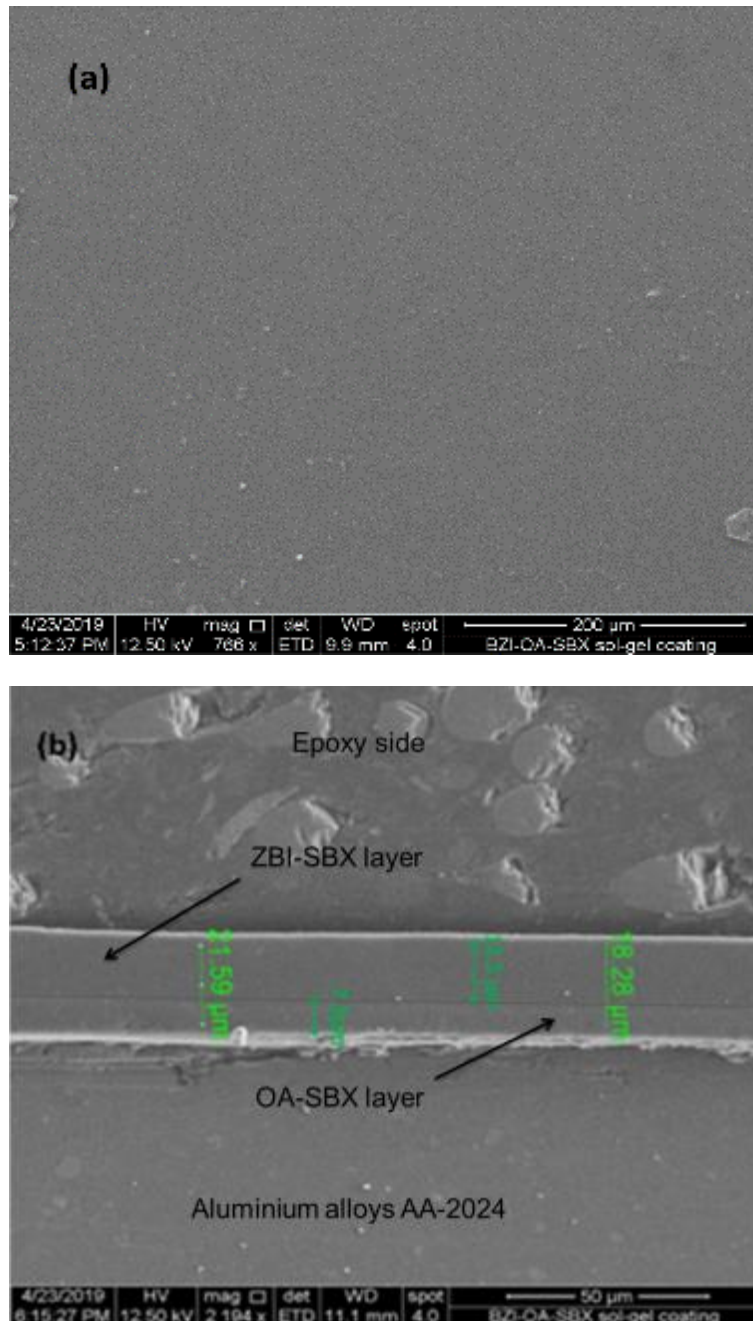
Figure 6-30 (a) surface morphology and (b) cross-section SEM

images for OA-BZI-SBX-80 sol-gel coating system

The EDX images and spectroscopy in Figure 6-31 can verify the chemical elements in the sol-gel such as Si, C, O and the small detected amount of nitrogen N reflects the small percentage of benzimidazole inhibitor in sol-gel these elements were homogeneously distributed on the coating surface.
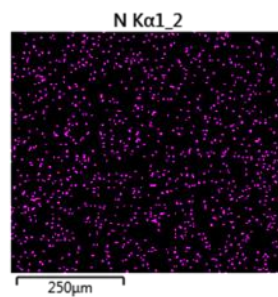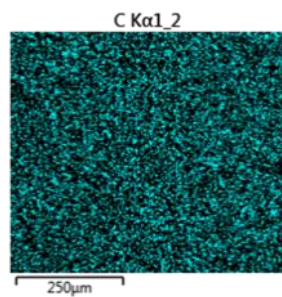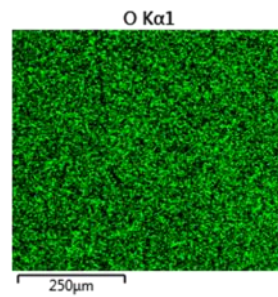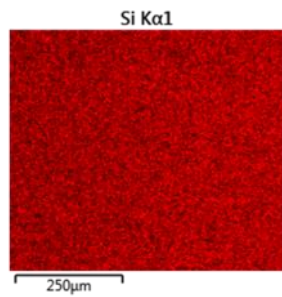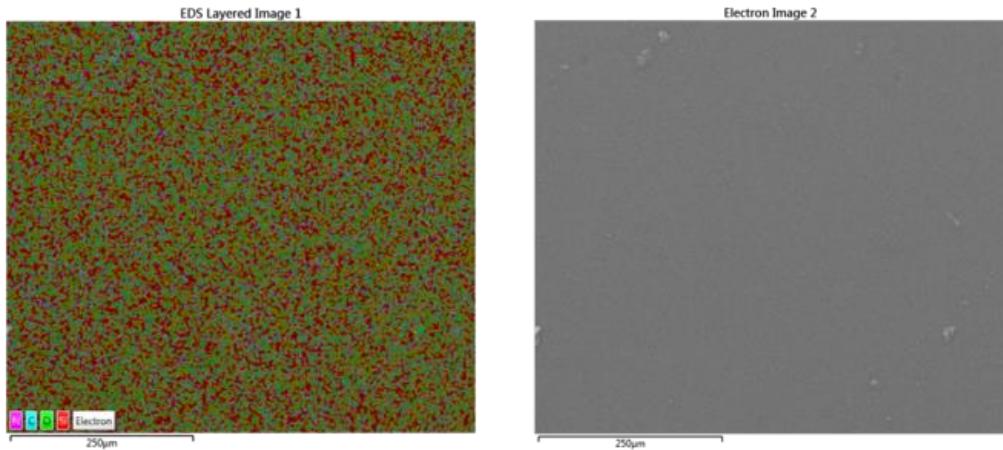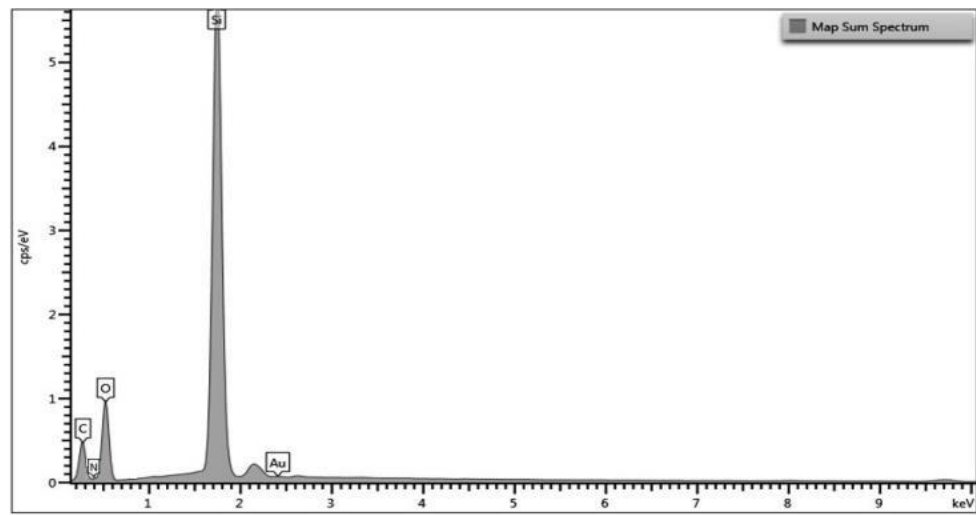
Figure 6-31 EDX mapping and spectroscopy for OA-BZI-SBX-80 coating system

6.5.2 Electrochemical impedance spectroscopy (EIS) analysis for sol-gel double-layer coating system OA-BZI-SBX-80

Tests were performed over a period of 1440 hours. Figure 6-32 and Figure 6-33 show impedance magnitude and phase angle plots for OA-BZI-SBX-80 coating systems. Starting with the Impedance data of the BZI-OA-SBX-80 sol-gel coated samples, as is shown in Figure 6-32, the general behaviour of the coating is as a protective corrosion inhibitor double-layer coating system with good capacitative behaviour.

After 24 hrs immersion, the impedance at the high frequency of 10^5 Hz starts from about 0.8×10^3 ohms. cm^{-2} reflecting the solution/ coating interface resistance (R_s). Then the impedance rises reflecting that capacitative behaviour attributed to coating protection and diffusion resistance. This reading reaches the higher magnitude at the low frequencies between 10 to 0.01 Hz with value about 5.0×10^6 ohms. cm^{-2} .

After 72 hrs of the immersion, there is a to slightly decrease in the impedance attributed to the slow diffusion in the coating to the metal surface but still maintains the same protection range.

After 120 hrs of immersion, it decreases significantly to about 1.2×10^6 ohms. cm^2 at low frequencies. The coating system continues to provide reasonable protection to reach after 216 hrs about 9.0×10^5 ohms. cm^{-2}. it kept this behaviour with a very small drop in impedance until 60 days with an overall magnitude of 7.1×10^5 ohms. cm^2 .

Correspondingly, the phase angle θ Figure 6-33 showed two time-constants in the first immersion day reflecting the two-layer system. From 9th day the three time-constants started forming. The first one started from 10^5 to 10^3 Hz, the second one began from 10^3 to 1 Hz, and the third one started from 1 to 0.01 Hz, these time-constants tributes to the two layers of OA and BZI with the creation of aluminium oxide film on the metal surface.
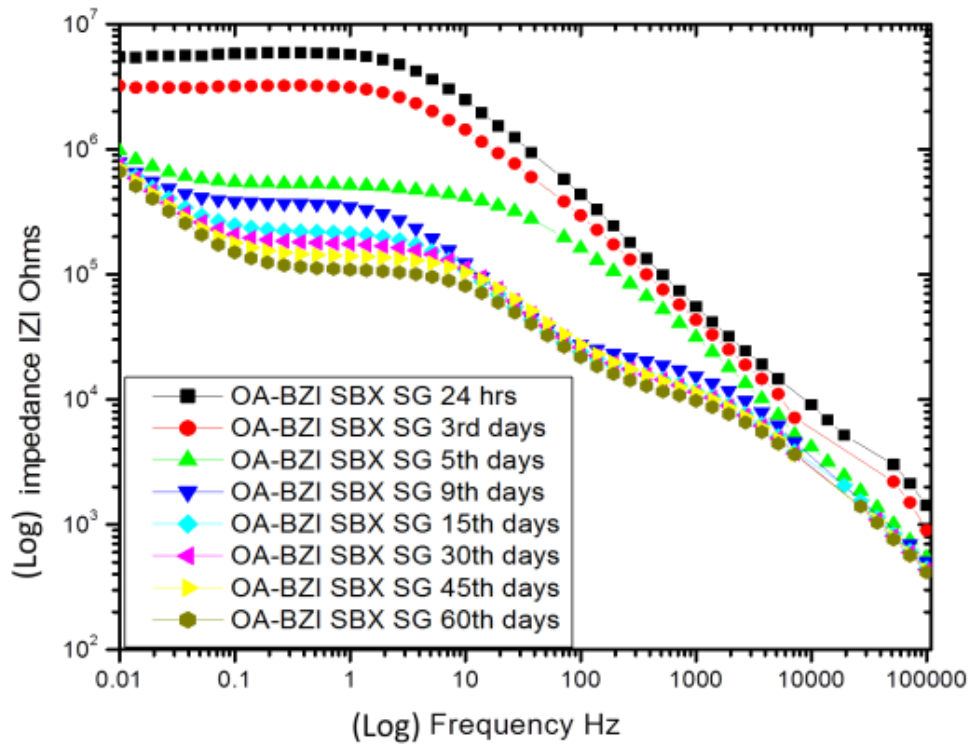
Figure 6-32 Impedance behaviour of BZI-OA-SBX-80 sol-gel coating system in 3.5% NaCl
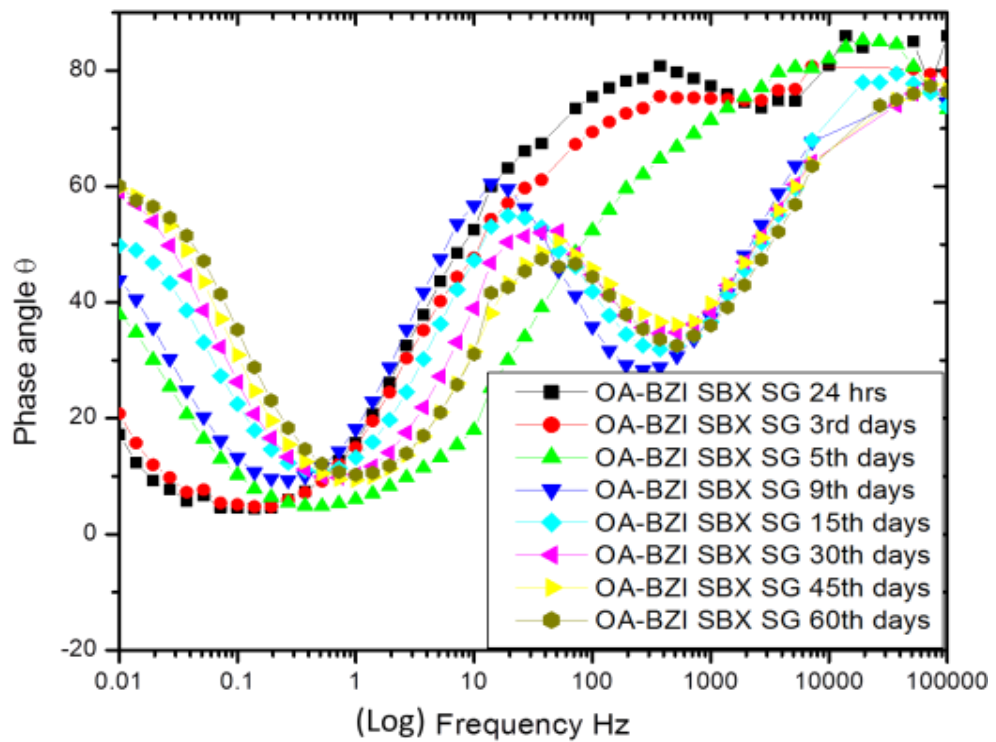
Figure 6-33 Phase angle response of BZI-OA-SBX-80 sol-gel coated system in 3.5% NaCl

6.6 Investigating the corrosion protection behaviour for double layer BZI-OA-SBX-80 sol-gel coating system by using equivalent circuits fitting and modelling

Figure 6-34 shows Nyquist plots for the BZI-OA-SBX-80 coating system from 1st to the 15th day. These EIS data were used for fitting to obtain the equivalent circuits by using ZSimpwin electrochemical impedance spectroscopy (EIS) data analysis software.
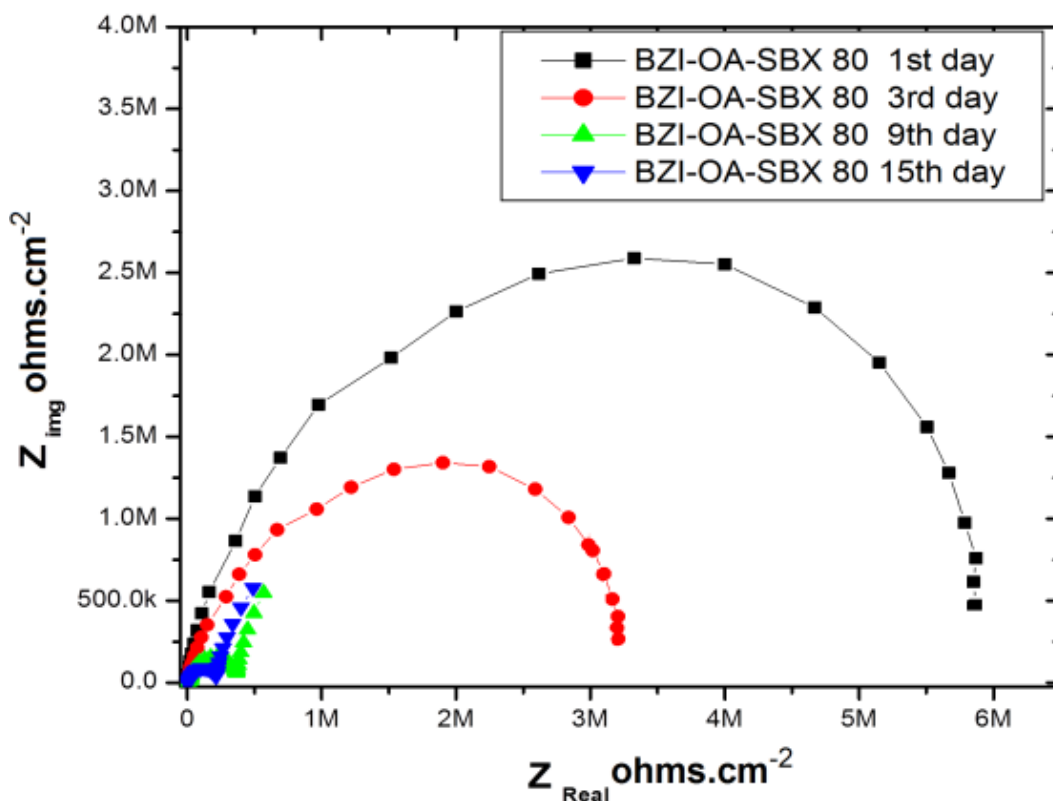
Figure 6-34 Nyquist plots for BZI-OA-SBX 80 coating system

The fitted EIS data plots for BZI-OA-SBX-80 sol-gel coating system for 24 hr, 72 hrs and 216 hrs were given in Figure 6-35 respectively showing the change in the equivalent circuits from tow time-constants to three time-constants after 216 hrs.
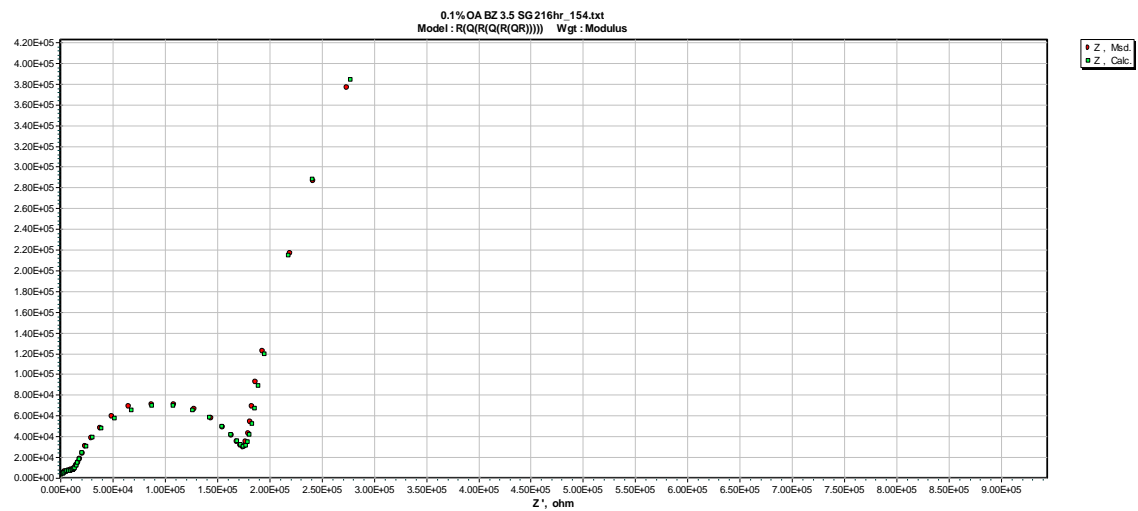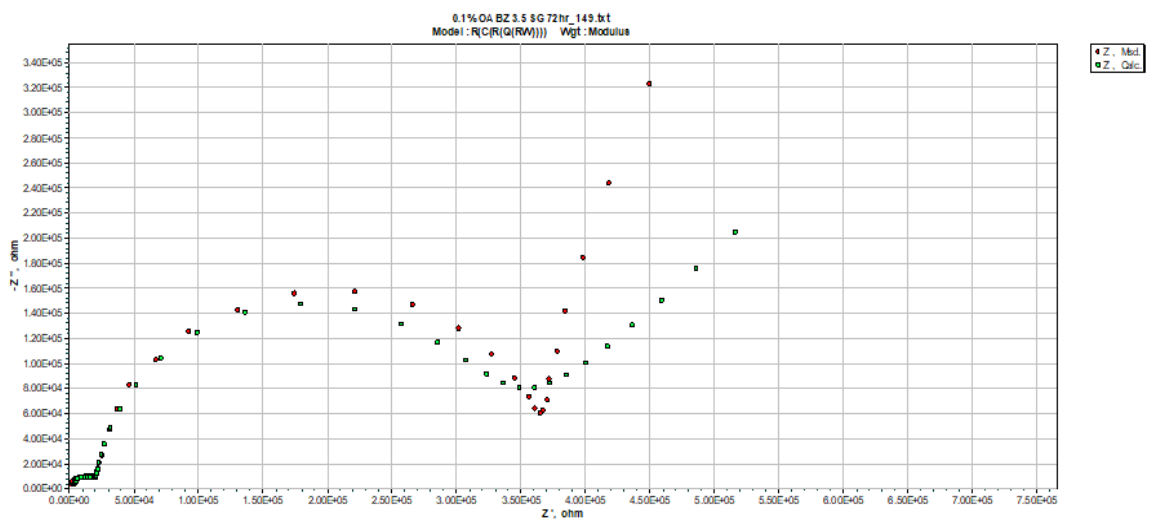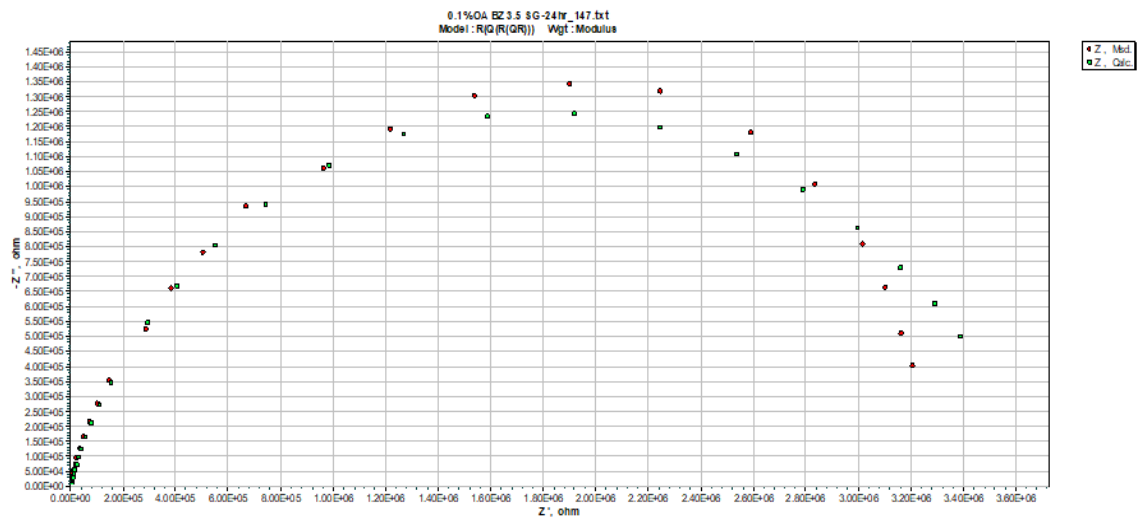
Figure 6-35 EIS data fitting for OA-BZI-SBX-80 in 24hr, 72hrs and 216hrs

Table 6-5 below shows the fitted data obtained from EIS spectra for the BZI-OA-SBX sol-gel coating after various immersion times in 3.5% w/v NaCl solution.

The elements used for the equivalent circuits here were: solution resistance (R_s), coating resistance (R_{ct}), coating constant phase elements (Q_{ct}). The interfacial layer with OA/BZI film resistance (R_{iL}), the interfacial layer with OA/BZI capacitance (Q_{iL}), passive layer resistance (R_p), passive layer capacitance (Q_p), and a Warburg diffusion element (W_{iL}) [151].

Table 6-5 The fitted data obtained from EIS spectra for the OA-BZI-SBX-80 sol-gel coating after various immersion times in 3.5% w/v NaCl solution.

	immersion time (h)	Of Trial System		
Element	24	72	216	360
Circuit	R(Q(R(QR)))	R(Q(R(Q(RW))))	R(Q(R(Q(R(QR)))))	R(Q(R(Q(R(QR)))))
R_s	112	162	185	129
Q_{Ct}	2.362E-8	6.127E-8	2.372E-8	2.188E-8
n	0.7022	1.0	0.858	0.8363
R_{ct}	1.788E6	1.974E5	1.671E5	1.109E4
Q_{iL}	1.922E-9	1.418E-7	1.517E-7	2.455E-7
n	1	0.954	0.892	0.829
R_{iL}	3.702E6	2.970E6	2.076E5	1.034E5
W_{iL}	-	1.009E-5	-	-
Q_p	-	-	1.745E-5	1.771E-5
n	-	-	0.934	0.898
R_p	-	-	2.612E6	9.011E6
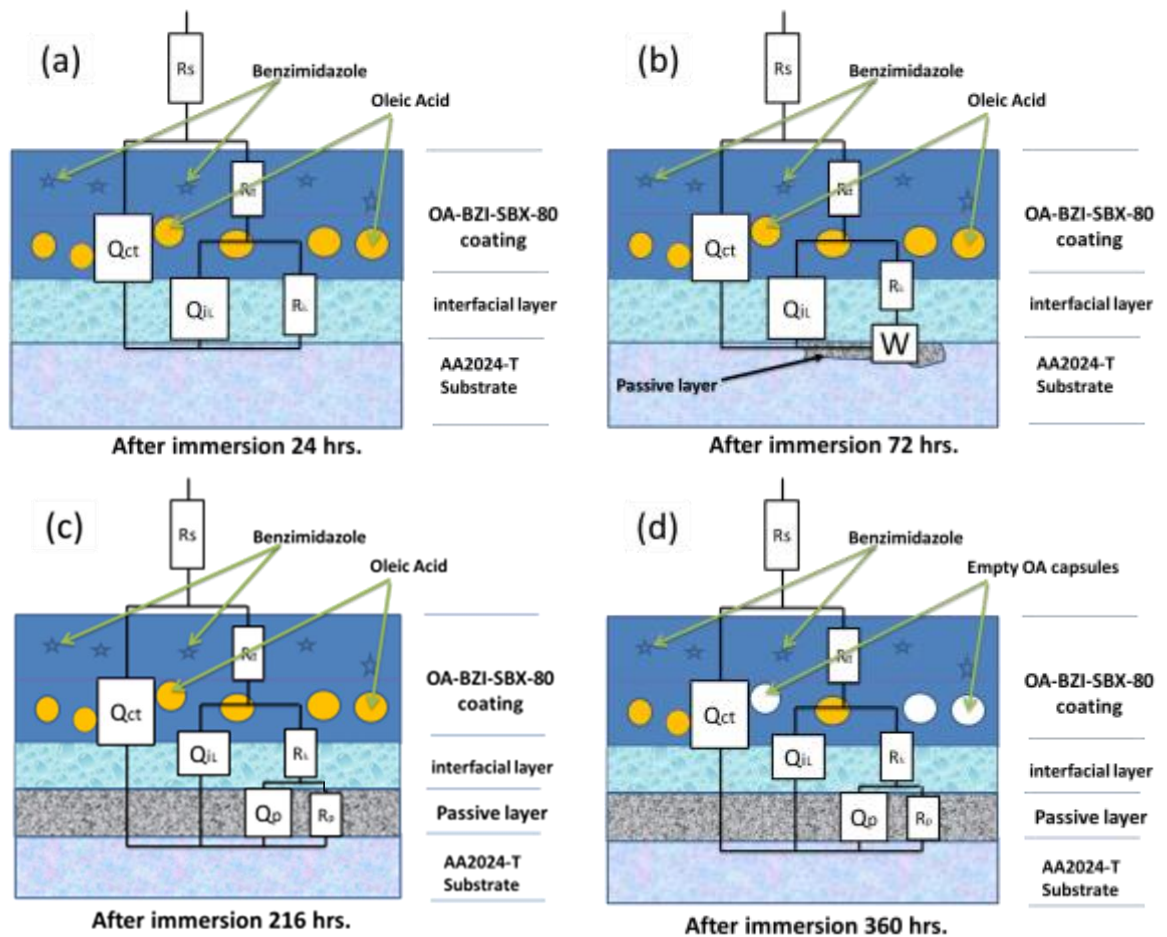
Figure 6-36 the Fitting modelling for OA-BZI-SBX-80 sol-gel coating system in 24 hrs, 72 hrs, 216 hrs and 360 hrs

From the first day of immersion, the BZI-OA-SBX-80 sample exhibit different behaviour from control SBX-80. It is started with three resistance elements and two time-constants, as shown in Figure 6-36(a).

However, after 72 hours of immersion in Figure 6-36(b). BZI-OA-SBX-80 sample shows a new response the coating EIS fitting results indicate very small element (W_{iL}) which might be from the effect of diffusion in the interfacial layer and creating oxide layer. In Figure 6-36(c) shows after 216 hrs the response changed to three time-constants which that also can be seen in Figure 6-33 the phase angle diagram clearly, The time-constants element can be explained as the following; the first time-constant arises in the high-frequency range and may be attributed to barrier properties of the coating, the second one may be attributed to the resistance of the active OA/BZI interfacial layer and the third one may be attributed to the resistance of passive layer on the substrate surface as shown in Figure 6-36 (d).
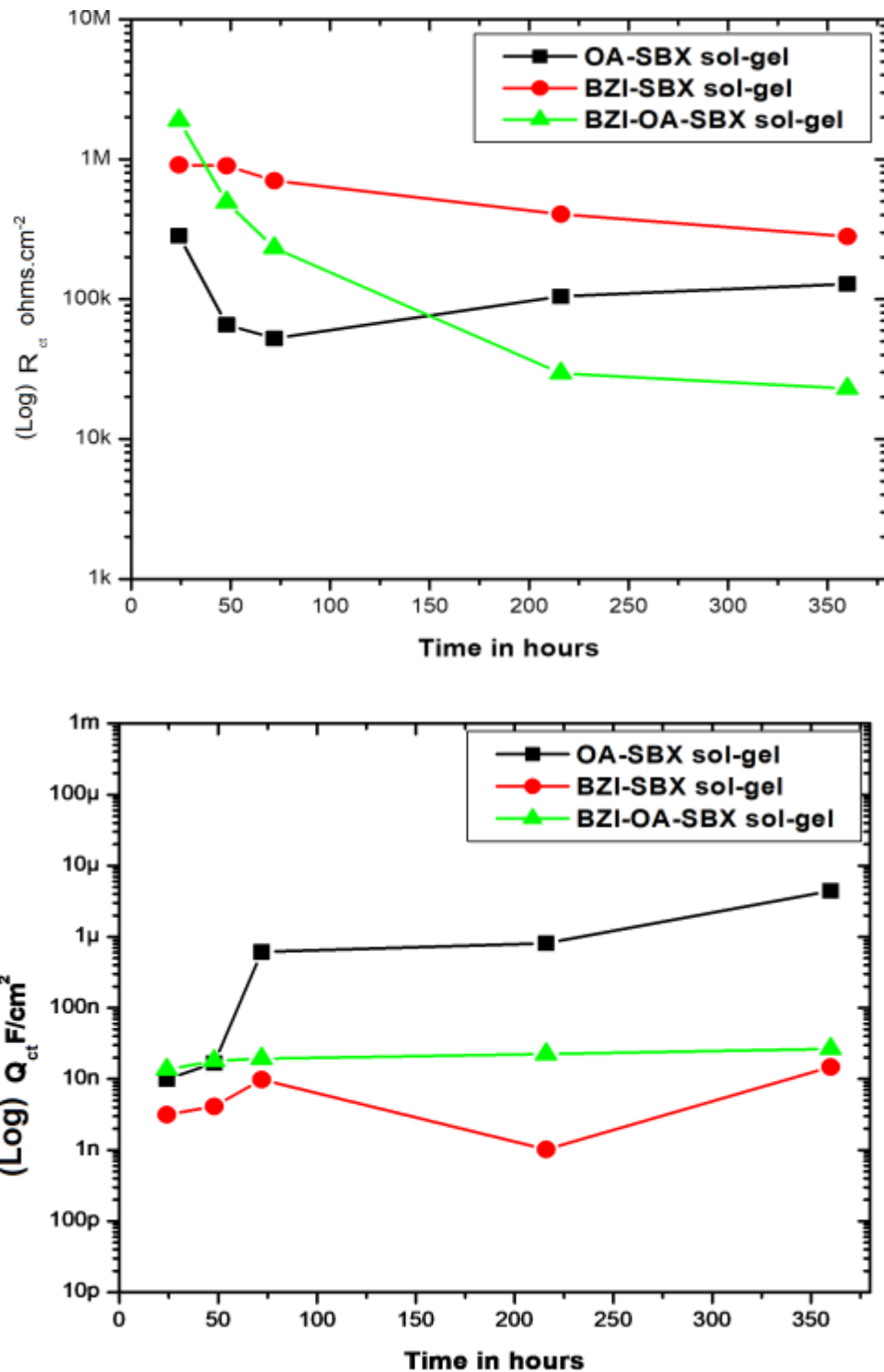
Figure 6-37 Graphs showing coating resistance and coating constant phase elements for OA-SBX-80, BZI-SBX-80 and BZI-OA-SBX-80 Coatings systems

The degradation of the corrosion protective characteristic of the coatings was studied between one and 360 hours immersion, as shown in Figure 6-37. After one hour immersion, the coating resistance (R_{ct}) of the BZI-OA-SBX-80 coating is approximately one order of magnitude more prominent than the OA-SBX-80 coating and half of the order

magnitude bigger than BZI-SBX-80 coating, which indicates that the BZI-OA-SBX coated sample has a satisfactory initial coating resistance.

After 48 hours, the resistance of the BZI-OA-SBX-80 coating resistance decreased from 1.9×10^6 ohms.cm^{-2} to 4.92×10^5 ohms.cm^{-2}, before continuing to decline throughout the remainder of the test. This reduction may be due to the weakening of the coating protection as exposure time increases. After 216 hours the coating resistance of the BZI-OA-SBX-80 dropped to 2.95×10^4 ohms.cm^{-2}. then after 360 hours remaining relatively consistent for the remainder of the test period. With the comparison to the BZI-SBX sol-gel coated sample the behaviour is changed to demonstrate a kind of stability reflected in the levelling-off of the coating resistance value starting from 9.1×10^5 ohms.cm^{-2} remaining relatively consistent for the remainder of the test period. These resistances of coated systems have a corresponding coating constant phase element (Q_{ct}) with capacitance behaviour of 1.356×10^{-8}, 9.913×10^{-9} and 3.15×10^{-9} F.cm^{-2} for BZI-OA-SBX-80, OA-SBX-80 and BZI-SBX-80 respectively after one hour of immersion. Due to coating performance degradation, the BZI-OA-SBX-80 coating capacitative effect stayed levelled off during the period of 360 hrs with an average of 2.0×10^{-8} F.cm^{-2}. Also, the BZI-SBX-80 showed levelling off in the same magnitude about 3.0×10^{-9} F.cm^{-2}. The mixed coating system BZI-OA-SBX-80 gave the advantages of both systems which meant it retained its corrosion protection ability longer than the two mono coating system.

6.7 Sixth Chapter Summary

Benzimidazole and oleic acid revealed excellent corrosion protection when combined with the base SBX formula.

The highest initial EIS impedance came from the BZI sol-gel coating (BZI-SBX-80). Oleic acid has excellent durability, which can make the coating last longer with moderate protection. However, oleic acid creates encapsulation in sol-gel affects the overall impedance. After a long time of immersion, these OA capsules were consumed, which could cause leakage of electrolyte solution into the coating to the metallic surface that might lead to coating to failure.

The combined system of using both benzimidazole and oleic acid together in the sol-gel formula can bring the advantages of initial impedance and the durability of the coating which can last more than three months in 3.5% NaCl without visual signs of corrosion.

Chapter 7- Analysing the Mechanical Properties of Hybrid Organic-Inorganic Sol-Gel Coatings with and without Inhibitors

Overview

In this chapter will present the general mechanical performances of Sol-gel coatings system by examining the coatings mechanical properties of film hardness, nano-indentation and adhesion.

7.1 Micro-hardness

The microhardness for all sol-gel coatings systems with and without inhibitors was measured; these samples were started by using the hardness tester machine with Vickers indenter with a 50-10 g force load. The bare aluminium alloy AA2024-T3 substrate was also tested for comparison. Table **7-1** shows the microhardness values of all coatings and the bare sample. The effect of adding the PFOTS precursor on the original SBX-80 formula leads to a decrease in the hardness level from 62.8 HV0.01 in the SBX coating to 24.6 HV0.01 in the F-SBX coating.

Table 7-1 Micro-hardness test results

No	Sample name	Hardness Values
1	*AA2024-T3*	*146.95 HV 0.05*
2	*SBX-80 sol-gel coating*	*62.8 HV 0.01*
3	*F-SBX sol-gel coating*	*24.6 HV 0.01*
4	*OA-SBX-80 sol-gel coating*	*30.8 HV 0.01*
5	*BZI-SBX-80 sol-gel coating*	*87.8 HV 0.01*

Since the meaning of the hardness is the resistance of a material to localised plastic deformation means the new F-SBX-80 coating was less resistant to deformation which makes it more plastic allowing the coating to be capable of absorbing the mechanical stress lead it reducing the chance of the cracking. The effect of adding the benzimidazole as an inhibitor on the original SBX-80 formula is to increase the hardness from 62.8 HV0.01 in the SBX coating to 87.8 HV0.01 in the BZI-SBX-80 coating, which means the new BZI-SBX-80 coating has more resistance to deformation which makes it harder and denser.

However, this might increase the possibility of cracking, and that is why 3.5% BZI was added to the sol-gel as this represents the limit of the critical thickness not affecting and making the coating crack easily.

The effect of adding oleic acid to the sol-gel formula is affecting the hardness of the coating by reducing to 30.8 HV0.01. This might be due to the lubrication property of the fatty acid, which can reduce the friction inside the sol-gel matrix.

7.2 AFM nano-indentation

The definition of Young's modulus is a measure of the ability of a material to withstand changes in length when under lengthwise tension or compression. This referred to the effect was apparent on the coating to change that mechanical behaviour allowing this modified coating suiting and adsorb the residual stresses from the heat treatment, and as a result, will reduce micro-cracking due service.
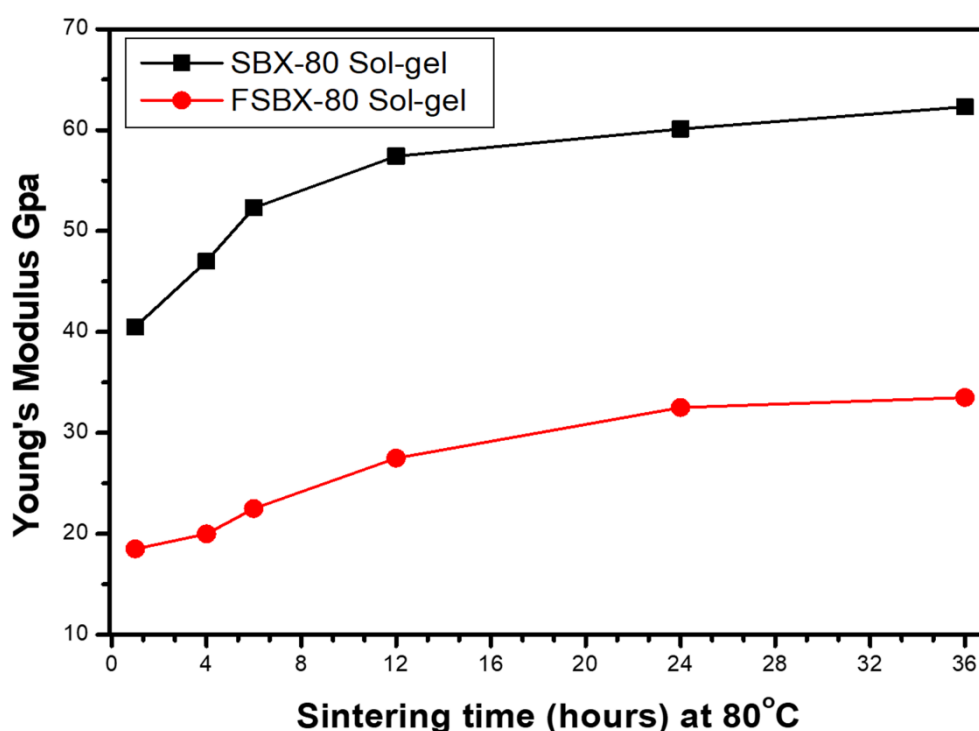
Figure 7-1 The relation between Young's Modulus of Sol-gel coatings and the long sintering time at 80ºC

AFM nano-indentation was used to investigate the changes in elasticity property for both types of sol-gel coatings SBX and F-SBX sol-gel at long curing in 80ºC. Figure 7-1 is shown the graph of the relation between Young's modulus and long sintering at 80ºC to both Sol-gel coatings obtained by AFM nano-indentation and the effect of long sintering time at 80ºC.

The readings of AFM nano-indentation is confirming that the effect of adding the PFOTS precursor to the base SBX formula is causing the decrease in the young's modulus values from an average of 54.5 Gpa in the original SBX-80 to 24.5 Gpa in the dried modified F-SBX-80 coating film after 8 hours at 80°C.

7.3 Adhesion tests

The sol-gel systems have excellent adhesion on aluminium alloy AA2024-T3 substrates. However, mechanical adhesion can be checked more by using the cross-cut adhesion test and the pull-off test.

7.3.1 Pull off adhesion test

The results of the tests are shown in Figure **7-2.** The sol-gel coating SBX-80 had excellent adhesion on AA2024 compared to other coating systems. However, all the enhanced sol-gel coating systems, including the double layer BZI-OA-SBX, revealed a drop in the adhesion pull-off force value. In addition, the F-SBX-80 coating adhesion test fails after maximum reading after roughening the surface at 2.1 MPa without any sign of coating delamination which reported as glue failure; this may be attributed to the hydrophobic property of this coating, which reduces the adhesion of the glue and dollies.

Figure **7-3** presents images of the samples after pull-off testing, along with their corresponding dollies. The test was performed in 5 times repetitions. Despite, the colourless coating of sol-gel coatings, the images show that different levels of delamination.

The mechanical adhesion significantly decreased with the addition of VCI inhibitors such as benzimidazole and oleic acid, in the BZI-SBX, OA-SBX-80 and BZI-OA-SBX mixed systems.
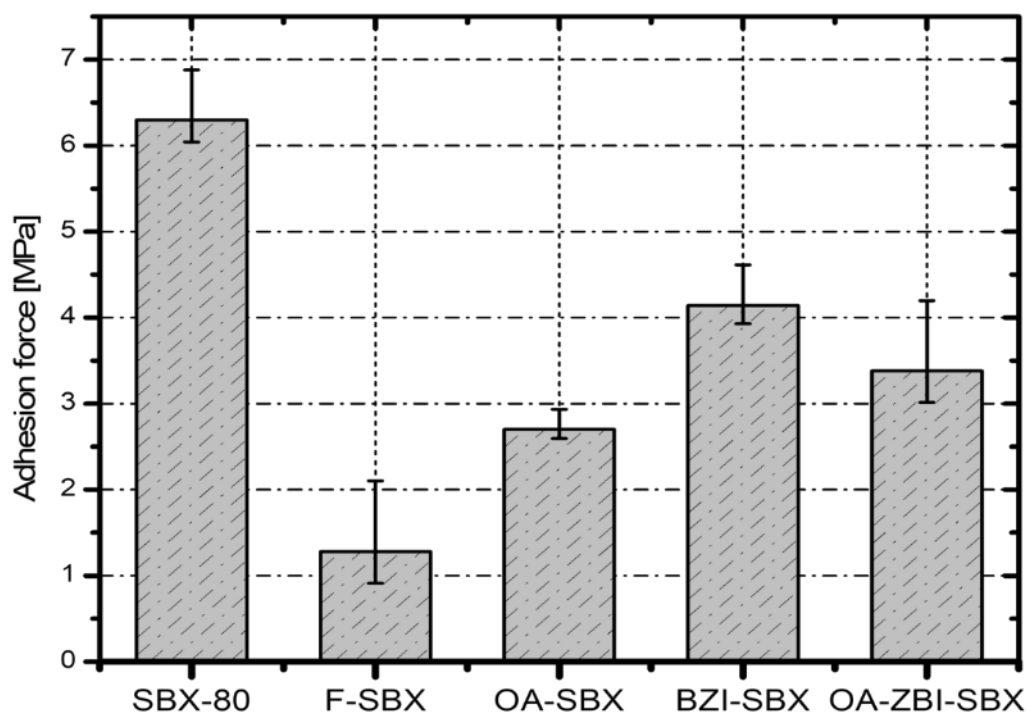
Figure 7-2 Pull-off adhesion test results of sol-gel coating systems

The SBX-80, OA-SBX-80 and BZI-SBX-80 sol-gel coatings did not show complete coating delamination on the dollies which can be reported as an adhesive failure. The OA-BZI-SBZ-80 coating system shows different responding as mixed Adhesive and cohesive failure. The failure of taking the reading for the F-SBX-80 adhesion requires another supporting test which was cross-cut adhesion test. Table 7-2 shows the adhesive and cohesion failure reading for all tested samples.

Table 7-2 The adhesion reading and type for all tested samples

Samples name	Adhesion mean (MPa)	Max	Min	Standard deviation	Attribute	comments
SBX-80	6.30	7.00	5.5	0.517	95%A/B	Adhesive failure
F-SBX-80	1.25	2.10	0.5	0.822	0%A/B	Glue failure
BZI-SBX-80	4.14	4.6	3.4	0.472	90%A/B	Adhesive failure
OA-SBX-80	2.70	2.9	2.4	0.234	40%A/B	Adhesive failure
BZI-OA-SBX-80	3.40	4.5	2.8	0.730	55%A/B,20%B	Adhesive, cohesive failures
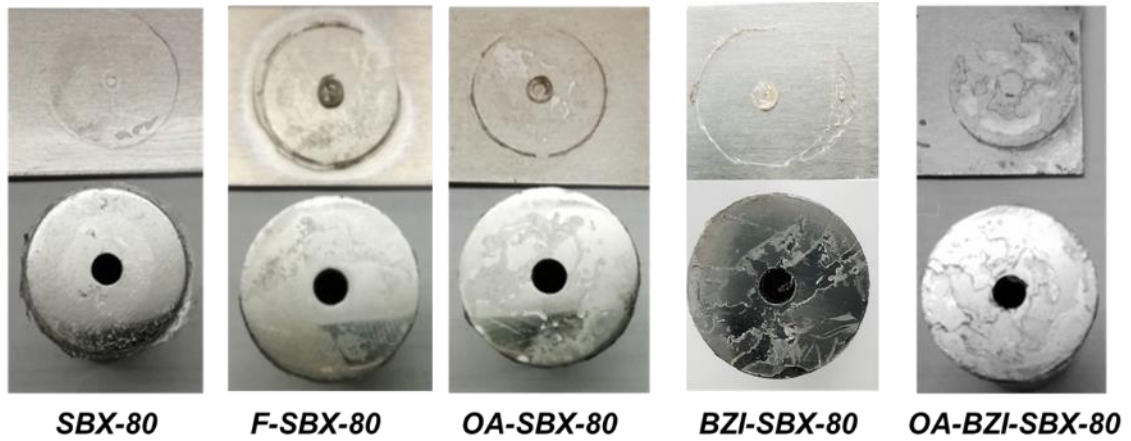
Figure 7-3 images of the pull-off test on coated samples with their dollies

7.3.2 Overall cross-cut adhesion test

The results of the cross-cut adhesion test are shown in Figure **7-4**. The cross-cut test was applied for all coated samples in support of the results of the pull-off test. Also, this test was used to evaluate the initial adhesion performance on every sample alone, as shown in Table **7-3**.

Table 7-3 cross-cut adhesion results of all sol-gel coated samples

No	Sample name	Classification	% of the removed area
1	*SBX-80*	5B	0%
2	*F-SBX-80*	4B-5B	< 5%
3	*OA-SBX-80*	5B	0%
4	*BZI-SBX-80*	4B	< 5%
5	*BZI-OA-SBX-80*	4B	< 5%
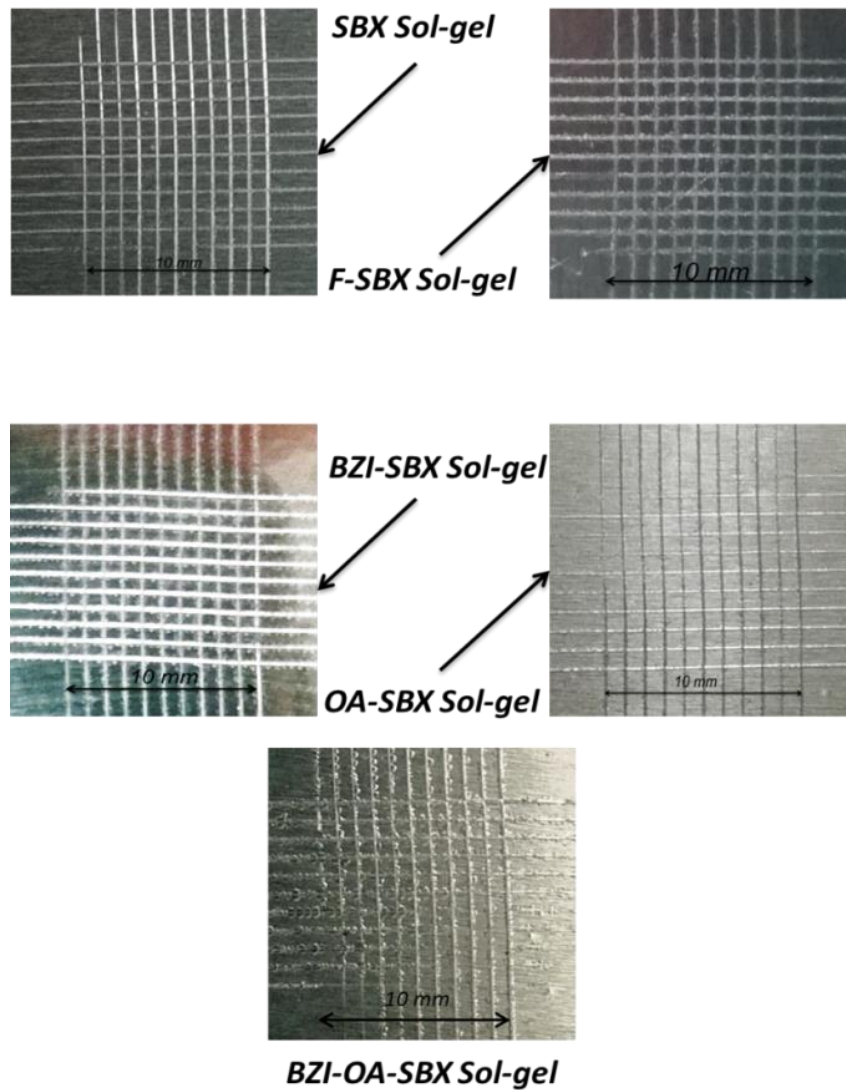
Figure 7-4 the cross-cut adhesion test of different sol-gel coating systems

The results indicate that all sol-gel coatings have a good adhesion level that making them capable of providing protection against delamination and service in the contrast of the other technique.

7.4 Seventh Chapter Summary

The hardness measurement revealed that depending on the additive type, the hardness would change. Adding the fluorinated additive in F-SBX-80 sol-gel is reduced the hardness, while benzimidazole increases the hardness level on BZI-SBX-80. The affecting of adding oleic acid was less-significant to the hardness of the sol-gel matrix.

The Young's Modulus is changed depending on adding the additive precursors. Also, the time of curing in the fixed temperature can play a significant part in the change of Young's Modulus reading.

The initial adhesion properties values of all sol-gel coatings system were acceptable from the standards perspective.

Chapter 8- Conclusion

This research project investigating and reporting new approaches and applications of mixed sol-gel with film-forming (VCI) corrosion inhibitors, e.g. in this project were benzimidazole (BZI) and oleic acid (OA). These approaches were investigated systematically to evaluate the performance against corrosion, and the main findings and conclusions were listed below:

8.1 Optimum formulation and restrictions

- The base SBX sol-gel formula was enhanced by adding fluorinated precursor PFOTS that gave the highest water contact angle, and this was done by adding 1.5% v/v, to the basic SBX formula and hydrolysed for 24 hours.

- The effect of adding PFOTS to the base SBX formula was limited other inhibitors due to the hydrophobic effect.

- The best combination of oleic acid to SBX sol-gel is produced by adding the oleic acid to the sol-gel within the ratio 0.1 to 0.5 % v/v. This was attributed to the creation of some oleic acid enrichment capsules, which act as film-forming inhibitors but reduce the strength of sol-gel coating when it becomes unfilled.

- The best combination of benzimidazole and SBX sol-gel is produced by adding benzimidazole to the SBX sol-gel with a maximum ratio of 3.5 % v/v which increses the protection without increasing the brittleness of the sol-gel coating that causes cracks and delamination on the substrate.

- Curing for 4 hours at 80ºC was good enough to demonstrate appropriate stability for all sol-gel coating systems.

8.2 Corrosion performances conclusion

- Bare aluminium alloy 2024-T3 is very susceptible to corrosion when it immersed in 3.5% NaCl solution.

- Applying oleic oil only on the surface can protect the AA2024-T3 from direct atmospheric corrosion and in 3.5% NaCl solution. However, the created film attachment on the surface is fragile and can be easily removed. Pitting appears after three days of direct immersion.

- The oleic oil film adsorption on the AA2024-T3 was observed since the carboxylic group was changed to the bridging connection to the metal surface.

- Benzimidazole only has good protection on AA2024-T3 in direct immersion and can last for more than five days without the creation of pits.

- The benzimidazole film-forming (adsorption) was observed visually, and by SEM and EDX on the metallic surface as a film.

- The base SBX Sol-gel formula can provide good barrier protection without the presence of any inhibitor. The protection can last for at least ten days in 3.5% NaCl solution before cracks and pitting appears visually on the coating surface.

- Fluorinated F-SBX sol-gel coating offerings good corrosion protection. This is due to the enhancement from the fluorinated function groups in PFOTS precursor, which can perform as barrier protection due to its hydrophobicity.

- Oleic acid /base SBX sol-gel formula showed good corrosion protection that lasted for up to one month without the appearance of cracks or pitting corrosion.

- Benzimidazole SBX sol-gel formula is considered good to use for corrosion protection and can last up to one month. Adding benzimidazole inhibitor to the sol-gel matrix can provide active protection due to the high electronegativity. The highest impedance can be gained by this inhibitor.

- The mixed system of BZI/OA sol-gel can provide high impedance protection. This coating system lasted for more than three months without appearing to show any sign of corrosion on the coating or metal surface.

8.3 Mechanical testing conclusion

- The effect of adding PFOTS to the sol-gel reduced the value of Young's Modulus and hardness levels as compared to the base SBX sol-gel.

- Post-immersion cracking is reduced by adding PFOTS precursor to the basic SBX sol-gel formula.

- The hydrophobic property of PFOTS has enhanced the sol-gel coating allowing it to be used as a monolayer or as top coating on a complete system.

- Sol-gel only offering excellent adhesion on AA2024-T3 substrates as observed from cross-cut and pull-off testing techniques.

- Oleic acid / sol-gel coating revealed a reduction in the adhesion of the combination to the AA2024-T3 substrate. And this might be attributed to surface wettability of active molecules.

- Benzimidazole/ sol-gel coating revealed an increase in the hardness and brittleness of the coatings.

Chapter 9- Future work

During the course of this PhD project, the following future works have been identified:

- Further optimising and improving to BZI / sol-gel system to use for protecting AA 2024 and other Aluminium alloys in acidic and alkaline medium.

- Further optimising and improving to oleic acid /sol-gel system with more investigated on the adsorption mechanism on the surface of AA2024-T3 and other aluminium alloys in acidic and alkaline medium.

- Further study the chemical interaction of inhibitors with sol-gel and inhibitors with aluminium alloys surface.

- Further understanding of the chemical nature of the group connection of Al-O-C and Al-O-N chemical compounds and as this may lead to the understanding of reactions with similar material, this can be achieved by using the chemical analytical techniques including NMR, FTIR and Raman.

- Further development to the fluorinated sol-gel formula to suit adopting corrosion inhibitors without reacting or affecting the cross-links of the sol-gel coating.

- Further investigation should be carried on the sol-gel to adopt another type of inhibitors. For instance, by adding phosphate and polyphosphate derivatives inhibitor such as Zinc dialkyldithiophosphates (ZDDP), or by using Chemisorption as self-assembled monolayered and active corrosion protectors, or by using oil and gas corrosion inhibitors such as Benzalkonium chloride that could be working on steel alloys.

- Further investigation of using SBX sol-gel formula with BZI or OA inhibitors for corrosion protection to work on carbon steel alloys or zinc alloy AZ 31.

- Study foiling protection that could be offered by SBX sol-gel formulas with BZI or OA for marine application.

- Further studies to use other precursors excluding MTMS and TEOS to make the sol-gel more adaptable to a wide range of corrosion inhibitors

- Study the applying of salt spray test on the sol-gel with and without film-forming inhibitors coated samples as this is one of the industrial trustee techniques.

- Study and performing simulation on cracking, mechanical fracture and critical thickness of the sol-gel films for one-layer system or multi-layer systems.

References

[1]   K. A. Chandler, *Marine and offshore corrosion*. London: Butterworth & Co Ltd, 1985.

[2]   J. Davis, "Alloying: understanding the basics-light matels and alloys," in *Materials Science and Technology*, ASM International Staff, Ed. ASM International®, 2001, pp. 351–416.

[3]   N. Palaniswamy and R. Bhaskaran, "Global Cost of Corrosion: A Historical Review," in *ASM International Handbook: Corrosion Materials Vol B13*, Vol 13B., ASM International, 2007, pp. 621–628.

[4]   M. Mostafa, "Hybrid sol-gel /polyaniline coating for the corrosion protection of AA2024," PhD Thesis, Sheffield Hallam university, 2009.

[5]   D. Wang and G. P. Bierwagen, "Sol–gel coatings on metals for corrosion protection," *Prog. Org. Coatings*, vol. 64, no. 4, pp. 327–338, Mar. 2009.

[6]   M. May, H. Wang, and R. Akid, "Bond strength of hybrid sol-gel coatings with different additives," *J. Coatings Technol. Res.*, vol. 10, no. 3, pp. 407–413, 2013.

[7]   M. R. Detty, R. Ciriminna, F. V. Bright, and M. Pagliaro, "Environmentally benign sol-gel antifouling and foul-releasing coatings.," *Acc. Chem. Res.*, vol. 47, no. 2, pp. 678–687, 2014.

[8]   J. Aljourani, K. Raeissi, and M. A. Golozar, "Benzimidazole and its derivatives as corrosion inhibitors for mild steel in 1M HCl solution," *Corros. Sci.*, vol. 51, no. 8, pp. 1836–1843, 2009.

[9]   M. M. Osman, R. A. El-Ghazawy, and A. M. Al-Sabagh, "Corrosion inhibitor of some surfactants derived from maleic-oleic acid adduct on mild steel in 1M of H2SO4," *Mater. Chem. Phys.*, vol. 80, no. 1, pp. 55–62, 2003.

[10]   C. Verma and E. Ebenso, "Volatile corrosion inhibitors for ferrous and non-ferrous metals and alloys: A review," *Int. J. Corros. Scale Inhib.*, vol. 7, no. 2, 2018.

[11]   F. Maia, J. Tedim, A. D. Lisenkov, A. N. Salak, M. L. Zheludkevich, and M. G. S. S. Ferreira, "Silica nanocontainers for active corrosion protection," *Nanoscale*, vol. 4, no. 4, p. 1287, 2012.

[12]   M.Hassn, "Mellitah Oil & Gas B.V," 2017. [Online]. Available: https://mellitahog.ly/en/. [Accessed: 12-Mar-2019].

[13] G. H. Koch, M. P. H. Brongers, N. G. Thompson, Y. P. Payer, and Virmani J H, "Corrosion Costs and Preventive Strategies in the United States [summary of the US FHWA Report publication No. FHWA-RD-01-156]," Ohaio, 2002.

[14] American Petroleum Institute, "American Petroleum API 571 Code 2nd Edition," 2011.

[15] R. Akid, "Corrosion of Engineering Materials," in *Handbook of Advanced Materials: Enabling New Designs*, 1st ed., J. Wessel, Ed. New Jersey: Wiley, 2004, pp. 487–540.

[16] A. Agarwal, A. Tyagi, A. Ahuja, N. Kumar, N. De, and H. Bhutani, "Corrosion aspect of dental implants—An overview and literature review," *Open J. Stomatol.*, vol. 04, no. 02, pp. 56–60, 2014.

[17] D. Talbot and J. Talbot, *Corrosion science and technology*, 3nd Edit. London: CRC Press ; Taylor and Francis distributor, 2018.

[18] G. Koch *et al.*, "International Measures of Prevention , Application , and Economics of Corrosion Technologies Study," ASM International, Houston, Texas, 2016.

[19] R. Montoya, O. Rendón, and J. Genesca, "Mathematical simulation of a cathodic protection system by finite element method," *Mater. Corros.*, vol. 56, no. 6, pp. 404–411, 2005.

[20] K. G. Genootschap, "History of Cathodic Protection," *Royal Belgian Institute of Marine Engineers*, 2017. [Online]. Available: http://www.gallois.be/gg10/gg130/ggSearch_articles/opvragen_artikels_2.php. [Accessed: 21-Feb-2019].

[21] R. Singh, "Need for the Study of Corrosion," in *Corrosion Control for Offshore Structures*, R. Singh, Ed. Boston: Gulf Professional Publishing, 2014, pp. 3–6.

[22] H. P. Hack, *Designing cathodic protection systems for marine structures and vehicles*, 1st ed. West Conshohocken, Pa.: ASTM International, 1999.

[23] B. N. Popov, "Cathodic Protection," in *Corrosion Engineering*, vol. 3, Elsevier, 2015, pp. 599–637.

[24] D. A. Jones, *Principles and Prevention of Corrosion*, 2nd ed. Pearson Education Limited, 1996.

[25] M. . Ali, "Asset corrosion management contracts: Issues and improvements.," *Mater. Perform.*, vol. 50, no. 1, pp. 56–59, 2011.

[26] The Technical Team of the Energy Institute, *Guidance for corrosion management in oil and gas production and processing*, vol. 1. LONDON: Energy Institute, 2008.

[27] M. F. Ashby, *Materials Selection Mechanical Design*, 5th Edit. Oxford: Butterworth-Heinemann, 2017.

[28] I. Polmear, D. StJohn, J.-F. Nie, and M. Qian, "The Light Metals," *Light Alloy.*, pp. 1–29, 2017.

[29] M. Ashby, S. Arnold, and D. Cebon, "Materials Selection for Aerospace Systems," NASA/TM—2012-217411 Materials, Cleveland, Ohio, 2012.

[30] M. Satish Reddy and D. Neeraja, "Aluminum residue waste for possible utilisation as a material: a review," in *Sadhana - Academy Proceedings in Engineering Sciences*, 2018, vol. 43, no. 8, pp. 1–8.

[31] ASTM International, "Standard Specification for Aluminum and Aluminum- Alloy Sheet and Plate," West Conshohocken, B209− 14, 2010.

[32] ASTM International, "ASTM code B209 − 14 Standard Specification for Aluminum and Aluminum-Alloy Sheet and Plate," vol. 25. ASTM International, West Conshohocken, p. 16, 2016.

[33] S. Wu *et al.*, "The Sparse Recovery Autoencoder." University of Texas, Austin, Texas, p. 23, 2018.

[34] R. G. Buchheit, R. P. Grant, P. F. Hiava, B. Mckenzie, and G. 1. Zender, "Local Dissolution Phenomena Associated with S Phase (AI2CuMg) Particles in Aluminum Alloy 2024-T3," *J. Electrochem. Soc.*, vol. 144, no. 8, p. 2621, 1997.

[35] Z. Aburas, "Microstructural characterisation and corrosion studies of excimer laser-treated aluminium alloy AA2024-T351," PhD Thesis , Manchester University, 2013.

[36] W. M. Haynes, D. R. Lide, and T. J. Bruno, *CRC Handbook of Chemistry and Physics (Internet Version)*, 97th Edit. London: CRC Press ; Taylor and Francis distributor, 2017.

[37] Nithya, Xuan, and Yipin, "Pourbaix Diagram for Aluminum," 2016. [Online]. Available: http://ucibiomems.net/wp-content/uploads/2016/11/Pourbaix-Diagram-

of-Aluminum.pdf. [Accessed: 20-Feb-2019].

[38] S. Wernick, R. Pinner, and P. G. Sheasby, *The Surface Treatment and Finishing of Aluminum and its Alloys*. ASM International®, 2001.

[39] P. R. Roberge, *Corrosion engineering: principles and practice*. New York: McGraw-Hill, 2008.

[40] A. Boag, A. E. Hughes, A. M. Glenn, T. H. Muster, and D. McCulloch, "Corrosion of AA2024-T3 Part I: Localised corrosion of isolated IM particles," *Corros. Sci.*, vol. 53, no. 1, pp. 17–26, 2011.

[41] C. Luo, "Role of Microstructure on Corrosion Control of AA2024-T3 Aluminium Alloy," PhD Thesis , University of Manchester, 2011.

[42] C. Vargel, *Corrosion of Aluminium*, First edit. Oxford: ELSEVIER SCIENCE B.V, 2004.

[43] I. Polmear, D. StJohn, J.-F. Nie, and M. Qian, "Physical metallurgy of aluminium alloys," in *Light Alloys*, Fifth Edit., Oxford: Butterworth-Heinemann, Elsevier Ltd, 2017, pp. 31–107.

[44] S. C. Wang and M. J. Starink, "Precipitates and intermetallic phases in precipitation hardening Al–Cu–Mg–(Li) based alloys," *Int. Mater. Rev.*, vol. 50, no. 4, pp. 193–215, 2005.

[45] A. C. Okafor and C. Nnadili, "Evaluation of the effects of corrosion on fatigue life of clad aluminum alloy 2024-T3-riveted lap joints with acoustic emission monitoring," *Journal of Failure Analysis and Prevention*, vol. 12, no. 6, pp. 670–682, 2012.

[46] N. N. Andreev and Y. I. Kuznetsov, "Volatile inhibitors of metal corrosion . I . vaporization," *Int. J. Corros. Scale Inhib*, no. 1, pp. 16–25, 2012.

[47] D. M. Bastidas, E. Cano, and E. M. Mora, "Volatile corrosion inhibitors: A review," *Anti-Corrosion Methods Mater.*, vol. 52, no. 2, pp. 71–77, 2005.

[48] OSHA Tech Staff, "OSHA's Hexavalent Chromium Standard," U.S. Department of Labor Occupational, Boston, USA, 3373–10 2009, 2009.

[49] J. Zak, "Hex Chrome PEL Guidance: An overview of the employee exposure monitoring required for compliance with the new OSHA standard," *OSHA's Stand Review*, Chicago, pp. 41–43, 2006.

[50] Authenticated US Goverment info, "Occupational Safety and Health Admin," no. 1. GPO, New York, pp. 131–142, 2007.

[51] I. Lukovits, E. Kálmán, and F. Zucchi, "Corrosion Inhibitors—Correlation between Electronic Structure and Efficiency," *Corrosion*, vol. 57, no. 1, pp. 3–8, 2001.

[52] K. A. Yasakau, M. L. Zheludkevich, S. V Lamaka, and M. G. S. Ferreira, "Mechanism of corrosion inhibition of AA2024 by rare-earth compounds," *J. Phys. Chem.*, vol. 110, no. 11, pp. 5515–5528, 2006.

[53] H. Wang and R. Akid, "Encapsulated cerium nitrate inhibitors to provide high-performance anti-corrosion sol-gel coatings on mild steel.," *Corros. Sci.*, vol. 50, no. 4, pp. 1142–1148, 2008.

[54] B. A. Rani and B. J. Basu, "Green Inhibitors for Corrosion Protection of Metals and Alloys: An Overview," *Int. J. Corros.*, vol. 12, no. 1, pp. 1–15, 2012.

[55] S. Gangopadhyay and P. A. Mahanwar, "Recent developments in the volatile corrosion inhibitor (VCI) coatings for metal: a review," *J. Coatings Technol. Res.*, vol. 15, no. 4, pp. 789–807, 2018.

[56] J. Hicks and C. Cracauer, "Vapor Corrosion Inhibitors in Fire Suppression Systems , case study of TEG 159X - Building Fire Protection Systems: Corrosion and Deposit Control," *Cortecvci*, 2013. [Online]. Available: https://www.cortecvci.com/Publications/Papers/NACE-Fire-Protection-Systems .ppt%0A%0A. [Accessed: 02-Jan-2018].

[57] M. M. Antonijevic and M. B. Petrovic, "Copper corrosion inhibitors. A review," *Int. J. Electrochem. Sci.*, vol. 3, no. 1, pp. 1–28, 2008.

[58] M. Antonijevic, S. Milic, M. Petrovic, M. Radovanovic, and A. Stamenkovic, "The Influence of pH and Chlorides on Electrochemical Behavior of Copper in the Presence of Benzotriazole," *Int. J. Electrochem. Sci*, vol. 4, no. July, pp. 962–979, 2009.

[59] E. Stupnišek-Lisac, A. Gazivoda, and M. Madžarac, "Evaluation of non-toxic corrosion inhibitors for copper in sulphuric acid," *Electrochim. Acta*, vol. 47, no. 26, pp. 4189–4194, 2002.

[60] J. Clark, "Lecturer in Heterocyclic chemistry," *University of Glasgow*. Glasgow, p. 107, 2012.

[61] J. J. Li, *Name reactions in Heterocyclic Chemistry*, 1st ed. Hoboken, New Jersey:

John Wiley & Sons. Inc, 2005.

[62]   J. B. Wright, "The Chemistry of the Benzimidazoles.," *Chem. Rev.*, vol. 48, no. 3, pp. 397–541, Jun. 1951.

[63]   P. K. Gupta, "Herbicides and fungicides," in *Biomarkers in Toxicology*, Elsevier Inc., 2014, pp. 409–431.

[64]   E. Gutiérrez, J. A. Rodríguez, J. Cruz-Borbolla, J. G. Alvarado-Rodríguez, and P. Thangarasu, "Development of a predictive model for corrosion inhibition of carbon steel by imidazole and benzimidazole derivatives," *Corros. Sci.*, vol. 108, pp. 23–35, Jul. 2016.

[65]   E.A. Frame, "Evaluations of preservative engine oil containing vapor-phase corrosion inhibitor and a simplified engine preservation technique," in *Interim Report BFLRF No. 269*, San Antonio, Texas, 1991, pp. 19–131.

[66]   G.E. Fodor, "The Inhibition of Vapor-Phase Corrosion: a Review Interim Report BFLRF No. 209," San Antonio, Texas, 1986.

[67]   I. B. Obot, A. Madhankumar, S. A. Umoren, and Z. M. Gasem, "Surface protection of mild steel using benzimidazole derivatives: Experimental and theoretical approach," *J. Adhes. Sci. Technol.*, vol. 29, no. 19, pp. 2130–2152, 2015.

[68]   F. Grillo, D. W. Tee, S. M. Francis, H. A. Früchtl, and N. V. Richardson, "Passivation of copper: Benzotriazole films on Cu(111)," *J. Phys. Chem. C*, vol. 118, no. 16, pp. 8667–8675, 2014.

[69]   J. Colreavy, B. Duffy, R. Varma, Padinchare Covilakath, H. Hayden, and M. Oubaha, "Organosilane Coating Compositions and Use Thereof," Patent No: WO 2009/069111 A2, 2009.

[70]   S. Vijaykumar, O. Prakash, S. Raghavan, K. Ramachandra, and D. Reddy, "Sol-gel coating compositions including corrosion inhibitor-encapsulated layered metal phosphates and related processes," Patent No: US 2018 / 0194949 A1, 2018.

[71]   National Center for Biotechnology Information., "Oleic acid - PubChem - CID 445639," *PubChem Compound Database*, 2019. [Online]. Available: https://pubchem.ncbi.nlm.nih.gov/compound/445639. [Accessed: 02-Jan-2019].

[72]   North American Olive Oil Association, "What is High Oleic Oil," *North American Olive Oil Association*, 2012. [Online]. Available: https://www.aboutoliveoil.org /what-is-high-oleic-oil. [Accessed: 02-Jan-2019].

[73] D. Ben Hmamou *et al.*, "Corrosion Inhibition of Steel in 1 M Hydrochloric Acid Medium by Chamomile Essential Oils," *Int. J. Electrochem. Sci.*, vol. 7, no. 3, pp. 2361–2373, 2012.

[74] J. Zhao and G. Chen, "The synergistic inhibition effect of oleic-based imidazoline and sodium benzoate on mild steel corrosion in a CO_2 -saturated brine solution," *Electrochim. Acta*, vol. 69, pp. 247–255, 2012.

[75] W. Zhang, Z. Guanghua, and Z. Junfeng, "Polyethylene glycol oleic acid based imidazoline water-soluble corrosion inhibitor and preparation method thereof," Patent No: CN107385450 (A), 2017.

[76] M. A. Malik, M. A. Hashim, F. Nabi, and S. A. Al-thabaiti, "Anti-corrosion Ability of Surfactants : A Review," *Int. J. Electrochem. Sci*, vol. 6, pp. 1927–1948, 2011.

[77] M. A. Migahed and A. M. Al-Sabagh, "Beneficial role of surfactants as corrosion inhibitors in petroleum industry: A review article," *Chem. Eng. Commun.*, vol. 196, no. 9, pp. 1054–1075, May 2009.

[78] R. J. Jouet, A. D. Warren, D. M. Rosenberg, V. J. Bellitto, K. Park, and M. R. Zachariah, "Surface Passivation of Bare Aluminum Nanoparticles Using Perfluoroalkyl Carboxylic Acids," *Chem. Mater.*, vol. 17, no. 11, pp. 2987–2996, May 2005.

[79] A. E. Hughes, I. S. Cole, T. H. Muster, and R. J. Varley, "Designing green, self-healing coatings for metal protection," *NPG Asia Materials*, vol. 2, no. 4. pp. 143–151, 2010.

[80] William H. Simendinger, "Antifouling Coating Composition," Patent No: US 6,559,201 B2, 2003.

[81] R. Suleiman *et al.*, "Comparison of selected inhibitor doped sol-gel coating systems for protection of mild steel," *Corros. Eng. Sci. Technol.*, vol. 49, no. 3, pp. 189–196, 2014.

[82] C. J. Brinker and G. W. Scherer, *Sol-gel science: the physics and chemistry of sol-gel processing*, 1st ed., vol. 3, no. 10. New York: Academic Press, 1990.

[83] H. S. Nalwa, "Organic-Inorganic Hybrid Materials from Sonogels," in *Handbook of Organic-Inorganic Hybrid Materials and Nanocomposites*, H. S. Nalwa, Ed. American Scientific, 2003, pp. 241-270 SRC-GoogleScholar FG-0.

[84] S. S. Pathak and S. Khanna, "Sol–gel nano coatings for corrosion protection," *Met.*

Surf. Eng., vol. 12, no. 1, pp. 304–329, 2012.

[85]   C. J. Brinker, "Hydrolysis and condensation of silicates: Effects on structure," *J. noncrystalline solids*, vol. 100, no. 1 SRC-GoogleScholar FG-0, pp. 31–50, 1988.

[86]   L. Hench and J. West, "The Sol-gel Process," in *Chemical Reviews*, vol. 90, no. 1, 1990, pp. 33–72.

[87]   J. Claudionico, "Image of Sol-Gel Technology Stages," *Wikimedia Commons*, 2013. [Online]. Available: https://commons.wikimedia.org/ wiki/File: SolGel TechnologyStages.svg. [Accessed: 20-Jun-2019].

[88]   M. A. Cusanovich, "The Chemistry of Silica," *J. Chem. Educ.*, vol. 57, no. 11, p. A324, 1980.

[89]   P. Gómez-Romero and C. Sanchez, "Hybrid Materials, Functional Applications. An Introduction," *Funct. Hybrid Mater.*, no. June 2017, pp. 1–14, 2005.

[90]   G. Kickelbick, "Introduction to hybrid materials," in *Hybrid Materials*, Weinheim, Germany: Wiley-VCH Verlag GmbH & Co. KGaA, 2007, pp. 1–48.

[91]   T. Gurunathan, S. Mohanty, and S. K. Nayak, "Hyperbranched polymers for coating applications: A Review," *Polym. Plast. Technol. Eng.*, vol. 55, no. 1, pp. 92–117, Jan. 2016.

[92]   A. J. Atanacio, B. A. Latella, C. J. Barbé, and M. V. Swain, "Mechanical properties and adhesion characteristics of hybrid sol-gel thin films," *Surf. Coatings Technol.*, vol. 192, no. 2–3, pp. 354–364, 2005.

[93]   J. Livage and C. Sanchez, "Sol- gel chemistry," *Journal of Non-Crystalline Solids*, vol. 145, pp. 11–19, 1992.

[94]   O. Lev *et al.*, "Sol−Gel Materials in Electrochemistry," *Chem. Mater.*, vol. 9, no. 11, pp. 2354–2375, Nov. 1997.

[95]   W. Trabelsi, L. Dhouibi, F. Matoussi, and E. Triki, "Modification of corrosion behavior of stainless steels with a poly-m-methoxytoluene coating," *Synth. Met.*, vol. 151, no. 1, pp. 19–24, May 2005.

[96]   S. S. Pathak, S. K. Mendon, M. D. Blanton, and J. W. Rawlins, "Magnesium-based sacrificial anode cathodic protection coatings (Mg-Rich Primers) for aluminum alloys," *Metals (Basel).*, vol. 2, no. 3, pp. 353–376, 2012.

[97]   A. S. Hamdy and D. P. Butt, "Environmentally compliant silica conversion coatings

prepared by sol-gel method for aluminum alloys," *Surf. Coatings Technol.*, vol. 201, no. 1–2, pp. 401–407, 2006.

[98] A. Tiwari, L. H. Hihara, R. Atul, H. Lloyd, A. Tiwari, and L. H. Hihara, "Sol-Gel route for the development of smart green conversion coatings for corrosion protection of metal alloys," in *Intelligent Coatings for Corrosion Control*, 2nd ed., A. Tiwari, J. Rawlins, and L. H. Hihara, Eds. Boston: Butterworth-Heinemann, 2015, pp. 363–407.

[99] R. Figueira, I. Fontinha, C. Silva, and E. Pereira, "Hybrid Sol-gel coatings: smart and green materials for corrosion mitigation," *Coatings*, vol. 6, no. 1, p. 12, 2016.

[100] M. L. Zheludkevich, I. M. Salvado, and M. G. S. Ferreira, "Sol-gel coatings for corrosion protection of metals," *J. Mater. Chem.*, vol. 15, no. 48 SRC-GoogleScholar, pp. 5099–5111, 2005.

[101] N. V. Murillo-Gutiérrez, F. Ansart, J. P. Bonino, S. R. Kunst, and C. F. Malfatti, "Architectural optimization of an epoxy-based hybrid sol-gel coating for the corrosion protection of a cast Elektron21 magnesium alloy," *Appl. Surf. Sci.*, vol. 309, pp. 62–73, 2014.

[102] T. H. Kuo, C.-J. Weng, C.-L. Chen, Y.-L. Chen, C.-H. Chang, and J.-M. Yeh, "Electrochemical investigations on the corrosion protection effect of poly(vinyl carbazole)-silica hybrid Sol–gel materials," *Polym. Compos.*, vol. 33, no. 2, pp. 275–281, 2013.

[103] H. Wang and R. Akid, "A room temperature cured sol-gel anticorrosion pre-treatment for AA 2024-T3 alloys," *Corros. Sci.*, vol. 49, no. 12, pp. 4491–4503, 2007.

[104] M. Fedel, E. Callone, M. Fabbian, F. Deflorian, and S. Dirè, "Influence of Ce3+ doping on molecular organization of Si-based organic/inorganic sol-gel layers for corrosion protection," *Appl. Surf. Sci.*, vol. 414, pp. 82–91, 2017.

[105] F. Yu and R. Akid, "Corrosion protection of AA2024-T3 alloy by modified hybrid titania-containing sol-gel coatings," *Prog. Org. Coatings*, vol. 102, pp. 120–129, 2017.

[106] M. S. Sharifiyan, A. Shanaghi, H. Moradi, and P. K. Chu, "Effects of high concentration of benzotriazole on corrosion behavior of nanostructured titania-alumina composite coating deposited on AA 2024 by sol-gel method," *Surf.*

Coatings Technol., vol. 321, pp. 36–44, 2017.

[107] W. S. Tait, *Electrochemical impedance spectroscopy fundamentals, an introduction to electrochemical corrosion testing for practicing engineers and scientists*. Racine, Wisconsin, USA: PairODocs Publications, 1994.

[108] N. Cogger and N. J. Evans, "An introduction to electrochemical impedance," *Solartron Anal.*, vol. 155, no. 6, pp. 1–14, 1999.

[109] Gamry instruments, "Basics of Electrochemical Impedance Spectroscopy," *Application Note*, 2016. [Online]. Available: http://scholar.google.com/scholar?hl=en&btnG=Search&q=intitle:Basics+of+Electrochemical+Impedance+Spectroscopy#2. [Accessed: 01-Feb-2017].

[110] J. Scully, "Polarization resistance method for determination of instantaneous corrision rates.," *NACE Int.*, vol. 56, no. 2, pp. 199–218, 2000.

[111] D. H. Johnson, "Origins of the equivalent circuit concept: The voltage-source equivalent," *Proc. IEEE*, vol. 91, no. 4, pp. 636–640, 2003.

[112] E. P. Randviir and C. E. Banks, "Electrochemical impedance spectroscopy: an overview of bioanalytical applications," *Anal. Methods*, vol. 5, no. 5, p. 1098, 2013.

[113] S. Jiménez, G. Tejera, G. Torrado, and R. Mirza, "Interpretation of open circuit potential of two titanium alloys for a long time immersion in physiological fluid," *Bull. Transilv. Univ. Braşov*, vol. 2(51), no. 1, pp. 196–204, 2009.

[114] Gamry instruments, "Getting Started with Electrochemical Corrosion Measurement Introduction," *Gamry instruments*, 2011. [Online]. Available: https://www.gamry.com/assets/Application-Notes/Getting-Started-with-Electrochemical-Corrosion-Measurement.pdf. [Accessed: 21-Jan-2019].

[115] F. J. Ansuini and J. R. Dimond, "Factors Affecting the Accuracy of Reference Electrodes," *Repr. from Mater. Perform.*, vol. 33, no. 11, pp. 14–17, 1994.

[116] S. Wang, "Corrosion Resistance and Electrocatalytic Properties of Metallic Glasses," in *Metallic Glasses - Formation and Properties*, vol. 395, no. tourism, InTech, 2016, pp. 116–124.

[117] J. Hilher, "The electron microscope in the determination of particle size characteristics," in *Symposium on New Methods for Particle Size Determination in the Subsieve Range-ASTM*, 1941, pp. 90–95.

[118] V. K. Zworykin, "Scanning Electron Microscope ASTM Bulletin 1942," Philadelphia USA, 1942.

[119] K. C. A. Smith, O. C. Wells, and D. McMullan, "The fiftieth anniversary of the first applications of the scanning electron microscope in materials research," *Physics Procedia*, 2008. [Online]. Available: http://dx.doi.org/10.1016/ j.phpro.2008.07.073.

[120] Purdue University, "Scanning Electron Microscope," *Purdue University*, 2016. [Online]. Available: https://www.purdue.edu/ehps/rem/laboratory/equipment safety/Research Equipment/sem.html#1. [Accessed: 23-Jan-2019].

[121] K. Boberg, "Slideshare.net . SEM, AFM, and 3 Profiler Introduction," *Linkedin Slideshare*, 2015. [Online]. Available: https://www.slideshare.net/ bitesizedlife/sem-afm-3dtraining. [Accessed: 28-Jan-2019].

[122] G. Zeng, Y. Duan, F. Besenbacher, and M. Dong, "Nanomechanics of Amyloid Materials Studied by Atomic Force Microscopy," *At. Force Microsc. Investig. into Biol. - From Cell to Protein*, no. May 2014, 2012.

[123] S. Chatterjee, S. S. Gadad, and T. K. Kundu, "Atomic Force Microscopy A Tool to Unveil the Mystery of Biological Systems," *Resonance*, no. July, pp. 622–642, 2010.

[124] BRUKER, "Multimode-8 Atomic Force Microscopy (AFM) user Manual," California, USA, 2008.

[125] Alicona, "Infinite Focus G5," *data sheet*. Alicona, Ohaio, p. 1, 2018.

[126] J. Wang, Y. Yu, and D. Chen, "Research progress on the ultra hydrophobic surface topography effect," *Chinese Sci. Bull.*, vol. 51, no. 19, pp. 2297–2300, 2006.

[127] R. Förch, H. Schönherr, and A. T. A. Jenkins, *Surface Design: Applications in Bioscience and Nanotechnology*. Morlenbach: Wiley-VCH, 2009.

[128] Sheffield Hallam University, "Contact angle Goniometer Measurement," *MERI-SHU web page*, 2015. [Online]. Available: https://www.shu.ac.uk/ research/specialisms/materials-and-engineering-research-institute/facilities/ contact-angle-measurement. [Accessed: 01-Feb-2019].

[129] K. G. Kabza and K. Cochran, "From Polarimeter to Contact Angle Goniometer - Inexpensive Conversion of Laboratory Equipment," *J. Chem. Educ.*, vol. 74, no. 3, p. 322, 1997.

[130] G. Bracco and B. Holst, "Contact Angle and Wetting Properties," in *Springer Series in Surface Sciences*, vol. 51, no. 1, Springer, 2013.

[131] H. Günzler and A. Williams, *Handbook of Analytical Techniques*. Weinheim, Germany: Wiiey-VCH Veriag GmbH & Co, 2008.

[132] ASTM International, "Standard Test Method for Pull-Off Strength of Coatings Using Portable Adhesion Testers," West Conshohocken, Pa. USA, D4541-17, 2017.

[133] A. A. Tracton, *Coatings Technology Handbook*, Third Edit. Boca Raton, FL, USA: Taylor & Francis Group, 2006.

[134] ASTM International, "Standard Test Methods for Rating Adhesion by Tape Test," West Conshohocken, Pa. USA, D3359-17, 2017.

[135] ASTM International, "Standard Test Methods for Vickers Hardness and Knoop Hardness of Metallic Materials," ASTM International, West Conshohocken, Pa. USA, E92-17, 2019.

[136] Struers Energy Certainty, "Duramin-40 - hardness tester Struers," *Struers Energy Certainty*, 2019. [Online]. Available: https://www.struers.com/en-GB/Products/ Hardness-testing/Hardness-testing-equipment/Duramin-40#references. [Accessed: 20-May-2019].

[137] R. Ferencz, J. Sanchez, B. Blümich, and W. Herrmann, "AFM nanoindentation to determine Young's modulus for different EPDM elastomers," *Polym. Test.*, vol. 31, no. 3, pp. 425–432, 2012.

[138] R. Yang, N. Xi, C. K. M. Fung, K. Seiffert-Sinha, K. W. C. Lai, and A. A. Sinha, "The Emergence of AFM Applications to Cell Biology: How new technologies are facilitating investigation of human cells in health and disease at the nanoscale," *J. Nanosci. Lett.*, vol. 2, no. 1, pp. 87–101, 2011.

[139] ASTM International Team, "ASTM B209M-14-Standard Specification for Aluminum and Aluminum-Alloy Sheet and Plate (metric)," *ASTM International*, 2014. [Online]. Available: https://compass-astm-org.hallam.idm.oclc.org/ download/B209M.37282.pdf. [Accessed: 01-Feb-2019].

[140] H. Wang and V. Kumar, "Transparent and conductive polysiloxanes / PEDOT:PSS nanocomposite thin films with a 'water-impermeable' property to significantly enhance stability of organic–inorganic hybrid solar cells," *RSC Adv.*, vol. 5, no. 13,

pp. 9650–9657, 2015.

[141] N. Birbilis and B. Hinton, "Corrosion and corrosion protection of aluminium," in *Fundamentals of Aluminium Metallurgy; Production, Processing and Applications*, R. Lumley, Ed. Oxford: Woodhead Publishing Limited, 2011, pp. 574–604.

[142] N. V. Usoltseva, V. V. Korobochkin, M. A. Balmashnov, and A. S. Dolinina, "Solution Transformation of the Products of AC Electrochemical Metal Oxidation," *Procedia Chem.*, vol. 15, no. December, pp. 84–89, 2015.

[143] M. Finšgar and J. Jackson, "Application of corrosion inhibitors for steels in acidic media for the oil and gas industry: A review," *Corros. Sci.*, vol. 86, pp. 17–41, 2014.

[144] D. Brett, *Oil and gas industry projects*, 2nd ed., vol. 90, no. 4. CRC Press ; Taylor and Francis distributor, 2012.

[145] Thermo scientific, "Knowledge base infrared spectral interpretion." Thermo Fisher Scientific, Madison, USA, pp. 1–77, 2009.

[146] I. V. Chernyshova, S. Ponnurangam, and P. Somasundaran, "Adsorption of fatty acids on iron (hydr)oxides from aqueous solutions," *Langmuir*, vol. 27, no. 16, pp. 10007–10018, 2011.

[147] S. Loehle, "Understanding of adsorption mechanisms and tribological behaviors of C18 fatty acids on iron-based surfaces: a molecular simulation approach," PhD thesis. Université de Lyon, 2014.

[148] S. Mohan, N. Sundaraganesan, and J. Mink, "FTIR and Raman studies on benzimidazole," *Spectrochim. Acta Part A Mol. Spectrosc.*, vol. 47, no. 8, pp. 1111–1115, 1991.

[149] R. R. Sahoo and S. K. Biswas, "Frictional response of fatty acids on steel," *J. Colloid Interface Sci.*, vol. 333, no. 2, pp. 707–718, 2009.

[150] T. Kobayashi and H. M. Hugel, "Special issue, organo-fluorine chemical science-inventing the fluorine future," in *Applied Sciences*, Basel, Switzerland: Multidisciplinary Digital Publishing Institute (MDPI), 2012, pp. 1–283.

[151] A. Yabuki, H. Yamagami, and K. Noishiki, "Barrier and self-healing abilities of corrosion protective polymer coatings and metal powders for aluminum alloys," *Mater. Corros.*, vol. 58, no. 7, pp. 497–501, 2007.

[152] R. Arrabal, B. Mingo, A. Pardo, M. Mohedano, E. Matykina, and I. Rodríguez, "Pitting corrosion of rheocast A356 aluminium alloy in 3.5wt.% NaCl solution," *Corros. Sci.*, vol. 73, no. 1, pp. 342–355, Aug. 2013.

[153] L. Wen, Y. Wang, Y. Zhou, J. H. Ouyang, L. Guo, and D. Jia, "Corrosion evaluation of microarc oxidation coatings formed on 2024 aluminium alloy," *Corros. Sci.*, vol. 52, no. 8, pp. 2687–2696, 2010.

[154] R. Mohan and A. Joseph, "Corrosion protection of mild steel in hydrochloric acid up to 313 K using propyl benzimidazole: Electroanalytical, adsorption and quantum chemical studies," *Egy. J. Pet.*, vol. 27, no. 1, pp. 11–20, Mar. 2018.

[155] N. Kovačević and A. Kokalj, "Analysis of molecular electronic structure of imidazole- and benzimidazole-based inhibitors: A simple recipe for qualitative estimation of chemical hardness," *Corros. Sci.*, vol. 53, no. 3, pp. 909–921, 2011.

[156] Z. fang Cao *et al.*, "Formation of a hydrophobic and corrosion resistant coating on manganese surface via stearic acid and oleic acid diethanolamide," *Colloids Surfaces A Physicochem. Eng. Asp.*, vol. 555, no. April, pp. 372–380, 2018.

[157] Sandra Kay Young, "Sol-Gel Science for Ceramic Materials," in *Material Matters "Sigma-Aldrich,"* 2006, vol. 1, no. 3, pp. 8–9.

[158] J. D. Mackenzie, "Applications of the sol-gel process," *J. Non. Cryst. Solids*, vol. 100, no. 1–3, pp. 162–168, 1988.

[159] S. B. Lyon, R. Bingham, and D. J. Mills, "Advances in corrosion protection by organic coatings: What we know and what we would like to know," *Prog. Org. Coatings*, vol. 102, pp. 2–7, 2017.

[160] O. Lev *et al.*, "Organically modified sol-gel sensors," *Anal. Chem.*, vol. 67, no. 1, pp. 22–30, 1995.

[161] J. Brassard, D. K. Sarkar, and J. Perron, "Fluorine Based Superhydrophobic Coatings," *Appl. Sci.*, vol. 2, no. 2, pp. 453–464, 2012.

[162] D. Kumar *et al.*, "Development of durable self-cleaning coatings using organic-inorganic hybrid sol-gel method," *Appl. Surf. Sci.*, vol. 344, pp. 205–212, 2015, doi: 10.1016/j.apsusc.2015.03.105.

[163] F. Malekmohammadi, A. Sabour Rouhaghdam, and T. Shahrabi, "Effect of heat treatment on corrosion properties of mixed sol gel silica–titania (7:3) coating," *J. Non. Cryst. Solids*, vol. 357, no. 3, pp. 1141–1146, Feb. 2011.

[164] D. Fernando *et al.*, "The influence of precursor addition order on the porosity of sol–gel bioactive glasses," *Dent. Mater.*, vol. 34, no. 9, pp. 1323–1330, Sep. 2018.

[165] B. El Ibrahimi, A. Jmiai, L. Bazzi, and S. El Issami, "Review :Amino acids and their derivatives as corrosion inhibitors for metals and alloys," *Arabian Journal of Chemistry*, King Saud University, Agadir, pp. 1–32, 2017.

[166] A. Fateh, M. Aliofkhazraei, and A. R. Rezvanian, "Review of corrosive environments for copper and its corrosion inhibitors," *Arab. J. Chem.*, no. 1, pp. 1–63, 2017.

[167] E. M. Fayyad, K. K. Sadasivuni, D. Ponnamma, and M. A. A. Al-Maadeed, "Oleic acid-grafted chitosan/graphene oxide composite coating for corrosion protection of carbon steel," *Carbohydr. Polym.*, vol. 151, pp. 871–878, Oct. 2016.